Air Force Institute of Technology

# AFIT Scholar

3-2005

# Experimentation and Analysis of Composite Scarf Joint

Benjamin M. Cook

**EXPERIMENTATION AND ANALYSIS OF COMPOSITE SCARF JOINT**

THESIS

Benjamin M. Cook, Captain, USAF

AFIT/GA/ENY/05-M03

**DEPARTMENT OF THE AIR FORCE**
**AIR UNIVERSITY**

# AIR FORCE INSTITUTE OF TECHNOLOGY

**Wright-Patterson Air Force Base, Ohio**

APPROVED FOR PUBLIC RELEASE, DISTRIBUTION UNLIMITED

The views expressed in this thesis are those of the author and do not reflect the official policy or position of the United States Air Force, Department of Defense or the United States Government.

AFIT/GA/ENY/05-M03

EXPERIMENTATION AND ANALYSIS OF COMPOSITE SCARF JOINT

THESIS

Presented to the Faculty

Department of Aeronautics and Astronautics

Graduate School of Engineering and Management

Air Force Institute of Technology

Air University

Air Education and Training Command

In Partial Fulfillment of the Requirements for the

Degree of Master of Science in Aeronautical Engineering

Benjamin M. Cook

Captain, USAF

March 2005

APPROVED FOR PUBLIC RELEASE, DISTRIBUTION UNLIMITED

ii

AFIT/GA/ENY/05-M03

EXPERIMENTATION AND ANALYSIS OF COMPOSITE SCARF JOINT

Benjamin M. Cook, BS
Captain, USAF

Approved:

/signed/

_____          _____
Anthony N. Palazotto (Chairman)                      date

/signed/

_____          _____
Professor Marina B. Ruggles–Wrenn (Member)           date

/signed/

_____          _____
Professor Theodore Nicholas (Member)                 date

AFIT/GA/ENY/05-M03

## Abstract

Composite bonded scarf repairs were examined by experimentally measuring and analytically predicting the residual curing strains and strains due to mechanical loading. To accomplish this a three prong approach was used: a full strain field through a repaired laminate's thickness was measured for both a loaded specimen and a specimen with the residual strain released, models were developed for comparison to both states, and data was collected for large tensile test specimens at various stages of being scarf repaired. A ~14:1 straight scarfed one-inch wide specimen was used to collect Moiré interferometry data to measure a full field strain due to mechanical loading and strain release. A three-dimensional thermo mechanical linear elastic analysis using an Air Force Research Laboratory in-house stress analysis program B-Spline Analysis Method (BSAM) results were correlated to the Moiré interferometry test results. Three large tensile test specimens were tested as manufactured, three were tested with a scarfed hole in the center, and the remaining were tested with a scarf repair centered on a hole in the center. The strain gage results from the panels are presented. An additional feature of this work was to document each of the difficulties present in the given methods incorporated in this research.

*To my father*

## Acknowledgements

There have been so many people that have been very helpful in developing my thesis. Greg Schoeppner, my sponsor, and Dr. Anthony Palazotto, my adviser, gave particular insight and guidance throughout my thesis. If this thesis is any good, it is Greg's fault.

I would like to thank David Mollenhauer for running the Moiré interferometer. Greg, David, and Endel Iarve deserve thanks for guidance with the BSAM program.

I want to thank Paul Childress for his assistance and technical prowess. The help from AFRL/MLS was essential in providing key information on the adhesives and in running the large specimen tensile testing. Ron Esterline, and others at MLBC, gave time, critical input, and assistance.

Additionally, I would like to thank my fellow astro students for their help. Finally, special thanks to my wife for her support.

<div align="right">Benjamin M. Cook</div>

**Table of Contents**

# List of Figures

# List of Tables

EXPERIMENTATION AND ANALYSIS OF COMPOSITE SCARF JOINT

## I. Introduction

**Motivation**

Programs to extend the life of the aging Air Force fleet will undoubtedly have an increasing reliance on adhesively bonded repairs and the life expectancy of the adhesive repairs will need to be extended. The use of adhesively bonded composite patches on curved surfaces is pervasive for maintaining and repairing both composite and metallic structures. In particular, the repair of advanced stealth aircraft requires the use of flush patches that do not change the outer mold line of the aircraft. Restoration of the stiffness and strength of composite aircraft structures with flush scarf or step lap repairs is an enabling technology for maintaining fleet readiness. Further understanding of the scarf joint is needed to continue to make repairs easier, better, and more cost effective.

**Background**

A composite scarf joint is a bond between two separate laminates, where the bondline is at a set angle between the two laminates. This joint is used to maintain a high strength while joining two adherends. The scarf repair is a patch that is bonded into the parent material using a scarf joint. A scarf repair gains back much of the original parent laminates strength, while still maintaining the parent laminate's surface contour.

Research on composite scarf joints or repairs has been addressed using many different experimental and analytical tools. Traditional methods, such as testing structures after a repair has been made and analysis methods such as classical laminate plate theory, have been used for a long time. More recently, finite element modeling and other modeling methods have been applied to the understanding of the complexities of the scarf joint.

Knox, Chotard and Charalambides (2001) are good examples of research on scarf joints through experimentation. Knox studied glass-reinforced epoxy piping systems that used composite tapered pipe joints during assembly of the system. Scarfed pipes were tested under a bending load and uniaxial tension, with the experimental results compared to a finite element model consisting of layers of orthotropic homogeneous lamina and an isotropic adhesive layer. The finite element code made reasonable predictions on the failure and demonstrated failure in both the adhesive and composite. Chotard and others (2001) proposed using external scarf patches on pultruded structures as a low cost method of regaining most of the structures strength, possibly more than 85% of the strength of an undamaged structure, after four point bending static and fatigue testing on numerous specimens. Testing showed that, depending on the load geometry, the 85% strength restoration percentage was achieved. Charalambides and others (1998a) also studied static and fatigue loading properties in flat panels. Properties from large undamaged panels were compared to large panels with centrally located repairs. He discovered that static properties were similar, but fatigue properties were inferior in the repaired panels. At the same loading, the repaired panels were only able to last to a few percent of the load cycles that a parent panel did. After testing, multiple finite element

models were created that matched the experimental results from the static and fatigue studies on flat panels. The material properties of the laminate were modeled in two different ways; the first treated the composite as a homogeneous orthotropic material with smeared properties and the other model gave orthotropic and anisotropic properties to each ply depending on fibre orientation (Charalambides and others, 1998b).

Simplified models have also been developed to further understand and predict the failure and properties of a scarf joint. Baker and others (2004:317-319) mentions a simple strength of materials analysis calculation of shear stresses in scarf joints, Figure 1, when the stiffness and coefficient of expansion is similar in the adherends.



$$t' = t/\sin\theta$$
$$\sigma_T = P\sin^2\theta/t \qquad \tau = P\sin\theta\cos\theta/t$$
so $\quad \sigma_T/\tau = \tan\theta = \theta(\text{radians})$
for adherend failure before adhesive yield
$$P_{max} = \sigma_u t < \tau_P t/\sin\theta\cos\theta$$
thus $\quad \theta < \tau_P/\sigma_u \ (\text{radians})$
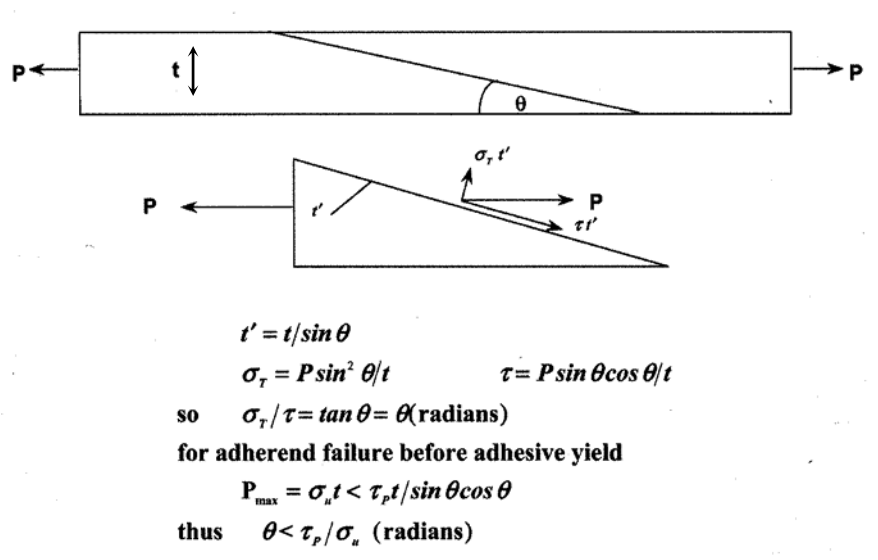
**Figure 1. Simple strength of materials analysis of a scarf joint (Baker, 2004:317)**

Here t is thickness of laminate, $\theta$ is the scarf angle, P is the applied load on the laminate, $\sigma_T$ is the uniform normal stress, $\tau$ is the uniform shear stress, $\tau_P$ is the shear stress in the elastic condition, $\sigma_u$ is the ultimate normal stress, and $P_{max}$ is the ultimate applied load. A

simple algebraic formula was developed that set a lower bond approximation for

properties of a scarf joint by Hart-Smith (1973):

$$\frac{\tau_{av}}{\tau_p} = etr(1) + \frac{[1 + etr(1)]ctherm(1)}{\lambda * L} + \frac{a}{L}\left\{[1 - etr(1)] - \frac{[1 + etr(1)]ctherm(1)}{\lambda * L}\right\} \qquad (1)$$

where $\tau_{av}$ is average adhesive shear stress in psi, $\tau_p$ is plastic (maximum) adhesive shear

stress in psi, etr(1) is adherend extensional stiffness ratio, ctherm(1) is a non-dimensional

adherend thermal mismatch coefficient, $\lambda$ is exponent of elastic shear stress distribution

(in$^{-1}$), L is the overlap or bond length in inches, and a is the extent of plastic stress state in

adhesive at the end of the bonded joint in inches. The Federal Aviation Administration

commissioned a report by Ahn and Spinner (2000) to develop models and computer

programs in MATLAB to predict the failure of bonded joints using data from testing

various joints to failure. The failure trends from the model matched the failure trends

from the experimental testing, but the absolute load values at failure did not match. The

models developed were recommended for design guidelines and not for actual failure

value predictions.

Classical laminate plate theory has also been used to model composite adhesive-

bonded joints. Using this theory and an adhesive linear elastic constitutive model, Zou

and others (2004) predicted solutions for bonded single lap and single strap joints in

composites that are balanced and symmetric. These results compared favorably to finite

element modeling. Mortensen and Thomsen (2002) developed a unified approach for

adhesive bonded joints modeling the adherends as beams or wide plates in cylindrical

bending and the composite adherends as generally orthotropic laminates using classical

laminate theory. The approach was verified by comparing with finite element models.

From these studies and others, it should be noted that finite element analysis is often used as a comparison to experimental data or as a verification of other modeling techniques. In 2004, a new modeling approach in finite element analysis, the NISA program, was investigated that models bonded composite scarf joints through a two-dimensional plane stress approach maintaining the laminated nature of the composite adherends. Failure predictions of composite joints under tensile loading from this new method were compared favorably to published experimental results for various scarf angles (Odi and Friend, 2004).

Three-dimensional analysis methods have been developed to analyze composites. Hinrichsen and Palazotto (1986) developed a quasi-three-dimensional finite element analysis that allowed for large rotations of the structure, but restricted the element to small strains. The comparison of linear and nonlinear predictions in thick orthotropic plates from published analytical and numerical results verified the model. Another 3-D finite element stress analysis by Soutis and Hu (1998) used in conjunction with a simple closed form solution for a composite scarf joint type bonded repair was used to predict failure loads. If the joint is subjected to uniaxial compression, the finite element analysis model predicted more than 80% undamaged strength recovery by setting an optimal scarf angle of 7°. The model was in good agreement with experimental strength data.

The use of cubic spline basis functions in the development of a finite element code has also been employed for predicting through-the-thickness displacement values for a composite plate (Hinrichsen and Palazotto, 1988). The cubic spline maintains consistent interlaminar shear strains by insuring compatibility of lamina interface displacements and their first and second derivatives. Iarve (1996) furthered the use of

splines by modeling a hole in a AS4/3501-6 laminate under uniaxial tension with a polynomial spline approximation. He used the cubic spline for not just through the thickness calculations, but in all three orthogonal directions. The results in a three-dimensional full field solution were validated in the vicinity of the hole's edge and showed excellent agreement to observed interlaminar stresses (Iarve, 1996). Using the program developed by Iarve and others, called the B-Spline Analysis Method or BSAM for short, Bowman (2001) modeled the residual stresses at the edge of a two layer composite composed of an adhesive layer and metallic layer. The experimental method used to validate the model was a technique called Material Removal for Free Edge Evaluation (MRFEE). The material at the edge was removed layer-by-layer while using Moiré interferometry to measure displacements caused from releasing residual curing strains with each layer. The three-dimensional full field model, using BSAM, was compared to the experimental results with excellent correlation (Bowman, 2001). The Moiré interferometry data is taken at the surface of the material and therefore contains a large amount of edge effects or deformation resulting from the three-dimensional nature of the material. Because of this, a three-dimensional model is needed for comparison, precluding a more simple a plane strain calculation being used.

Further use of Moiré interferometry and the BSAM was done at Air Force Research Laboratory's Materials Directorate. A bonded lap joint with IM6/3501-6 quasi-isotropic adherends was modeled and the predictions were compared to measurements of residuals free-edge strains taken with Moiré interferometry (Schoeppner, Mollenhauer, and Iarve, 2004). The techniques developed and demonstrated by Bowman (2001) Schoeppner, Mollenhauer and Iarve (2004) were followed for this thesis.

**Problem Statement**

The objective of this thesis is to analytically predict and experimentally measure the strains due to mechanical loading and the residual curing strains in a composite bonded scarf repair. To accomplish this a three prong approach was used: a full strain field through a repaired laminate's thickness was measured for both a loaded specimen and a specimen with localized residual strain released, models were developed for comparison to both states, and data was collected for large tensile test specimens at various stages of being scarf repaired.

**Overview of Thesis**

Chapter 2 contains a summary of the methods used to create the specimens for Moiré interferometry testing and the large panel tensile testing specimens. Twelve unidirectional tape $[+45/0/-45/90]_s$ composite laminate panels approximately 24" by 12" were made of IM6/3501-6 and cured per the manufacturer's recommended cure cycle. Three one-inch tensile Moiré interferometry test coupons were manufactured with a 1:20 scarf angle in the middle of the coupon using FM 300-05M adhesive to bond the joint. A diffraction grating was then applied to the edges of the coupons in the region of the bondlines. Ten 22.5" by 5.24" tensile testing specimens were prepared from the 24" by 12" panels: three were virgin, three were circular scarfed at a 1:20 angle in the center, and four were scarfed and repaired. The scarfing of the panels was done using a scarfing machine, which allows for repeatability. For the repair, each of the removed plies was replaced with a repair ply of the same orientation creating a patch, which was co-bonded

7

on to the specimen using FM 300-05M film adhesive.  All the specimens were tabbed and strain gages were applied.

Chapter 3 compares the free-edge strain field results from the tensile loading of the one-inch scarfed tensile test specimen to the BSAM model.  Moiré interferometry data was collected for one of the specimens in both an unloaded and loaded state for mechanical loading strain calculations.  The strains were calculated and compared to a three-dimensional thermo-mechanical linear elastic analysis performed using an Air Force Research Laboratory in-house stress analysis program B-Spline Analysis Method (BSAM).  A model was generated to match the mechanically loaded case and some correlation was shown, specifically with the critical shear strain measurements.

Chapter 4 compares the results of Moiré interferometry residual strain data collected from the one-inch scarfed tensile test specimens to a BSAM model.  A Moiré tensile testing specimen was cut in the bondline region through the thickness to locally release the residual curing stresses.  Moiré interferometry data was taken before and after cutting, which was used to calculate the residual strains.  Additional BSAM models were created to collectively represent the strain changes in the specimen due to cutting.  Some correlation was shown, though large signal noise limited the matching between data sets.

Chapter 5 discusses the results from tensile testing to failure of the large tensile testing specimens.  Strain gage data was analyzed and the data was analyzed preliminarily.  The results followed the expected results.

In Chapter 6, conclusions and recommendations for follow-on work are given.

## II. Methodology

### Straight Scarf Specimens

For testing the load and residual strains in a laminate, one-inch by ten-inch straight scarf joint tensile test specimens were prepared and tested with Moiré interferometry. A further explanation of Moiré interferometry is included in Chapter 3. During the manufacturing sequence, the material was laid up and cured prior to being scarfed and then bonded back together with an adhesive film. The bonded panels were then cut to the proper dimensions. A diffraction grating was bonded to the edge of the specimens in preparation for Moiré data collection. Testing procedures for the loaded specimen are explained. After collection of mechanical load data, the tensile specimen was then cut to a two inch length in preparation for residual strain Moiré measurements. The test steps for the residual Moiré data collection are outlined.

#### Panel Manufacture

Twelve 12 inch by 24 inch panels were laid up using IM6/3501-6 epoxy pre-impregnated carbon fiber unidirectional tape orienting the fibers of the lamina to $[45/0/-45/90]_s$, with a total thickness of 0.044". A Teflon porous peel ply, and Teflon nonporous ply were placed on either side of the layups. The layups were placed on a tool plate, to ensure flatness of the final specimen. Bleeder and breather clothes were placed over the Teflon covered layups to ensure uniform vacuum transfer during curing. Vacuum bags with an edge sealant, or a special double-sided tape, were used to seal the encased layups to the tool plate (Figure 2 and Figure 3).
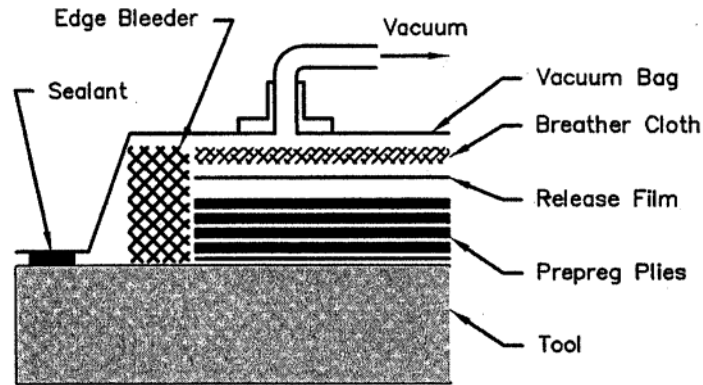
**Figure 2.  Schematic diagram of vacuum bag layup, indicating various layers used (Baker, 2004:125)**
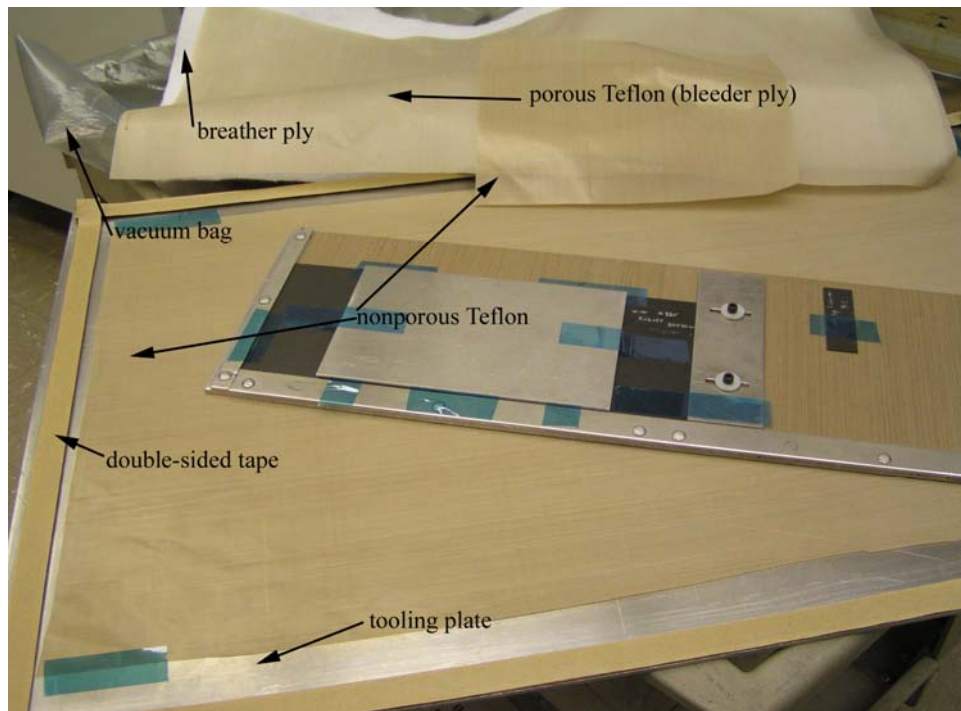


**Figure 3.  Photograph of a typical autoclave curing setup**

The layups were cured in pairs, using the manufacturer's recommended autoclave cure

cycle of applying vacuum, ramping the temperature at five degrees Fahrenheit per minute

to 250° F, holding for one hour, pressurizing to 100 psi, ramping at five degrees

Fahrenheit per minute to ~350° F, maintaining for two hours, then cooling down the

layups at five degrees Fahrenheit to 100° F and release pressure. The cured panels had no major internal flaws as determined by ultrasonic C-scanning. A visual inspection verified no major surface flaws, and revealed a minor flaw in one panel to be discussed later.

**Specimen Manufacture**

One panel was randomly selected (from the panels that appeared to have no minor flaws) to be used for manufacturing of the straight scarfed coupon specimens. This panel was trimmed on all edges by approximately a half inch, to eliminate the epoxy rich edges as well as the flashing generated during autoclave curing. The panel was cut with a wet diamond bladed radial arm saw into four equal sections measuring approximately five inches wide by ten inches long. Careful attention was taken to panel aligning the panel for cutting, using the top 45° ply to ensure the panel edges were cut at 0° and 90°.

In order to create an idealized scarf joint for testing, one of the one-inch wide edges of each coupons was ground at an angle of 1:20, thereby creating the scarf angle. This scarf angle was selected because it is commonly used in composite repairs on aircraft. Since the thickness of the laminate was approximately 0.04", or 0.005" per ply, the length of the scarf from the tip of the scarf to the top ply of the laminate was anticipated to be approximately 0.8 inches. Matching pairs of scarfed sections were created, maintaining the top ply's fiber orientation on both sides of the joint. To do this, one section was scarfed from the bottom and the matching section was scarfed from the top as illustrated in Figure 4.
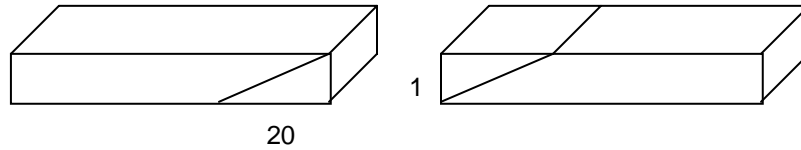
**Figure 4.  Illustration of straight scarf alignment**

In order to increase the precision of the scarf angle, an attempt was made to have the sections machine ground, but this created unsatisfactory results.  The sections had scarfs that were not at a constant angle and the top ply was damaged from scoring the surface, marking the scarf's anticipated termination.  During sanding, plies were removed causing the laminate to become unsymmetric in the scarf region.  The unsymmetric nature of the laminate induces a bending extension coupling, due to residual curing stresses.  During the original machine grinding, the sections were not held flat and the laminate tip tended to bend upward, which caused more material to be removed from the tip, resulting in a non-uniform scarf angle.  The method that was finally used to obtain satisfactory scarf angles was hand scarfing.  The laminates were taped to the backing plate.  Using metal guides to maintain the scarf angle, a sanding block was rubbed back and forth on the edge of the laminate, as shown in Figure 5.  During hand sanding the laminate remained flat due to the backing plate due to the double-sided tape and an acceptable scarf angle was obtained.  The final angle was approximately 1:13.6.  Even though this was a lower than expected scarf angle, because the exposed plies were fairly consistent in length over the width of the section, which revealed that the scarf angle was constant over the width, the new scarf angle was deemed acceptable.  Hand scarfing a straight panel took approximately four hours for the first panel and three hours for each panel afterward.

12
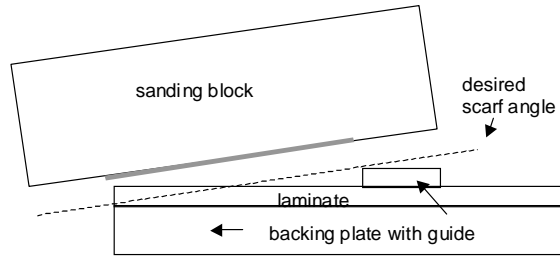
**Figure 5. Illustration of hand sanding technique for straight scarf angle in laminate**

FM 300-05M was selected to bond the two matching sections together. The main reasons for selection was 1) availability and 2) the adhesive is a 350°F cure system, which allows co-curing the repair patch for 350°F cure composite resins. The adhesive film was cut to match the scarfed sections width. An anticipated adhesive length was calculated to be 0.88" using the designed angle of the scarf, anticipated thickness of cured adhesive, and the average measured thickness of the laminate, all shown in Figure 6. But length needed to be modified due to the measured scarf angle being lower (1:~13.63) than the desired scarf angle and the variation of the scarf angle across the width, both of which were due to manual hand sanding variability. Overlaying the matched sections created a length of 0.88", which is reasonable when compared to the desired scarf length. Additionally, if more than the needed amount of adhesive was applied, the excess would flow out of the joint, thereby maintaining the bondline thickness.
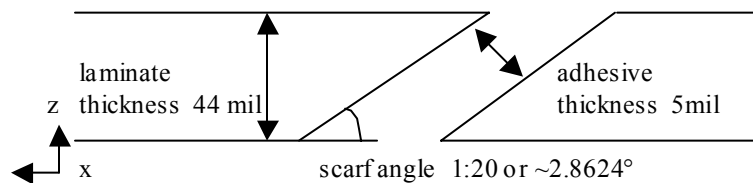


**Figure 6. Scarf angle and adhesive thickness illustration**

13

Each bond surface had been sanded during scarfing, but further surface preparation was needed prior to bonding. The surfaces were wiped with dry, clean, lint free paper until the paper came away clean. The surfaces were solvent then wiped with acetone.

To keep the two adherend sections and the adhesive from shifting during autoclave curing, a jig was made, shown in Figure 7. The jig held the sections in both the horizontal and vertical directions maintaining parallel scarfed edges. The jig was placed on a tooling plate and a caul plate was placed on the top of the panel to keep the panel from warping during autoclave curing.



**Figure 7. Jig to align and stabilize straight scarfed panels during autoclave curing**

The adhesive was autoclave cured according to manufacturer's recommended cure cycle, as follows: apply 45 psi pressure, 90-minute ramp to 350° F, and hold for 60 minutes.

Approximately ¼" on the edges of the bonded sections were removed; to avoid possible edge effects in the specimens from the adhesive curing cycle. These edge pieces were examined under the microscope and used to verify the bondline thickness and scarf angle. After curing, the sections were cut into three specimens for tensile loaded Moiré testing. Each of the three specimens were one inch wide and ten inches long with the scarf bond region at the mid length, following the recommendation from ASTM D-

3039M for tensile testing specimens. A photograph taken with the microscope was used to measure the bondline and scarf angle by comparing pixel counts to pixel counts of the thickness of the laminate, which is a known value. The bondline was of uniform thickness in the center of the joint, but the top and bottom of the bondline expanded in thickness, which can be seen in Figure 8.



**Figure 8. Photograph o f the bondline viewed through the thickness**

### Application of Diffraction Grating

As part of the process of applying a diffraction grating, the three specimens were prepared for bonding. The set of specimens with spacers between each specimen were clamped together. The side edges of all the specimens were aligned to make sure they were all on the same plane and were perpendicular. The specimens were wet sanded together to ensure that each edge was flat, uniform, and had minimal rounding of the through the thickness edge. A piece of sand paper was placed on a flat surface and the specimens were drawn across the wet sandpaper. When all of the edge surfaces were being sanded, then the surface was considered flat enough to continue the process. The specimens were dried at 100° C under vacuum for a few hours. Next, the edge surfaces were cleaned of debris and carbon dust with lens paper and acetone, until the lens paper no longer showed debris and the surface appeared clean.

Adhesive is applied to the surface of the specimens to mimic the shape of the diffraction grating (Figure 9) when the grating mold is placed on it. SK-9 Lens Bond, an ultraviolet (UV) light cured adhesive, was applied to wet the surface. A cross line

diffraction grating mold with 1200 lines per mm was placed on the edges of the

specimens using orientation alignment marks as indicated in Figure 10.
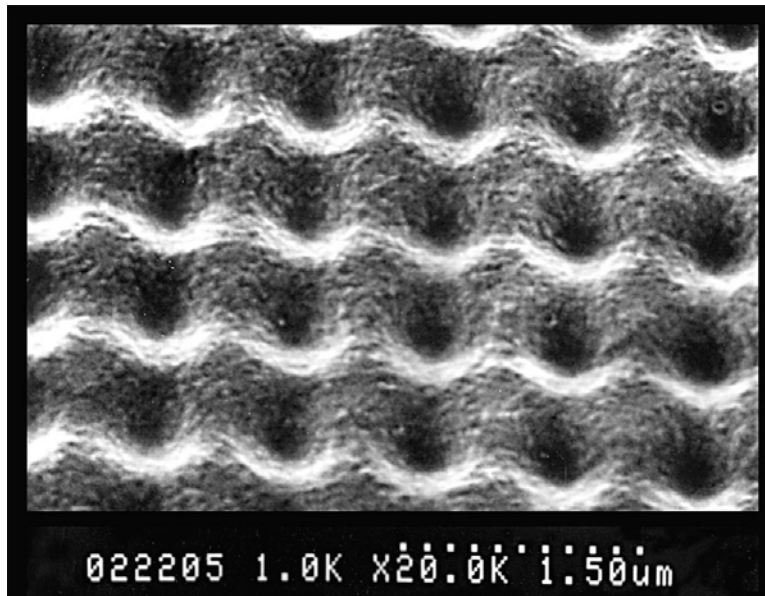


**Figure 9.  Microscopic photograph of a diffraction grating provided by David Mollenhauer, AFRL**
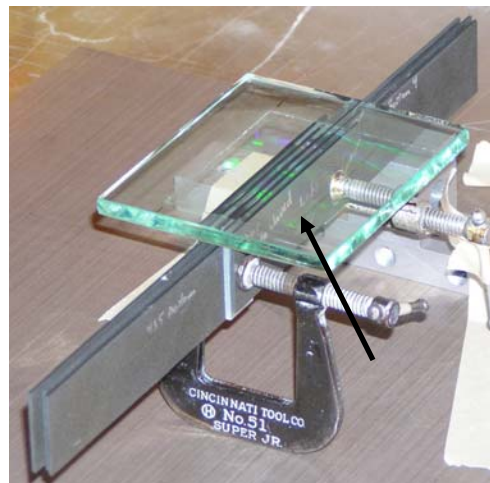


**Figure 10.  Diffraction grating being applied to specimens using SK-9 Lens Bond**

An attempt was made to cure the adhesive, but due to the presence of oxygen near the

edges, the adhesive was unable to be cured even with a high intensity and extended

exposure to the curing UV lamp.  This same problem had occurred on other specimens

made earlier, but only near the edges of the much wider surface. The specimens were very thin, and therefore oxygen was able to penetrate over the entire specimen. To apply a different adhesive, the surface had to be re-prepared per the method described above. Another adhesive, PC-10C that cures at room temperature, was then prepared for application. Per manufacturer's directions, PC-10C was mixed in correct ratios per weight with a hardener (PCH-10C) and debulked in a centrifuge, removing as many bubbles as possible. After coating the specimens with the adhesive, the set of three specimens was placed on another diffraction grating mold previously coated with a thin aluminum layer, making sure to align the grating with the specimens' edges. When the grating adhesive was completely cured, bubbles remained in the adhesive degrading the image of the diffraction grating on the specimens. Since this adhesive left a large flashing, or bonding adhesive on the side of the specimen thereby increasing the width of the specimen edges, the surface area became large enough to cure the SK-9, a UV cured adhesive. Therefore the surface was prepared a third time, making sure to not remove the flashings left from the PC-10C adhesive. With the additional surface area from the flashing, the diffraction grating surface was successfully placed on the specimen. Since the adhesive is visually transparent, photographs through a microscope were taken that could later be matched to the Moiré interferometry data results.

The gratings on the specimens' edges were then coated with a thin layer of aluminum using vapor deposition. Aluminum was evaporated in a high vacuum chamber where the specimens had been placed with the diffraction grating in direct line with the reservoir of aluminum. More detail on vacuum deposition can be found in *High Sensitivity Moiré* (Post and others, 1994:24).

**Moiré Interferometry Testing Under Tensile Loading**

The following is an overview of the procedures used to collect the Moiré interferometry data, which was used to determine the full field strains on the edges of the specimen.  A specimen was placed into a special load fixture (Figure 11) being held by wedge grips, with one side of the grips mounted to a load cell and the other to a loading screw.
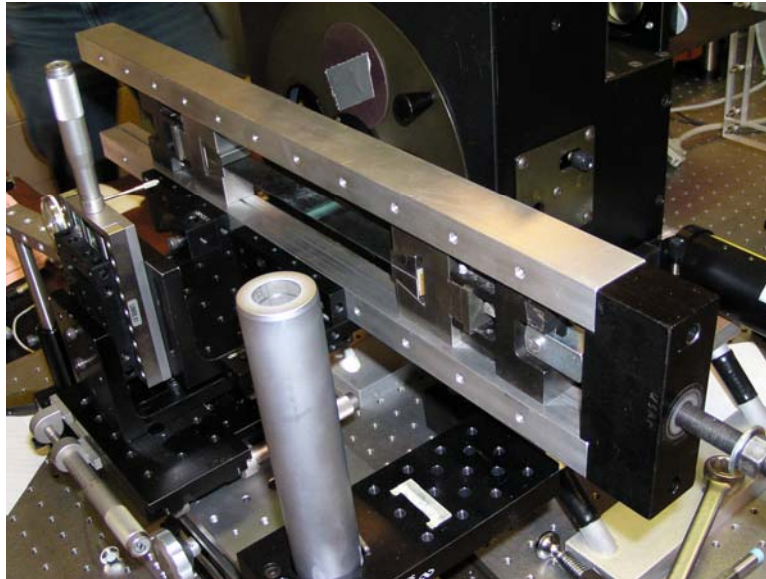


**Figure 11.  Moiré interferometer with specimen installed in the tensile loading jig**

By turning the screw a tensile load could be applied and monitored through the load cell. The fixture was aligned to the Moiré interferometer, centering the scarf joint in the center of the intersection of the lasers.  A fine alignment between the laser and the diffraction grating was then performed, minimizing the quantity of fringe patterns in the null state, or a condition of the specimen that is used as a baseline condition.  A comparison of the fringe patterns at a null state with the fringe patterns at a loaded state, or any state where the change to the specimen from the null state is the effect that is trying to be measured,

will provide the strain data caused by the loading of the specimen. Looking at the fringe pattern, a minor flaw in the diffraction grating was located as a reference for aligning the specimen between data collection, thereby maintaining the area being collected between states. Additionally, a major diffraction grating flaw was visually located and camera pixel locations recorded, to be used to align the data collected with the photograph of the surface. This would allow correlation of the results with actual features on the specimen. A slight misalignment of the panels during autoclave curing caused a slight bend in the specimen. After the specimens were cut from the panel, the bend was noticeable. The bend caused the middle of the specimen to be about half the laminate thickness above the ends of the ten-inch long specimen. After a 50 lbf tensile load was applied to stabilize the specimen and straighten some of the bend in the specimen, data for a null field were taken in both the axial (x direction) and through the thickness (z direction). The fixture was then moved slightly, to view an adjoining area and collect null field data. From the one-inch wide strength testing specimens, which is noted in the Appendix A, an ultimate load of approximately 4000 lbf was determined. Taking into account that the joint was bonded and therefore decreases the strength, the expected ultimate load was decreased by 20 percent. Also, a factor of safety of four was applied to assure the specimen did not break during the Moiré test. The applied load was 1050 lbf, which was applied to the first specimen, resulting in some cracking at a load of approximately 800-900 lbf. Specimen cracking would relieve some of the residual stress, and therefore this specimen's data was rejected for Moiré analysis. The load for the second Moiré specimen was then lowered to the 550 lbf and test data was taken for both areas and directions.

**Moiré Interferometry Testing for Residual Strain**

The ten-inch scarf specimen was cut down to two inches long to fit into the existing residual strain testing jig, Figure 12.  From the ten-inch specimen, the scarfed joint was centered for cutting out of the two-inch specimen.
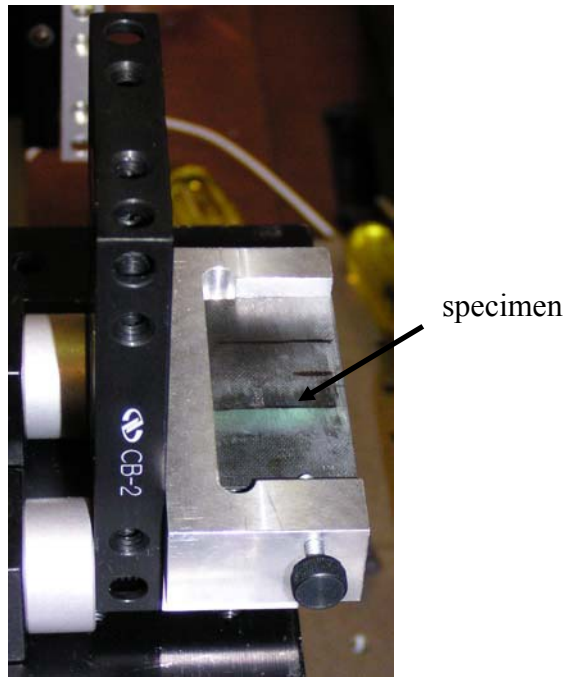


specimen

**Figure 12.  Photo of the Moiré interferometry residual strain testing jig**

The jig is designed to hold the smaller specimen in a consistent location, even after it has been removed and then reinserted.

The smaller specimen after being placed in the jig had null field data taken from the same area that was used in the earlier load testing.  The specimen was then removed and cut through this area of interest, about a quarter inch into the specimen, as shown with the red lines in Figure 13.  This cut releases the residual stresses on both sides of the cuts, creating free edges.  After placing the specimen back in the same location in the jig, another data set was taken.  Minor specimen alignment, through translation or rotation of

the specimen, had to take place to keep each side of the cut aligned with the first data set

taken.
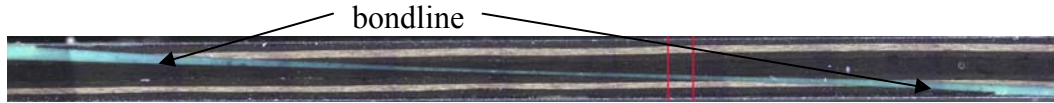


**Figure 13.  Photo of the through the thickness view of strain relief cut location**

**Large Tensile Testing Specimens**

To further analyze scarf joint strength and strain concentrations, large tensile test

panels were prepared and tensile tested to failure.  The same material used for the Moiré

specimens was cut to size.  The ends of the specimens were tabbed and drilled to

accommodate the testing fixture.  Three panels were scarfed in the center of the panel and

four panels were scarfed and repaired in the same location.  All of the panels, including

the three that were left virgin, were strain gaged in preparation for tensile testing.  The

test procedures are outlined below.

### Manufacture

Six of the twelve manufactured 12" by 24" panels were cut in half along the zero

ply direction, creating the twelve large 6" by 24" tensile testing specimens.  Each

specimen was cut to the same dimensions, taking care to align the cuts with the laminate

orientation.  The final dimensions of the specimens, after cutting off the edges to

eliminate manufacturing caused edge effects, cutting to square the specimens with fiber

orientation, and then tensile cutting each specimen to the same width, were 5.24 inch by

22.5 inch with the 0° fibers along the 22.5" direction.  The width was chosen to allow for

two specimens to be cut from the 12 x 24 inch panels as well as keep the length long

enough to satisfy ASTM D-3039M requirement for tensile testing specimens of length

equal to gripping length plus two times width plus gage length. The grips took

approximately two inches per end, and the area of interest was approximately three

inches in diameter.

Since ASTM D-3039M strongly recommended tabs and the fact that the only

available grips that were wide enough for the specimens used bolt fasteners, which would

weaken the grip area, tabs were selected for use during testing. The tabs were fiberglass

of uniform thickness and beveled towards the area of interest per the standard's

recommendation. The tabs were applied with EPON 828 epoxy, a room temperature cure

bonding system with EPI-CURE 3140 as the hardener. A specified hole pattern was used

for the grips, Figure 14, which had to be machined by a precision digital milling machine.

The hole locations were set by aligning the milling machine from the center of the panel

and not the manually bonded tabs, which ensured that the specimen would be pulled

uniformly from both ends without a bending moment.
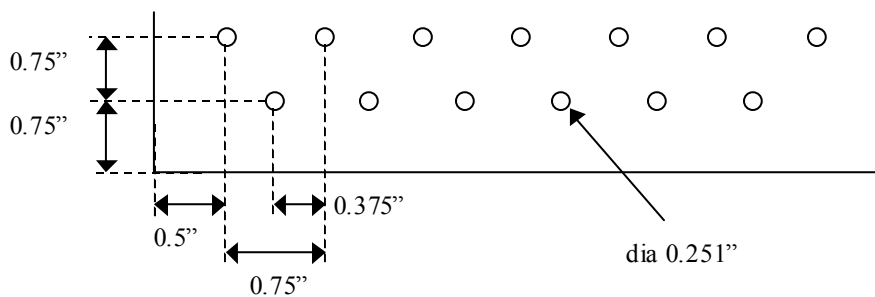


**Figure 14. Large specimen grip's hole pattern**

Three of the twelve specimens were tested in this configuration, virgin. The remaining

panels were scarfed and then half of those were repaired prior to testing.

**Scarfing**

As compared to the straight scarfed specimens that were hand sanded, the large

tensile test panels were scarfed in a circular pattern, commonly used in repairing aircraft,

using a more automated method. ASTM D-5766M-02a was used as a guide for setting

the dimensions of the large tensile testing specimens. The hole diameter was nominally

one inch, located in the center of the panel with a 1:20 scarf centered on the hole;

complete dimensions are shown in Figure 15.
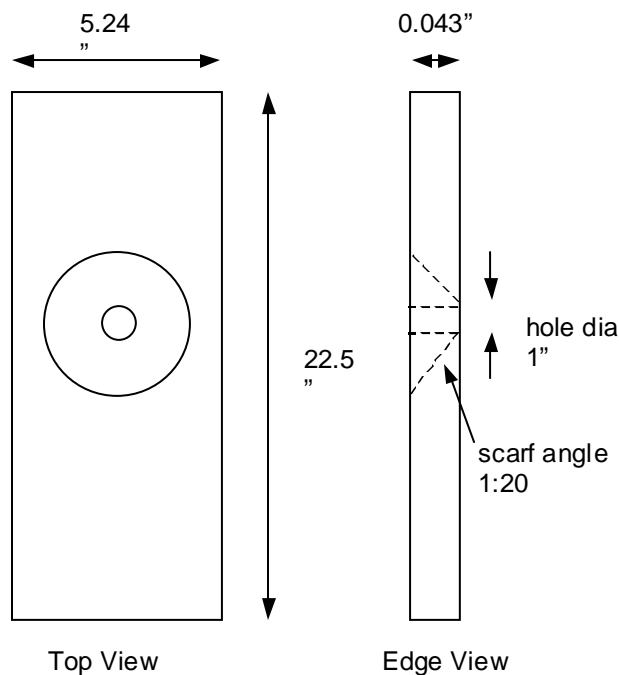


**Figure 15. Scarf panel dimensions and layout**

In order to increase the repeatability between each scarfing, a machine called a

"scarfomatic" was used, shown in Figure 16, provided by AFRL/MLS. The scarfomatic

holds a diamond bit and pneumatic grinder in place, while the whole grinder is rotated

and held at a set angle of 1:20. This cuts a circular hole at the set angle for each rotation

of the machine.  By slowly adjusting another gear, the grinder slowly moves towards the center of the hole, maintaining the scarf angle.  Eventually, the grinder cuts completely through the laminate, leaving a scarf at the exact angle set.



**Figure 16.  Scarfomatic with scarfed panel held by vacuum jig**

To further increase the repeatability, a jig was created below the scarfomatic to hold the specimen in place, assuring a panel centered hole each time.  The jig used posts that slide into three of the tensile testing grip's screw holes for alignment.  Two of the posts were bolts that also held the ends of the specimen down.  A piece of fiberglass, the same thickness as the tabs, was placed under the specimen to give additional support to the specimen while grinding.  During grinding the specimens tended to curl upward as layers were removed.  As each ply was ground away, a locally unsymmetrical layup remained.  When the final ply of each specimen was ground away, there was not enough stiffness left in the laminate to keep the unsymmetrical laminate from curling into the grinder and thereby change the scarf angle of the last few plies.  To overcome this

problem, a vacuum table was fabricated and placed below the area being ground. Small

holes were drilled in the plate and fiberglass panels below scarfed portion, yet not under

the center hole of the scarf. By applying a vacuum to these holes and coating the back of

the panel with a water-soluble gel, the specimen remained flat and stable throughout the

grinding process.

Scarfing followed a set procedure to ensure repeatability. First the scarfomatic

was leveled on a flat surface, in this case the jig holding the specimen. The center of the

scarfomatic was aligned with the center of the specimen. To determine where the

scarfomatic center was, the grinder horizontal control was set at zero and lowered until

touching the jig's surface. The grinder was then rotated around, scribing a minute circle

that had a corresponding center with the scarfomatic. After aligning the centers for the

first time, scribe marks were made on the jig where the legs of the scarfomatic touched so

that future alignments would not be necessary. The horizontal control was adjusted until

the grinder did not interfere with placing the specimen. The specimen was placed in the

jig after coating the bottom with a water-soluble gel, which enhanced the applied vacuum

used to hold the specimen in place. The horizontal control was then set to the calculated

scarf radius, with the center of the scarf located at zero. For a laminate thickness of

0.044", center hole of one inch, and scarf angle of 1:20, the radius was 1.38 inches. After

trial and error, the last ply on a 0.044" thick specimen would show width equivalent to

the other ply widths, if the horizontal value was set to 1.33 inches. The grinder was then

lowered until it was barely above the surface. The grinder was turned on and rotated;

making sure the surface was virgin on this first rotation. Using very small increments the

grinder lowered and rotated until the surface was barely marred. At this point the height

25

was set by tightening the vertical gear thereby maintaining the height during subsequent rotations of the grinder. The grinder was brought towards the center of the rotation by adjusting the horizontal controlling gear after each rotation. If the horizontal gear was rotated more than a quarter turn, per rotation of the grinder, the specimen pushed up on the grinder changing the scarf angle. The lowering and rotating continued until the scarf was complete.

### Wet Layup and Co-bonding of Scarf Repair

Even with the scarfomatic's repeatability, each panel had variability in hole diameter, scarf diameter, and concentricity of both diameters. Patch plies, with the same orientation as the specimen's plies and with one additional overlap ply, were manufactured. In order to simplify patch manufacture, a circle of a set size was selected for each layer. First the outside and inside diameters of all of the specimens were averaged, resulting in diameters of 2.7 inches and 1.07 inches respectively. The average diameters were then subtracted from each other giving an eight-ply scarf of 1.63 inches. The radius for each circle to be used in the patch manufacturing was selected for consistency between each ply. 0.5, 0.65, 0.75, 0.85, 0.95, 1.05, 1.15, 1.25, and 1.6 inches are the radii if the patch plies are distributed evenly over the average scarf width. The inside ply of the repair patch was a plug, to cover the hole, while the outside ply was an overlap ply to hold the patch onto the repaired laminate and therefore was larger than an even distribution would dictate.

Two stencils were made with a clear mylar plastic film etched with the radii of each patch layer concentrically located. A razor blade or scissors were used for the

cutting.  Using the stencil as a guide, circles were drawn on the paper backing of the prepreg, one for each of the needed patches at that size.  The stencil was then cut down to the next smaller radius and used again as a guide for drawing the circles for each patch.  This process was repeated until all of the patch layers had been individually drawn on the back of the prepreg.  Industrial strength scissors and a razor blade were then used to cut out each circle.  As each circle was cut, care was taken to draw the ply orientation on the backing, which allowed for ply alignment later.

The circular cut lamina were then stacked together to form the patch layup.  The first ply was placed on the inside circle of the stencil, oriented in the 0° ply direction.  This orientation was selected since the most strength would be needed in 0° direction during tensile testing.  The remaining plies were oriented to match the laminate plies in from the bottom of the specimen to the top.  Care was taken to align each ply with the respective circle at the proper fiber orientation and then removing the backing prior to applying the next layer.

The adhesive was then cut to match the outside radius of the top ply.  A hole aligned to the outside circle was then drawn and cut matching the plug.  This gave the adhesive a donut-like appearance.  The actual distance that the adhesive had to cover, i.e. the hypotenuse of the 1:20 scarf triangle, was closely approximated by the linear distances used since the scarf angle was lower than initially designed.  Additionally the adhesive would flow during curing and fill in any possible gaps and voids.

Originally, it was desired to cure the patches and then separately cure the patch to the specimen.  There were two reasons for not doing this:  there was no way to hold the shape of the patch while curing to ensure a matching cross section to the scarfed

27

specimens, and even if there could have been a way to maintain a set cross section, each scarfed specimen was slightly different than the others. The solution was to do a wet layup and co-cure the patch with the adhesive. The cure temperature of the first adhesive selected was approximately 2-3 times lower than the cure temperature of the laminate. A different adhesive, FM-300M-05 was then selected that had a matching cure temperature of 350° F with the laminate. The primary reasons for selecting this adhesive were: matching cure cycle temperature with the laminate, a film adhesive that ensured a more uniform bondline, and availability. The cure cycles were different for the adhesive and laminate. Both manufacturers, Cytec Fiberite (adhesive) and Hexel Corporation (prepreg), were contacted via telephone or email and both stated that the cure cycle for the laminate would work fine for curing both the laminate and adhesive. Therefore, the cure cycle originally used to cure the laminate with some minor modifications was used as follows: 5° F per minute on warming and cooling cycles, no hold temperature was used, and 80 psi instead of 100 psi. Standard vacuum bagging preparation with a base plate as described earlier was again utilized. The adhesive and then the patch were aligned and oriented to the top ply of the laminate prior to curing preparation and after normal bonding surface preparation as presented for the straight scarf joint.

### Application of Strain Gages

Due to limitations in Moiré interferometry, strain gages were used on the large tensile test specimens. The Moiré interferometer was limited in viewing area to two inches by two inches and it was inadvisable to relocate and adapt the interferometer for use with the tensile test machine. Strain gaging prior to the tensile testing was done with

28

the philosophy of maximizing the amount of pertinent data. The data collection hardware limited the data channels to sixteen, two of which were used for load and crosshead displacement. During actual testing the crosshead displacement channel did not provide any data. NASA Reference Publication 1092 was consulted for placement of the strain gages, especially the location of the gages used for specimen alignment verification during testing. When possible a 0°-45°-90° rosette was used for the centrally located strain gage to account for possible misalignment between the strain gage and the specimen. If, due to data collection limitations, only two channels were available a 0°-90° rosette or two strain gages place at a 0° and 90° were used. For all three types of specimens, the "virgin" specimen, scarfed specimen, and repaired specimen, consistency in placement was followed as much as possible, as shown in Figure 17.
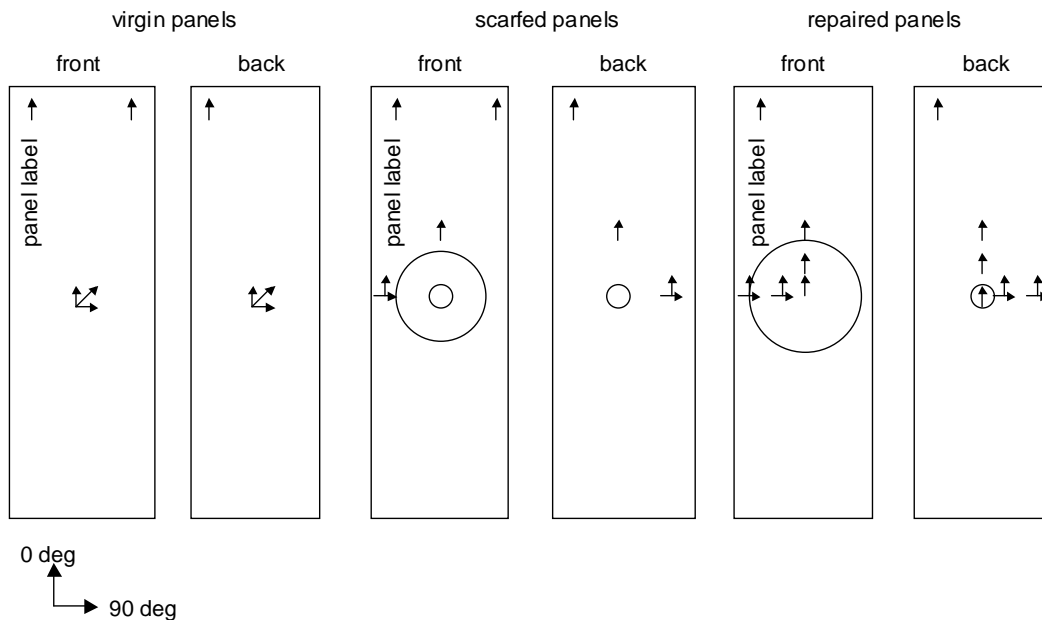


**Figure 17  Virgin, scarfed, and repaired panel strain gage location and orientation**

29

Locations on the front were often matched with the exact location on the back. The scarfed and repaired specimens required more gaging to match the more complex geometry and configuration. Within the three groups of specimens, all of the specimens were gaged the same. On the repaired specimens, the alignment strain gages were placed on the specimens but no data was collected for two reasons. All previous specimens did not show misalignment and all of the specimens were drilled at the same machine shop to the same specification for the grip hole placement. The data from the other strain gage placement was judged to be more valuable than the alignment verification data.

**Tensile Testing**

The ten specimens, three virgin panels, three scarfed panels, and four scarfed and repaired panels were tensile loaded to failure. During manufacture, two other specimens were damaged and could not be used in the final tensile testing. The order of testing was from the easiest set up to the hardest setup, or first the virgin panels and finally the repaired panels. Each panel was placed in the bolted grips, which contained sand paper on either side of the plates to increase gripping, Figure 18.



**Figure 18. Large tensile specimens being bolted into the test fixture**

Each specimen was placed in the tensile pulling machine before all the strain gage leads were soldered onto the gages. After soldering the leads, the gages were connected to the data collection terminals. The strain gages were labeled, per Figure 19, and connected to the appropriate data acquisition channels. Since the one-inch strength specimens (discussed in Appendix A) had a tendency to break apart in an explosive manner during tensile testing, special care was taken to wear proper protective equipment such as goggles and a protective shield was placed between the specimen and the machine operators. After all the gages were soldered and connected to the terminals, the gages were checked for proper signal and the Wheatstone bridge was balanced to zero, Figure 20. The test followed the ASTM D-3039-M prescribed constant head displacement rate of 0.05 inches per minute. Data was collected until failure.
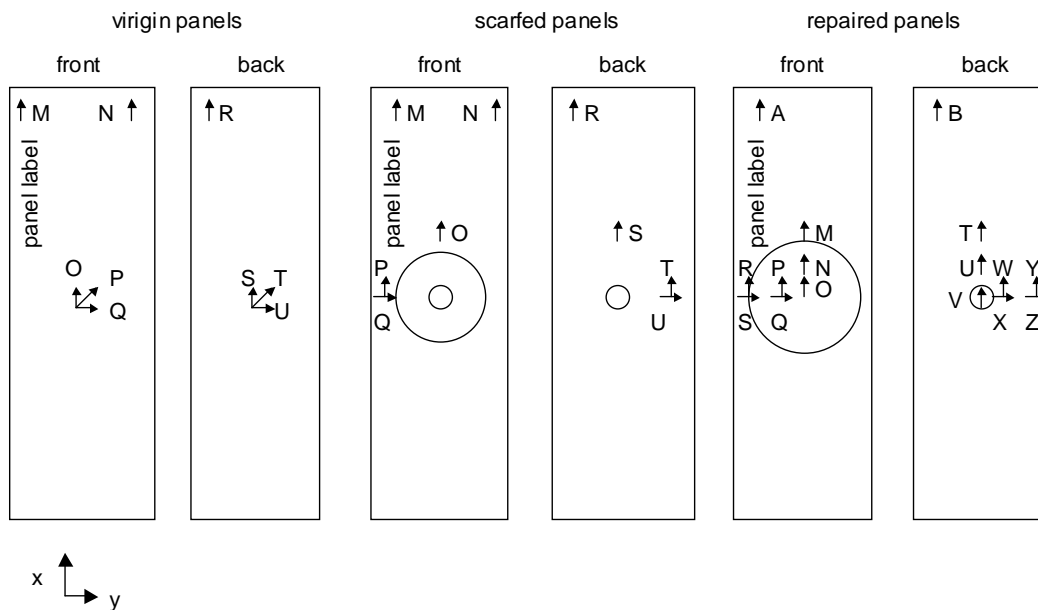


**Figure 19. Virgin, scarfed, and repaired panel strain gage labeling**
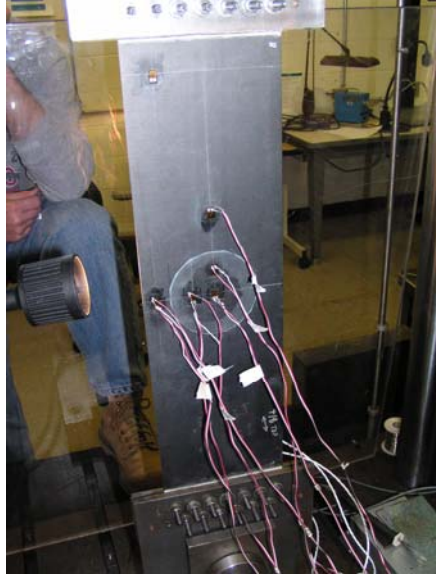
**Figure 20. Test setup of large tensile specimens to include soldered strain gages**

### III.  Modeling and Experimental Measurement of Tensile Loaded Scarf Joint

**Techniques Used**

The best way to explain two important features used in this thesis, Moiré interferometry and the B-Spline Analytical Model (BSAM), is to paraphrase from Schoeppner, Mollenhauer, and Iarve (2004:121-122).  A full explanation of the technique and the principles behind the Moiré interferometry can be found in Post (1994). Additionally, a more complete explanation of using Moiré interferometry to measure residual strains is given by Bowman (2001).  A more comprehensive explanation of BSAM is included in Iarve (1996) or Schoeppner and others (2004).

**Moiré Interferometry**

Moiré interferometry is an experimental technique used to measure full field in plane surface displacements using two polarized beams of light shined on a diffraction grating bonded to a specimen.  The reflection of the two beams result in interference, thereby creating a fringe pattern used for displacement analysis.  The fringe patterns are produced for both the x and z directions on a specimens edge by changing the incident angle of the polarized beams (see Figure 21).
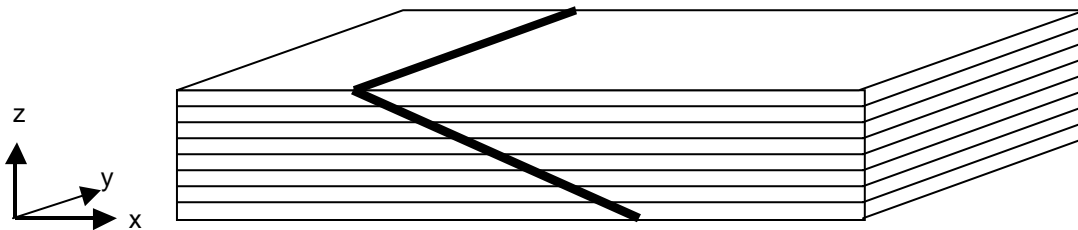


**Figure 21  Sketch of scarf joint with coordinate system**

Comparison of the fringe pattern from the null or initial displacement state (displacement field from the unloaded specimen ) is subtracted from the altered state's (displacement field from the loaded specimen ) fringe pattern to obtain the displacement field.  In this thesis, two different specimen configuration displacement fields were measured:  1) the free-edge strain field changes due to the application of an x-direction axial load and 2) the free-edge residual strain field changes resulting from the introduction of a cut perpendicular to the free-edge surface.  The x and z direction fringe patterns are related to the specimen displacements by:

$$U_X(x,z) = \frac{1}{f} N_X(x,z), \qquad U_Z(x,z) = \frac{1}{f} N_Z(x,z) \qquad (2)$$

where $U_X$ and $U_Z$ are the displacements in the x and z directions, $N_X$ and $N_Z$ the fringe orders from the same direction's fringe patterns, and $f$ is two times the frequency of the diffraction grating used.  In these experiments a diffraction grating of 1200 lines per mm was used.

A digital camera was used to collect the Moiré data and the data was processed with a digital phase-shifting method found in (Lassahn, 1994).  The resulting displacement data matrix has the same dimensions as the resolution of the digital camera.

**B-Spline Analytical Model (BSAM)**

B-Spline Analytical Model (BSAM) is computer code developed by Endel Iarve, David Mollehauer, and Greg Schoeppner at Air Force Research Laboratories that uses B-spline based approximation functions to model composite laminates.  The code is executed similar to finite element analysis programs.

A variable continuity approximation is generated and used for displacement approximations (Iarve, 1996). These approximations are from piecewise polynomial three-dimensional functions $X_i(x)$:

$$\mathbf{u}(\mathbf{x}) = \sum X_i(\mathbf{x})\mathbf{U}_i \tag{3}$$

with $U_i$ as displacement approximation coefficients and $i$ is an index that varies from 1 to the number of approximation functions used. $X_i(x)$ are three dimensional shape functions made from one dimensional sets of B-spline functions. The functions are combined in each coordinate direction to create the three dimensional results. "Polynomial splines of degree $n$ over an interval *[a,b]* with subdivision $a=x_0<x_1 \ldots < x_m=b$ are arbitrary piecewise polynomials of degree less than or equal to $n$ at the intervals *[$x_i$, $x_{i+1}$], i=0, m-1*. If the spline is constructed so that at every internal node $x_i$ has $n-d_i$ continuous derivatives, then $d_i$ is called the defect of the spline in the node $x_i$. The defect of the spline designates the maximum number of discontinuous derivatives over all nodes $k=max\{d_i\}$. If the defect $k=1$, then $u(x) \in C^{(n-1)}$; and in the case of $k=n$, one obtains the $C^0$ continuous traditional *p=n* approximation." (Schoeppner, Mollenhauer, and Iarve 2004:121) Since the constitutive equations are based on elastic behavior, BSAM assumes that the material is not in the plastic region of the stress-strain curve.

An advantage of using B-splines is that the displacements at the end nodes or boundary conditions can be set to match the coefficients of the spline functions. Boundary conditions can then be simply imposed by manipulation of the spline coefficients. The residual curing stresses and strains in the specimens were derived from a linear thermoelastic constitutive model. Near the free edge, singularities exist between

dissimilar material and plies oriented in different directions.  BSAM models these

singularities using an asymptotic solution, however, the asymptotic solution is not used

for the solutions in this thesis.  BSAM also has the capability of modeling failure using

various failure criteria, such as maximum stress, maximum strain, Hashin's, strain

invariant, and others, though the failure criteria was not used in this thesis.

**Moiré Data Analysis**

The collection of Moiré data begins with identifying a flaw in the diffraction

grating so that the measured displacement and subsequent strain fields can be accurately

mapped to the specimen.  The white ellipse on the right side of the specimen shown in

Figure 22 was used for position referencing.  This photograph matches the field of view

of the Moiré interferometer during testing and can be directly compared to all full field

plots.  The boundaries were calculated using the measured thickness of the laminate as a

reference value in converting the pixel values of the Moiré data to actual dimensions.

Then the actual dimensions on the specimen were converted into pixel values of the

microscopic photograph of the specimen.

The null field fringe patterns were recorded at a load of 49 lbf.  After loading the

specimen to 549 lbf, the load altered fringe pattern was recorded.  During loading the

specimen rotated slightly and had a slight rigid body displacement in the field of view of

the digital camera.  The rigid body displacement was expected and the flaw in the

diffraction grating is used for realigning the specimen in the field of view after loading.

The rotation was primarily due to a very slight misalignment of the two scarfed

adherends during the adhesive bondline cure cycle.  The slight bending of the specimen

36

and the fact that the scarf joint is not symmetric about its mid-plane in the bondline

region, caused the orthotropic laminate to become non-orthotropic and have a nonzero

bending-extension coupling matrix.  Therefore when tension was applied to the

specimen, local bending or rotation occurs.  The specimen was rotated back to the same

orientation in the field of view by rotating the entire loading fixture, but this caused the

specimen to be slightly out of focus from the original camera settings.  Two different sets

of load altered fringe pattern data were taken to determine the better method of collecting

the data:  one data set at the camera settings originally used to take the first null fringe

pattern data and the second taken after manually re-focusing the interferometer to account

for the rotation of the specimen.  Preliminary processing of the data showed that the

manually re-focused interferometer data was better in quality; the expected displacement

trends were more clearly discernible.
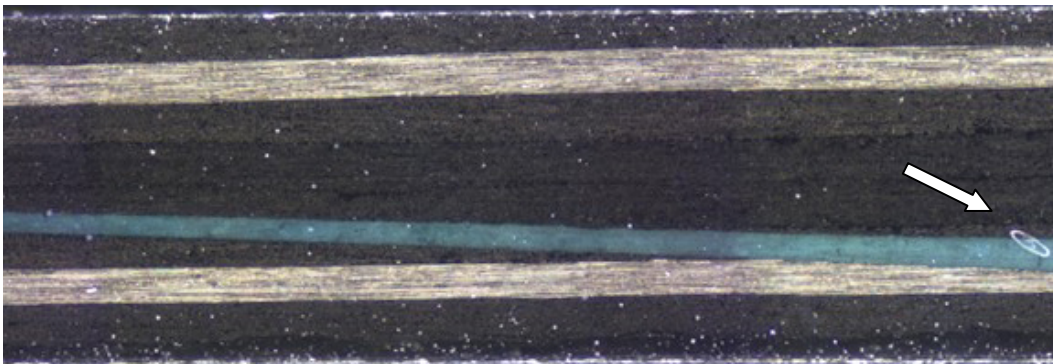


Figure 22.  Photo of the specimen showing the location of the Moiré data's field of view

The data collected with the Moiré interferometer and associated digital camera

was post processed using the steps presented in Appendix D.  A masking set of data was

used to eliminate the propagation of errors that are inherently found in the diffraction

grating, Figure 23.  The blue areas are assigned zero values and the red are assigned unit

values.  After processing of the data, the zero mask can be used to eliminate errors from the zero valued areas found in the field of view.  The process is similar in theory to a painter using masking material to keep paint from spreading to a non-working surface.  The smaller flaws in the data were filled in using a linear interpretation from five data points in the neighborhood of the filled data.  Actual data values in unfilled regions remained untouched during this process.  The origin was shifted to the lower left corner of the specimen from the default location of the upper left with the positive z value directed downward.  During the processing, the data was only smoothed after the strains had been calculated from the displacements.  As part of the data processing, the strains was smoothed, or averaged with neighboring strain values and then multiplied by the zero mask, thereby eliminating some noise and spikes in the data set.  All strains for this thesis were smoothed ten times.  More smoothing made the visual trends blend into the background levels of strain.  The two dimensional matrix of strain values was then converted to a picture by assigning a color scale to the strain values and placing a colored pixel at the associated screen location from the matrix location.



**Figure 23.  Zero mask used for processing tensile loaded specimen's Moiré dataset**

**Model Generation**

BSAM required the following information for modeling the scarf joint: material properties, geometry of the specimen, and boundary conditions. The material properties for IM6/3501-6 were provided by Dr. Ran Kim at Air Force Materials Directorate, shown in Table 1.

Table 1.  Material Properties for IM6/3501-6 at room temperature

| | |
|---|---|
| Longitudinal modulus, $E_1$ | 25.42 Msi |
| Transverse modulus, $E_2 = E_3$ | 1.42 Msi |
| Shear modulus, $G_{12} = G_{13}$ | 0.8 Msi |
| Poisson's ration, $\nu_{12}$ | 0.33 |
| Longitudinal CTE, $\alpha_x$ | 0.2 μ strain /°F |
| Transverse CTE, $\alpha_y = \alpha_z$ | 14.9 μ strain /°F |

The material properties for the adhesive, FM 300M (0.05 psf), were not as readily available. The manufacturer supplied material data did not specify modulus of elasticity or coefficient of thermal expansion, though design values for shear modulus were provided. Appendix B explains the methodology and experiments conducted for this thesis to measure the material values used for the modeling with the results summarized in Table 2. The adhesive was assumed to be isotropic even though an insignificant percentage of random mat carrier material was in the adhesive.

Table 2.  Material Properties of FM 300M (0.05 psf)

| | |
|---|---|
| Modulus of elasticity | 164,500 psi |
| Poisson' ratio | 0.38 |
| Coefficient of thermal expansion | 34.8 μ strain/°F |

Idealized scarf joint geometry was used in the model based on actual measurements of the specimen bondlines to set bounds for the laminate thickness and scarf bondline angle. The specimen's measured thickness was used to set the thickness of the model, with all eight plies assumed to be evenly distributed through the thickness. On either side of the bondline region of the scarf joint, two inches of laminate were modeled to allow for the strain fields of the model in the bondline to be representative of the strain field in the test specimen. Using photographs of the straight scarf joint specimen, measurements were taken for the exact scarf bondline profile, Figure 24 (the scale in the z-direction is much smaller than the x-direction) shows the location measurements plotted with a polynomial curve fitted to the measurements making the edges easier to visualize. The x-axis for this figure only, is measured from the original BSAM model origin, which located the start of the scarf joint at two inches from the edge of the model. Pixel values from the photograph were converted to actual measurements by using the known dimension of the laminate thickness for scaling in both the x and z directions. When the diffraction grating was applied to the specimen, sanding could have thinned the specimen near the top and bottom edges thereby changing the thickness of the specimen and skewing the calculation. Additionally, the slight misalignment of the adherends in the specimen made the z-direction measurements vary minutely from the actual z-directional measurements. A more accurate height could be obtained through measuring from the bottom surface of the specimen at each location instead of assuming a constant x value for the bottom surface. During modeling, the specimen was examined and it was discovered that the diffraction grating had been applied to the opposite side of the specimen that was initially intended. A simple flip of the specimen during grating

40

application must have caused this.  To account for this sign reversal, the laminate was
modeled with a layup of [-45/0/45/90]$_s$ instead of [45/0/-45/90]$_s$.
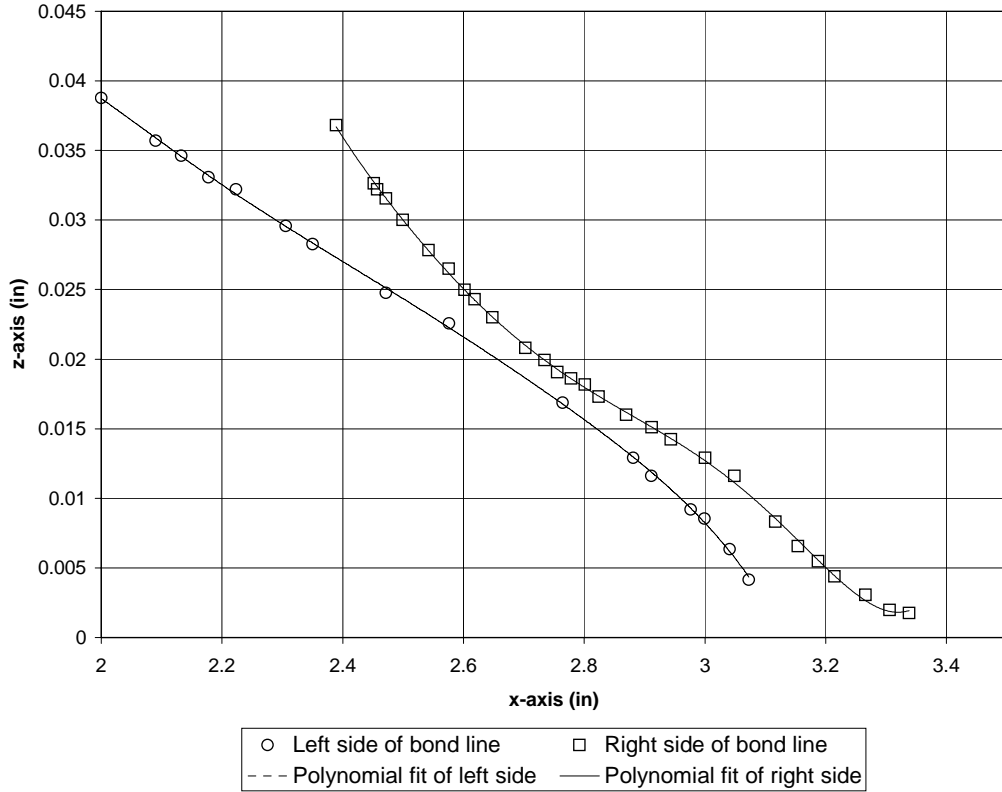


**Figure 24.  Data and fitted curves for bondline location in straight scarf specimen**

A straight-line approximation of the bondline interface curves of Figure 24 was used in

the BSAM model whereby a uniform bondline was modeled.  Measurement of a previous

scarfed bondline thickness using the same adhesive and measurements of this bondline

led to a set value of 0.005" measured normal to the bondline interface.

For comparison with the Moiré data, strain output data from the three dimensional

BSAM result was extracted into a two-dimensional matrix.  The three dimensional results

can be viewed in MATLAB$^®$ or another post processing software package.  The model's

mesh was output to MATLAB$^®$ and screen captured, Figure 25 and Figure 26.  The

41

origin for the model was placed at approximately 1.4" away from the start of the scarf or exactly 2" from the left side of the cut that will be discussed in the next chapter. The isometric view shows that the mesh is more refined in the x-y plane (the width of the specimen) towards the edges to allow greater resolution where the edge effects occurred. The different colors are used to distinguish the adherends and adhesive. The mesh is evenly and extensively refined through the thickness of the model as shown in Figure 26.
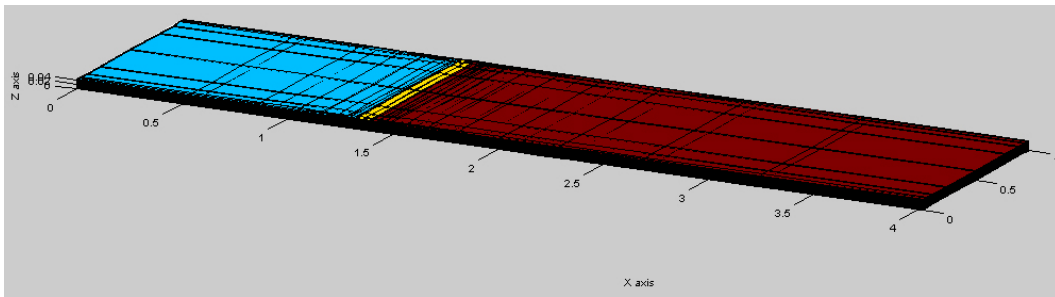


**Figure 25. Screen capture of isometric view of the mesh output for mechanically loaded model in MATLAB®**
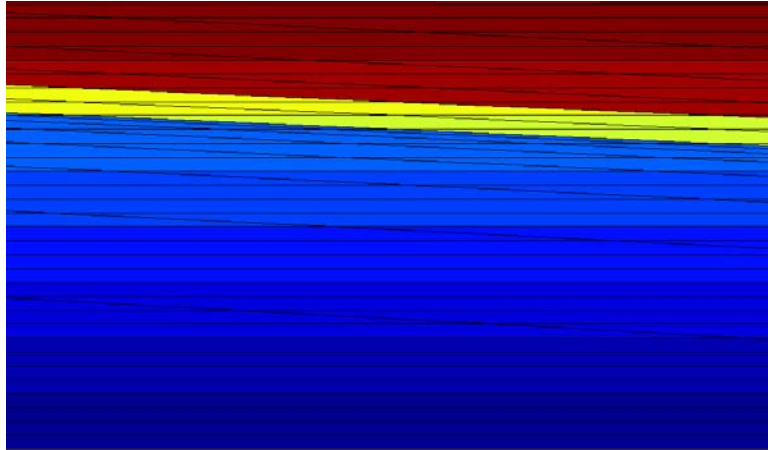


**Figure 26. Screen capture of MATLAB® mesh output of x-z plane at x=~1.8" and y=0" for mechanically loaded model**

For comparison to Moiré data, only the edge view surface corresponding to the Moiré interferometry field of view was extracted from the model. Additionally only the strains in the x-direction, strains in the z-direction, and x-z plane shear strains can be calculated

42

from the Moiré displacement data. BSAM data was also extracted for the x-z plane located ¼" into the width of the specimen for comparison to the BSAM data on the edge surface. Similar to the Moiré data, the two-dimensional matrix of strain values was converted to an image. A complete set of BSAM data is included in Appendix E, which includes all six components of the strain tensor.

**Mechanically Loaded Specimen Results**

In the process of making the specimen and during testing, multiple sources of possible errors were introduced into the results. During specimen manufacture a few variations from the ideal scarf joint specimen were noted as follows: a slight misalignment in the scarf, multiple diffraction grating applications, and possible sanding of the specimen edges thereby damaging the diffraction grating at the top and bottom of the specimen. While Moiré testing the following was also noted: flaws in the applied diffraction grating, minor vibrations during Moiré testing, and possible flaws in the Moiré interferometer diffraction grating. These deviations were noted in the methodology chapter and will be discussed further in the section later in this chapter on Moiré interferometry noise.

A full field view of the strains for both the BSAM and Moiré data was generated for $\varepsilon_{xx}$, $\varepsilon_{zz}$, and $\gamma_{xz}$ fields. Full field strain views are shown on the same color scale (Figure 27), white is used to show strains larger than the set maximum bound and black is used to show all strains below the set lower bound with the colors of the rainbow (red, orange, yellow, green, blue, and indigo) distinguishing the strains in between the maximum and minimum bounds. The upper and lower bounds for all full fields shown

are 0.008 and -0,008 micro strain respectively.  At axial x-coordinate locations 0.0 mm,

1.0 mm, 2.0 mm, 2.5 mm, and 2.8 mm, measured from the ordinate at the left side of the

field of view, $\varepsilon_{xx}$, $\varepsilon_{zz}$, and $\gamma_{xz}$ strain data as a function of the z-coordinate from the Moiré

and BSAM strain fields were extracted and compared.  Due to noise in the Moiré

interferometry data discussed in a later section of this chapter, five concurrent columns of

data at each z-coordinate location were averaged for line plot comparison of the BSAM

model at the same location to help in noise mitigation.

−0.0075 −0.0037 0.0000  0.0037  0.0075
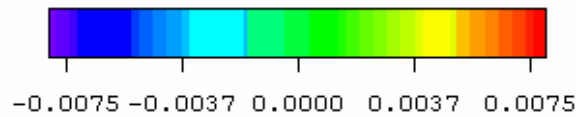
**Figure 27.  Color scale, in micro strain, used for all full field strain views**

The $\varepsilon_{xx}$ data set showed very good correlation.  The $\varepsilon_{xx}$ strain did not show much

variation across the specimen, but both the model predictions and the measured results

have the same level of constant strain, since the background color of both the Moiré and

BSAM results match, shown in Figure 28 and Figure 29.  The model values at ¼" into the

specimen width also show very little differences from the surface results, Figure 30.  All

of the line plots showed the same general results and only the plot at 1 mm is included as

a representative sample, Figure 31.
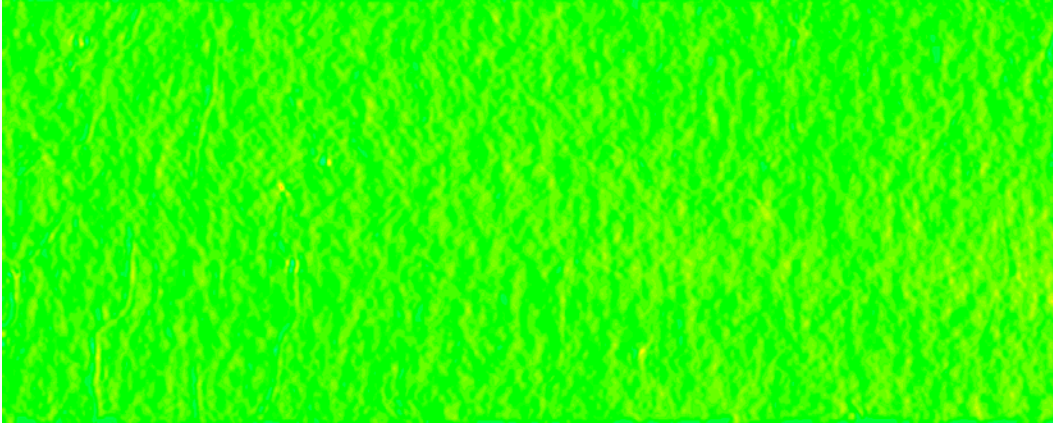
**Figure 28. Full field $\varepsilon_{xx}$ strains from processed Moiré data for tensile loaded specimen**
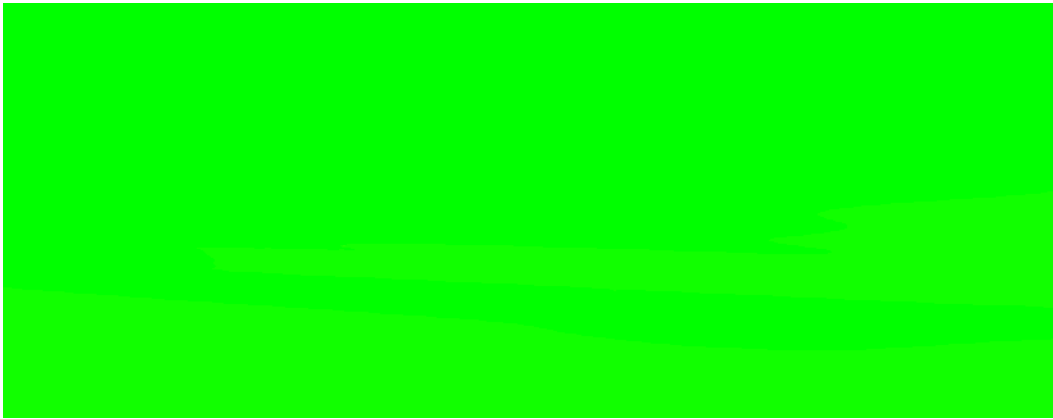


**Figure 29. Full field $\varepsilon_{xx}$ strains extracted from BSAM at edge of model for tensile loaded specimen**



**Figure 30. Full field $\varepsilon_{xx}$ strains extracted from BSAM at ¼" into model width for tensile loaded specimen**
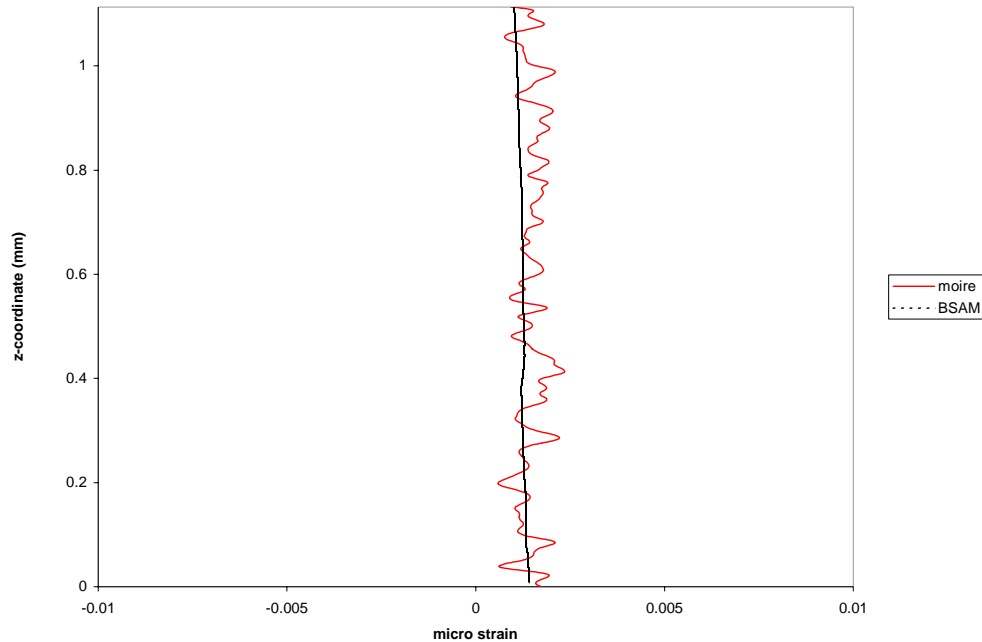
**Figure 31.  Comparison of Moiré and BSAM for $\varepsilon_{xx}$ strain through thickness at ~1mm from end of tensile loaded specimen**

The $\varepsilon_{zz}$ data set shows little correlation.  The $\varepsilon_{zz}$ strain from the BSAM model shows minor variations only across the full field view that showed the difference in various plies, Figure 33, while the strain calculated from the Moiré interferometry data show much larger variations but still distinguished various plies from each other, Figure 32.  The BSAM model at ¼" from the edge, show that the strain magnitudes have decreased, but the general trends match the data extracted from the BSAM data at the edge of the specimen, Figure 34.  Line plots from the $\varepsilon_{zz}$ data set confirmed this.  Again, only the 1mm location is included as a representative sample of all the line plots, Figure 35.  In each line plot, the BSAM data remained fairly constant, while the Moiré data had significant oscillations with no apparent match in the trends.
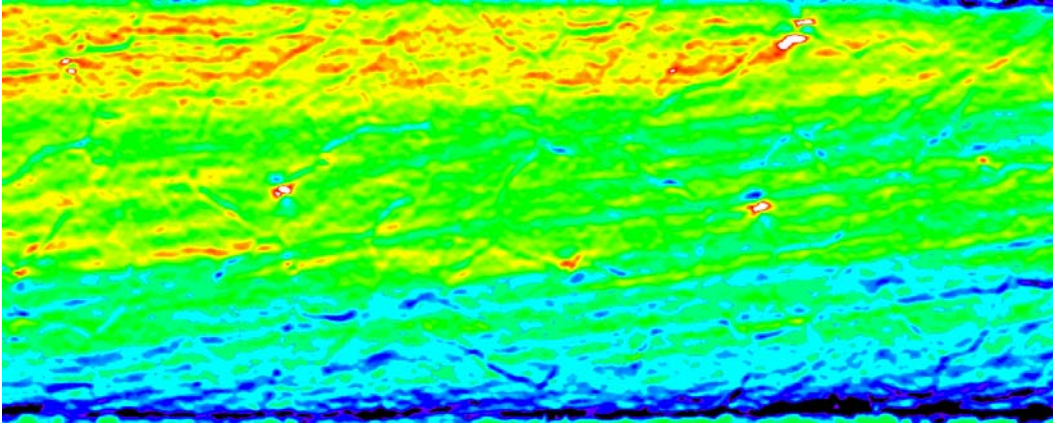
**Figure 32. Full field $\varepsilon_{zz}$ strains from processed Moiré data for tensile loaded specimen**
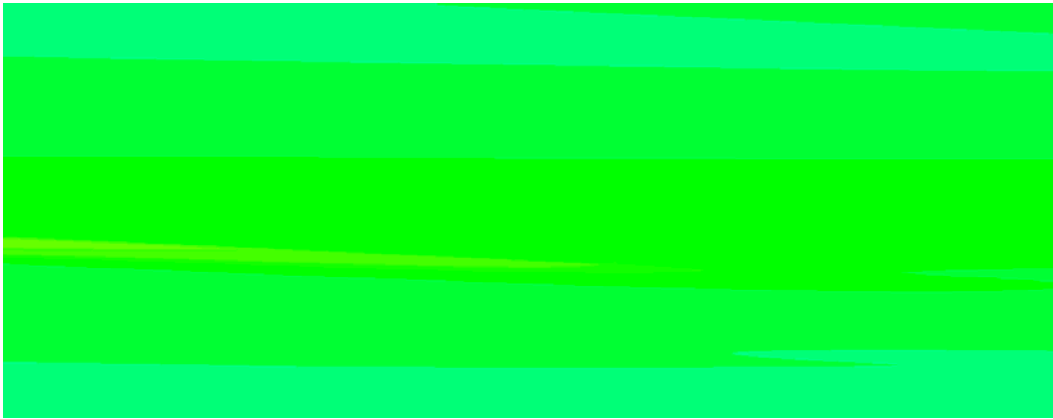


**Figure 33. Full field $\varepsilon_{zz}$ strains extracted from BSAM at edge of model for tensile loaded specimen**
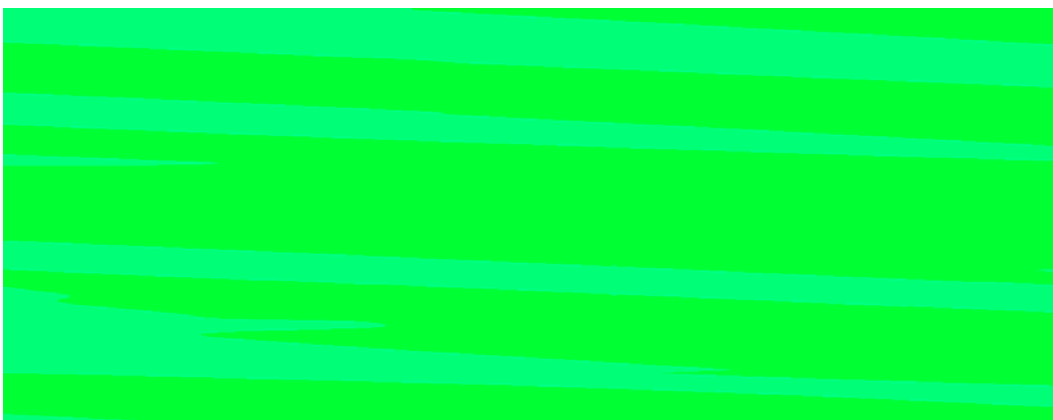


**Figure 34. Full field $\varepsilon_{zz}$ strains extracted from BSAM at ¼" into model width for tensile loaded specimen**

47
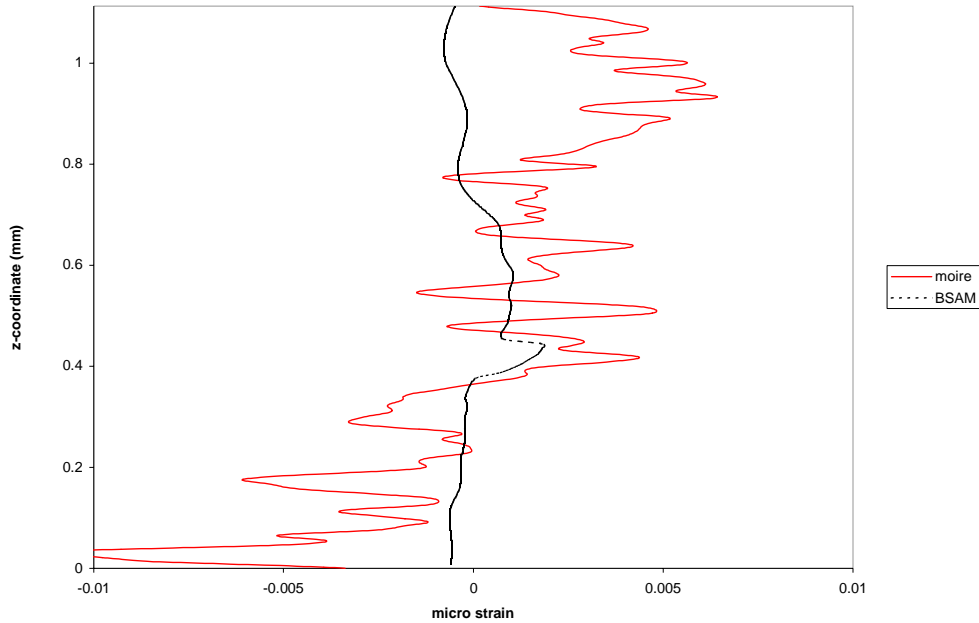
**Figure 35.  Comparison of Moiré and BSAM for $\varepsilon_{zz}$ strain through thickness at ~1mm from end of tensile loaded specimen**

The $\gamma_{xz}$ data set shows good correlation.  The general order full field strain view, shown by the color of the background, matches between the Moiré full field results and the BSAM results, Figure 36 and Figure 37.  There are two strong trends:  the upper blue shaded area, approximately where the 0° ply is located, shows a low shear strain field and the red area in the center, corresponding to the adhesive layer and where a ply terminates, shows much higher shear strains.  Once again, the BSAM model at ¼" from the edge being viewed shows good correlation with the surface trends, but a soften of the magnitude of the strains and elimination of manifestation of the free-edge singularities that are on the edge of the specimen, Figure 38.  All of the line plots are shown, Figure 39 through Figure 43, since the shear strain varies greatly over the specimen.  Each line plot

48

shows general directions and magnitudes matching from the BSAM model and Moiré

data calculations. In some cases, Figure 40 and Figure 42, the correlation is very good.
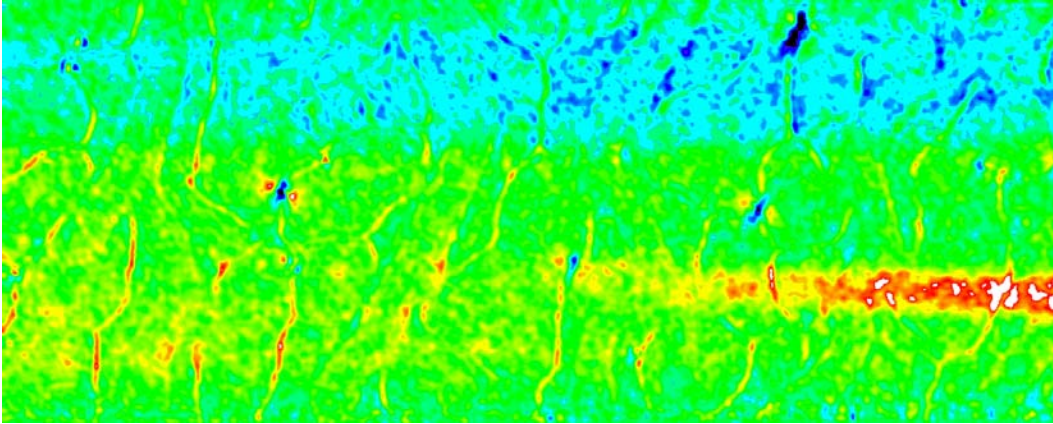


**Figure 36. Full field $\gamma_{xz}$ strains from processed Moiré data for tensile loaded specimen**
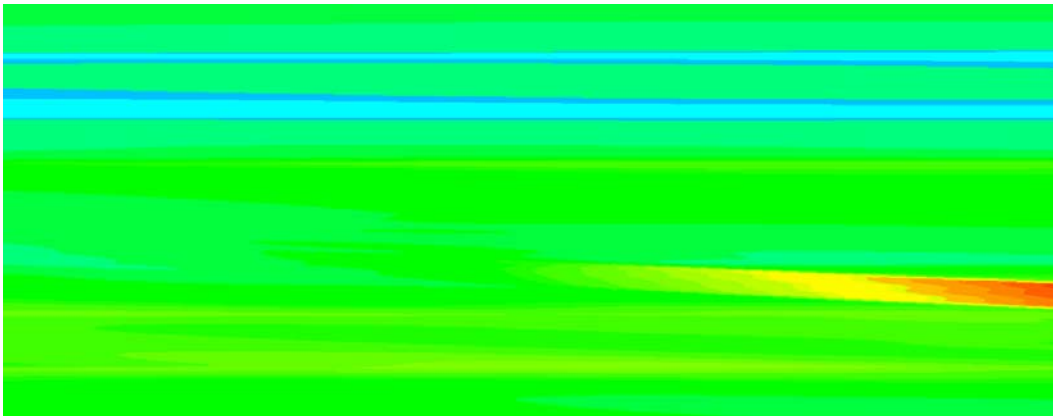


**Figure 37. Full field $\gamma_{xz}$ strains extracted from BSAM model for tensile loaded specimen**
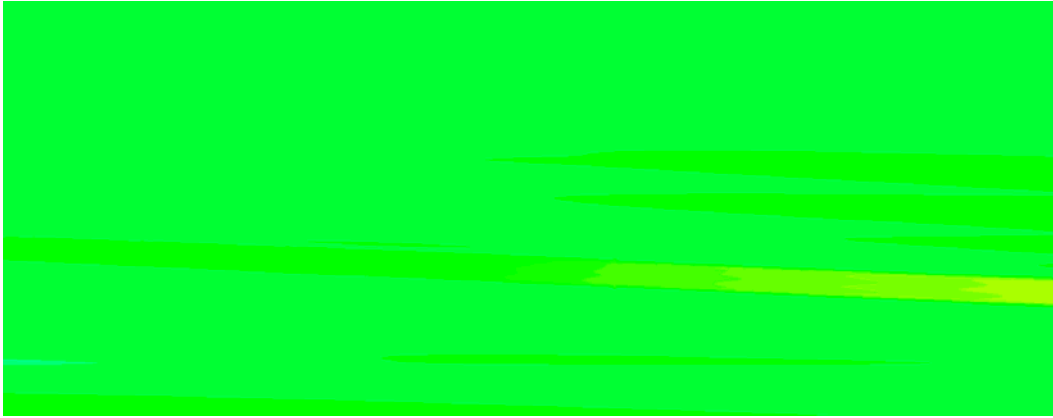
**Figure 38.  Full field γ$_{xz}$ strains extracted from BSAM at ¼" into model width for tensile loaded specimen**
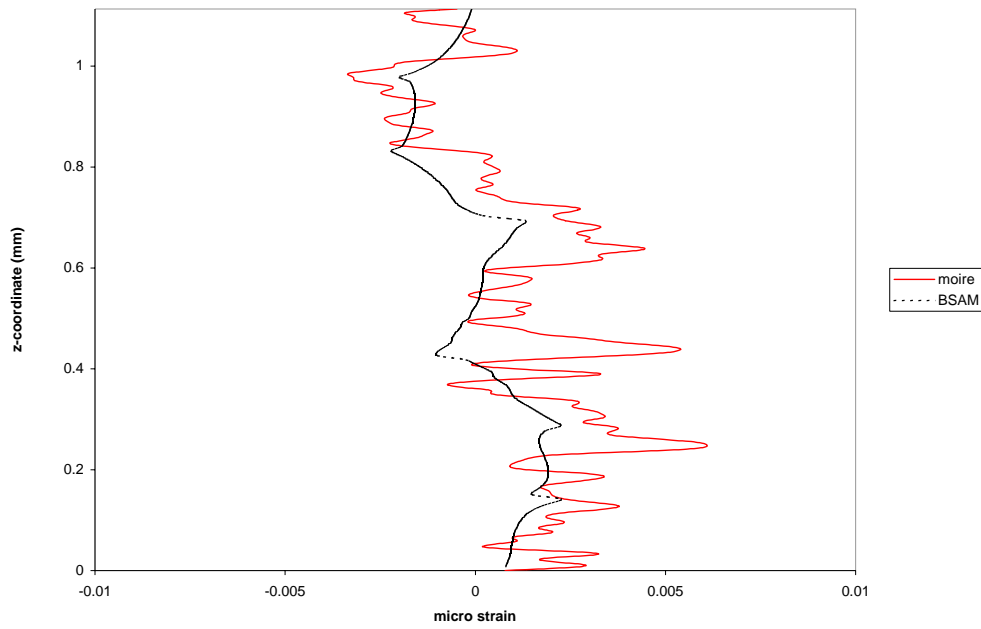


**Figure 39.  Comparison of Moiré and BSAM for γ$_{xz}$ strain through thickness at ~0mm from end of tensile loaded specimen**
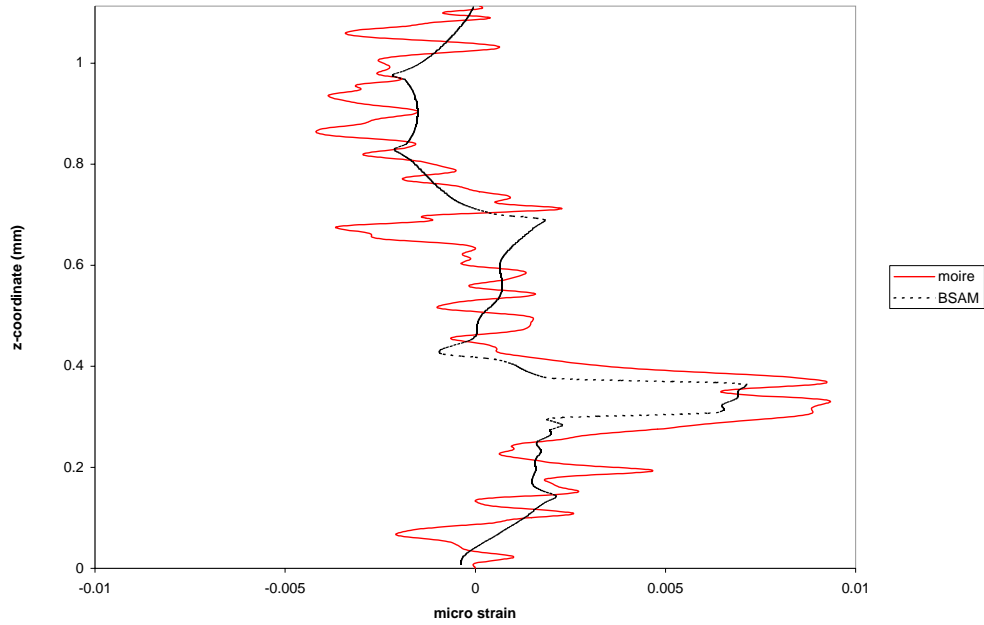
**Figure 40.  Comparison of Moiré and BSAM for $\gamma_{xz}$ strain through thickness at ~1mm from end of tensile loaded specimen**
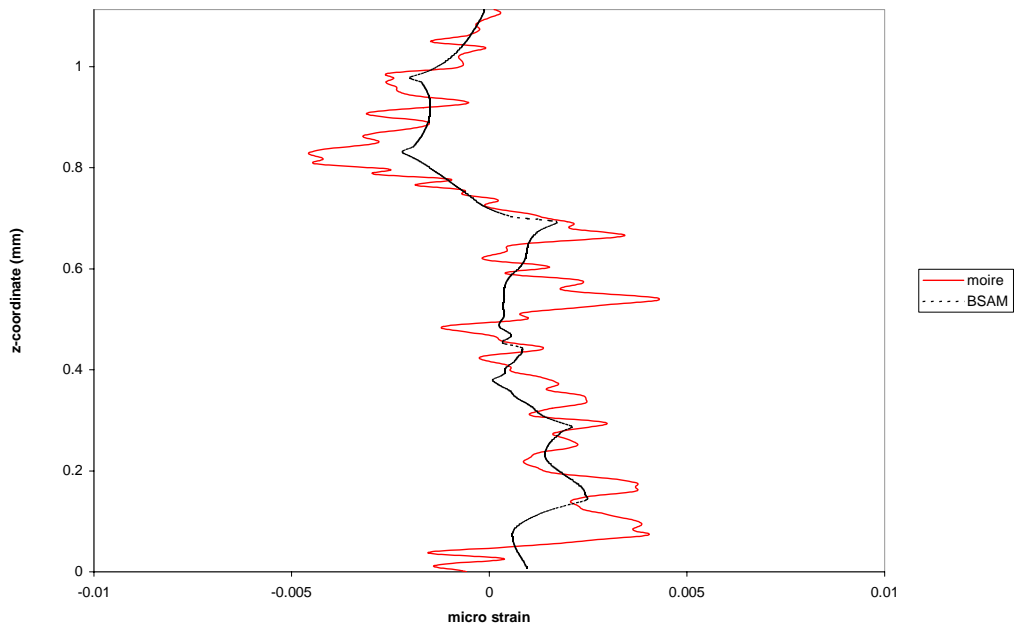


**Figure 41.  Comparison of Moiré and BSAM for $\gamma_{xz}$ strain through thickness at ~2mm from end of tensile loaded specimen**
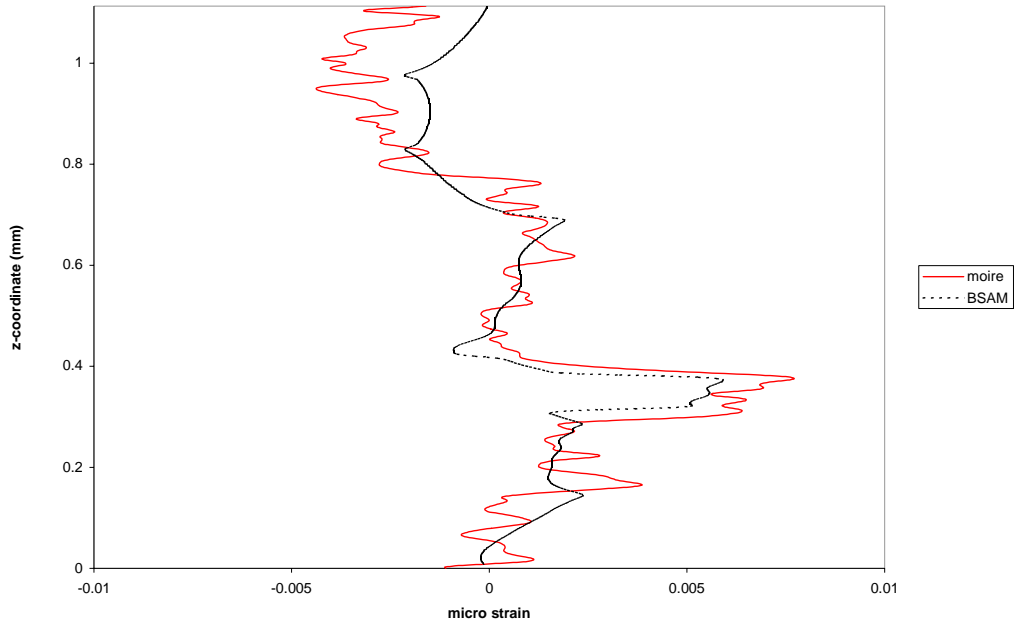
**Figure 42. Comparison of Moiré and BSAM for $\gamma_{xz}$ strain through thickness at ~2.5mm from end of tensile loaded specimen**
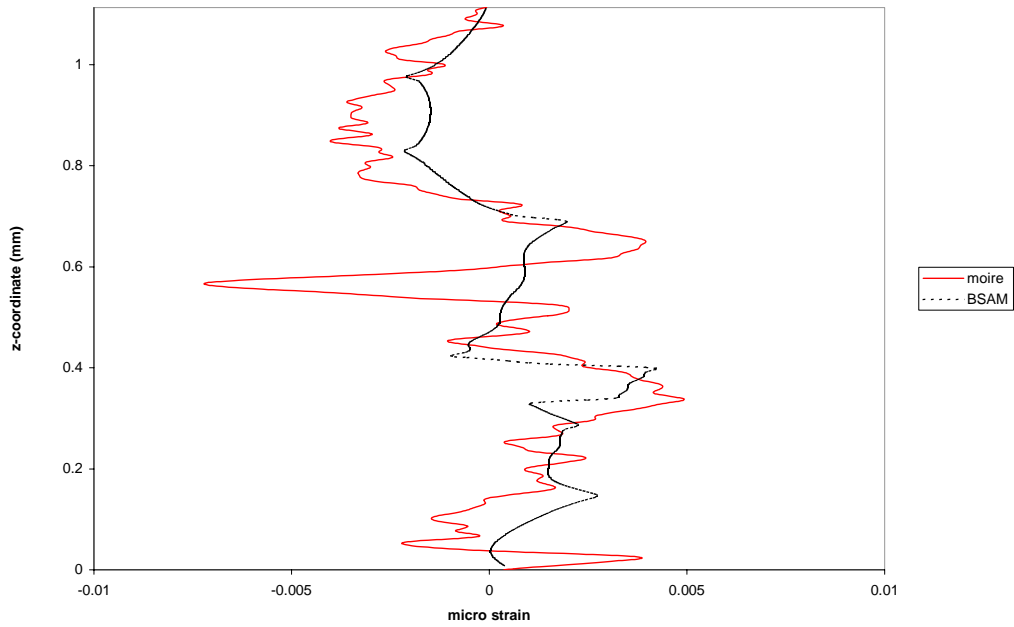


**Figure 43. Comparison of Moiré and BSAM for $\gamma_{xz}$ strain through thickness at ~2.8mm from end of tensile loaded specimen**

52

**Discussion of Moiré Data Noise**

Previous works by others, to include Schoeppner and others (2004) and Bowman (2001), have shown excellent correlation between BSAM and Moiré interferometry results. The Moiré interferometry data presented for a bonded composite lap joint by Schoeppner and others (2004) showed less noise than the data presented above, Figure 44.



a)



b)
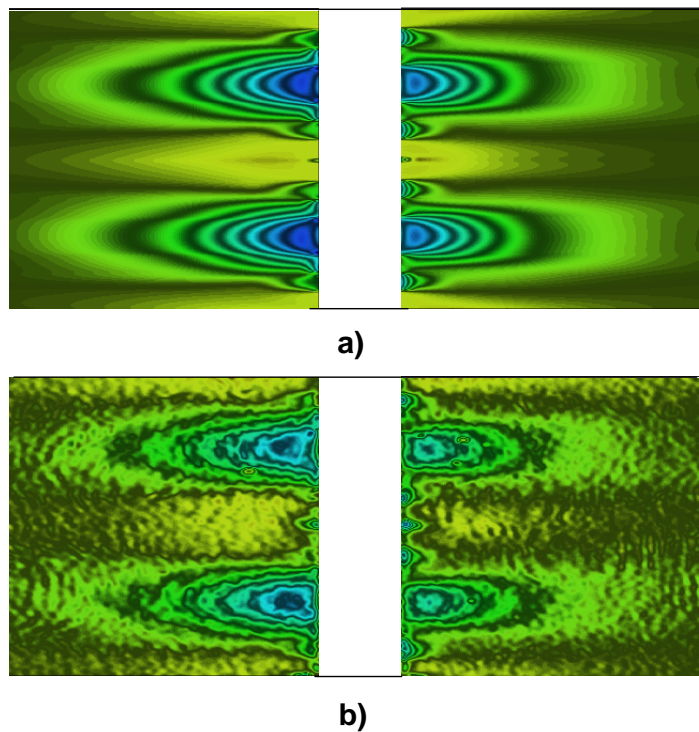
Figure 44. Axial strain $\varepsilon_x$ for the bonded specimen: a) BSAM prediction, b) Experimental Moiré measurement (Schoeppner and others, 2004:Figure 8)

Additionally, their line plots generated from the Moiré interferometry data for the lap joints were fairly smooth and matched closely to the BSAM results, Figure 45. However, the specimens in their work had ply thicknesses twice as thick as the ply thicknesses in this thesis work. The thinner ply thicknesses of the present work required higher fidelity

measurements to obtain the same level of confidence in the Moiré displacement and strain data. Also the scarf joint, analyzed in this thesis has a more complex strain field than the lap joint done by Schoeppner and others (2004). Comparison of the Moiré calculated data and BSAM data in the $\varepsilon_{xx}$ and $\varepsilon_{zz}$, where the magnitudes were expected to be relatively small, yields sporadic Moiré data results that appear to have a large amount of noise in the signal. In the case of the $\varepsilon_{zz}$ strain field, the noise is of the order of magnitude of the strain measurement of interest. This noise could come from many different sources, including: specimen fabrication, diffraction grating application process, deteriorated diffraction gratings, and vibrations introduced during Moiré data collection. The noise in the $\varepsilon_{zz}$ strain field will have direct influence on the shear strain fields, since the shear strain field is calculated using the $\varepsilon_{xx}$ strain and $\varepsilon_{zz}$ strain fields.
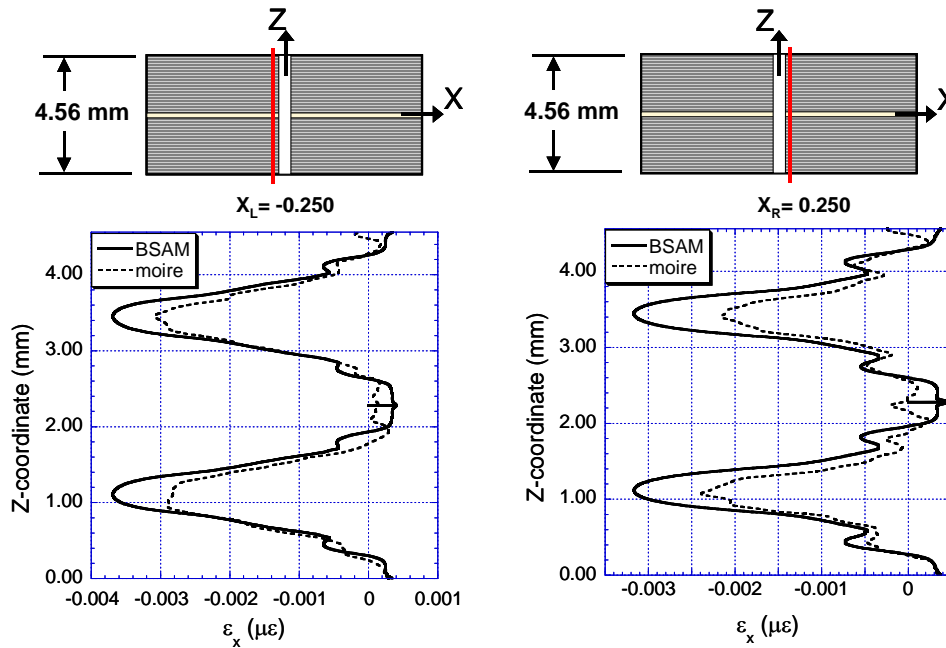


Figure 45. $\varepsilon_x$ comparison 0.250 mm from cut edge (Schoeppner and others, 2004:Figure 10)

During specimen fabrication, slight variations in the scarf length across the width of the specimen caused the specimen to be slightly misaligned. During loading the specimen did straighten, but a slight twist was noticed after the loading. The twist was so slight, that only under the very high magnification of the camera was the twist noticeable. The sides of the specimen in the field of view came into focus at different focus settings. A manual focus had to be used to collect the data, which could have introduced data noise.

As noted in the methodology chapter, the application of the diffraction grating was less than ideal. The adhesive normally used to create a grating on the surface was not available, and when a new batch of the adhesive was ordered the manufacturer had changed chemical formulation of the adhesive. The new adhesive formula produced unsatisfactory results, such as bubbles on the grating surface and other flaws, which was discovered just prior to the test preparations for this thesis. The adhesive that was used for this experiment was not the first choice of adhesives and the only way to apply the adhesive was by using the flash left over from a previous diffraction grating application attempt. It is possible that there was a chemical interaction between the two adhesives or that the adhesive did not completely bond to the surface. If the adhesive were incompletely bonded, the details of the strains on the surface of the laminate would not be transferred to the grating and therefore would not be measured correctly. Incomplete bonding is not likely, since some of the expected strain trends were visible even with the noise.

The diffraction grating mold can also deteriorate over time. The master grating that was used to make the all the diffraction grating molds at the Air Force Materials

Directorate appear to have deteriorated.  During testing, the grating showed a lot of inherent flaws, noticeable by adjusting the focus of the camera.  If the grating has no flaws, an adjustment of the camera can make the whole fringe field appear solid.  This grating and subsequent gratings made at the Air Force Materials Directorate showed speckling across the surface.  Even though using this flawed diffraction grating introduced noise into the results, it was the best available diffraction grating at the time of testing.  Upon initial inspection of the results, the noise appeared to be tolerable.  Only later after a full evaluation and comparison with BSAM did the extent of the noise become apparent.  Additionally, the Moiré interferometer uses an internal diffraction grating.  This grating has become suspect and, when new flawless diffraction gratings are available, will be checked.  If a flawless grating is viewed through the camera while the camera is adjusted to eliminate the fringe pattern, any flaws in the internal diffraction grating and mirrors will be apparent.

One of the concerns during testing is vibration of the specimen.  Small vibrations can create large amounts of noise in the data.  The Moiré interferometer is mounted on a isolation table to eliminate as much vibration as possible, but some vibration, especially lower frequencies, can still effect the results.  During the first week of testing, a large amount of vibration was noted and no data was able to be collected.  Even though this obvious large source of noise ceased, minor levels can be unnoticeably present.  The low level of signal also contributed to this.  The specimen was only loaded to 549 lbf, a higher load would have produced much higher strains and lowered the noise to signal ratio.  As noted in the methodology chapter, a higher load had been used initially with

another specimen that cracked under the load. Due to this failure, a more conservative load was used to ensure that the specimen did not fail during testing.

**Discussion of Results**

The fair comparisons of the Moiré interferometry results with the mechanical loading BSAM model take a step toward validating BSAM. All of the measured results were on the same order of magnitude as the results from the model, and in the case of the shear strain field, a good correlation with the model trends was apparent. Both the model and experiment showed strain concentrations and thereby stress concentrations where they were expected, in the adhesive and ply terminations. As noted before, noise was very high and did not allow a more satisfactory match between the model and experiment. A good correlation in trends was shown between the BSAM surface model data and the BSAM data at ¼" into the specimen width. As expected, the strain magnitudes, indicative of free-edge singularities, decreased in the interior of the specimen. Possible reasons for variations in the Moiré data from the model data could include the size of the specimen including ply thickness, complexity of the geometry, and BSAM's modeling of material transitions at the free edge.

The specimen was very thin in order to maintain a short scarf length, as noted earlier. Since the specimen was so thin, many problems were encountered during manufacturer, such as application of the diffraction grating and maintaining a sharp edge on the top and bottom of the specimen. Since the edges were close to the areas of interest, some edge defects caused in diffraction grating application and specimen

fabrication could have skewed the results. Possibly doubling the layers, such as was done in Schoeppner and others (2004) work, would yield better results.

The geometry of a scarf is more complex than many of the geometries previously modeled by BSAM. Just the complexity of the joint may have skewed the results from the model. More testing should be done to validate the results.

Finally, BSAM currently used idealized geometry and where material transitions occur at the free-edge steep strain gradients were introduced. These steep strain gradients to some degree exist in the specimen, but the Moiré interferometry technique smoothes them slightly. The steep strain gradients on the surface are passed through to the data via a diffraction grating that is stretched over the surface. This stretched diffraction grating smoothes the collected data to a slight degree. The BSAM model does not smooth the steep strain gradients. Also the model is idealized; not taking into account the variations in specimen manufacture. BSAM is now being modified to handle some of the variances, but until then the idealization of such a complex joint will affect the results.

**IV.  Modeling and Experimental Measurement of Residual Strains in Scarf Joint**

As noted in the Methodology chapter, the 10-inch coupon specimen was cut down to two inches for residual strain Moiré interferometry.  The null state full field fringe patterns were taken in the x and z directions with the specimen set in the jig.  The specimen was then cut in the center of the field of view about a third of the way through the specimen's width using a diamond bladed saw that was narrow and dry to minimize contamination and alterations to the diffraction grating.  A second set of x and z direction fringe patterns were taken with the specimen placed in the same field of view of the camera.

**Moiré Data Analysis**

Where as the previous chapter looked at the load-bearing portion of the BSAM model, this chapter focuses on the thermal effect modeling capability.  Moiré data was taken in a configuration that would measure the effects from releasing the residual strains through cutting the specimen.  The results will be compared to a combination of two BSAM models, which will be discussed later.  The Moiré data was processed using the same methodology for processing the Moiré data on the tensile loaded scarf specimen, except that data from each side of the cut had to be processed separately.  The field of view of the data taken for the residual strain calculation was slightly offset from the field of view where the tensile loaded data was taken, but both fields of view were the same size.  The blue lines shown in Figure 46 are the edges of the field of view for all Moiré data collected.  The left lines in each set of blues lines are the field of view for tensile loaded specimen and the right lines in each set are for the residual strain measurement

specimen.  The two red lines in the middle mark the location of the cut.  The thickness of the specimen was only ~1.13 mm, so the cut thickness was very small.  The white speckles in the photograph are flaws in the diffraction grating.  The zero mask used for processing the data on the left side of the cut, highlights the larger flaws in the diffraction grating, Figure 47.
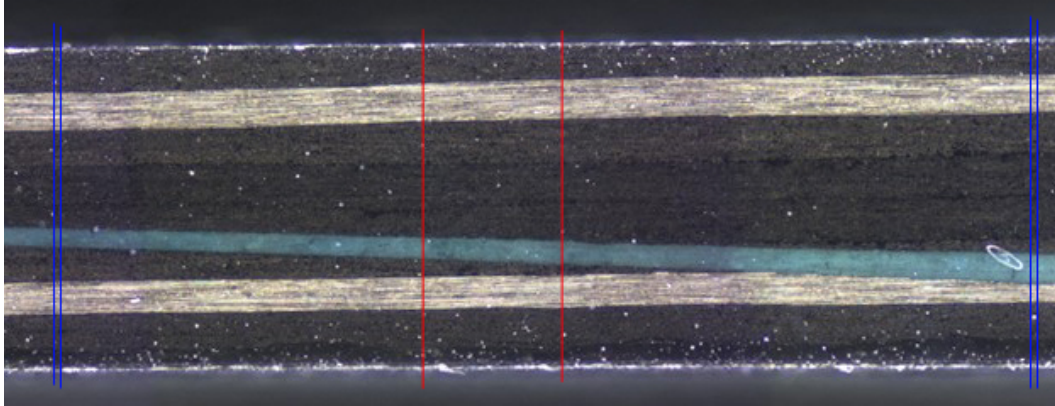


**Figure 46.  Photo view of whole residual strain measurement field**



**Figure 47.  Zero mask of the left side of cut specimen used from residual strain measurement**

An exact match can be seen in flaw location and size between the photograph and zero mask.  The left side of the cut and right side of the cut had to be processed separately, even though the initial null field before cutting included both sides.  After processing,

which included smoothing the strain data ten times using the same technique noted in the previous chapter, data from the calculation were extracted.  The data extracted from the Moiré calculations was the same size as the data extracted from the BSAM model for ease of comparison.

**BSAM Modeling**

The modeling for the residual strains was different than the methodology used for the tensile loaded specimen.  Two BSAM models had to be produced to correlate with the results of the Moiré data:  a model that incorporated the thermal curing effects without any applied mechanical load and a model that added free edges at the cut location.  The data from each model had to be extracted and processed to allow comparison to the Moiré data.

**Model Generation**

The releasing of residual thermal strains through cutting the specimen could not be modeled with a single BSAM model.  The strains measured in the Moiré interferometry test were not traditional residual strains, and therefore a combination of two BSAM models were used to obtain similar results to the Moiré data from cutting the specimen.  The first model was made using a modified version of the model used for the tensile loaded specimen.  Since there is a difference in the coefficient of thermal expansion of the laminate epoxy, laminate fiber, and the bonding adhesive, complex strains will result during curing at 350°F.  The mechanical loading model could be used by zeroing the traction boundary condition and doing a thermoelastic analysis for the curing stress.  The load was eliminated from the calculations, and the thermal effects

from cooling the specimen from autoclave curing temperatures to room temperature, approximately 280°F, were added to the model. Data was extracted from the model output to match the Moiré interferometer's field of view. The second model was for each side of the cut. Each side had a model that included a free edge where the cut was located. From each of these second models, data was extracted in the same plane as the field of view of the Moiré interferometer.

During modeling of the residual strain the local free-edge geometry had to be modeled with quadrilateral element whereas a triangular element would have been preferred. On the free-edges at the bondline interfaces, an artificial geometric singularity was introduced, allowing the model to better represent the idealized geometry for the free edge. The location of singularity in both the right and left side models are shown in Figure 48 and Figure 49. The top schematic in each figure shows the overall location of the scarf and plies, which are numbered according to BSAM's assignment of modeling segments. The lower schematic shows a blown up view of the areas where the singularity was introduced into the model. In all cases the singularity was introduced at locations that had a physical elastic singularity already located. Therefore the introduction of this geometric singularity was inconsequential.

Another model was generated to include the free edges from the cut. In idealizing the model, the geometry was created for the cut edge to be a free surface through the entire width of the specimen. Since the cut was at least 1/3 of the width through the specimen and only the surface effects were looked at with the Moiré data, this assumption is reasonable. The same thermal boundary conditions were applied to this model and data was extracted from the same locations as the previous model.
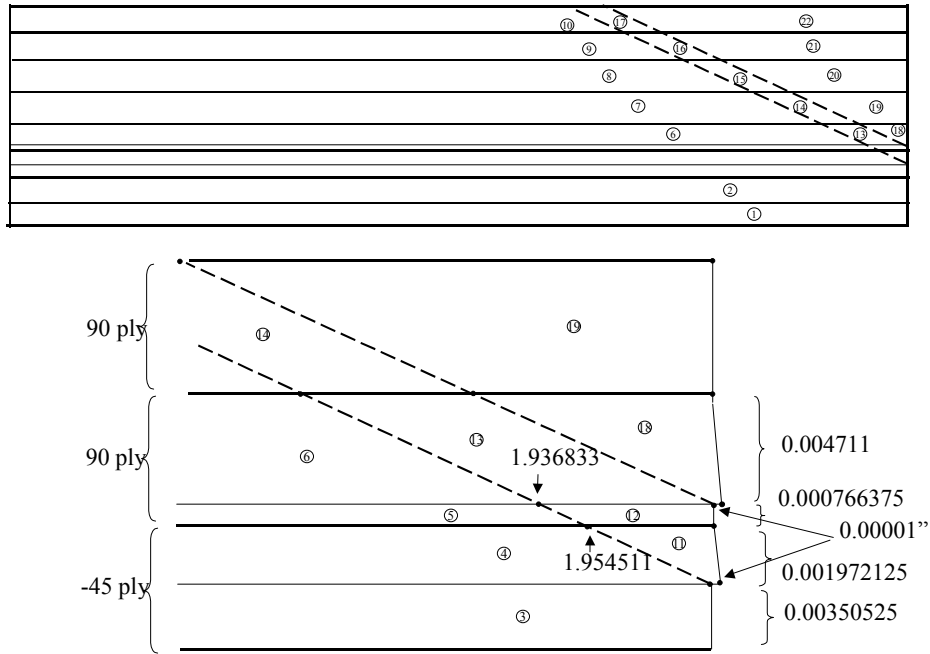
**Figure 48.  Schematic of the model for the left side of the cut surface**
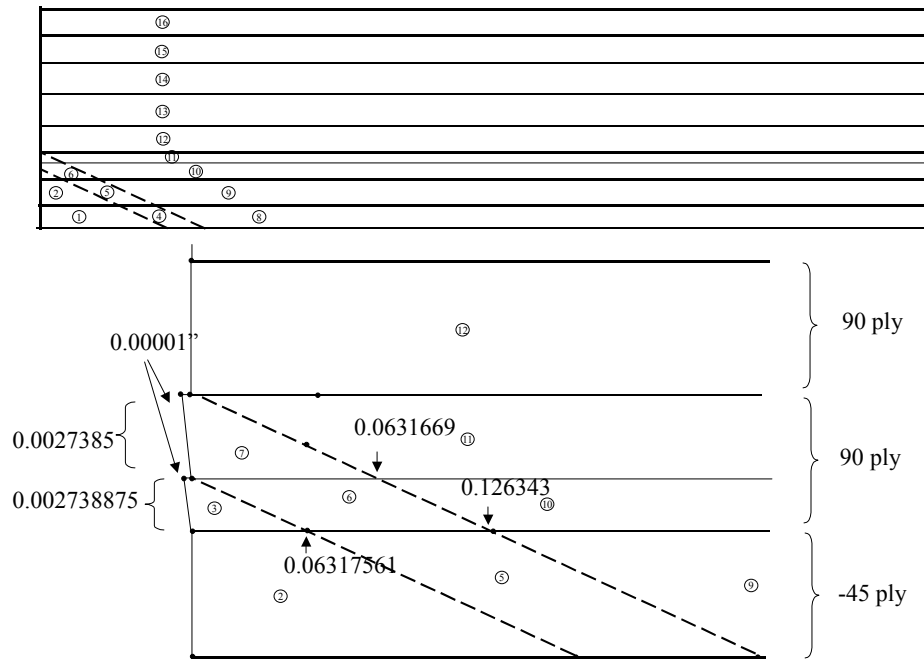


**Figure 49.  Schematic of the model for the right side of the cut surface**

The mesh for models that represent the left and right side of the cut were output to MATLAB® and screen captured, Figure 50 through Figure 52. The different colors are used to distinguish the adherends and adhesive. As previously discussed the origin for the left side model was set 2" from the cut edge. The isometric view of the model of the left side of the cut (Figure 50) shows that the mesh is more refined in the x-y plane (the width of the specimen) towards the edges to allow greater resolution where the edge effects occurred. The plies below and above the bondline are meshed evenly, with minor alterations as mentioned above and shown in Figure 51.
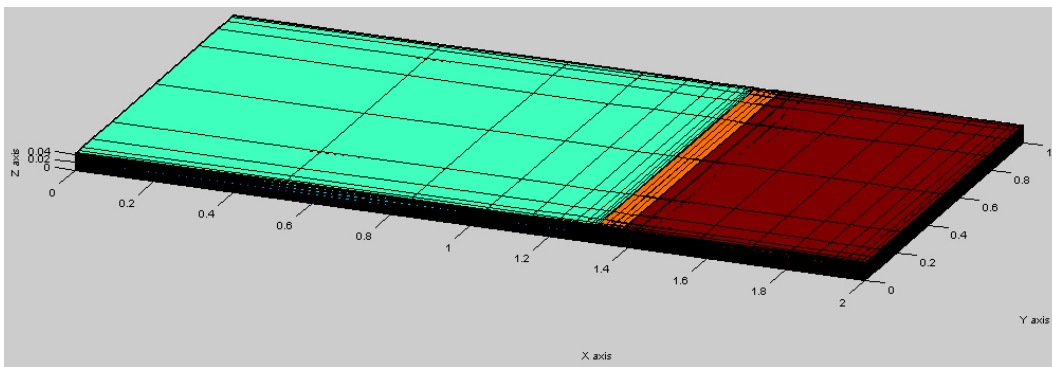


**Figure 50. Screen capture of isometric view of the mesh output for the model of the left side of the cut in MATLAB®**
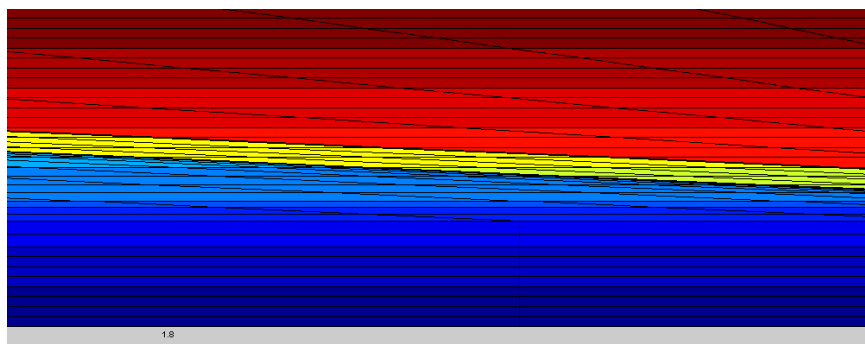


**Figure 51. Screen capture of MATLAB® mesh output of x-z plane at x=~1.8" and y=0" for the model of the left side of the cut (very near the cut edge)**

64

The origin for the model of the right side of the cut was set at the cut edge. Since the model was meshed similar to previous models, the isometric view is not shown. The through thickness view, Figure 52, shows the meshing complexities at the bondline, free-edge, and adjacent laminate plies' intersection.
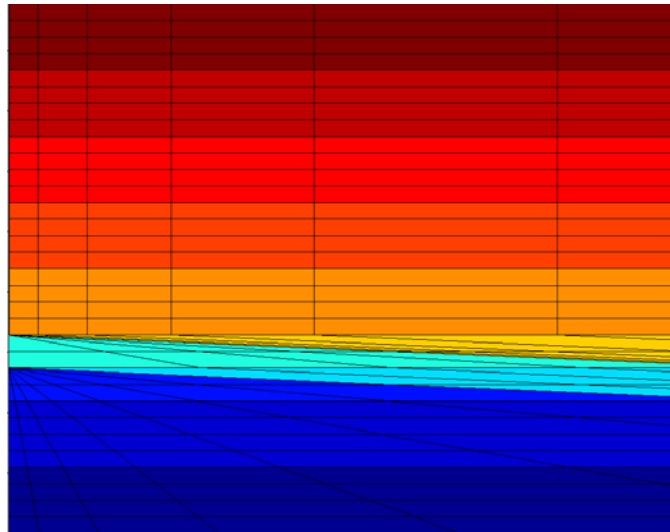


**Figure 52. Screen capture of MATLAB® mesh output of x-z plane at x=~0" and y=0" for the model of the right side of the cut**

### Data processing of model results

The two extracted data sets, one from each model, were then imported into the software program Transform and processed similar to the Moiré data. First, any gaps in the data were filled in. Some gapping occurs when the data is extracted from the model and sized to the same resolution as the Moiré data. The extracted data from the first model (uncut specimen) were subtracted from the second model's (cut specimen) data. This set of data can now be compared directly to the Moiré data. A complete set of BSAM data is included in Appendix E, which includes all six components of the strain tensor.

## Residual Strain Specimen Results

Surface features can be compared to the BSAM model and Moiré data through referencing the photographs of the areas being analyzed for the left and right sides of the specimen, Figure 53 and Figure 54 respectively.
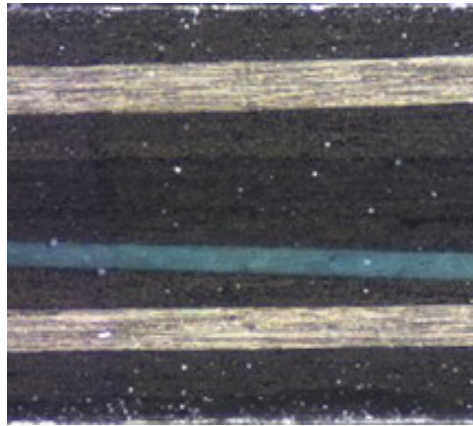


**Figure 53.  Photo view of left side used for residual strain measurement**
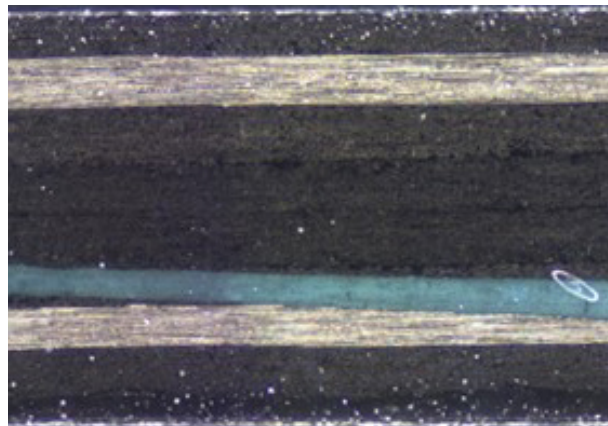


**Figure 54.  Photo view of right side used for residual strain measurement**

The photo of the right side is wider due to the location of the cut not being in the center of the field of view.  For ease in viewing the results, data on the right side that was farther away from the free edge than the data shown on the left side was truncated.  Data farther away from the free edge is less affected by cutting of the laminate.  At around 1mm away

66

from the cut edge, the data appears to be in the far field view. Data was collected at the edge of both sides of the cut by comparing the far field solution from the model to the experimental data. Additionally, the BSAM model data at ¼" into the width is shown for comparison. Full field strain views are shown on the same color scale (Figure 27), white is used to show strains larger than the set maximum bound and black is used to show all strains below the set lower bound with the colors of the rainbow (red, orange, yellow, green, blue, and indigo) distinguishing the strains in between the maximum and minimum bounds. The upper and lower bounds for all full fields shown are 0.008 and -0,008 micro strain respectively. When comparing to the Moiré results, remember the noise level discussion in the previous chapter.

The $\varepsilon_{xx}$ strain field shows some correlation between the BSAM and Moiré data. All full field results have the same general background color, denoting a match with the background strain levels, Figure 55 and Figure 56. The BSAM and Moiré fields on both the left and right side of the specimen match in general location for the strain concentration areas. Comparing the locations to the surface photo, Figure 53, the concentrations are at the 0° ply, top edge of the laminate, and bond adhesive intersections with the free edge. BSAM data extracted from ¼" into the width from the surface, or interior data, has a slight increase in strain concentration size and magnitudes, which was not expected.
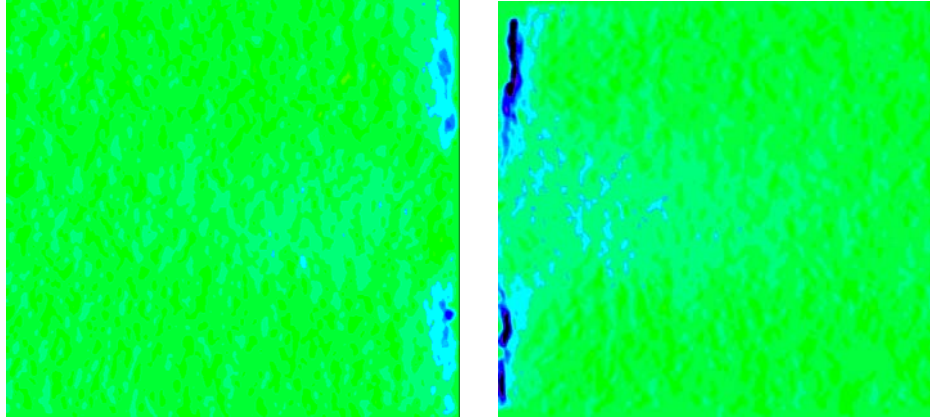
**Figure 55.  Full field $\varepsilon_{xx}$ strains from processed Moiré data for residual strain specimens**
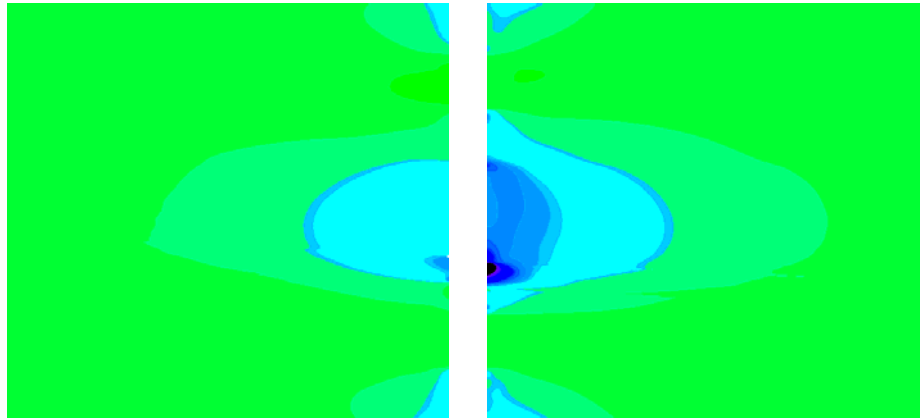


**Figure 56.  Full field $\varepsilon_{xx}$ strains extracted from BSAM at edge of model for residual strain specimens**
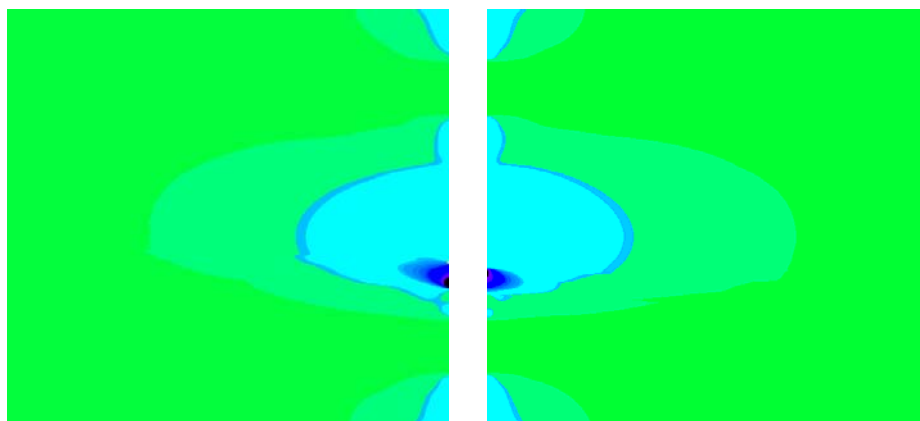


**Figure 57.  Full field $\varepsilon_{xx}$ strains extracted from BSAM at ¼" into width of model for residual strain specimens**

Line plot data for the left side shows good correlation at the far field location, Figure 60, but little correlation near the cut edge, Figure 59 and at the cut edge, Figure 58. The right side line plots show general trend matching near the cut edge and far field locations, Figure 62 and Figure 63, and no correlation on the edge, Figure 61. The data from on the edge is expected not to match between the model and Moiré data shown by previous work (Schoeppner and others, 2004). The discrepancies arise from damage to the diffraction grating at the edge during the cutting process and the singularities that are manifested in the BSAM model at the cut. The line plots also verify that the BSAM and Moiré data have the same order of magnitude for each data set.



**Figure 58. Comparison of Moiré and BSAM for $\varepsilon_{xx}$ strain through thickness at ~0.036mm from cut edge of left residual strain specimen**

**Figure 59.  Comparison of Moiré and BSAM for $\varepsilon_{xx}$ strain through thickness at ~0.2mm from cut edge of left residual strain specimen**



**Figure 60.  Comparison of Moiré and BSAM for $\varepsilon_{xx}$ strain through thickness at ~1.2mm from cut edge of left residual strain specimen**

**Figure 61. Comparison of Moiré and BSAM for $\varepsilon_{xx}$ strain through thickness at ~0.021mm from cut edge of right residual strain specimen**



**Figure 62. Comparison of Moiré and BSAM for $\varepsilon_{xx}$ strain through thickness at ~0.2mm from cut edge of right residual strain specimen**

71

**Figure 63. Comparison of Moiré and BSAM for $\varepsilon_{xx}$ strain through thickness at ~1.17mm from cut edge of right residual strain specimen**

The $\varepsilon_{zz}$ data has minor correlation between the BSAM and Moiré full field views. As before, the background strain levels match in all of the full field results. Towards the free edge (which is located between the left and right sides of the full field plots) strain concentrations exist at the intersection of the internal 45° plies and at the bond, Figure 64 and Figure 65. The Moiré full field plots show a large amount of noise, especially at the -45° plies, or the outside plies. The top and bottom edges of the diffraction grating were damaged. This also can be seen in the photographs of the laminate surface, Figure 53 and Figure 54, where the white dots and areas are diffraction grating imperfections. The far field solution should go to zero, since the null field and the altered state field should have identical strain in this area. All of the data from the model exhibits this, but the Moiré data in the $\varepsilon_{zz}$ data does not. This is plainly an effect of the noise level in the z-direction,

which was discussed in the last chapter. The interior data is lower in magnitude and size compared to the BSAM data taken at the edge surface, as expected.

The line plot data for $\varepsilon_{zz}$ on the left and right side of the cut show some correlation. The line plots from both have good correlation at the free edge, Figure 67 and Figure 70, but significantly less matching between the BSAM and Moiré data as the distance is increased away from the free edge, Figure 68, Figure 69, Figure 71, and Figure 72. This reveals the extent of the noise in the data, specifically in the $\varepsilon_{zz}$ strain fields.



**Figure 64. Full field $\varepsilon_{zz}$ strains from processed Moiré data for residual strain specimens**



**Figure 65. Full field $\varepsilon_{zz}$ strains extracted from BSAM at edge of model for residual strain specimens**

73

**Figure 66. Full field $\varepsilon_{zz}$ strains extracted from BSAM at ¼" into width of model for residual strain specimens**
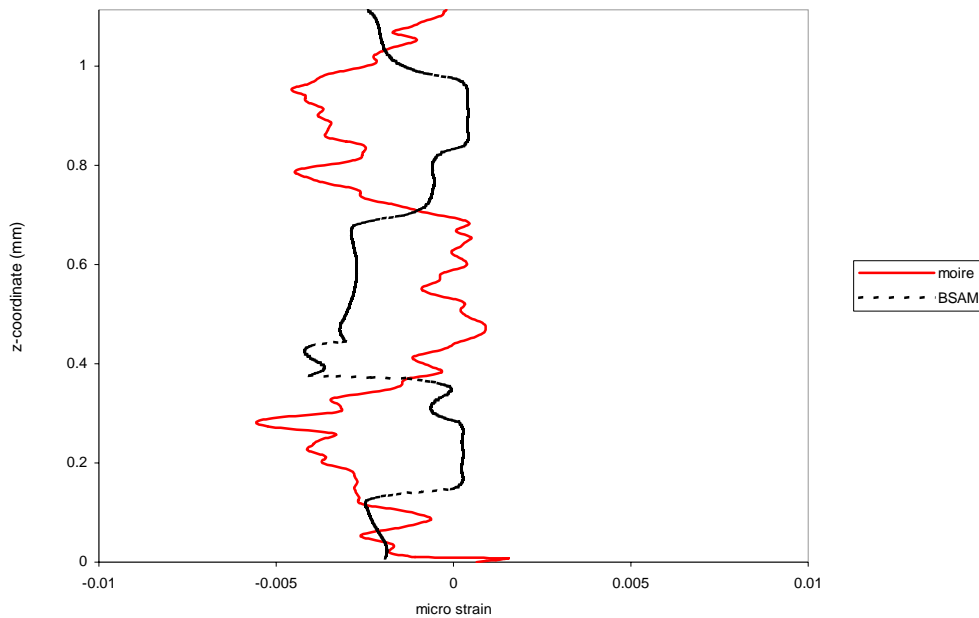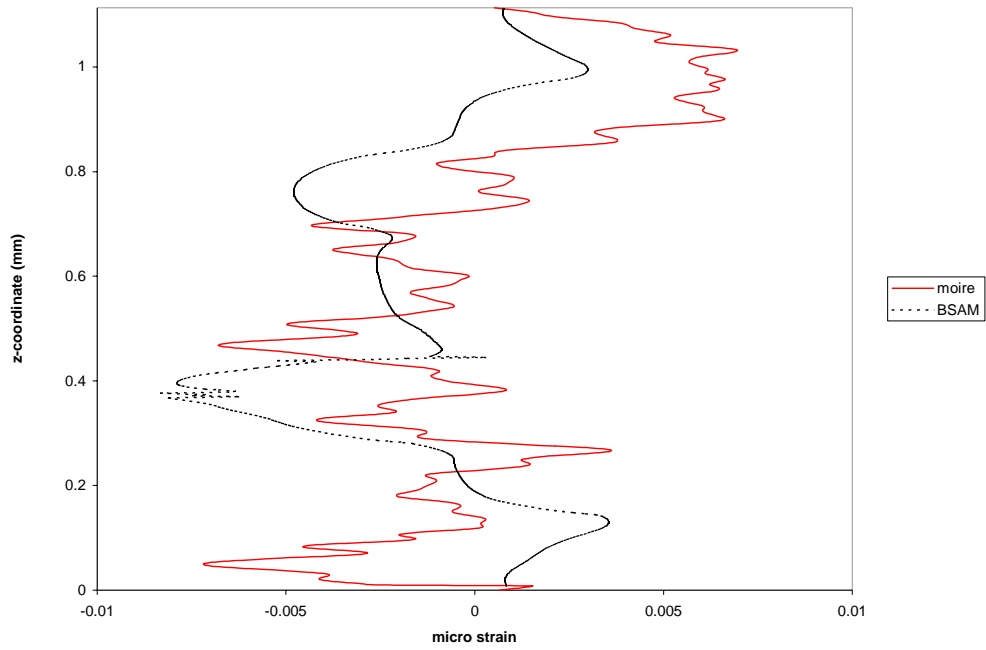


**Figure 67. Comparison of Moiré and BSAM for $\varepsilon_{zz}$ strain through thickness at ~0.036mm from cut edge of left residual strain specimen**
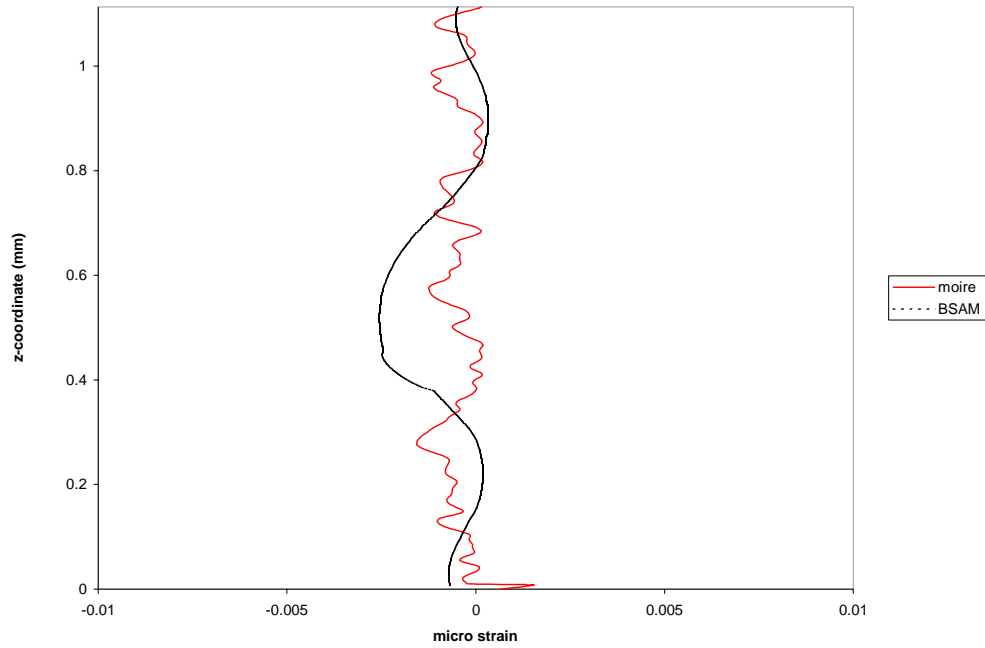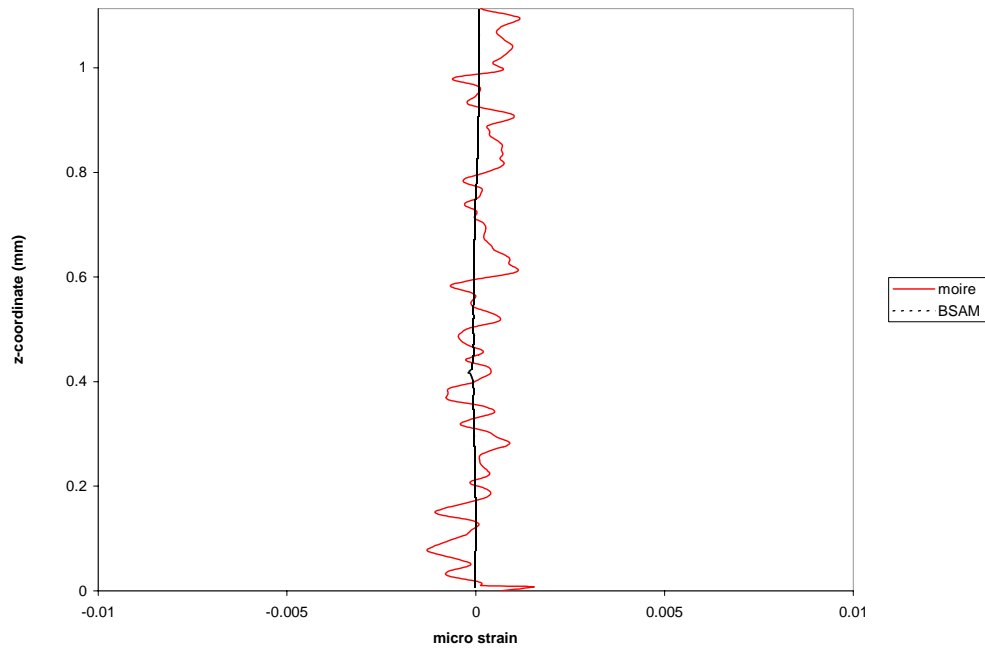
**Figure 68. Comparison of Moiré and BSAM for $\varepsilon_{zz}$ strain through thickness at ~0.2mm from cut edge of left residual strain specimen**
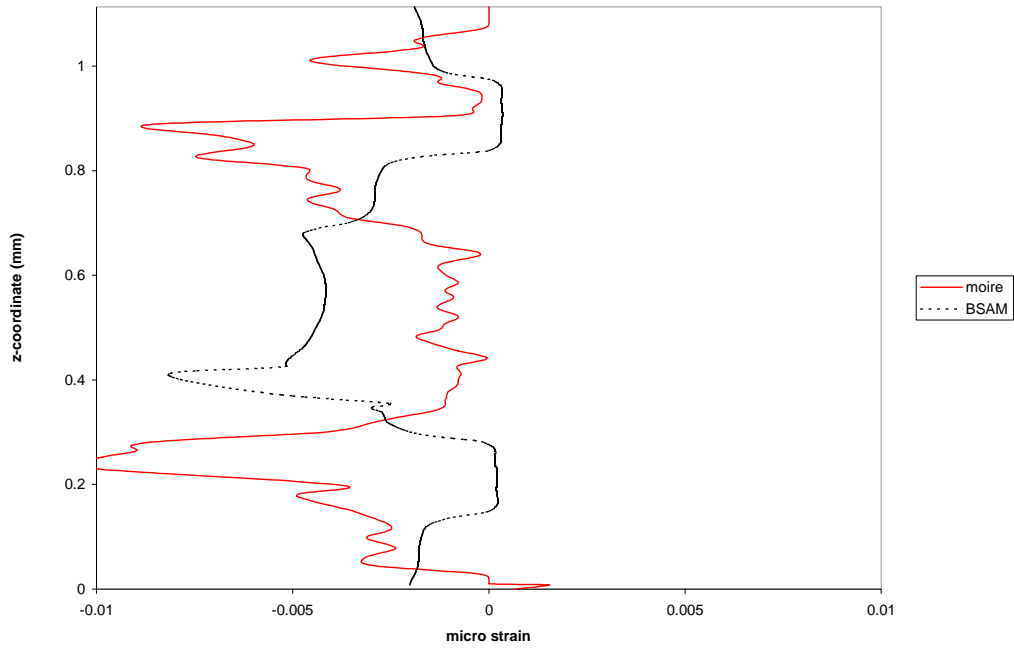


**Figure 69. Comparison of Moiré and BSAM for $\varepsilon_{zz}$ strain through thickness at ~1.2mm from cut edge of left residual strain specimen**

**Figure 70.  Comparison of Moiré and BSAM for ε$_{zz}$ strain through thickness at ~0.021mm from cut edge of right residual strain specimen**
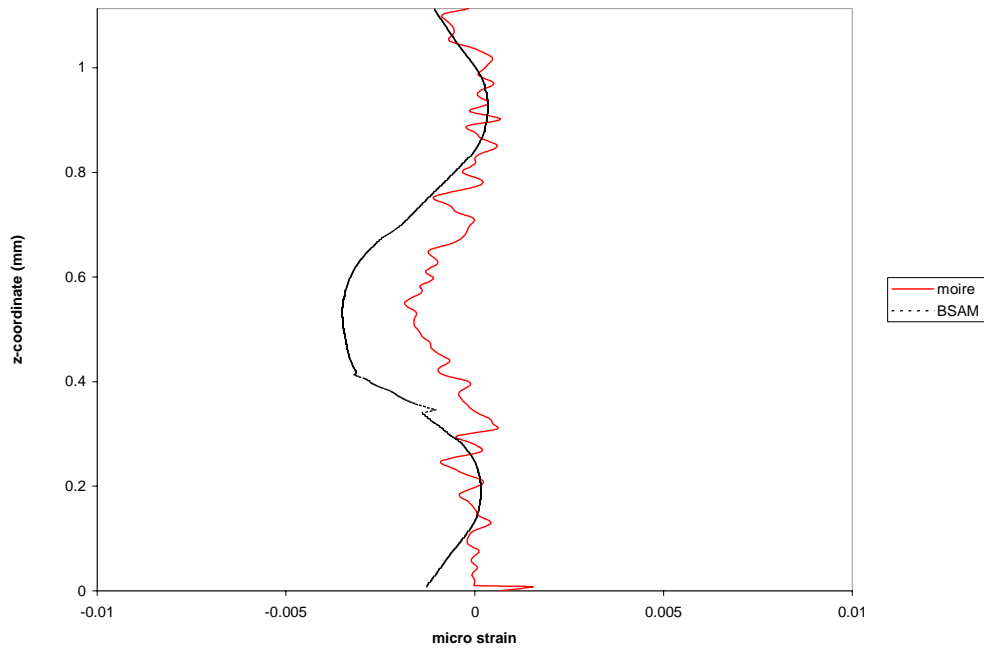


**Figure 71.  Comparison of Moiré and BSAM for ε$_{zz}$ strain through thickness at ~0.1mm from cut edge of right residual strain specimen**
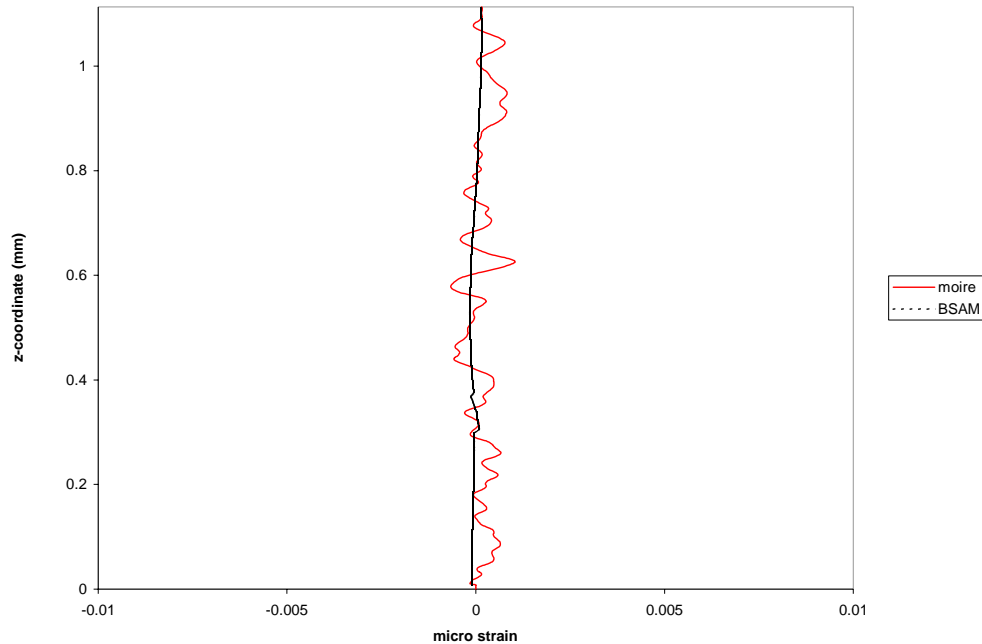
**Figure 72. Comparison of Moiré and BSAM for $\varepsilon_{zz}$ strain through thickness at ~1.17mm from cut edge of right residual strain specimen**

The $\gamma_{xz}$ full field results show good correlation. As before, the background strain matches and the strain concentration areas match and are at the expected locations, Figure 73 and Figure 74. Some peaks in the Moiré data may be attributed to flaws in the grating. Since the shear strain field is derived from the x and z directional data, the noise and flaws in the z-directional data affects the results. Though the ¼" width interior shear strain data on the right side of the cut decreases in size and magnitude at the strain concentrations, the left side surprisingly does not in the bondline region.
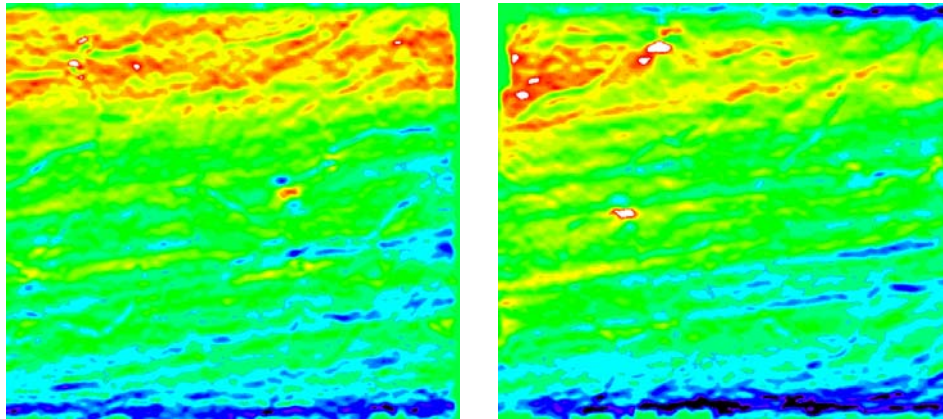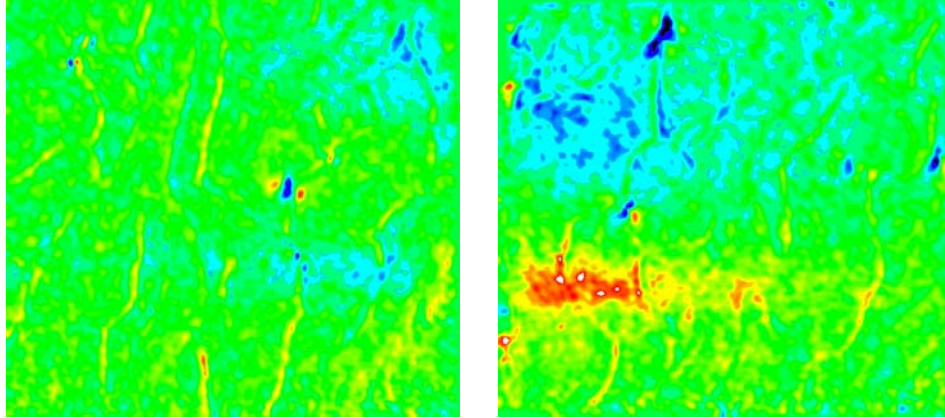
**Figure 73.  Full field γ$_{xz}$ strains from processed Moiré data for residual strain specimens**
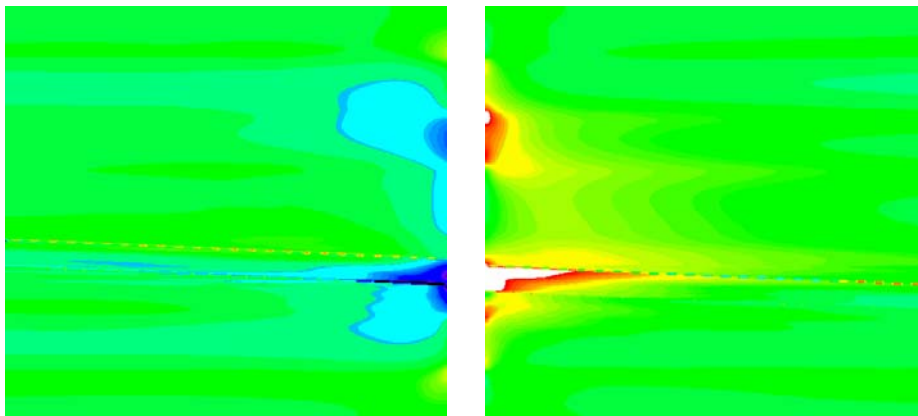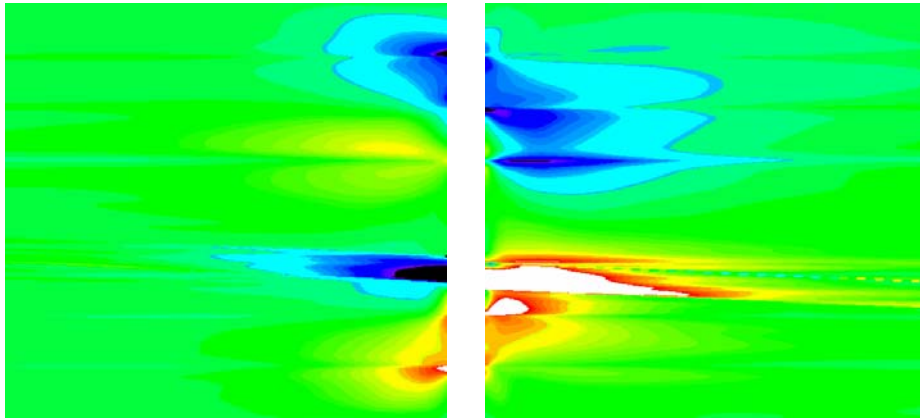


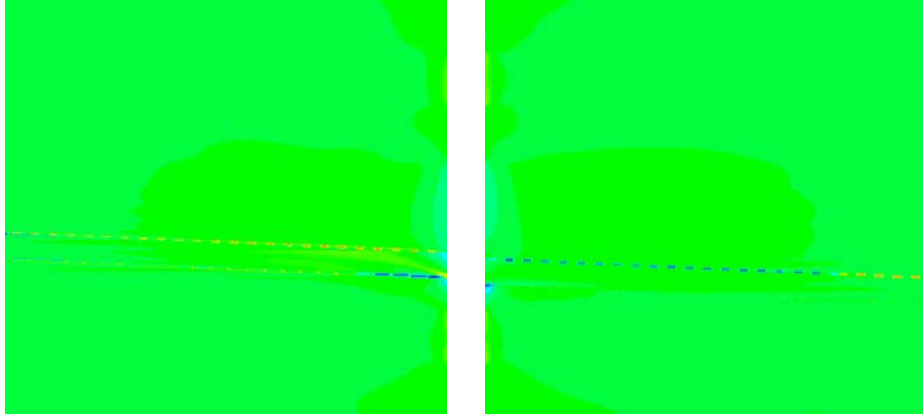**Figure 74.  Full field γ$_{xz}$ strains extracted from BSAM at edge of model for residual strain specimens**
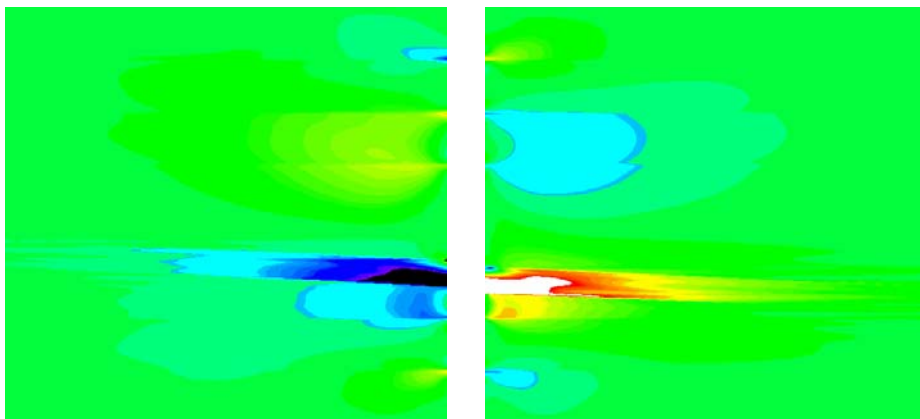


**Figure 75.  Full field γ$_{xz}$ strains extracted from BSAM at ¼" into width of model for residual strain specimens**

The line plot data of the BSAM results shows good correlation with the Moiré experimental results.  In Figure 76 through Figure 79, the BSAM data line shows the same trends as the Moiré test results.  The line plot data on the cut edge doesn't correspond as closely in the far field region and even at 0.2mm from the free edge, but the magnitude of all the data matches and some mismatching at the cut edge region is expected.  For example Figure 80, which shows the data at the right side edge has some matching in the middle of the specimen, but near the strain concentrations the results don't correlate.  This is expected, since the Moiré data is not expected to be accurate at the cut edge.  The remaining line plots, Figure 81 through Figure 83, show excellent correlation between the BSAM model and the Moiré experiment.
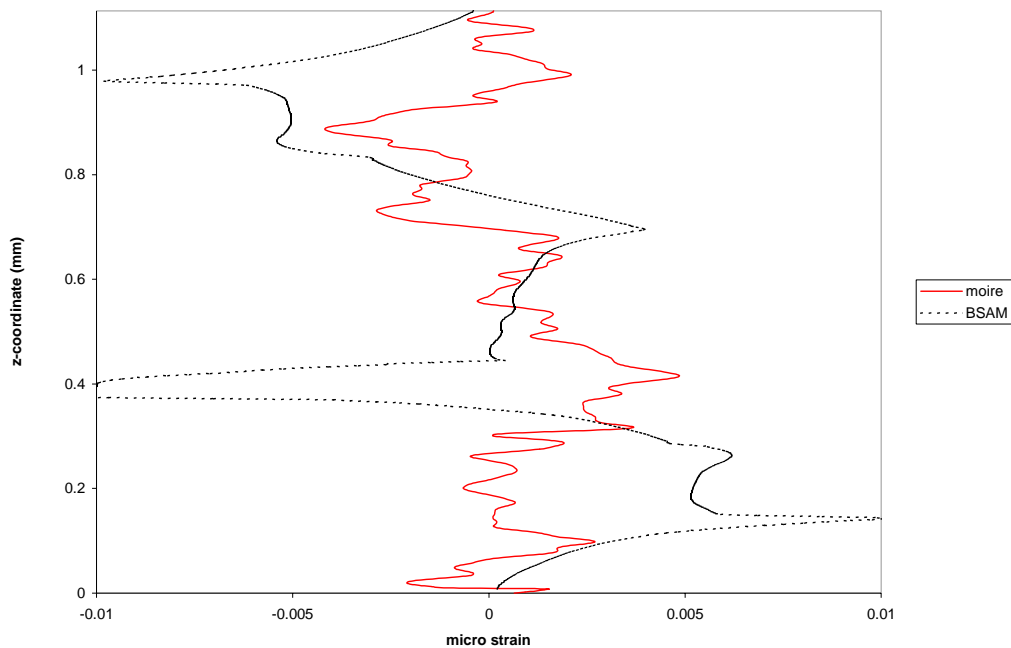


**Figure 76.  Comparison of Moiré and BSAM for $\gamma_{xz}$ strain through thickness at ~0.036mm from cut edge of left residual strain specimen**

79
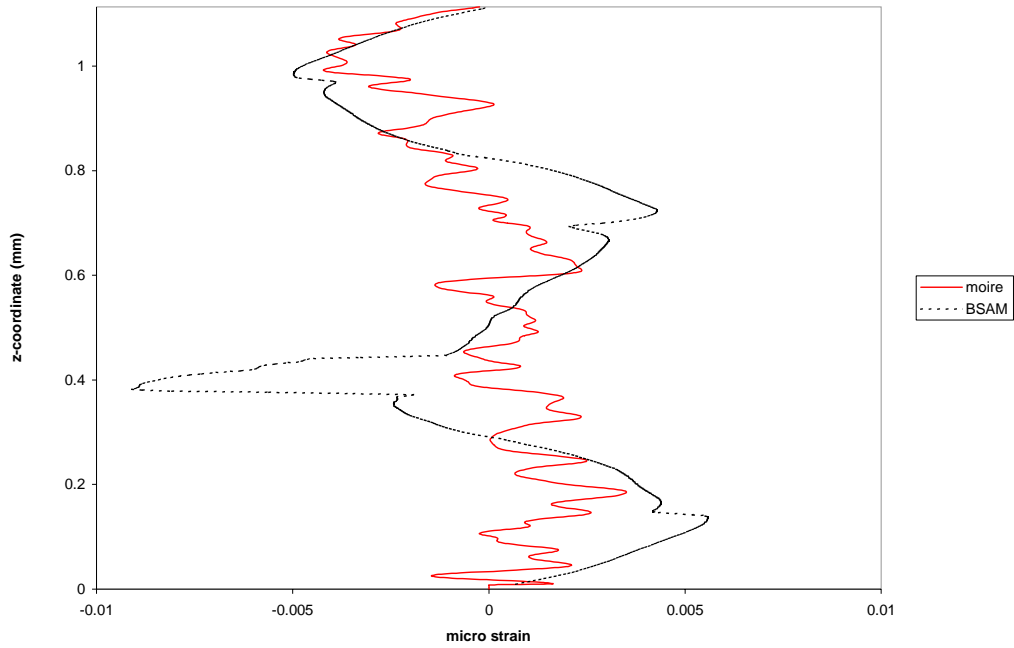
**Figure 77.  Comparison of Moiré and BSAM for $\gamma_{xz}$ strain through thickness at ~0.1mm from cut edge of left residual strain specimen**
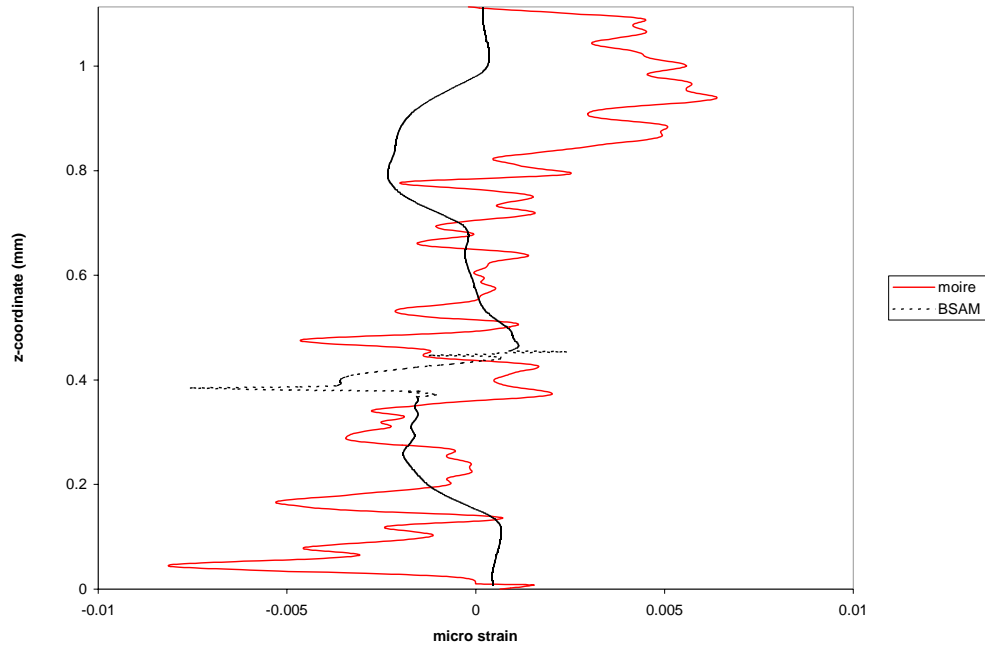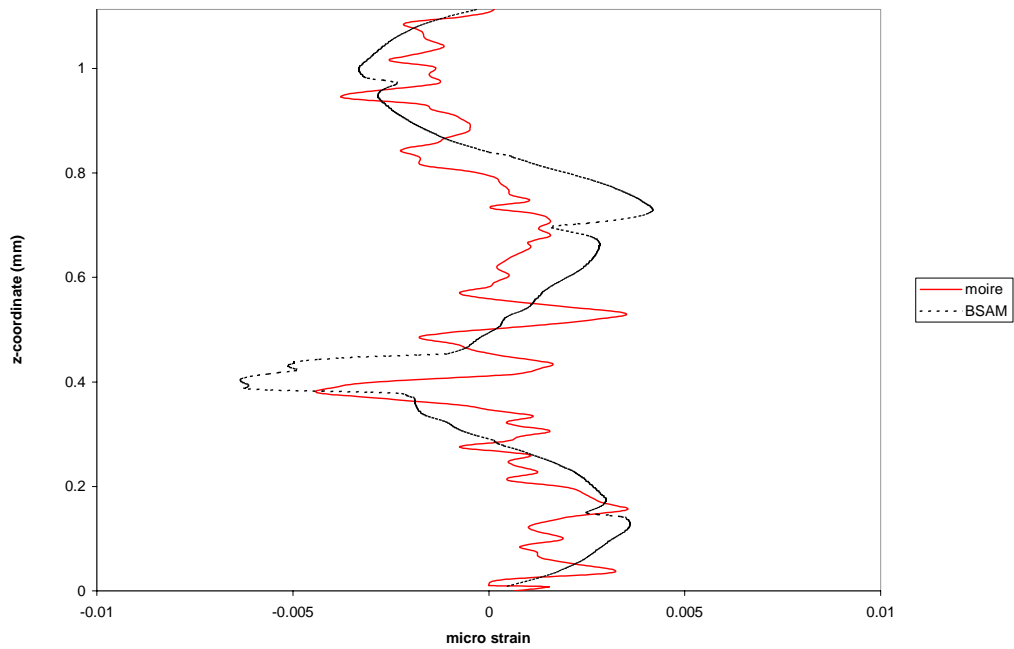


**Figure 78.  Comparison of Moiré and BSAM for $\gamma_{xz}$ strain through thickness at ~0.2mm from cut edge of left residual strain specimen**
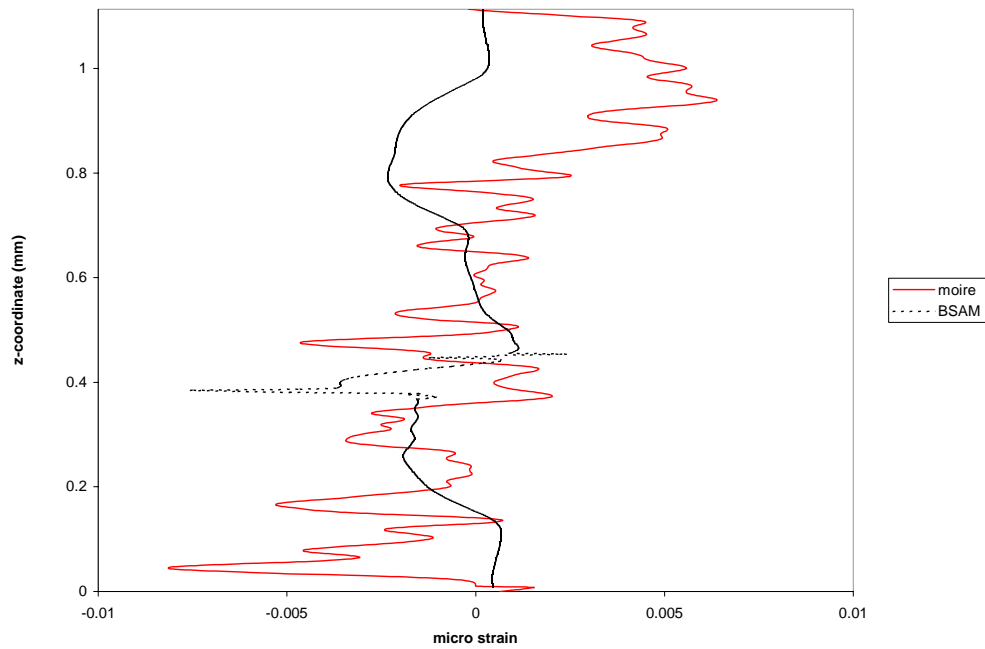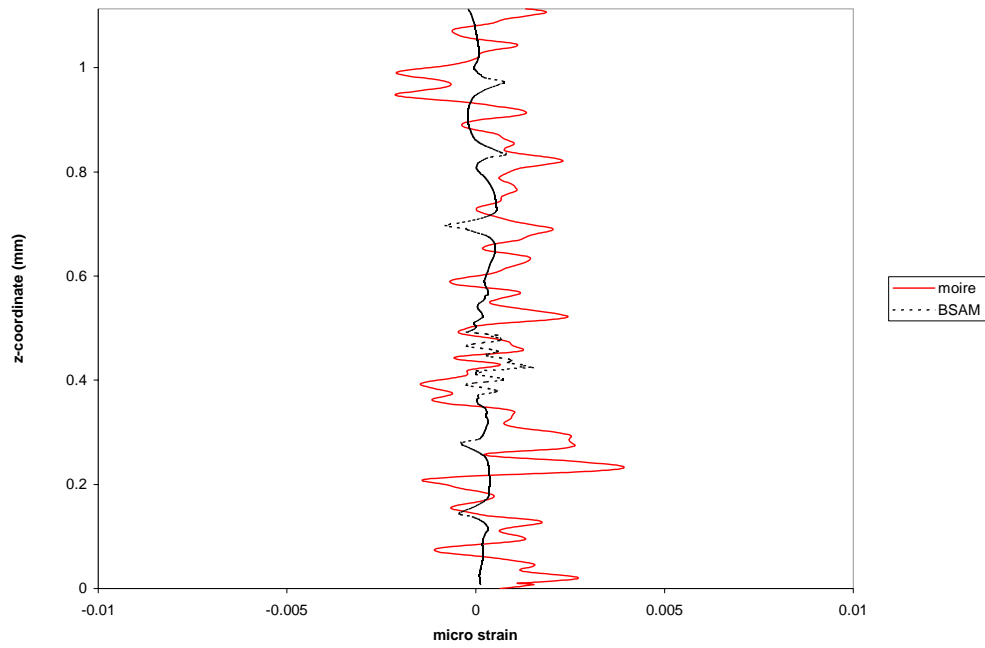
**Figure 79. Comparison of Moiré and BSAM for $\gamma_{xz}$ strain through thickness at ~1.2mm from cut edge of left residual strain specimen**
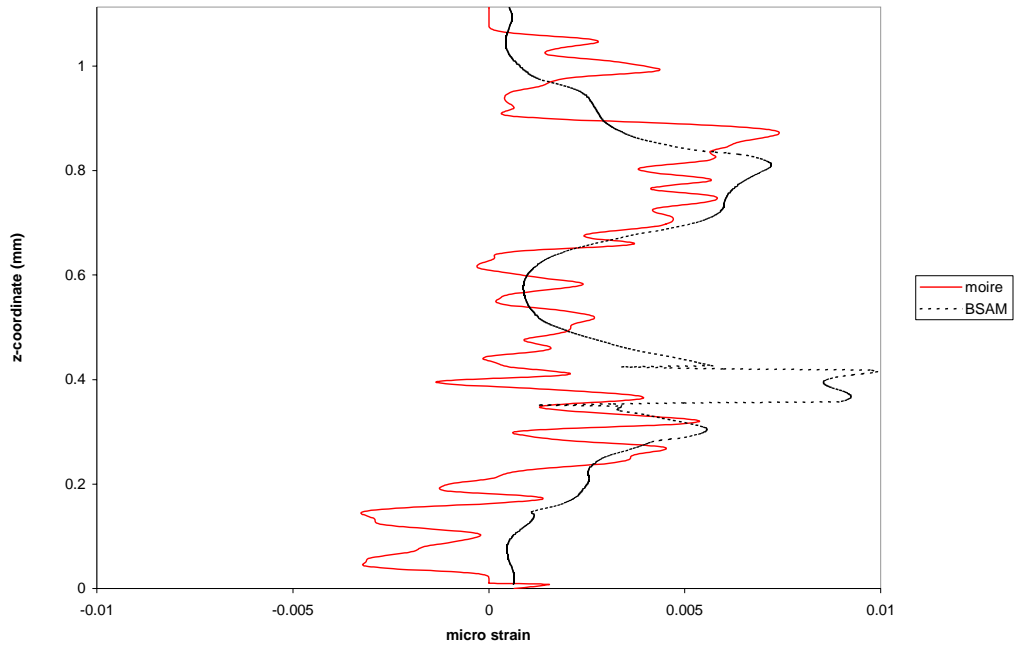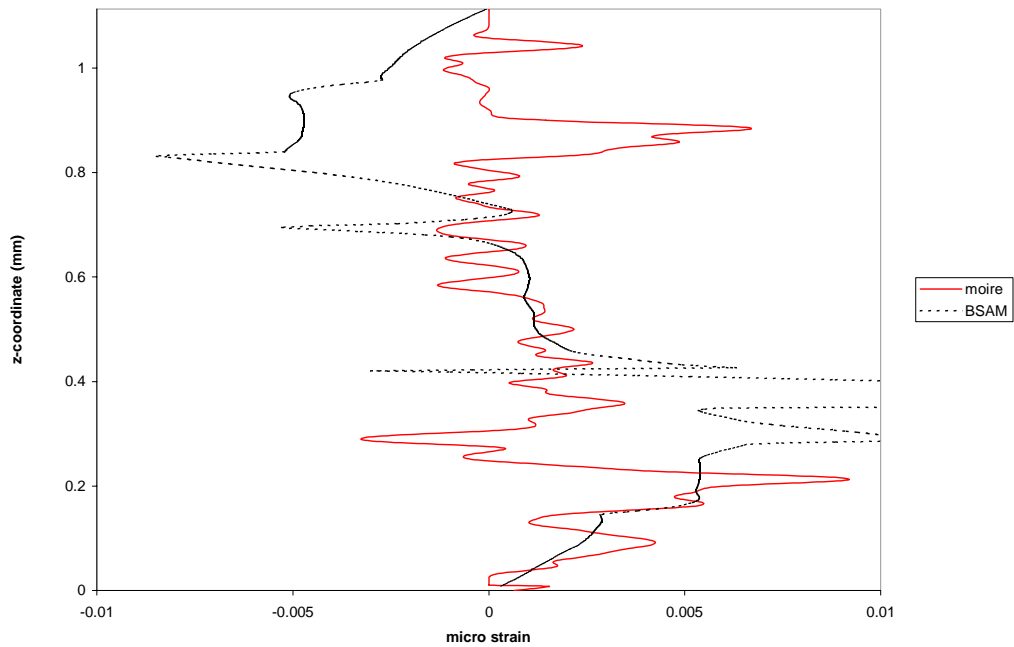


**Figure 80. Comparison of Moiré and BSAM for $\gamma_{xz}$ strain through thickness at ~0.021mm from cut edge of right residual strain specimen**
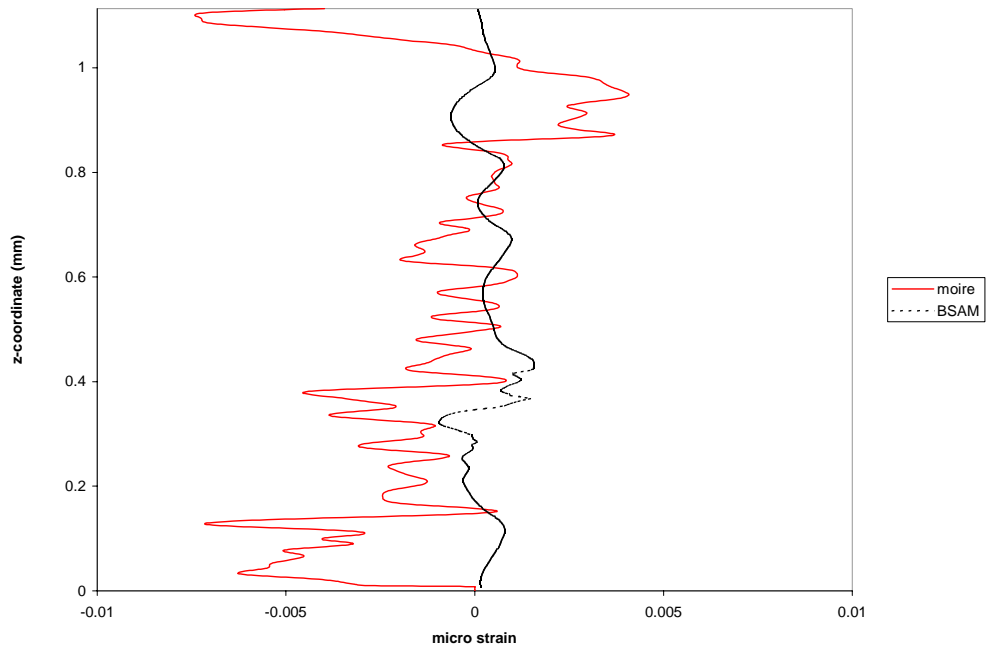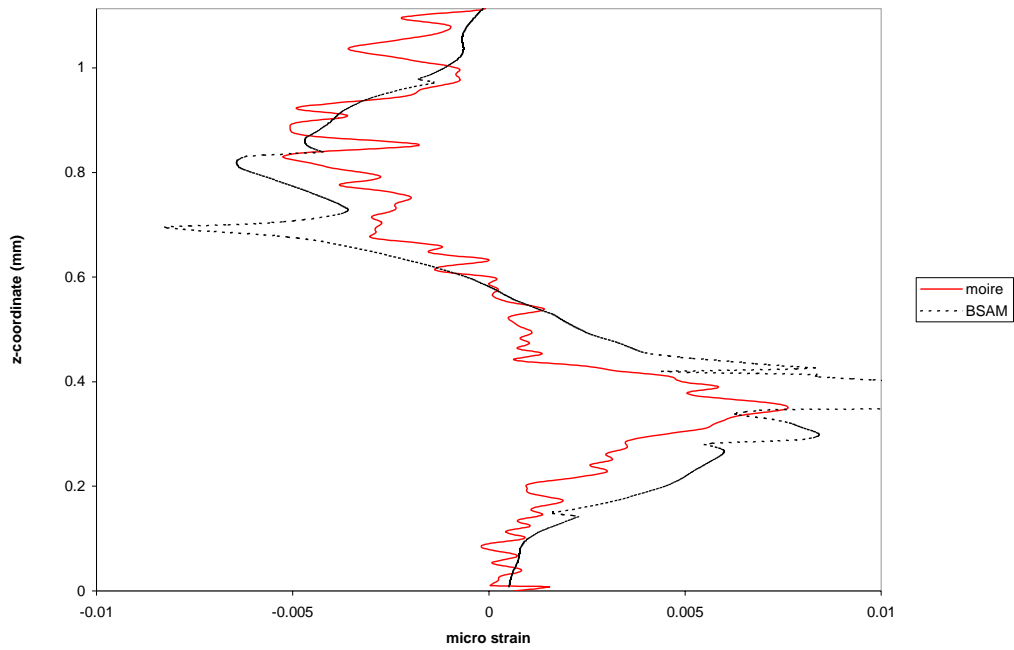
**Figure 81.  Comparison of Moiré and BSAM for $\gamma_{xz}$ strain through thickness at ~0.1mm from cut edge of right residual strain specimen**
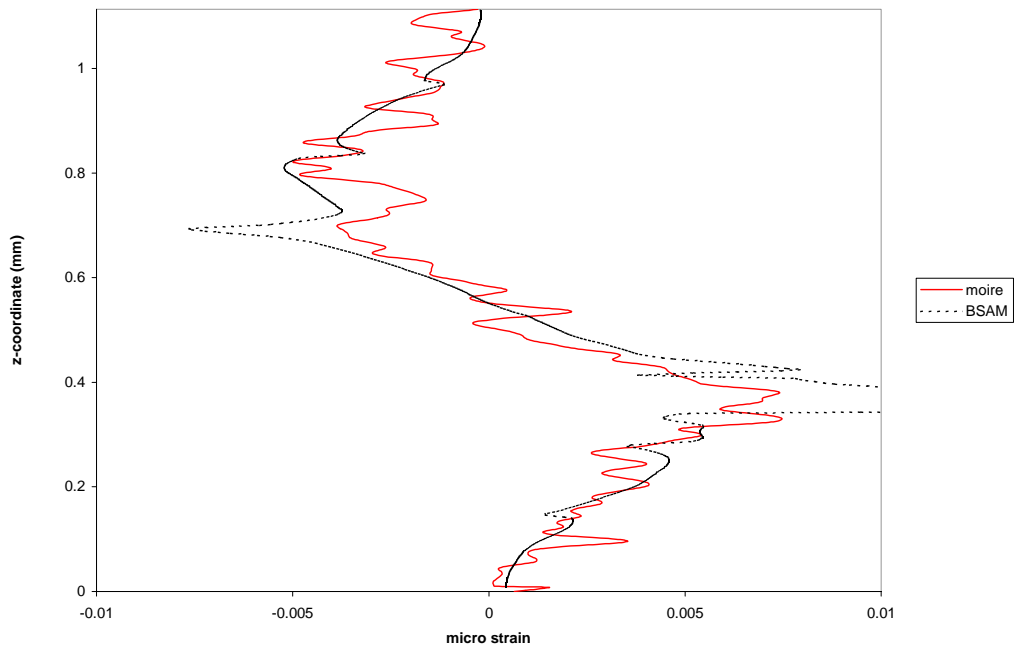


**Figure 82.  Comparison of Moiré and BSAM for $\gamma_{xz}$ strain through thickness at ~0.2mm from cut edge of right residual strain specimen**
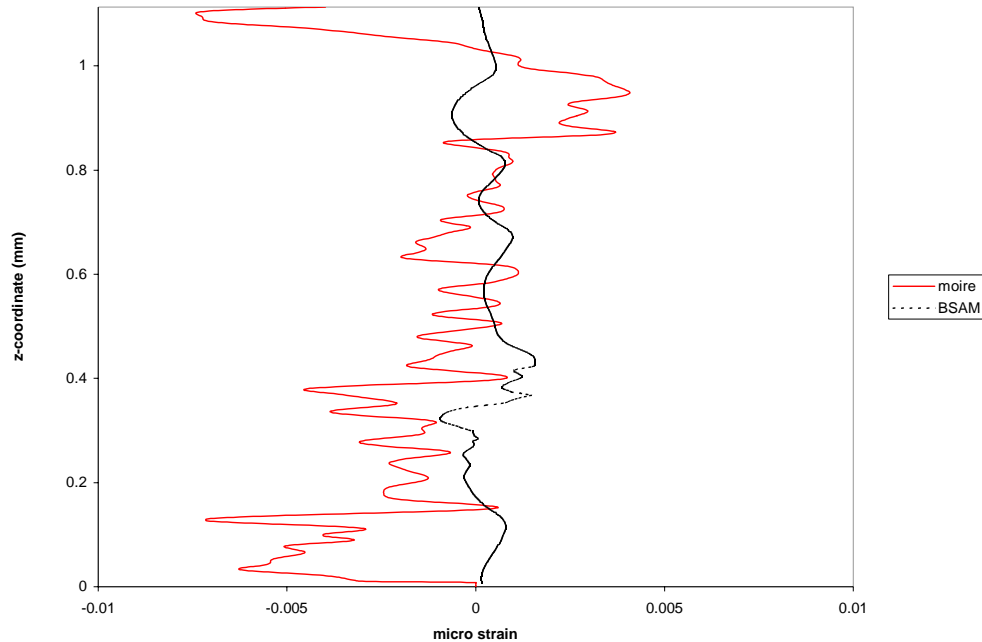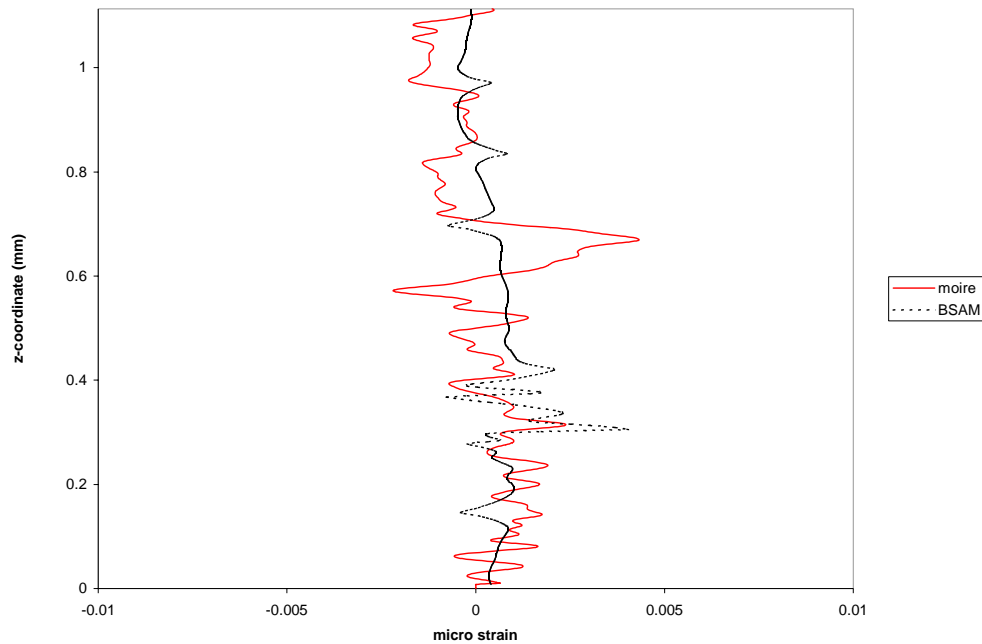
**Figure 83. Comparison of Moiré and BSAM for $\gamma_{xz}$ strain through thickness at ~1.17mm from cut edge of right residual strain specimen**

The far field, which should have zero values, reveals the amount of noise in the Moiré data. The noise level is high and in some cases may be larger than the strains being measured.

**Discussion of Results**

As with the tensile loaded straight scarf specimen data, the residual strain scarf data takes steps toward validating the BSAM modeling of a scarf joint. The previous chapter worked toward validating the mechanical load-bearing portion of the program, while this chapter concentrated on the thermal effect modeling capability. The results do show matching in the order of magnitude of the general strain level and location of the strain concentrations. Especially when the results were away from the cut edge, some

83

good correlations were shown.  The z-directional data did have a large amount of noise, but still showed some level of correlation.

Differences between the BSAM data and Moiré experimental data could be for the following reasons:  noise in the experimental data, size of the specimen, complexity of the geometry, and BSAM intrinsic limitations issue.  The noise issue has been thoroughly discussed in the previous chapter.  The size of the specimen, complexity of the geometry, and BSAM limitations issue were also discussed.  The modeling of the residual strain involved a more complex modeling method than the loading model since two models were needed.

## V.  Results and Discussion for Large Tensile Test Panels


As part of validating the analytically predicted scarf repair strains, data was collected for large tensile test specimens at various stages of being scarf repaired.  As compared to the idealization of the scarf joint in the previous two chapters, the round scarf repair is one step closer to actual composite repair configurations.  The circular scarf patch is a more complex joint that requires a full three dimensional analysis to understand the strains in the laminate.  As previously noted in the methodology chapter, large tensile test panels were prepared and tensile tested to failure.  The same material used for the Moiré specimens was cut to size.  The ends of the specimens were tabbed and drilled to accommodate the testing fixture.  Three panels were scarfed in the center of the panel and four panels were scarfed and repaired in the same location.  All of the panels, including the three that were left virgin, were strain gaged in preparation for tensile testing.  The test procedures were outlined below.

**Virgin Panel Results**

The specimen was attached to the load fixture by bolts that went through the first grip plates, into the aligned holes of the specimen tabs, and then through the second grip plate.  The bolts for the first specimen, panel 418T, were hand tightened, resulting in panel failure in the tab region through the bolt hole line, because of inadequate gripping pressure and tab adhesive failure.  For this initial specimen, the load was transferred from the loading fixture to the specimen through bolt bearing pressure, resulting in a tear out between the bolt holes.  In an effort to address the premature failure in the specimen tab

area, the panel was cut to a shorter length, a new tab was bonded on using the same adhesive originally used, and the panel was retested with ¼" finely threaded bolts torqued to 150 inch pounds, the maximum value recommended by a bolt manufacturer's catalog (Unbrako® Socket Screws, 1988). The bolt pressure allowed the load to be transferred from the load fixture to the specimens through shear loading of the tabs. This second test of panel 418T failed at approximately 15,000 lbf or an addition 2000 lbf higher load than the first test. Though this second test still failed by pulling out in the tab region of the panel, some of the 45° ply fibers also failed in the gage region of the panel. Proportional specimen cross-section scaling of the one-inch wide tensile strength specimen results (refer to Appendix C for details) to the 5.24" wide panels gave insight into the validity of the results. The one-inch wide coupons and the large 5.24 inch wide coupon had identical stacking sequences. Neglecting any non-proportional scaling factors, if the average failure load of 4500 lbf from the one-inch specimens is scaled up to the 5.24" width specimens, the ultimate load would be approximately 23,500 lbf. Since the panels have a larger width, statistically there should be more critical inherent flaws through the width of the panels than the one-inch tensile specimens. Therefore, a lower failure load value than 23,500 lbf would seem more appropriate. During the one-inch specimen tensile testing, cracking in the specimen was audible at around 3000 to 3500 lbf. Using this value as a failure initiation load would result in a scaled value for the 5.24" specimens of approximately 16,000 to 18,000 lbf, which was close to the second load test results for panel 418T. In addressing the tab adhesive, the technician who applied the tabs and an adhesive expert were consulted. The adhesive used to bond the tabs on was discovered to be capable of holding only 1000 lbf of shear per square inch. The tabs

were the full width of the specimen and approximately 2 ¼" long.  A review of the

original adhesive strength properties determined that the (designation of the adhesive)

adhesive shear strength was approximately 1000 psi.  An alternative adhesive with a

shear strength of 5000 psi was identified.  Only two options were available to address the

tab adhesive failure: 1) remove all of the tabs and rebond them with the alternative

stronger adhesive or 2) continue testing with the original tab adhesive.  Removal of the

tabs was deemed too risky, since the potential for damage to the specimens was high and

realigning the tab's holes with the holes in the panels appeared difficult.  Since panel

418T failed in the already weakened tab on the second test and the panel showed signs of

failure in center region with values close to an expected failure load, it was deemed

acceptable to continue with further testing with the original adhesive.  Tests of the

remaining virgin panels provided failure loads near those determined from scaling the

one-inch tensile test specimens' results, shown in Table 3.

Table 3.  Failure load values for virgin panels

| Specimen | Failure Load | Load for Audible Cracking | Load for Loud Cracking |
|---|---|---|---|
| 418B | 13306 | 2400 | 5000 |
| 422T | 18327 | 3400 | 8400 |
| 425B | 16342 | 2800 | 4300 |
| Average | 15992 | 2867 | 5900 |
| Standard Deviation | 2529 | 503 | 2193 |

The second virgin panel 425B failed simultaneously at two locations: 1) at the top

a partial failure in tab region and 2) in the gage section approximately two inches from

the bottom tab where the laminate split through the thickness along the 45° fiber line for

about three inches.  When examined under magnification, the failure in the gage section

87

at the bottom of the panel showed that some of the 0° oriented fibers failed as shown in

Figure 84.  The main failure of panel 425B occurred in the top tab region, as shown in
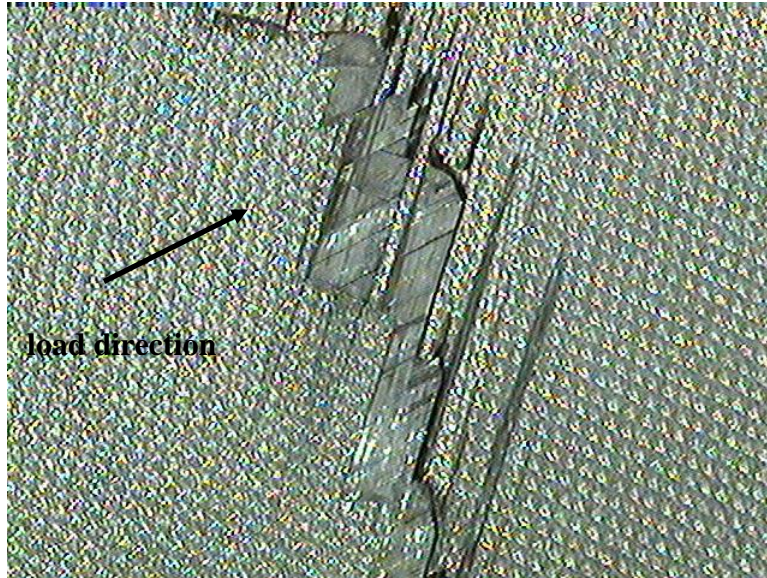
Figure 85.



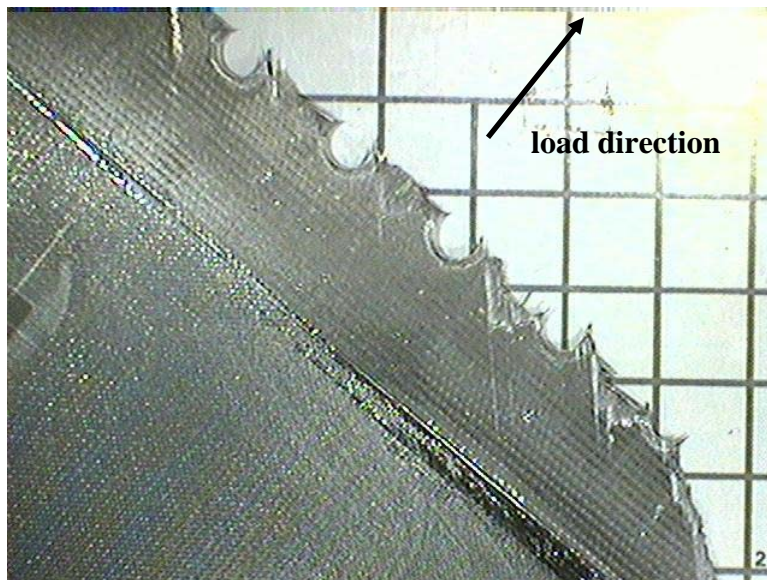**Figure 84.  Enlargement of 425B panel front after failure**



**Figure 85.  Enlargement of the area under 425B panel's tab after failure**

At the second bolt hole from the right edge of the specimen, the laminate failed along the 45° ply direction to the edge of the laminate. The remaining portion of the failure was along the line of bolt holes where the laminate had the smallest cross sectional area. Since the panel did not completely split in the gage section failure location, the measured failure load was not the ultimate load the panel could carry in an ideal testing situation. Alignment of the panel was verified by comparing the strain gages located near the tab at the top of the panel, Figure 19. Strain gages M and N were located on the front on opposite sides of the panel and comparing their data determines side-to-side eccentricity in the specimen loading. Comparison of the measured the N and R, located on the back side of the panel directly behind N, strain gages, determines the front-to-back eccentricity of the specimen loading. Data from all three strain gages correlated very well with each other, shown in Figure 86, indicating that the specimen was uniformly loaded.

For data presentation of the virgin panels, the average far field stress was calculated by dividing the load by the average cross sectional area. The average far field stress was assumed to be the same at all strain gage locations. Additionally, the data from M, N, and R correlated well with the O gage on the front center of the panel and S gage on the back center that were oriented in the 0° loading direction. All of the virgin panels showed this same correlation, refer to Appendix C. A comparison of all of the front-to-back strain gage data on all of the virgin panels, yielded a good match, refer to Appendix C.
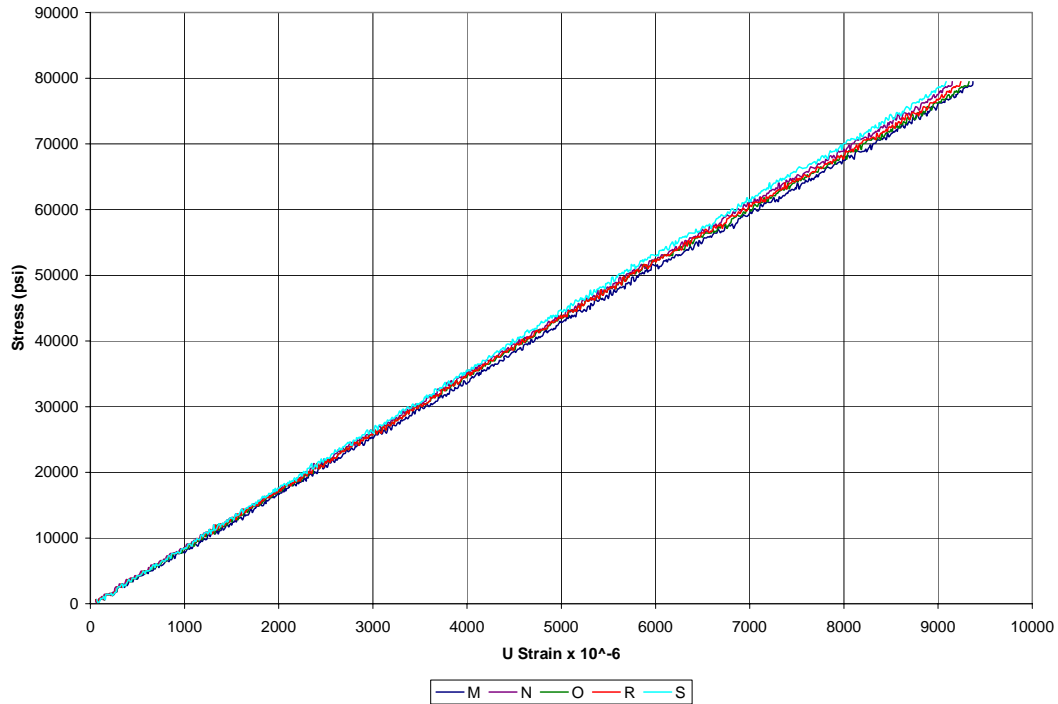
**Figure 86.  Panel 422T average far-field stress versus micro strain from 0° oriented strain gages**

## Scarfed Panel Results

At the beginning of testing of the scarfed panels, a limitation of the data

acquisition equipment was discovered.  Two types of strain gages were bonded to the

specimens, 350 Ω and 120 Ω resistance.  The data acquisition equipment did not allow an

adjustment in the Wheatstone bridge.  During the virgin panel testing, all of the strain

gages were 350 Ω resistance.  The scarfed panels had some 120 Ω resistance strain gages

installed, which were subsequently removed and replaced with 350 Ω resistance strain

gages.

All three of the scarfed panels, 419T, 423T, and 420B, broke through the center of

the scarf at load values shown in Table 4.  The center of the scarf had a smaller cross

sectional area than the rest of the panel, including the area under the tabs where the bolt

hole line was located.  The 45° plies delaminated away from the 0° plies, leaving ragged

appearance to the laminate at the fracture location, pictured in Figure 87 and Figure 88.

**Table 4.  Failure load values for scarfed panels in lbf**

| Specimen | Failure Load | Load for Audible Cracking | Load for Loud Cracking |
|---|---|---|---|
| 419T | 6661 | 3700 | 4500 |
| 420B | 7416 | 4000 | 4300 |
| 423T | 6976 | | 3800 |
| Average | 7018 | 3850 | 4200 |
| Standard Deviation | 379 | 212 | 211 |
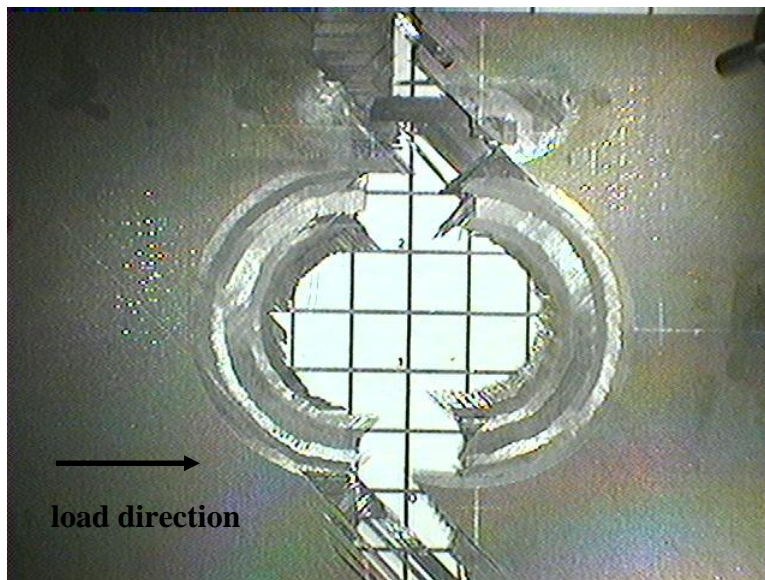


**Figure 87.  The front of panel 419T after failure**

Alignment of the panels was verified similar to the virgin panels.  Strain gages M

and N were located on the front on opposite sides of the panel with R located on the back

side of the panel directly behind N, identical to the virgin panels, Figure 19.  Data from

all three strain gages correlated very well with each other indicating no eccentricity in the

load introduction to the specimen, shown in Figure 89.

**Figure 88. The back of panel 420T after failure**



**Figure 89. Panel 423T load versus micro strain from select 0° oriented strain gages**

A comparison of the same strain gage location on all three of the scarfed panels,

yielded a good match for all of the strain gage channels except for Q and U (Figure 90),

for a complete list of all channels refer to Appendix C. The variation in strain gage

channel Q and U could have been from the slight variations in hole and scarf diameters,

listed in Table 5. A range of outside diameters are listed and refer to the x-direction

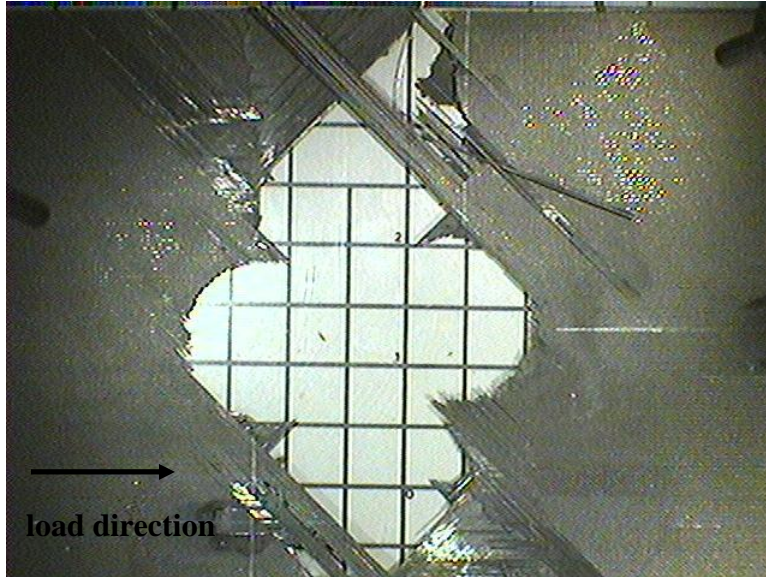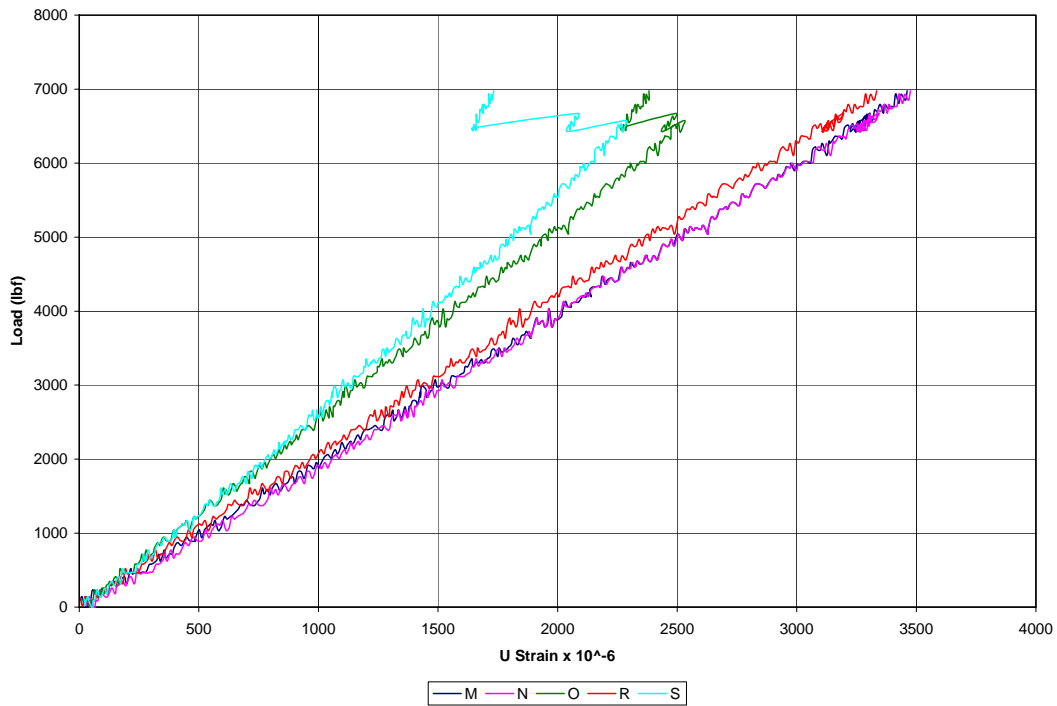measurement and the y-direction measurement since the scarfs were not perfect circles.

Panel 419T had a smaller cross sectional area due to the slightly larger scarf, which

accounts for the smaller failure load and for the greater strains experienced by the 90°

oriented strain gages on the sides of the scarfed hole.

**Table 5. Measured scarf and hole diameters in inches for scarfed panels**

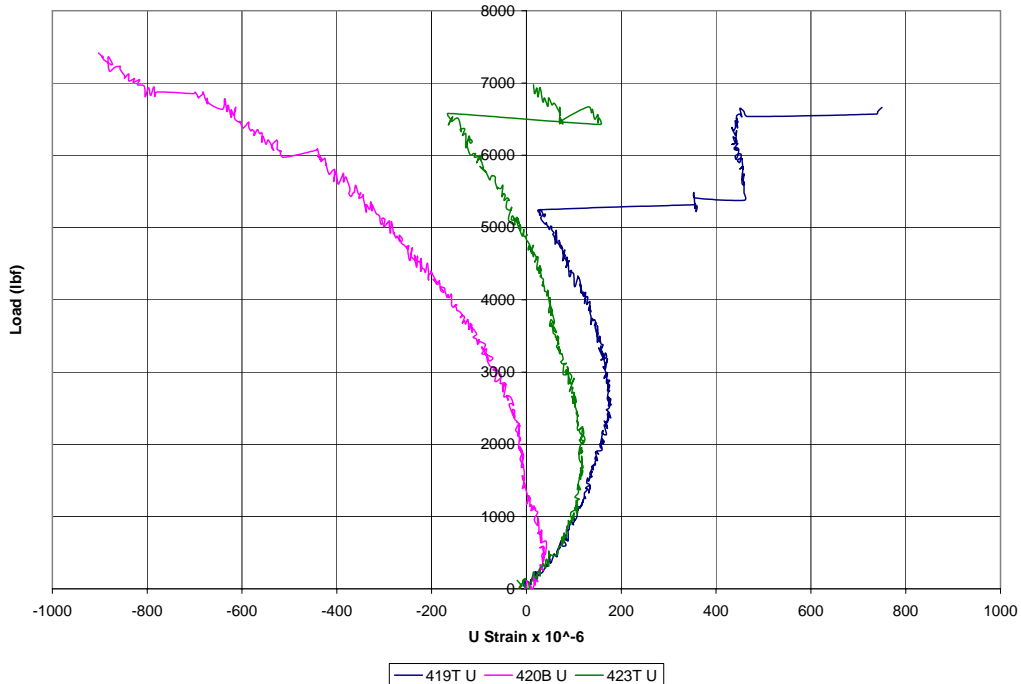| Panel | Outside Diameter | Hole Diameter |
|-------|------------------|---------------|
| 419T | 2.74 to 2.83 | 1.10 to 1.12 |
| 420B | 2.68 to 2.75 | 1.06 to 1.08 |
| 423T | 2.60 to 2.69 | 0.98 to 1.00 |



**Figure 90. Comparison of all scarfed panels stress versus micro strain on channel U**

93

**Repaired Panel Results**

For the four-repaired panel testing, the original bolts for the grips were replaced with new bolts since the bolts had evidence of yielding, noted when the tightening of the bolts became difficult. The yielding was due to continued over stress from testing and was anticipated. Additionally the new bolts were torqued to 175 inch pounds for added gripping and to avoid slippage in the grips leading to failure in the tab locations.

Panel 423B was tested first and failed in the tab region. During autoclave curing of the scarf patch onto the panels, the panels were subjected to 350° F. The adhesive used for bonding the tabs, is only rated for temperatures up to approximately 200° F and was considered usable only for room temperature applications. Inspection of the tab adhesive prior to testing the repaired panels showed a color and texture change from their pre-repair condition, from clear firmness to white chalky. The anticipated load capability of a scarf patch was approximately 80% of the original strength (Soutis and Hu, 1998) or approximately 14,500 lbf using the best ultimate load values from the virgin panels. Panel 423B failed at 14,966 lbf in the tab region with major damage to the upper portion of the panel in the gage section and some delamination had occurred in the scarf repair patch and parent panel. Since the failure was not through the scarf repair as expected, this area being considered the weakest portion of the laminate other than the bolt hole line under the tabs, it was decided to retab all remaining panels. Even though the failure load was close to the anticipated failure load, the failure was not in the gage section of the specimen. Additionally the tabs completely debonded from the panel when the gripping fixture was removed.

As noted earlier, removing and reapplying the tabs provided some difficulty. To remove the tabs from the untested repaired panels, each tab was immersed in liquid nitrogen. The coefficient of thermal expansion difference between the laminate and the adhesive caused the already weakened adhesive to fail, allowing the tabs to be removed with a putty knife or in some cases they just fell off. The remains of any old adhesive on the panels and tabs were removed through mild surface abrasion. A new room temperature cure adhesive, Hysol EA9394 two part resin/hardener epoxy system, was used to bond the tabs to the panels, using pins to realign the grip bolt holes in the tabs with the holes in the laminates. The adhesive needed to be cured at room temperature for a week to assure that it was thoroughly cured prior to testing. Each hole was redrilled to remove runoff adhesive in an attempt to not interfere with the gripping fixture. When fitting these retabbed panels into the gripping fixture, extra force had to be exerted to insert the bolts, requiring in some circumstances the use of a soft headed hammer.

The second repaired panel tested, 418T, failed through the center of the panel and scarf repair. During setup of the panel, strain gages O and U had spikes in the signal, which appeared to be loss of signal associated with a short in the lead wires. During analysis of the strain data, the signal spikes were removed because the values were the default value for the data collection software for an open strain gage bridge. Signal loss sometimes occurred for just a moment, but normally when the signal was lost no data was collectable afterwards from that gage. The patch was split in half with sections remaining attached to both halves of the panel, as shown in Figure 91 and Figure 92. The green material on the laminate is the adhesive used to bond the patch to the laminate. Both tabs and tab regions remained intact (see Figure 93). Adjacent to the tabs, some ply

95

failure and delamination occurred, but the tab adhesive showed no signs of failure (Table 6).
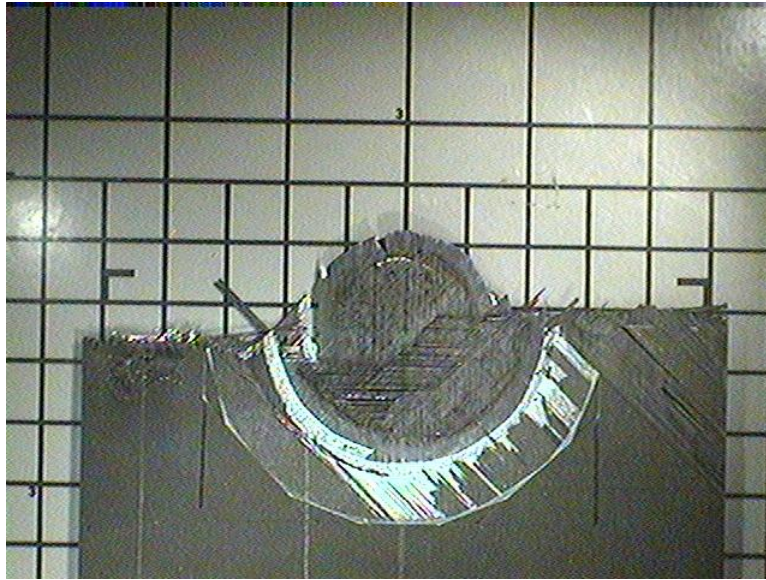


**Figure 91.  Front view of the bottom half of panel 418T after failure**



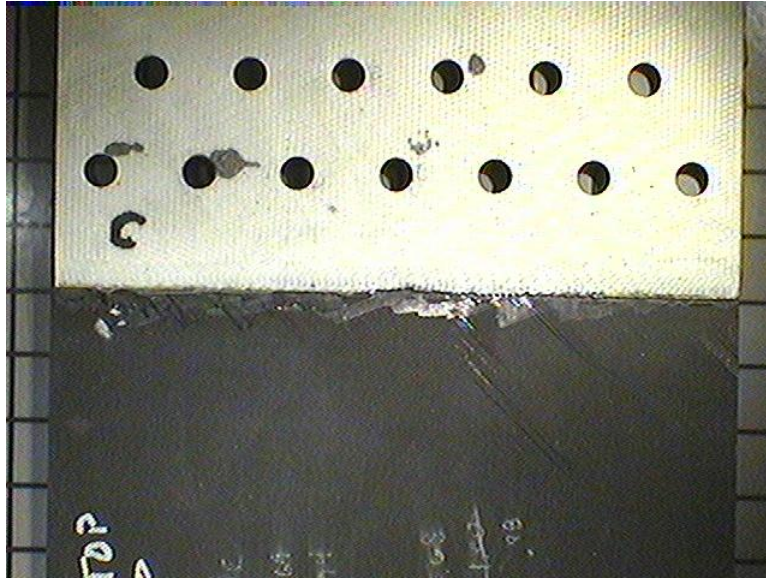**Figure 92.  Back view of the top half of panel 418T after failure**

**Figure 93. Front view of the bottom tab area of 418T after failure**

The two remaining panels failed in the same manner as the second panel 418T.

The failure loads are listed in Table 6.

**Table 6. Failure load values in lbf for repaired panels**

| Specimen | Failure Load | Load for Audible Cracking | Load for Loud Cracking |
|---|---|---|---|
| 418T | 15214 | 5600 | 12900 |
| 419B | 15207 | 8200 | 10000 |
| 422B | 14619 | 6000 | 10000 |
| 423B | 14966 | 5300 | 10000 |
| Average | 14883 | 6275 | 10725 |
| Standard Deviation | 295 | 1315 | 1450 |

During test setup of panel 422B, strain gage Q was pulled off of the panel and therefore

no data was collected for this channel during testing. The data was modified to a show a

zero value for data completeness. Panel 422B also had a slight variation in patch

configuration from the other panels; the patch ply layup was in reverse order. During

patch application, the panel was discovered to have been scarfed on the opposite side of the panel as compared the other panels. The patch was made with a reverse ply order to maintain the orientation match of the patch's plies with the parent panel's plies. The data appears to show no major deviation due to this change.

A comparison of the same strain gage location between all of the scarfed panels, yielded a good match for most of the strain gage channels (Figure 94), for a complete list of all channels refer to Appendix C.
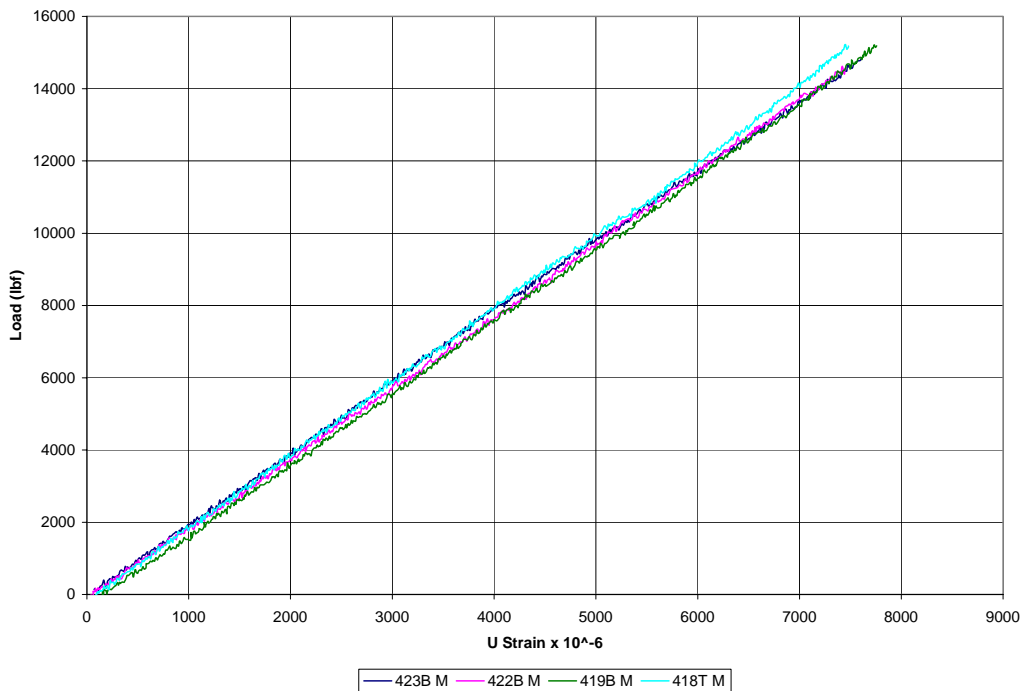


**Figure 94. Comparison of all repaired panels stress versus micro strain on channel M**

There was some variation notable in some channels, but all of the same channel strain gages followed the same trends. Some channels were lost near the end of the test, when either the strain gage completely debonded or when the gage partially debonded, which was expected. When the signal was completely lost, the data was zeroed, while a

partially debonded strain gage's data was plotted.  Some of the minor variation between

specimen results may be from the differences in hole diameter and outside scarf diameter,

listed in Table 7.  Panel 422B does not separate the horizontal and vertical strain

component measurements, since when the measurements were taken this panel's hole

diameters were deemed too large to include in the testing.  When two other panels, which

are not included in this thesis, were permanently damaged during autoclave curing of the

repair, panel 422B had to be repaired to maintain a minimum of three panels for each

type of tensile testing.  Complete measurements were not retaken.  The results from the

panel appear to be valid in spite of the enlarged scarf.

**Table 7.  Measured scarf and hole diameters in inches for repaired panels**

| Panel | Outside Diameter | Inside Diameter |
|-------|------------------|-----------------|
| 419T | 2.74 to 2.83 | 1.10 to 1.12 |
| 420B | 2.68 to 2.75 | 1.06 to 1.08 |
| 423T | 2.6 to 2.69 | 0.98 to 1.0 |
| 418T | 2.69 to 2.79 | 0.94 to 0.96 |
| 419B | 2.67 to 2.78 | 0.85 to 0.87 |
| 422B | 2.8 | 1.1 |
| 423B | 2.62 to 2.74 | 1.00 to 1.05 |

**Discussion of Results**

A comparison of the average ultimate loads achieved by each type of panel to the

other panels' average ultimate load yields the following:  the scarfed panels only retained

~44% of the virgin panels load bearing capability and the repaired panels carried ~93%

of the load of the virgin panels.  A higher value for the virgin panel's ultimate load was

used for three reasons:  1) the expected ultimate load value for the virgin large tensile

testing panels was 18,000 lbf from scaling the one inch tensile test results, 2) all of the

virgin panels failed in the tab regions, and 3) the standard deviation for the virgin panels

was much larger than the other two types of panels tested.  Using this higher ultimate

load value in the same comparisons yields:  the scarfed panels only retained ~38% of the

virgin panels load bearing capability and the repaired panels carried ~81% of the load of

the virgin panels.  This 81% value is much closer to the anticipated value of 80% noted in

results earlier.

Some of the strain gages on each of the three types of panels were placed in the

same location on each of the panels.  These strain gage channels are compared in this

section, thus verifying the data collected and consistency between all of the experiments.

To limit the amount of data on one graph, only one representative panel from each type

was selected to be shown.  Strain gage channels M, N, and R on the virgin and scarfed

panels were used to validate that the panels were aligned correctly and that no

eccentricity occurred during testing (Figure 95).  Additionally, this comparison shows

that all of the panels followed the same load versus strain curve.  On the virgin and

scarfed panels, strain gage channel O measured the strain in the 0° orientation at the

center of the panel on a section of the panel above the scarf, for the scarfed panel, Figure

19.  These channels were compared to strain gage channel M, located similarly in the

repaired panels with good correlation (Figure 96).  Oriented in the 90° directions, strain

gage channels Q in the virgin panel were located in the center of the panel, and channel Q

in the scarfed panel and S in the repaired panel were located to the side of the scarf.

Comparison of the two data sets, Figure 97, shows that the repaired panel has had much
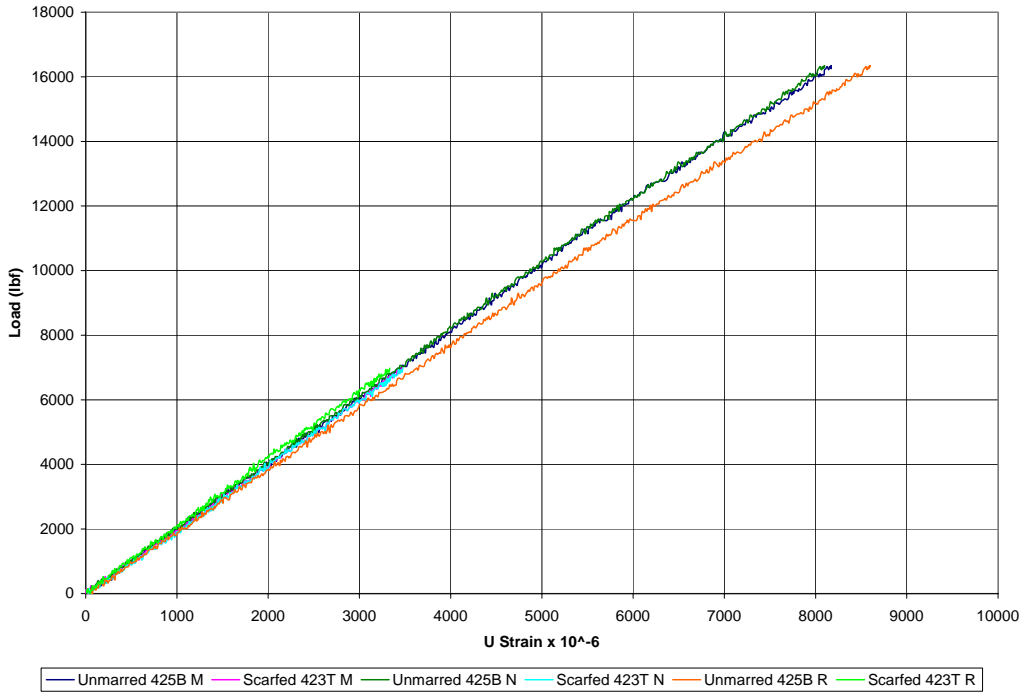
of the original stiffness restored with the patch.

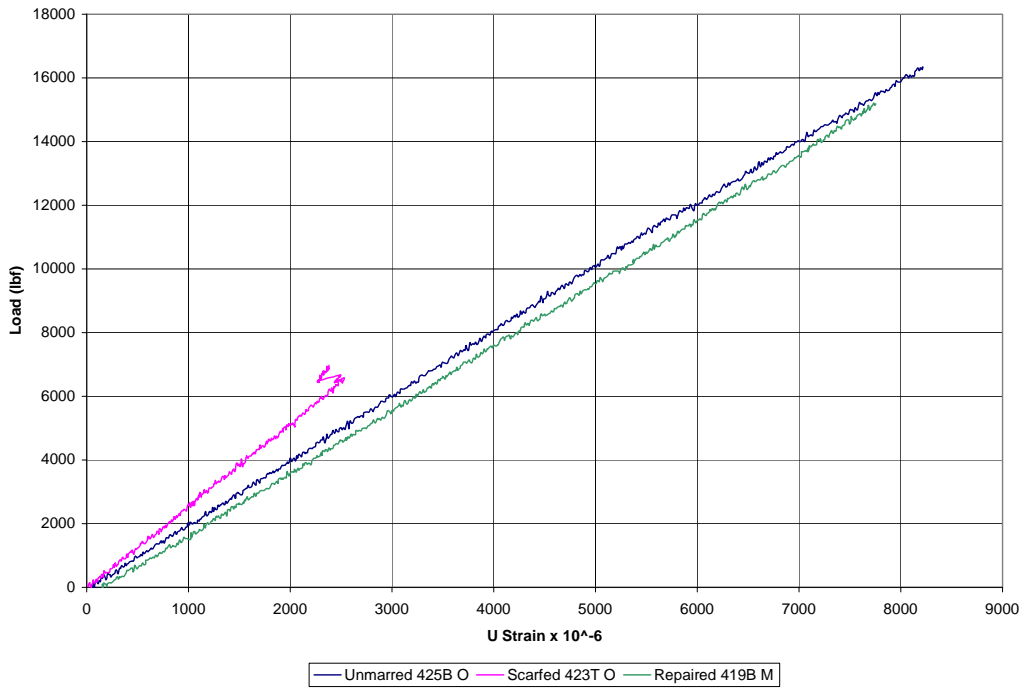**Figure 95. Strain gages M, N, and R for typical virgin and typical scarfed panel**



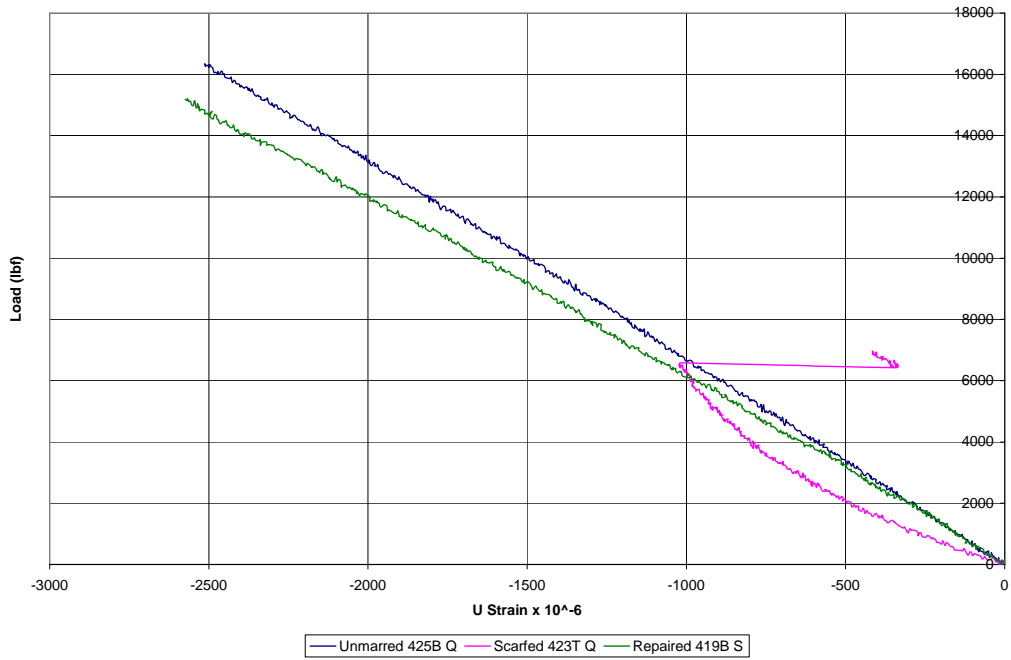**Figure 96. Strain gage O for typical virgin and scarfed panel, and M for typical repaired panel**

101

**Figure 97. Strain gage Q for typical virgin and scarfed panel, and S for typical repaired panel**

# VI. Conclusions and Recommendations

## Conclusions from Results

The results from both loaded straight scarf joint coupon and the residual strain scarf joint coupon show fair correlation with the applicable B-Spline Analysis Method's (BSAM) model results and take a step toward validating BSAM's capability to model scarf joints for both mechanical loading and residual strains. Even though the z-direction Moiré data was fairly noisy due in part to a bad diffraction grating, the results from the Moiré interferometry testing and the BSAM extracted data are within the same order of magnitude and clearly areas of strain concentrations were similar in both results. The x-directional strains and the shear strains also showed fairly good trend matching. The residual strain data showed correlation at times on the edge, which was unexpected, and correlation in the far field regions.

The large scarf repaired tensile loaded specimen's strain gage data verified that the testing was valid. The specimens failed in the center of the patch where the strain concentrations were shown in the straight scarf joint Moiré results. The repaired panels carried over 80% of the virgin panel load.

Though the steps in manufacturing all of the specimens were relatively straight forward, maintaining a high level of repeatability and precision in the specimens was much more difficult. Many necessary jigs had to be designed and manufactured, which increased the time needed to make the specimens. The learning curve, especially in scarfing, was very steep and significant numbers of practice panels were used.

**Key Lessons Learned**

There are three key lessons learned: care must be taken with the diffraction grating, a higher loading should be used during Moiré interferometry testing, and the scarf needs to be as uniform as possible. The large amount of noise seen in the Moiré data is mostly from the low quality of the diffraction grating. A better grating would yield better results. If a higher load had been possible, the signal to noise ratio would have been lower allowing much better Moiré interferometry testing results. Future work should try to make the loading force as high as possible. One possible method to do this is through manufacturing of a better quality straight scarf specimen. More accurate results from the BSAM model could have been achieved if the specimen was closer to the ideal that the data was modeling. A more uniform scarf joint would have gone a long way towards this end.

**Recommendations for Further Research**

The following is a list of recommended research work to further the goals of refining the BSAM model, continued validation of the model, and further understanding of the composite joint properties.

- Continue in the refinement of BSAM. A more robust method of curve matching data taken from specimens would yield more accurate results. Also a better method for extracting data from the model should be devised to limit man hours spent in data extraction. If the program were more user friendly, then possibly the code would come into further use, which would make more accurate composite material modeling available to the research community. These suggestions have

104

been shared with the BSAM programmers and will hopefully be implemented in the near future.

- Using a better diffraction grating than was used for this thesis, redo the Moiré interferometry experiment done in this thesis. This will verify the results from this thesis and give a better understanding of the variances that did exist between the model and experimental results.

- A complete data analysis of the large tensile test panel data should be done and compared to a BSAM model of the large tensile test specimens in all three configurations. This would further verify BSAM's capability and advance the understanding of how scarf patches fail.

- Do variations on the Moiré interferometry experiment and BSAM modeling done in this thesis by: modifying the scarf angle, change the ply orientations of the laminate layup, double up the plies with the current layup, use a different adhesive, or changing the laminate material used. Each variation would further validate the BSAM model and increasing understanding of the scarf joint. Some questions that should be addressed in the long term include: what is the optimal layup for the repair patch, how do ply orientations effect the scarf repair, and how does varying the materials used for the repair effect the overall joint properties?

- Often the ideal laboratory repair case, which was attempted in this thesis, is very different than the actual field level case used. A follow on thesis should make the experimental specimens more in line with the actual repairs done in field conditions, by lowering the cure temperatures, lowering cure pressures, and looking into curved surfaces. A further study of the repairs done in the field

105

would give the technicians applying the scarf patches a better understanding of

the expected results and what control parameters are important.

## Appendix A:  One-Inch Tensile Testing Specimens

**Methodology**

One of the 12-inch by 24-inch IM6/3501-6 panels with $[45/0/-45/90]_s$ layup previously discussed, was used to manufacture eighteen tensile testing specimens; ten inch long by one-inch wide, following ASTM D-3039M.  All specimen dimensions, except for thickness, were followed precisely from ASTM D-3039M.  The thickness was smaller than specified in the standard due to the necessity of matching the laminate layup used for the scarf coupons and scarf panels.  Each specimen was labeled for identification that allowed the location where the specimen was cut from on the panel to be distinguishable.  The identification included either R for right or L for left distinguishing which side of the panel the specimen was cut from and a number designating the specimen cutting order from the edge that section of panel.  The initial cut for the width and the final cut for the length was done on a diamond bladed radial arm saw.  Care was taken to align the cutting direction with the orientation of the 0° and 90° plies with the 0° ply running the length of the specimen.  The width was controlled to within a thousandth of an inch using a tensile cutting machine.  The tensile cuttig machine is similar in idea to a router table, but with a precision width adjustment and diamond grinder bit, pictured in Figure 98.  The width setting for the tensile cutting machine was based on the narrowest specimen, passing each specimen through before adjusting the machine to a narrower setting.  The final width was one inch.
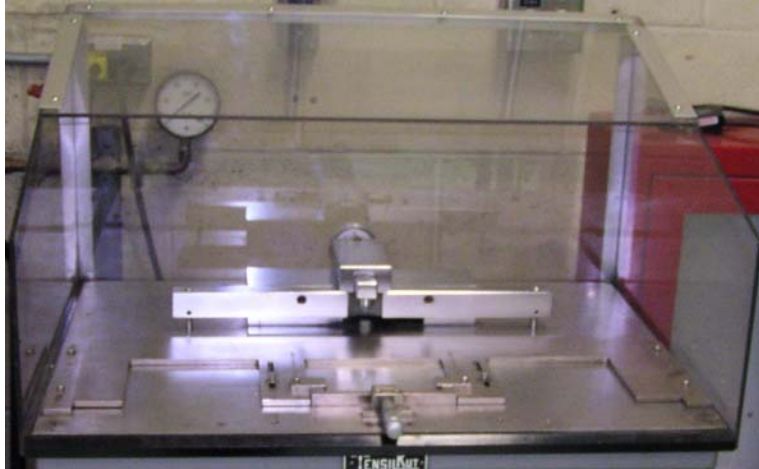
**Figure 98.  Tensile cutting machine**

The test was also performed in accordance with ASTM D-3039M.  Two inches on each end of the specimen were inserted into the grips, with emery cloth covering both ends of each specimen, per the standard's recommendation.  This left a gage length of six inches.  Hydraulic grips pressurized to approximately 360-380 psi were used to grip the specimens.  The technician recommended a minimum grip pressure of 36 percent of maximum anticipated tensile load over the entire surface area of the tensile specimen.  A preliminary test was run on one specimen, L-9, to verify the gripping ability of the emery cloth and to obtain an anticipated maximum tensile load.  This preliminary test was done on a different tensile testing machine than the machine used for the testing and had manually tightened grips.  No strain data was taken during this test, and the test was done at a displacement rate of 0.1 inch per minute, twice the recommended speed for testing.  This test specimen explosively failed at 4256 lbf after slipping once in the grips, and the grips then being retightened.  All subsequent testing was done with shielding around the specimen to contain the specimen pieces or taking care by keeping everyone sufficiently away from the specimen.  A one-inch extensometer was attached on some of the

specimens, which provided some strain information that was used in the analysis. The set

up of the gage and tensile machine is shown in Figure 99. All of the specimens were

dried out prior to testing by placing in a vacuum oven at 100° C for a weekend to avoid

effects from water absorption in the laminate. For the first three tests (L-4, L-8, and L-1),

the same emery cloth was used repeatedly until the fourth specimen L-2 slipped.

Therefore all subsequent tests were done with new emery cloth and at a higher grip

pressure; increased by approximately 100 psi. The test was done under displacement

control at a head displacement speed of 0.05 inches per minute.



**Figure 99. Elevation view of the test setup for tensile testing with extensometer**

## Results and Analysis

Final failure load and displacement for all testing is shown in Table 8, except for

specimen L-2 that has been discarded, since the grips slipped during testing. Load versus

displacement for all tests is shown in Figure 100 through Figure 104. It should be noted

that in Figure 100 one specimen appears to dip dramatically.  This was specimen L-2 and the dipping was caused by the grips slipping.  Graphically, all of the specimens followed roughly the same slope, with only one significant variation of L-2 due to the grips failing to hold the specimen during testing.  The ultimate load had a variance of 20% from the highest to the lowest values and a standard deviation of 287 lbf.  Some variation could be from slight differences in thicknesses, of about 1 mil from specimen to specimen.

**Table 8.  Final failure loads and displacements**

| Specimen | Ultimate Load (lbf) | Maximum Displacement (in) |
|---|---|---|
| L-1 | 4653 | 0.1193 |
| L-3 | 4744 | 0.112 |
| L-4 | 4882 | 0.121 |
| L-5 | 4581 | 0.107 |
| L-6 | 5044 | 0.1191 |
| L-7 | 4872 | 0.1257 |
| L-8 | 4924 | 0.1145 |
| R-1 | 4470 | 0.1172 |
| R-2 | 4365 | 0.1105 |
| R-3 | 4510 | 0.1181 |
| R-4 | 4479 | 0.1164 |
| R-5 | 4153 | 0.107 |
| R-6 | 4124 | 0.1097 |
| R-7 | 4335 | 0.1156 |
| R-8 | 4182 | 0.1096 |
| R-9 | 4398 | 0.117 |
| Average | 4544.75 | 0.114981 |
| Standard Deviation | 287.25 | 0.0052997 |
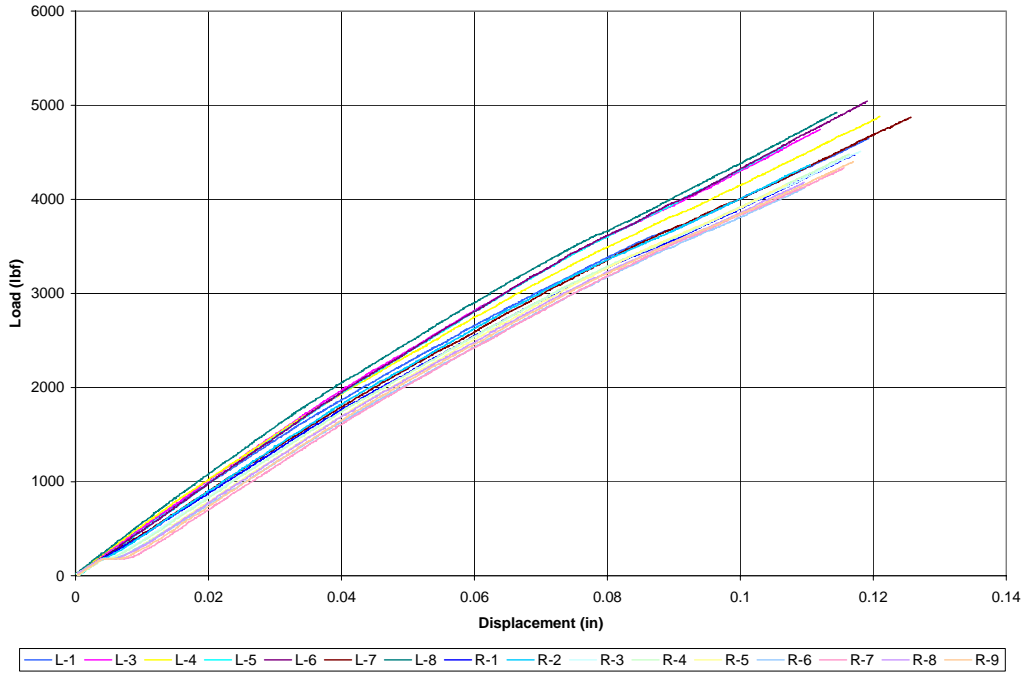
**Figure 100. All specimens load versus displacement data**
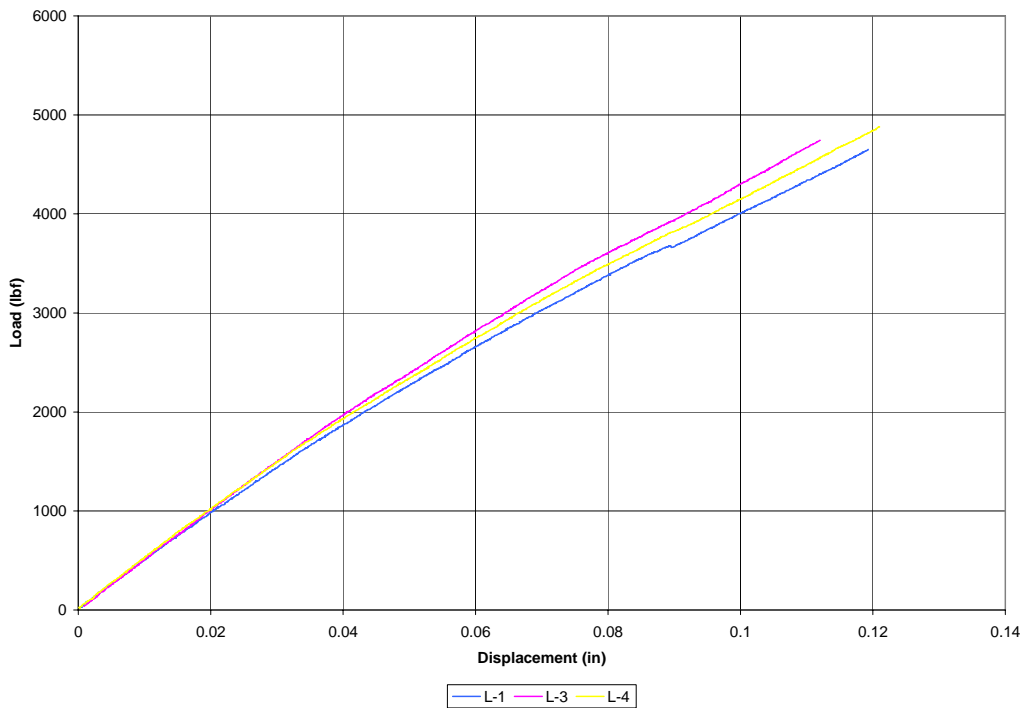


**Figure 101. Specimens L-1 thru L-4 load versus displacement data**

111
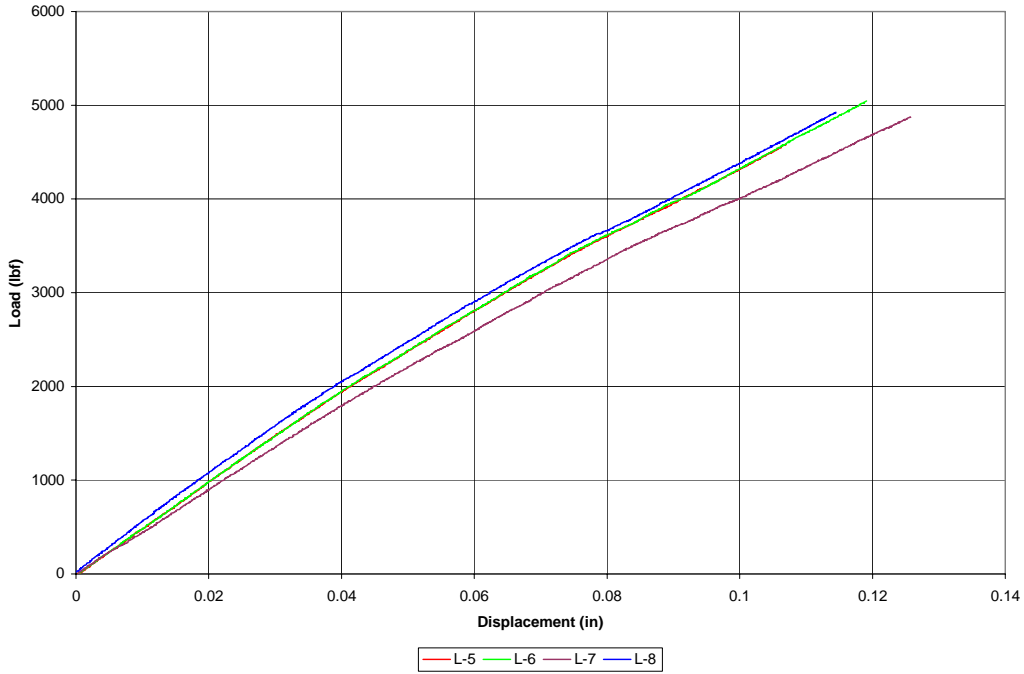
**Figure 102.  Specimens L-5 thru L-8 load versus displacement data**
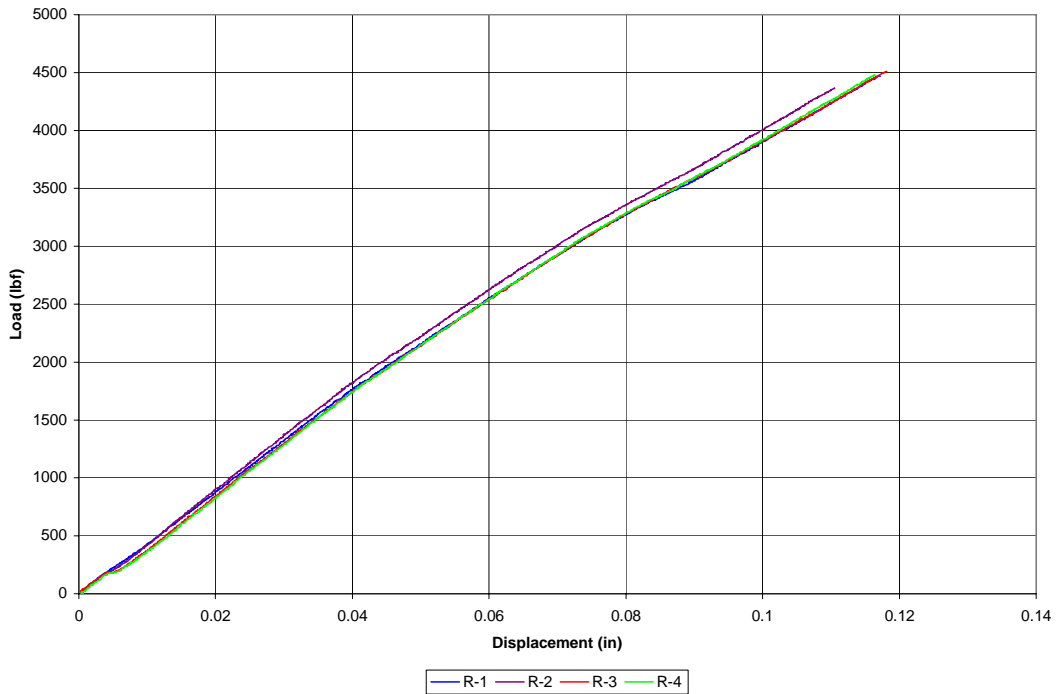


**Figure 103.  Specimens R-1 thru R-4 load versus displacement data**
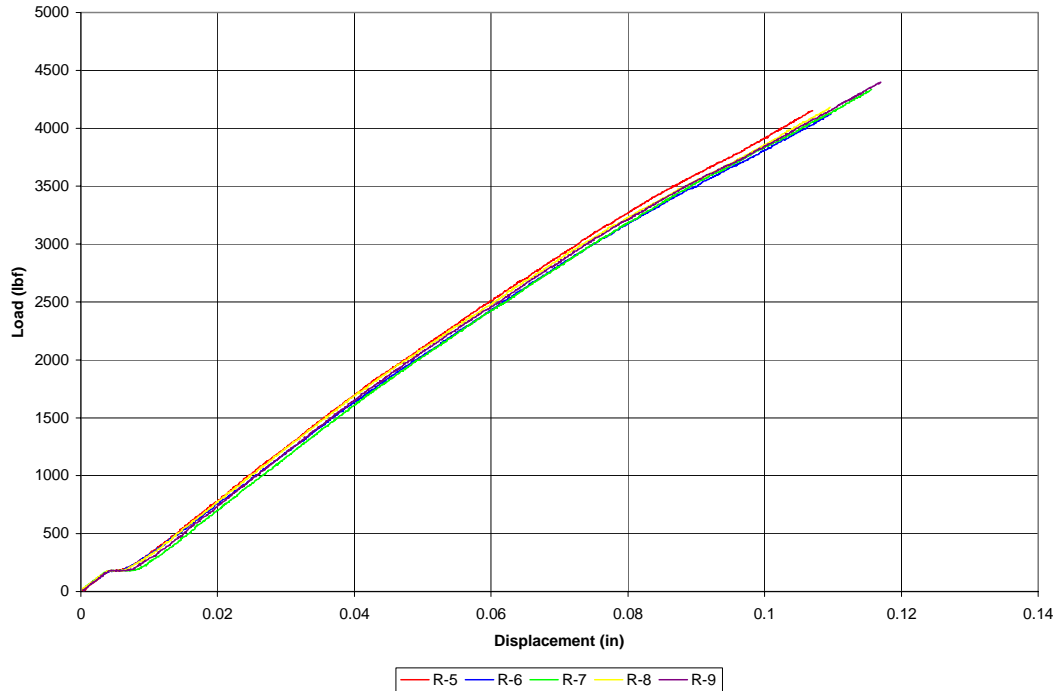
**Figure 104. Specimens R-5 thru R-9 load versus displacement data**

Assuming that the thickness and width for all of the specimens are the same, an average cross sectional area was used in calculating the stress:

$$\sigma = \frac{F_{load}}{A_{cross\_section}} \tag{4}$$

Additionally, the engineering strain was calculated from the head displacement using the following formula:

$$\varepsilon = \frac{\Delta L}{L_{gage}} \tag{5}$$

This assumes that all of the crosshead displacement is a result of strain in the gage section of the specimen. A comparison of the extensometer data for the four specimens where strain data was collected was done with this engineering strain in Figure 105. The extensometers often slipped on the specimen late in the test, shown where the line plots

113

drops towards zero while the stress is still increasing. Figure 107 through Figure 110 show the calculated stress versus engineering strain for all of the specimens. The u strain listed on the x-axis is micro strain x10$^{-6}$.

**Discussion**

During the tensile testing, all of the specimens delaminated near the mid plane, as shown in Figure 111. The laminate sides delaminated outward from the center of the thickness; some pulled apart completely through the width. Another interesting note is the explosive nature of some the specimens at failure, with parts being thrown in all directions.
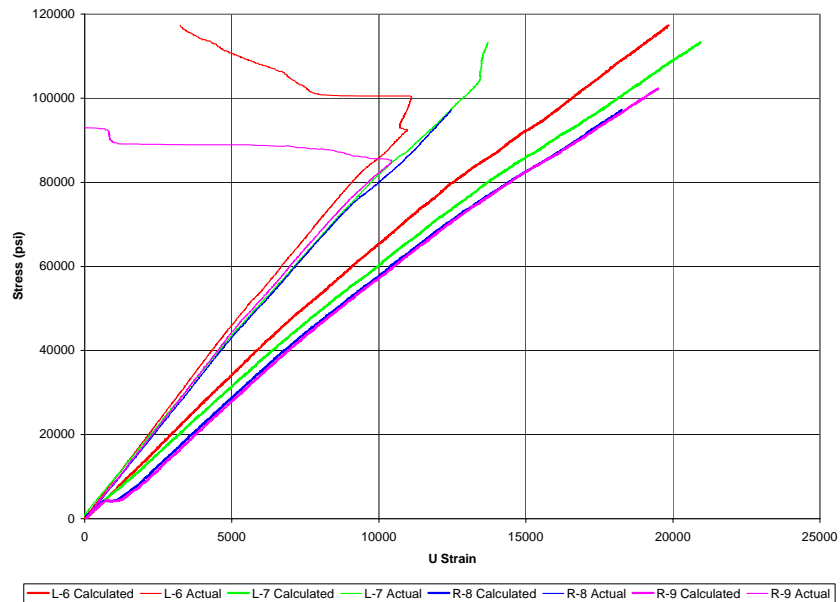


**Figure 105. Available extensometer data versus calculated strain data**
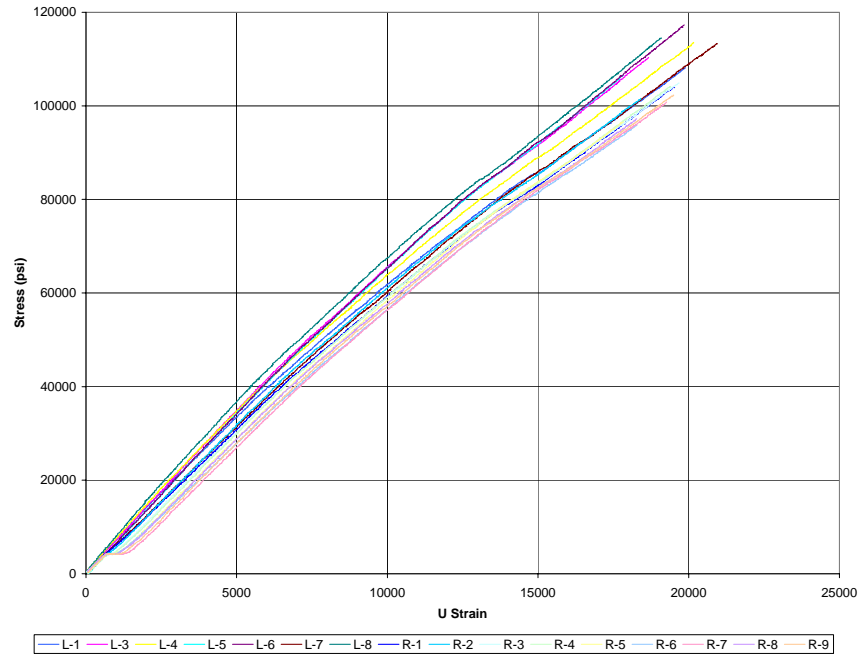
**Figure 106. All specimens stress versus u strain**
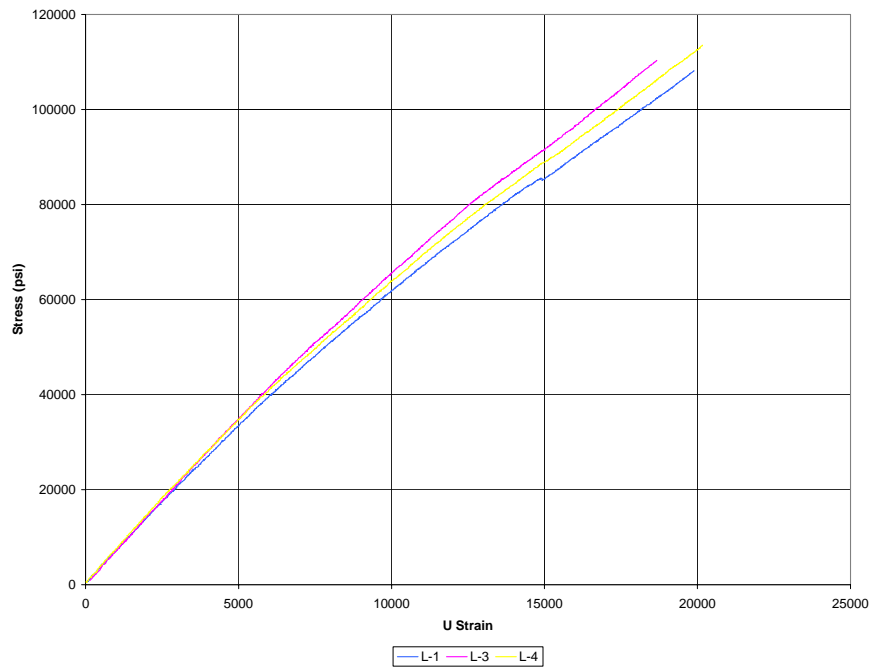


**Figure 107. Specimens L-1 thru L-4 stress versus u strain**

115
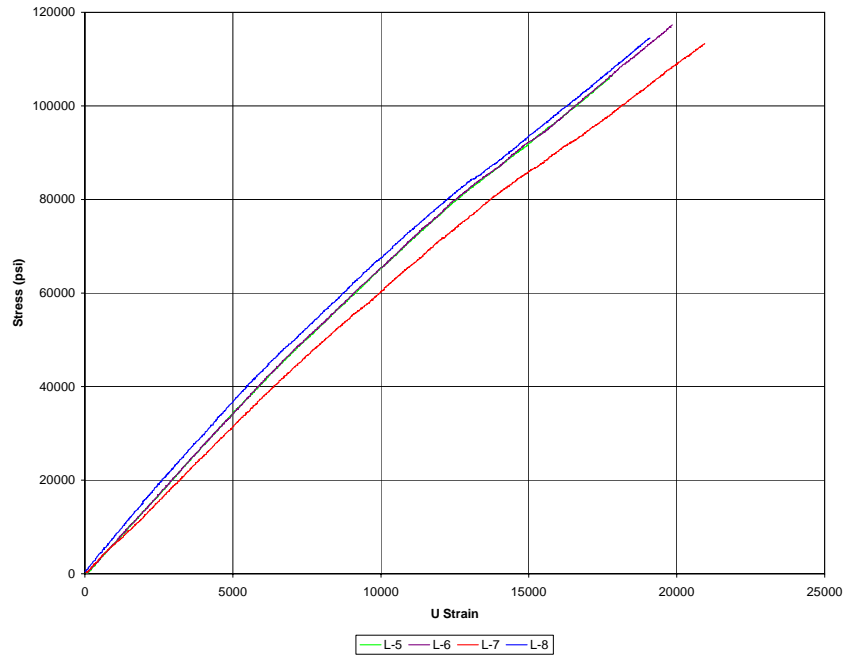
**Figure 108.  Specimens L-5 thru L-8 stress versus u strain**
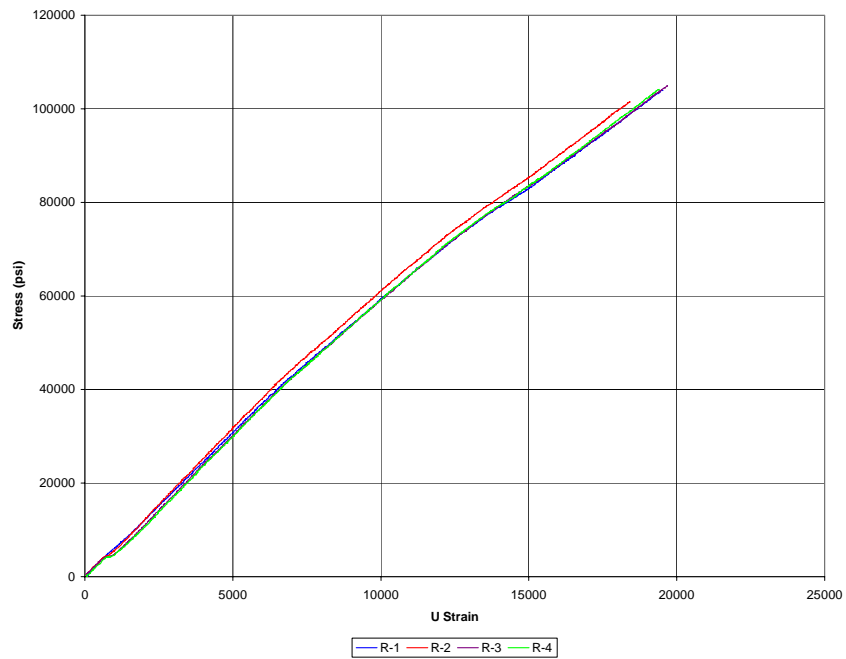


**Figure 109.  Specimens R-1 thru R-4 stress versus u strain**

116
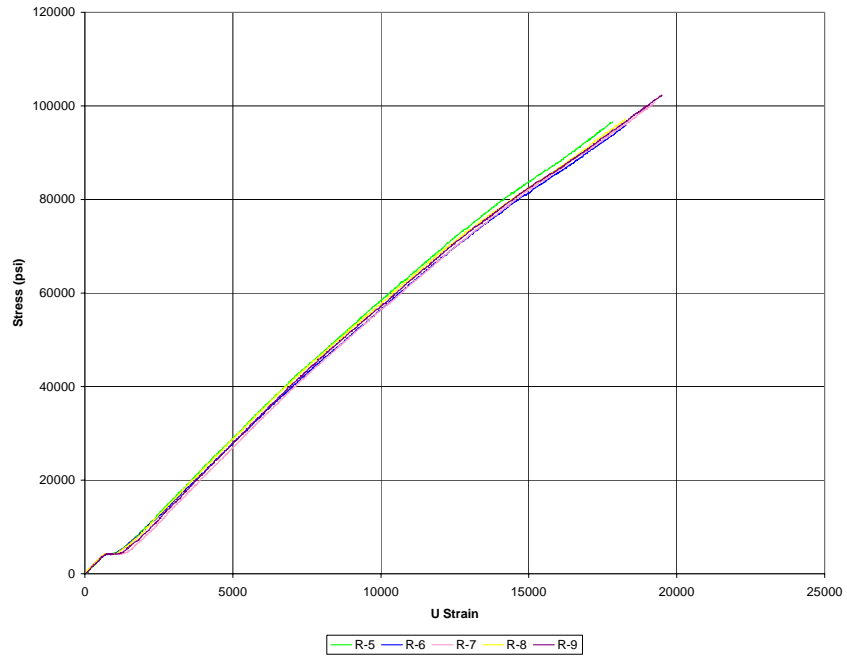
**Figure 110. Specimens R-5 thru R-9 stress versus u strain**



delamination
in width
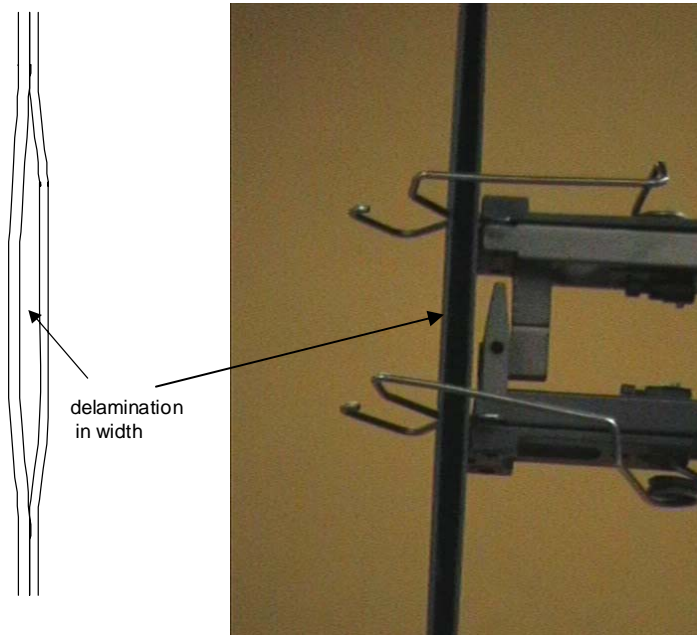
**Figure 111. Schematic and picture of tensile specimen delamination in the thickness**

**Appendix B: Material Values for FM 300M (0.05 psf) Adhesive**

In order to execute BSAM, material property values for all the models needed to be included. Since no manufacturing data was available on the material properties for FM 300M (0.05 psf), testing and data analysis to obtain the needed values was accomplished.

**Methodology**

A four-inch by four-inch neat adhesive plaque of FM 300M (0.05 psf), which contains a fiber mat carrier and is 0.05 inches thick, was made by stacking layers of adhesive film until the specimen was at least 0.1 inches thick. Since the carrier for the adhesive is a random fiber mat, no attention was paid as to whether each piece laid in the stack was oriented along the roll axis or not. Approximately 30 pieces each slightly greater than four inches by four inches were stacked together. Curing was done per the manufacturer's recommended cycle of: 90-minute ramp to 350° F and hold for one hour at 45 psi. A barrier was placed around the plaque during curing to keep the adhesive from flowing away from the mat. An ultrasound of the plaque showed that there were no major flaws or porosity internal to the plaque, but a slight warp was present. The plaque was then cut to four inches by four inches on the diamond bladed radial arm saw.

The plaque was cut into four specimens using a diamond bladed radial arm saw. Two of the specimens were four inches long by 0.751 inches wide by 0.234 inches thick and 0.753 inches wide by 0.226 inches thick. These specimens were used for tensile testing with strain gages to measure modulus of elasticity and Poisson's ratio for the

material.  Tensile testing was conducted in the x-direction on the two tensile testing specimens with a 0°-90° strain gage rosette attached to the center of the specimen.  One inch of each end was placed in hydraulic grips, leaving two inches for the gage length.

The remaining two specimens were cut to two inches by two inches and were used to measure the coefficient of thermal expansion.  Each specimen had a 0°-90° strain gage rosette, or two strain gages placed at 90° orientation to each other, bonded to the center of the specimens.  The specimens were placed into a temperature-controlled oven at room temperature, initially measured at 81° F.  The temperature was then varied from -10° to 190° F in the following manner:  changing the temperature at 4° F per minute for five minutes, holding temperature for 15 minutes to allow the specimens and chamber to reach equilibrium, and then repeating the previous steps until the whole temperature range had been covered.  The temperature was first increased to 190° F, then lowered to -10° F, and finally increased back to room temperature.  A compensating strain gage was used to eliminate the thermal effects from the strain gages used to measure the adhesive coefficient of thermal expansion.  A matching strain gage was mounted on a titanium silicate specimen placed in the chamber with the adhesive specimens.  Since titanium silicate has a coefficient of thermal expansion close to zero, the only strain measured by the gage was effectively the strain gage's expansion strain from the gage's coefficient of thermal expansion.  By subtracting the compensating gage's strain measurements from all of the strain adhesive specimens' measurements during testing, the coefficient of thermal expansion for the strain gages had no effect on the data.  Data was collected every minute during testing.

**Results and Analysis**

The tensile testing data was processed for presentation. The strain data collected from tensile testing was converted from voltage to inches per inches utilizing the gage factor, while the load data was converted to stress data by dividing the load in lbf by the cross sectional area in square inches. The results are shown in Figure 112. Since each specimen had two directions of strain gage data, all strains are plotted against stress. The two directions of strain gaging are also plotted against other in Figure 113. In both cases, the two specimen's results to be well matched.

The modulus of elasticity was determined by fitting a straight line to the stress versus strain data using the method of least squares, per ASTM E-111-97 direction. Since the material does not follow a linear stress-strain behavior, the tangent method was used in calculating the modulus. A very small amount of data at the very beginning of the curve, where the data was more likely to be linear, was used to generate the straight line. Within the first five seconds of data in one of the data sets, a large change, on the order of 50 times the average value in the neighboring data, in the strain was noted. For this reason, the first five seconds of data was eliminated from the calculation in all of the data sets. Only ten seconds of data, or 100 data points ranging from ~100 psi to ~250 psi, were used in the linear calculation. Figure 114 thru Figure 117 show the graphs of the full data sets, the data used for the linear fitting of the data, and the linear fits for both directions in both specimens. The linear fit was allowed to adjust the y intercept to better fit the data, not forcing the fitting line to cross the x-axis at zero, since the zeroing of the data could have been slightly off and strain gages tend to not be as precise at lower values. In all cases, the coefficient of determination or correlation ($R^2$) reveals very good

correlation between the data and the linear fit of the data.  The modulus of elasticity is the slope of the linear fit of the x-direction data and can be read directly from the figures. The slope of the y-direction data can be converted to the modulus of elasticity by dividing by the negative value by Poisson's ratio (ν).  Good correlation between all values was noted.

$$\nu = -\frac{y\_directional\_strain}{x\_directional\_strain} \tag{6}$$

$$x\_dir = -\frac{y\_dir}{\nu} \tag{7}$$
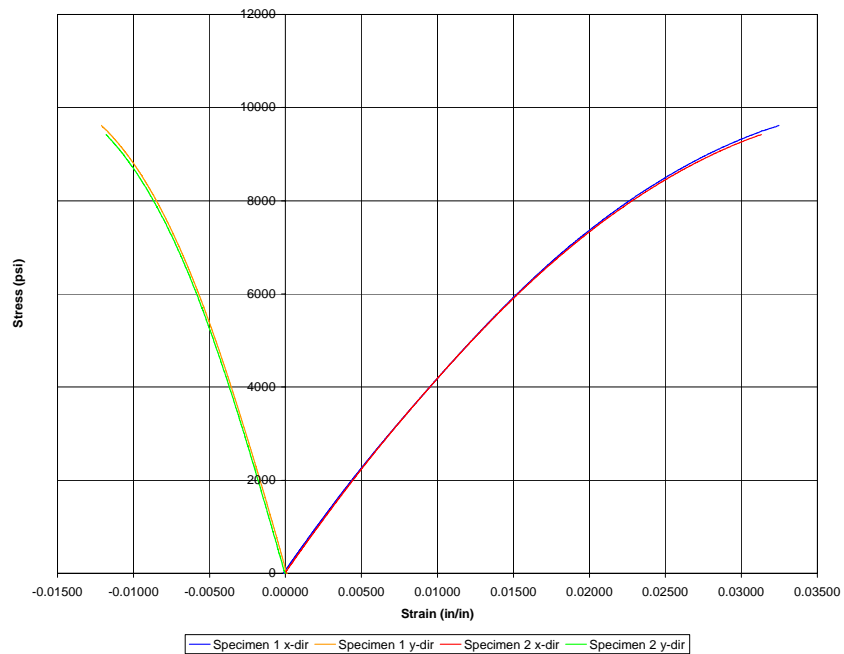


**Figure 112.  Stress versus strain for FM 300M (0.05 psf) specimens**
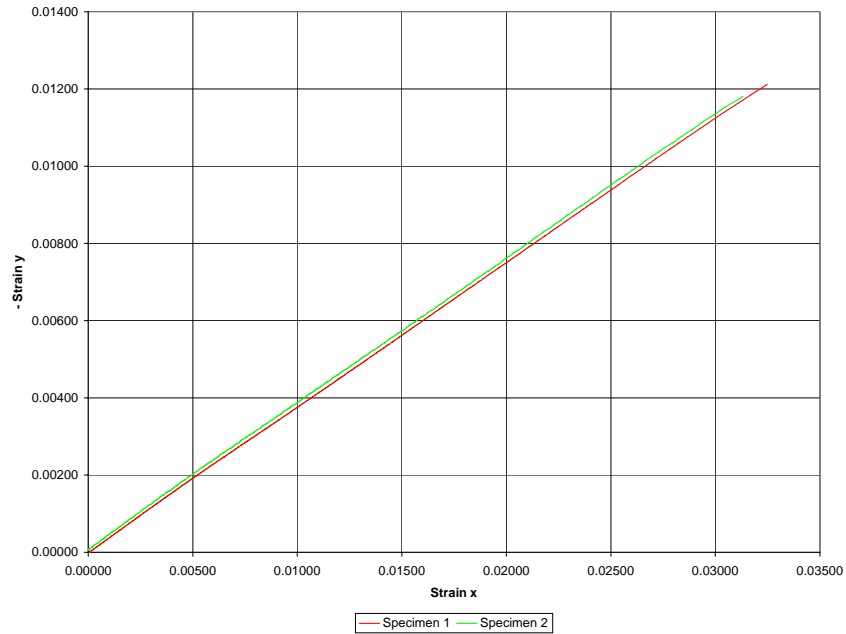
**Figure 113. X-directional strain versus negative y-directional strain in FM-300M specimens**
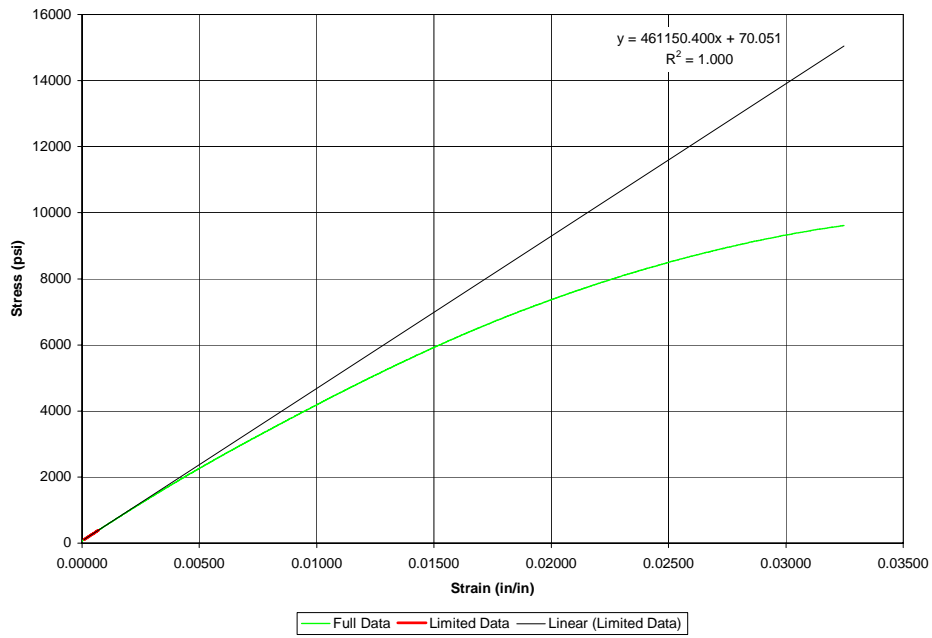


**Figure 114. Tensile test specimen 1 modulus of elasticity using x-directional strain**

**Specimen 1 Modulus from y-direction**

$y = 1179303.617x + 93.756$
$R^2 = 0.999$
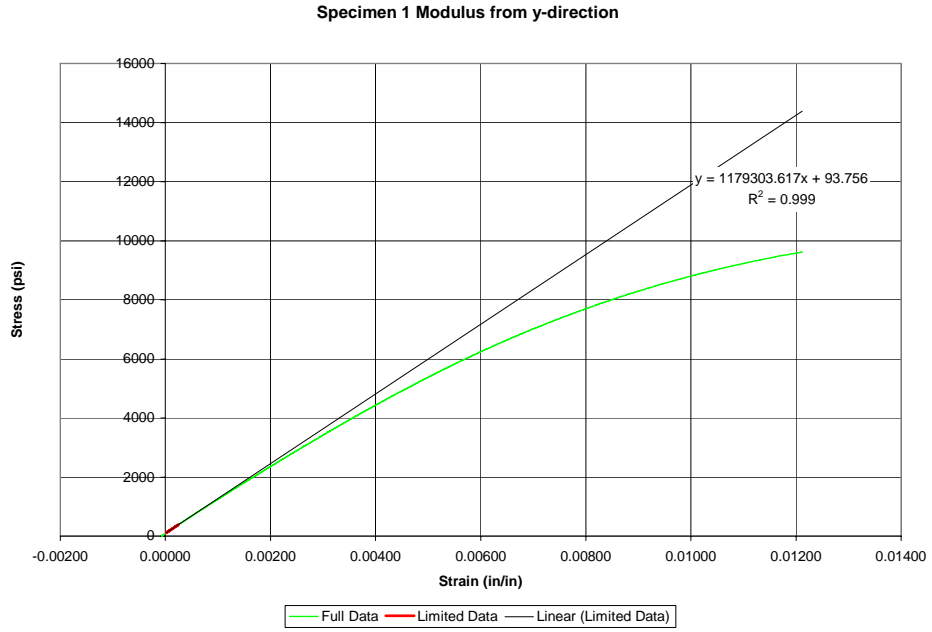
**Figure 115.  Tensile test specimen 1 modulus of elasticity using negative y-directional strain**



$y = 464391.601x + 23.677$
$R^2 = 0.999$
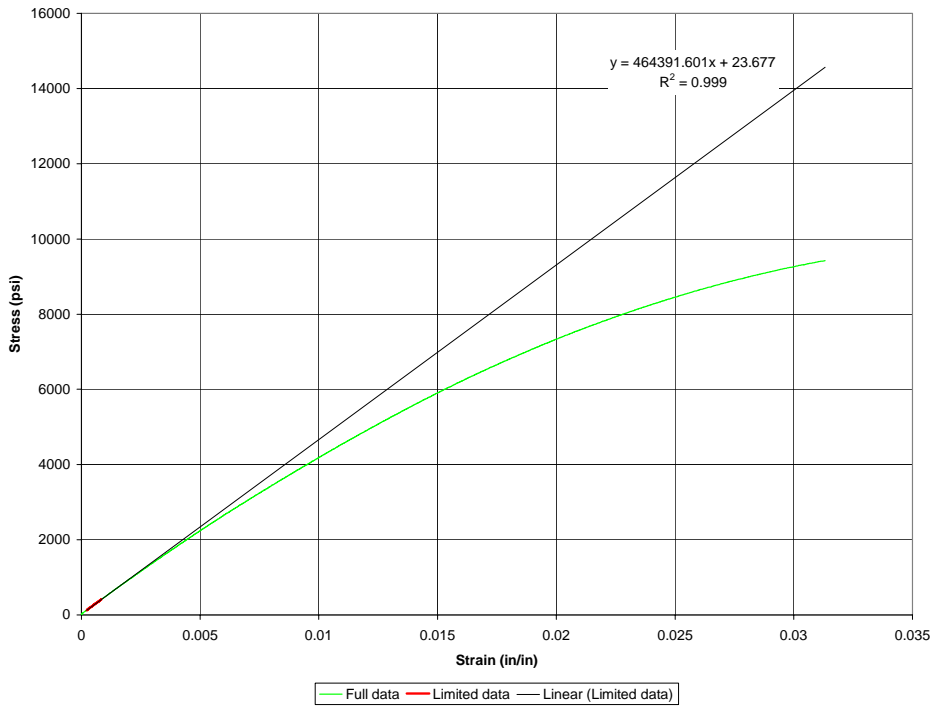
**Figure 116.  Tensile test specimen 2 modulus of elasticity using x-directional strain**
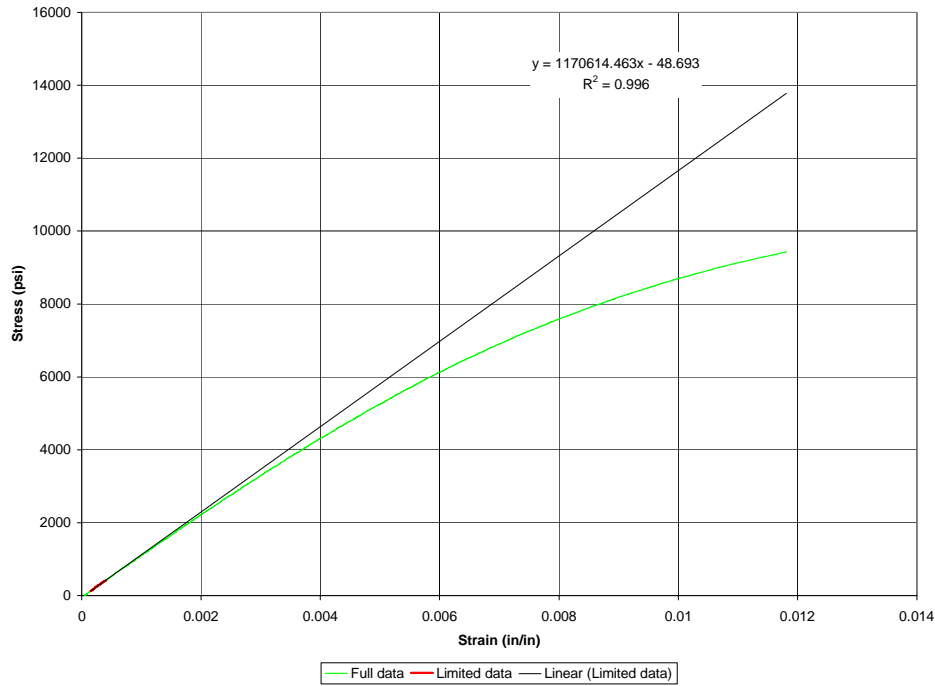
**Figure 117. Tensile test specimen 2 modulus of elasticity using negative y-directional strain**

ASTM E-132-97 was used as a guide to calculate Poisson's ratio.  The x-direction strain and the y-direction strain were plotted against each other, a line is fitted to the data using the method of least squares, and the slope of the fitted line is Poisson's ratio.  All data points were used in the calculation, since results for the shorter range used for the modulus of elasticity calculation above gave similar results to using the entire range of data.  Both specimens Poisson's ratio values are very close to each other, as shown in Figure 118 and Figure 119.  The coefficient of determination ($R^2$) for both linear interpolations are very near to one, showing good correlation between the linear fit and the actual data.

124
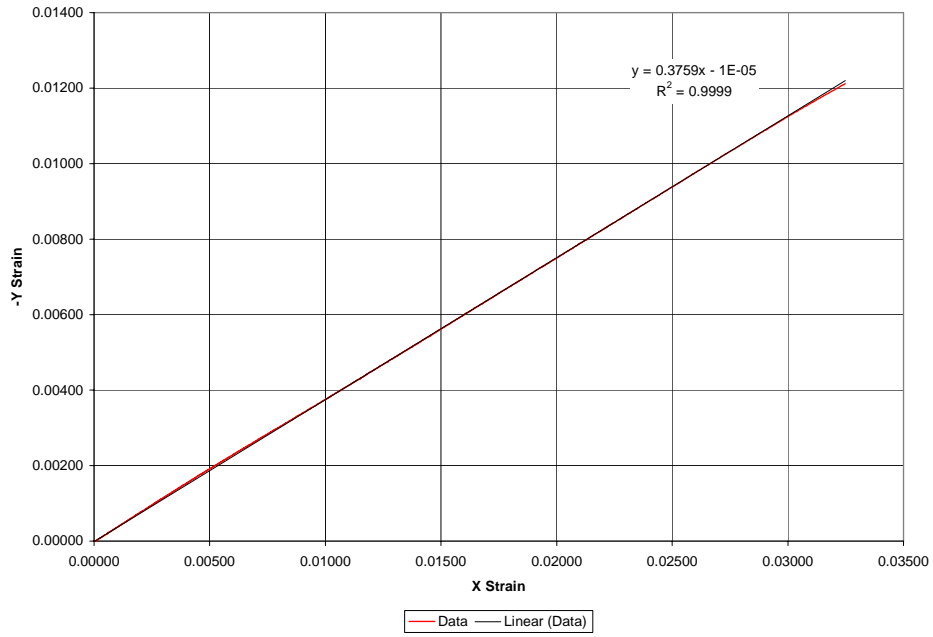
**Figure 118.  Tensile test specimen 1 Poisson's ratio**
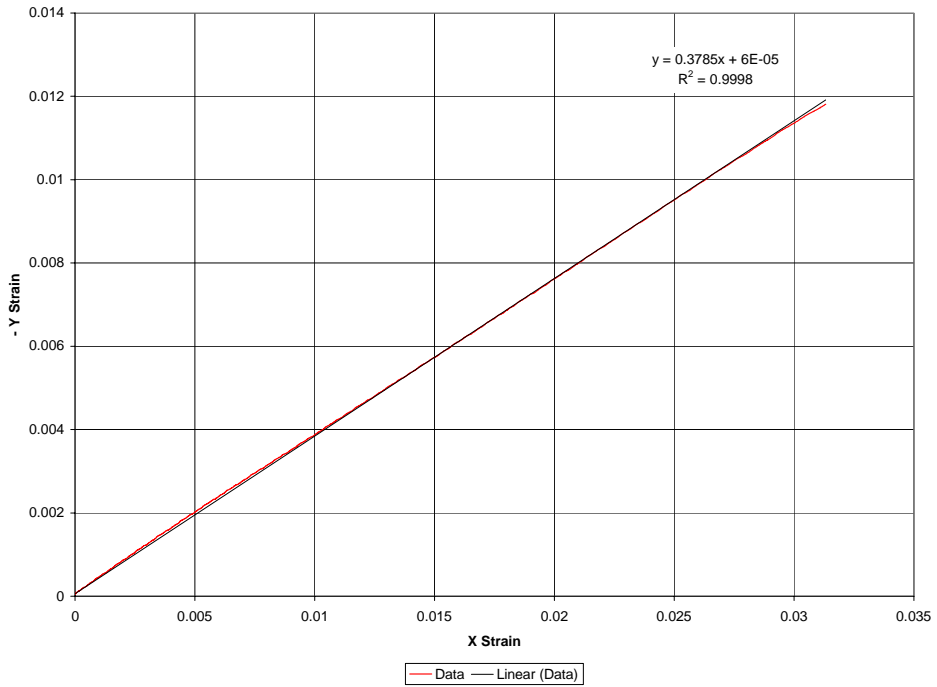


**Figure 119.  Tensile test specimen 2 Poisson's ratio**

The only value for the coefficient of thermal expansion needed was room temperature, therefore the coefficient of thermal expansion was calculated from a small subset of the full dataset. The full data set is shown in Figure 120, with all strain gage values plotted against the control chamber's temperature.
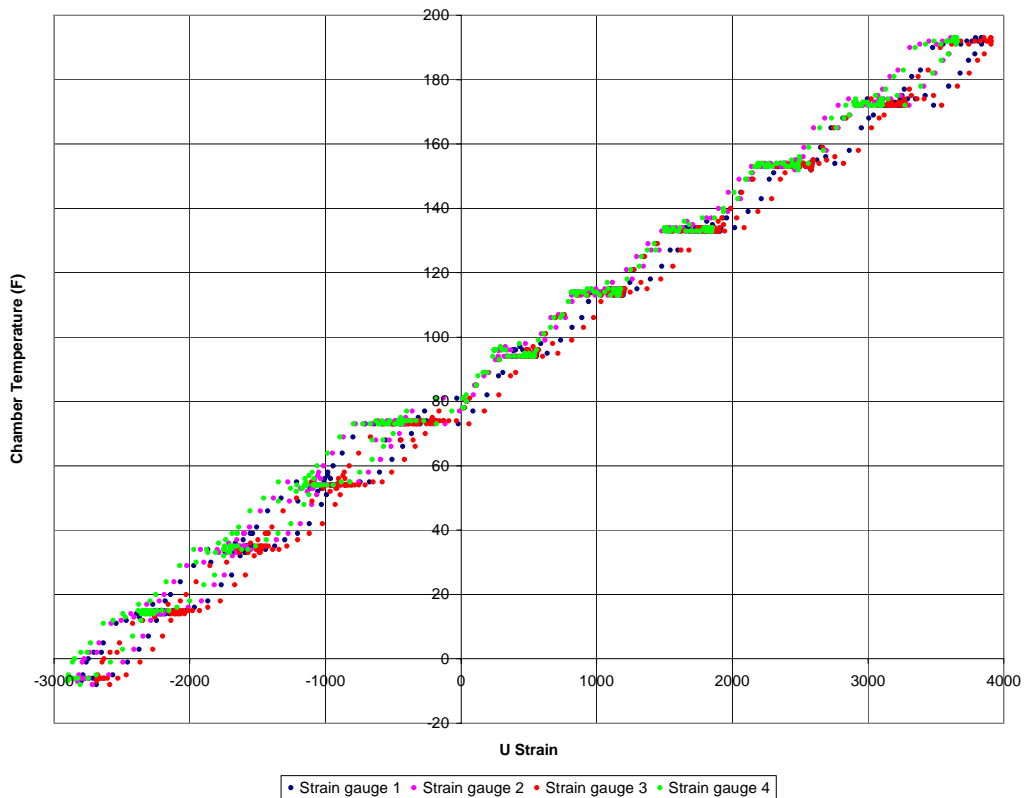


**Figure 120. All specimens and gage data for FM 300M (0.05 psf) CTE test**

ASTM E-831-03 was consulted, but not followed in the calculation of the coefficient of thermal expansion. The data for each strain gage was plotted and a linear fit using the method of least squares was used, shown in Figure 121 through Figure 124.

126
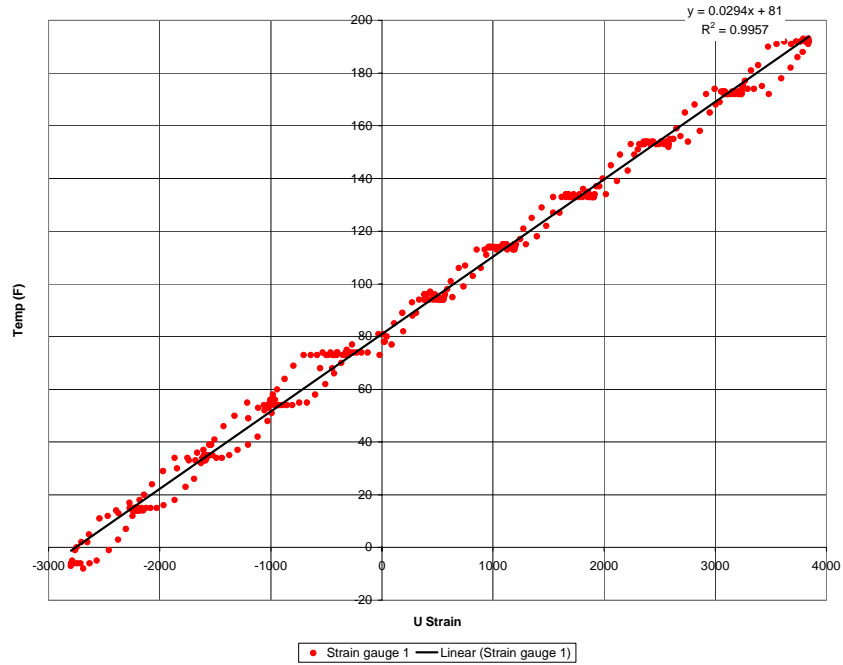
**Figure 121. CTE data for strain gage 1 for FM 300M (0.05 psf)**
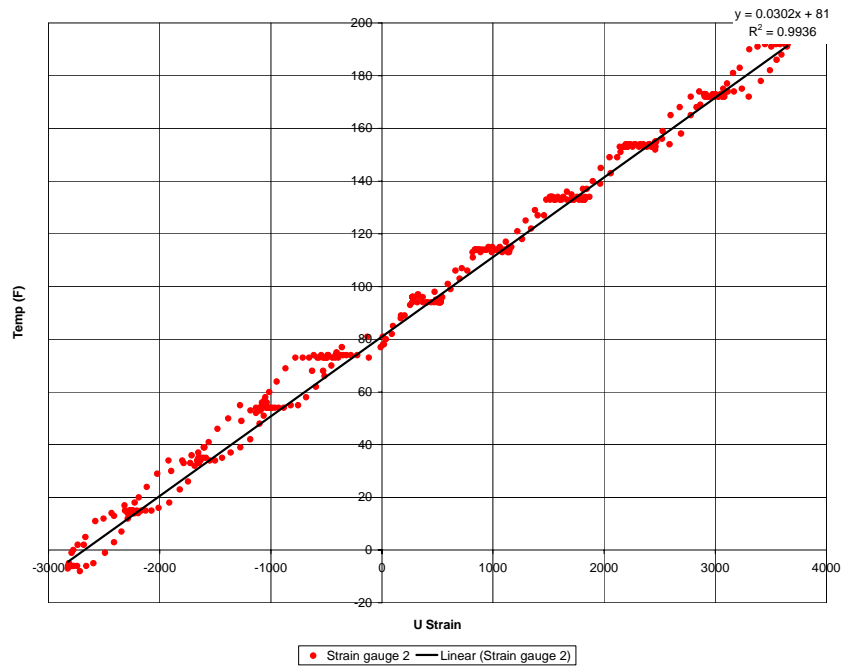


**Figure 122. CTE data for strain gage 2 for FM 300M (0.05 psf)**
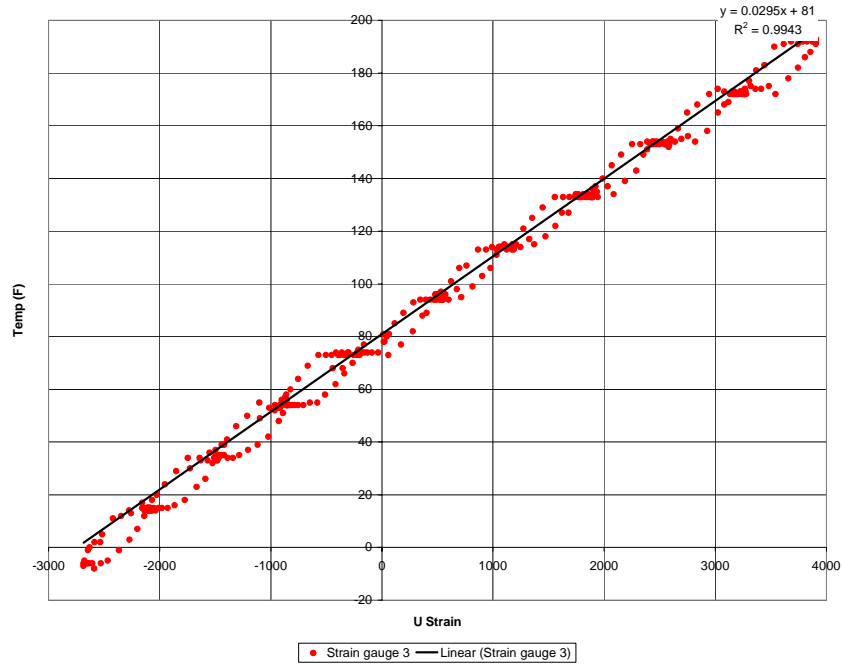
**Figure 123. CTE data for strain gage 3 for FM 300M (0.05 psf)**
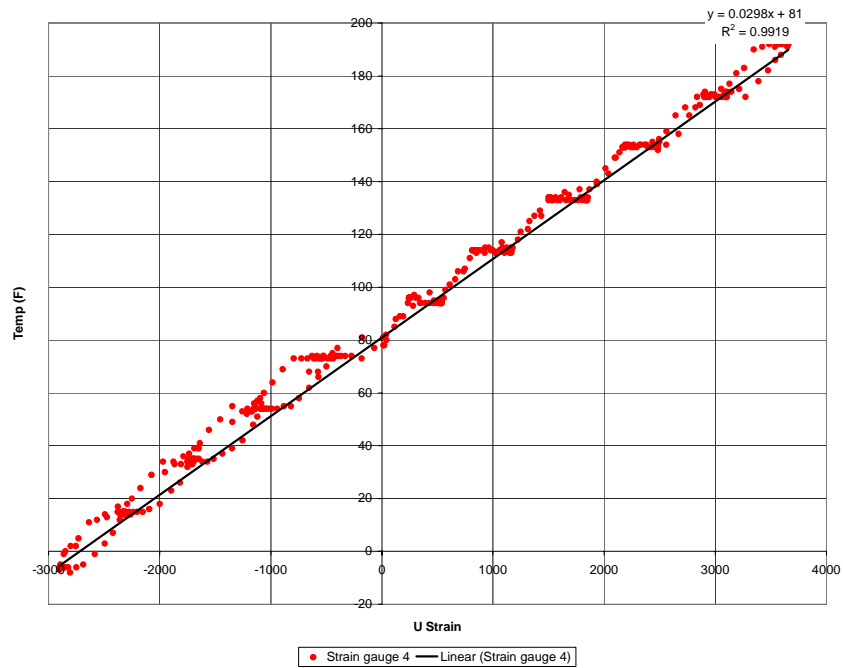


**Figure 124. CTE data for strain gage 4 for FM 300M (0.05 psf)**

Once again, the coefficients of determination (R2) for all of the linear interpolations are near to one. The graphs were plotted with the temperature on the y-axis for ease in plotting as well as in linear interpolation. The fitting lines were all forced to go through 81° F at zero strain. This was the start temperature for the test and when all of the strain gages were zeroed.

As can be seen, when the chamber temperature was incremented there was a lag in the strain gage's reading. The strain would then finally stabilize, prior to another chamber temperature increment. Only the steady state strain values were needed for the coefficient of thermal expansion calculation. The data was filtered in the following way: only data between 25-125° F was considered, the chamber temperature had changed by $\leq 2°$ F from the last data point, and the strain in all strain gages did not vary from the last reading by $\leq 5$ u-strain. This narrowed down the range of data considerably; from 400+ data points to 34. The overall value of the linear fit line's slope didn't change by much compared to the unfiltered data's linear fit, shown in Figure 125 through Figure 128. The coefficient of thermal expansion was calculated by inversing the slope of the linearly fitted line. Therefore the average value was approximately 34.8 micro strain per °F.

A comparison with manufacturer published data and equivalent epoxy resin was made. For an isotropic material, the modulus of elasticity (E) and shear modulus (G) are related by the following formula using the Poisson ratio ($v$):

$$E = 2G(1+v) \tag{8}$$

129
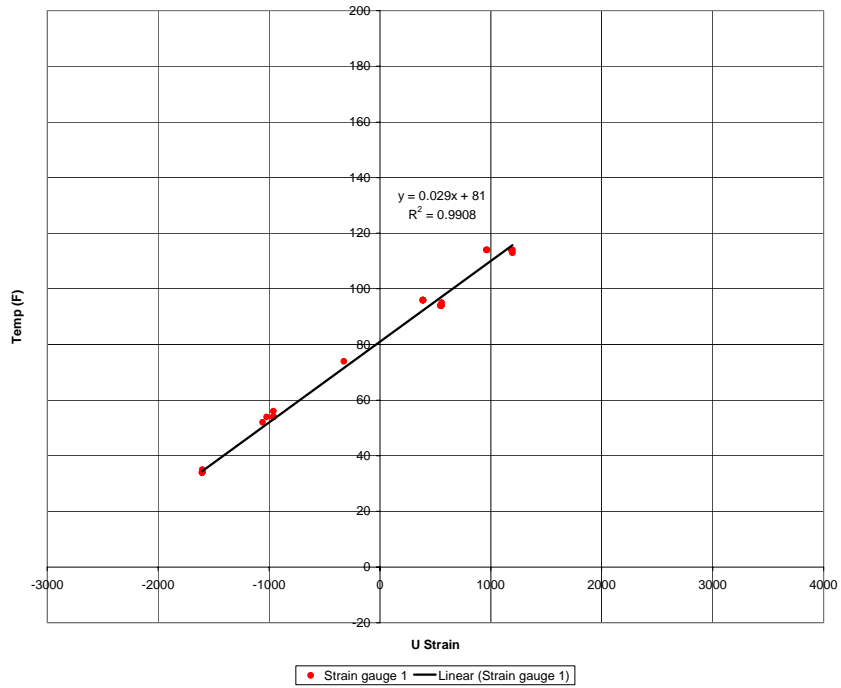
**Figure 125. Filtered CTE data for strain gage 1 for FM 300M (0.05 psf)**
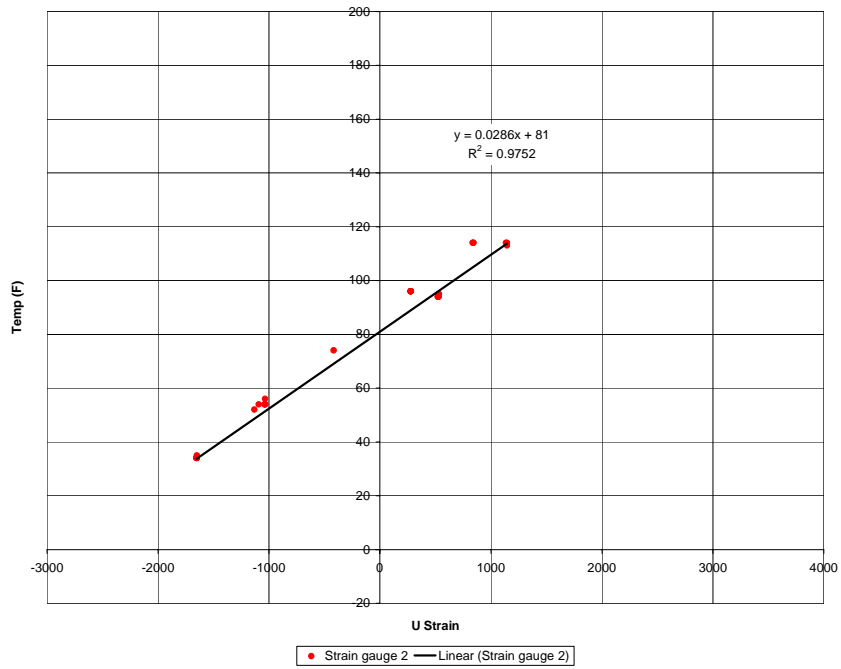


**Figure 126. Filtered CTE data for strain gage 2 for FM 300M (0.05 psf)**

130
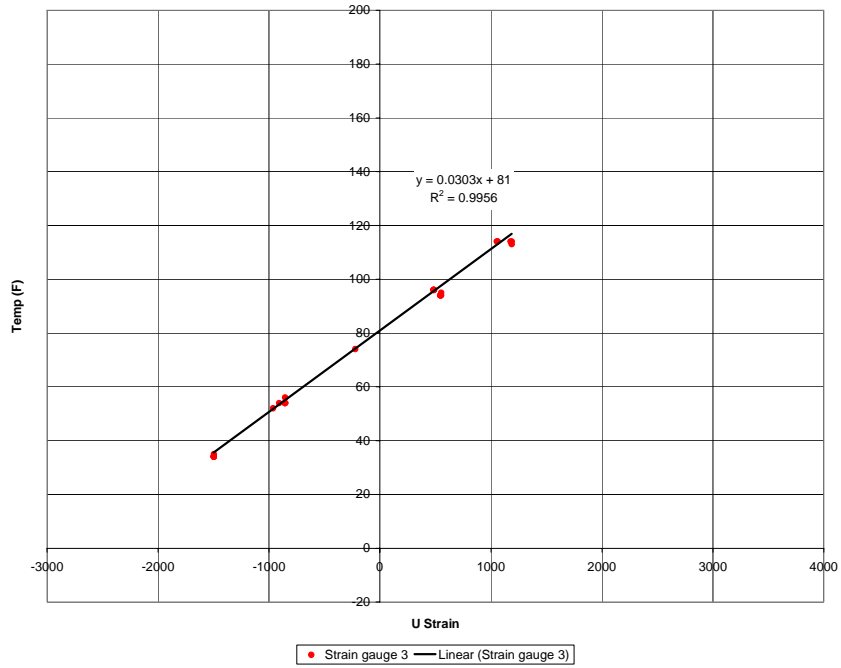
**Figure 127. Filtered CTE data for strain gage 3 for FM 300M (0.05 psf)**
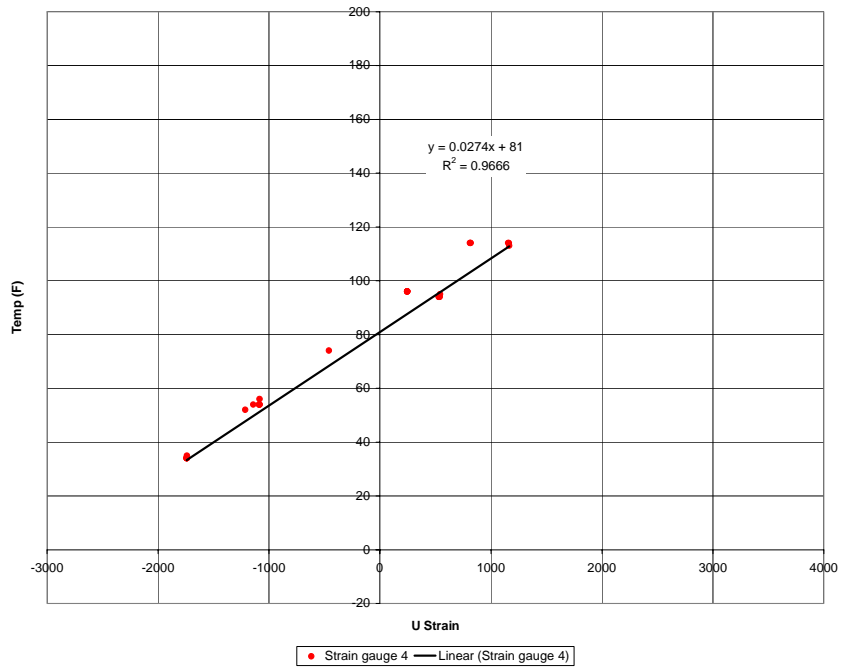


**Figure 128. Filtered CTE data for strain gage 4 for FM 300M (0.05 psf)**

131

Cytec Engineered Materials, the adhesive manufacturer, provided data on a FM 300-06M, which has a slightly thicker carrier mat than the adhesive used in this program, which creates a thicker bondline.  The manufacturer's adhesive data was for an adhesive cured using the same cycle as the plaque used in this thesis.  The manufacturer performed a KGR-1 testing method, which is an industrial standard testing of lap-shear in adhesives and is very different from the test conducted in this thesis.  For room temperature the average shear modulus was 93,507 psi, with a high value of 104,345 psi over the five room temperature tests; compared to the calculated value of 164,500 psi from this experimental data.  IM6/3501-6's matrix material is an epoxy resin similar to the FM 300M (0.05 psf) adhesive.  The material properties of both materials are shown in Table 2 to show that the values obtained are reasonable.

Table 9.  Comparison of material properties of FM 300M (0.05 psf) to IM6/3501-6 epoxy

|  | FM 300-05M Calculated Data | IM6/3501-6 AFRL/MLBC Data for the matrix direction |
|---|---|---|
| Modulus of elasticity | 164,500 psi | 1,420,000 psi |
| Poisson' ratio | 0.38 | 0.33 |
| Coefficient of thermal expansion | 34.8 μ strain/°F | 14.9 μ strain/°F |

# Appendix C:  Full Results for Large Tensile Test Panels

All of the x-axis charts for this Appendix are labeled as u strain, which means micro strain x10$^{-6}$.  For information on the strain gage location, refer to Figure 19.

## Results from Virgin Panels
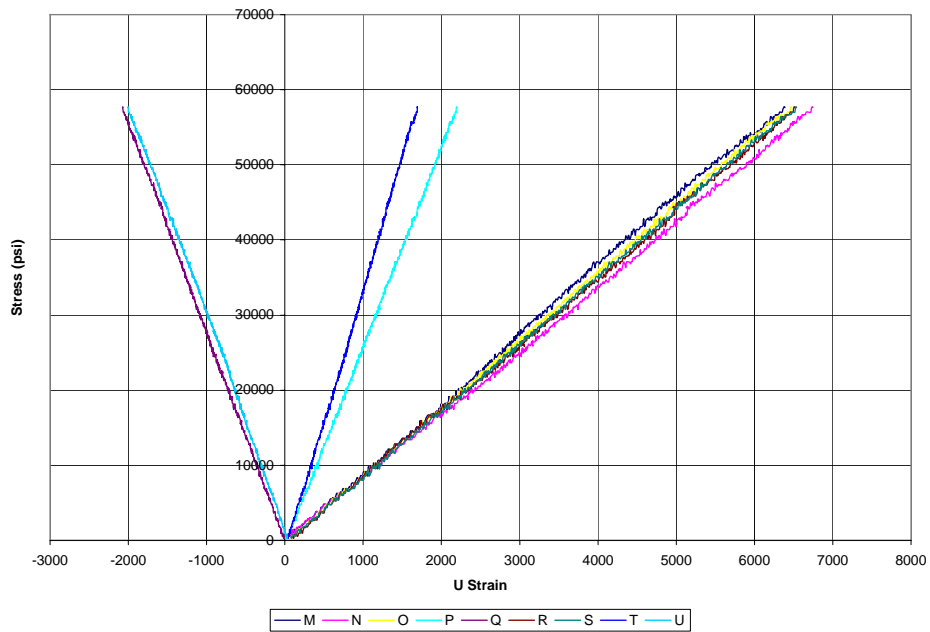


**Figure 129.  Panel 418B average stress versus micro strain from all strain gages**
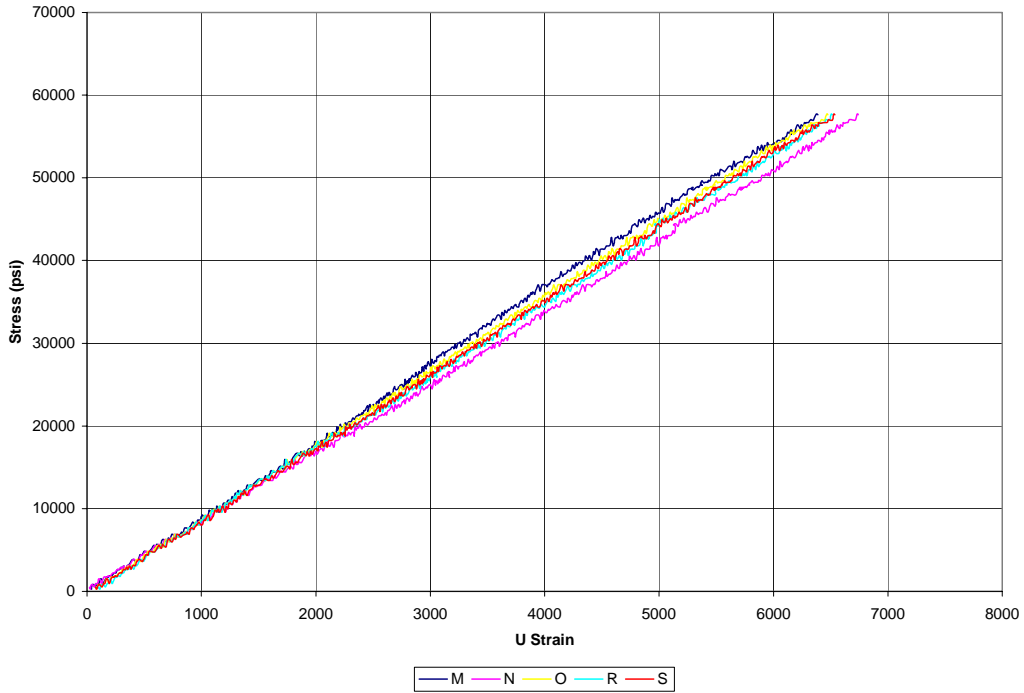
**Figure 130. Panel 418B average stress versus micro strain from 0° oriented strain gages**
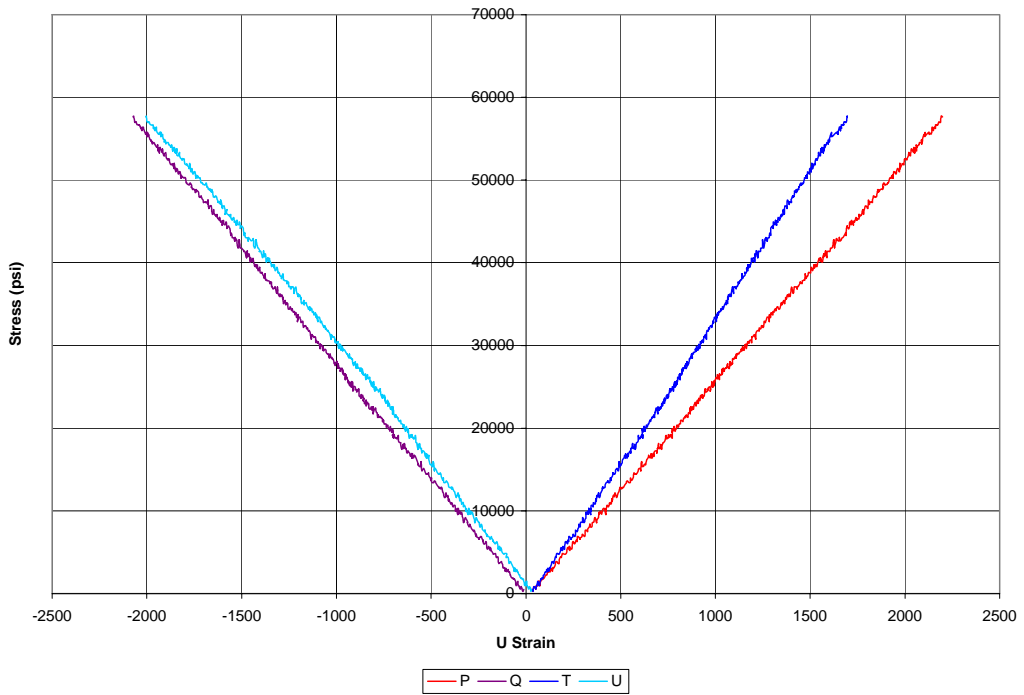


**Figure 131. Panel 418B average stress versus micro strain from non 0° oriented strain gages**

134
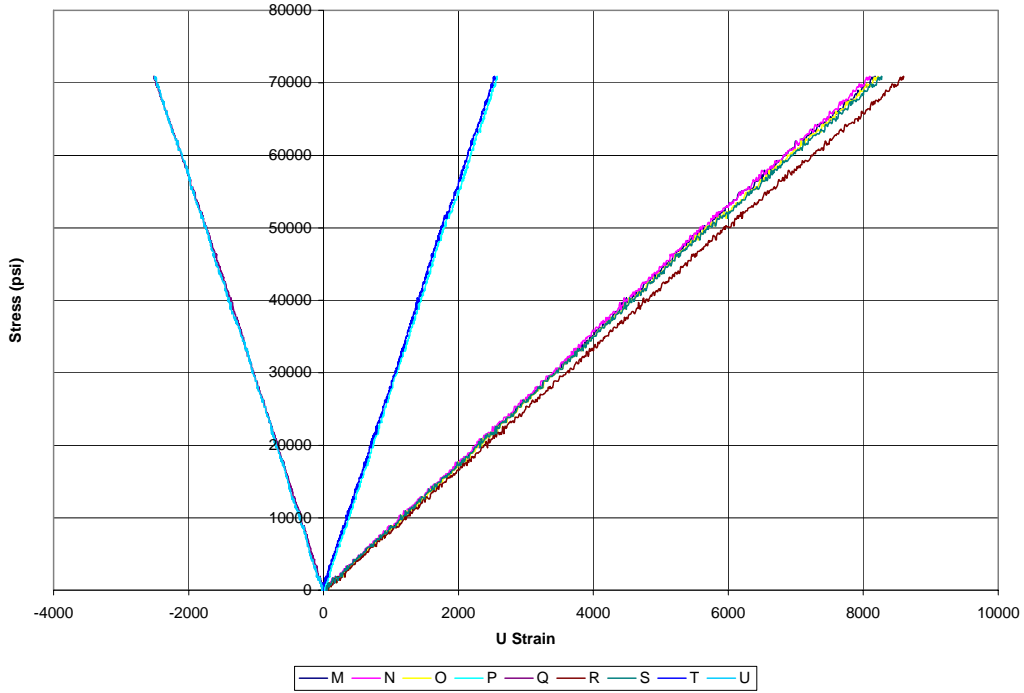
**Figure 132. Panel 425B average stress versus micro strain from all strain gages**
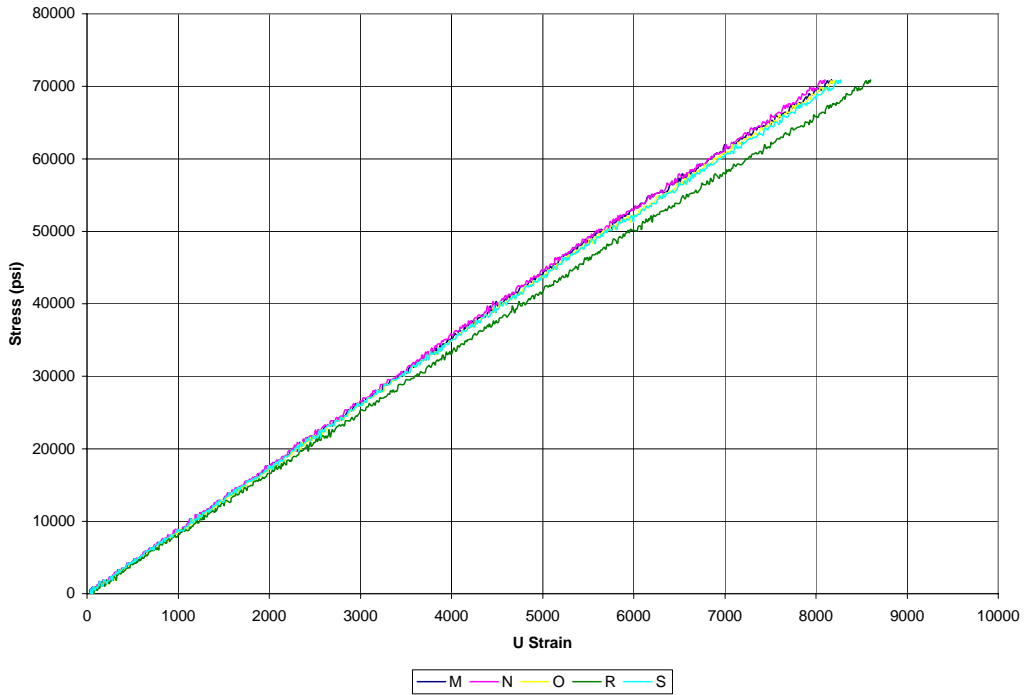


**Figure 133. Panel 425B average stress versus micro strain from 0° oriented strain gages**

135
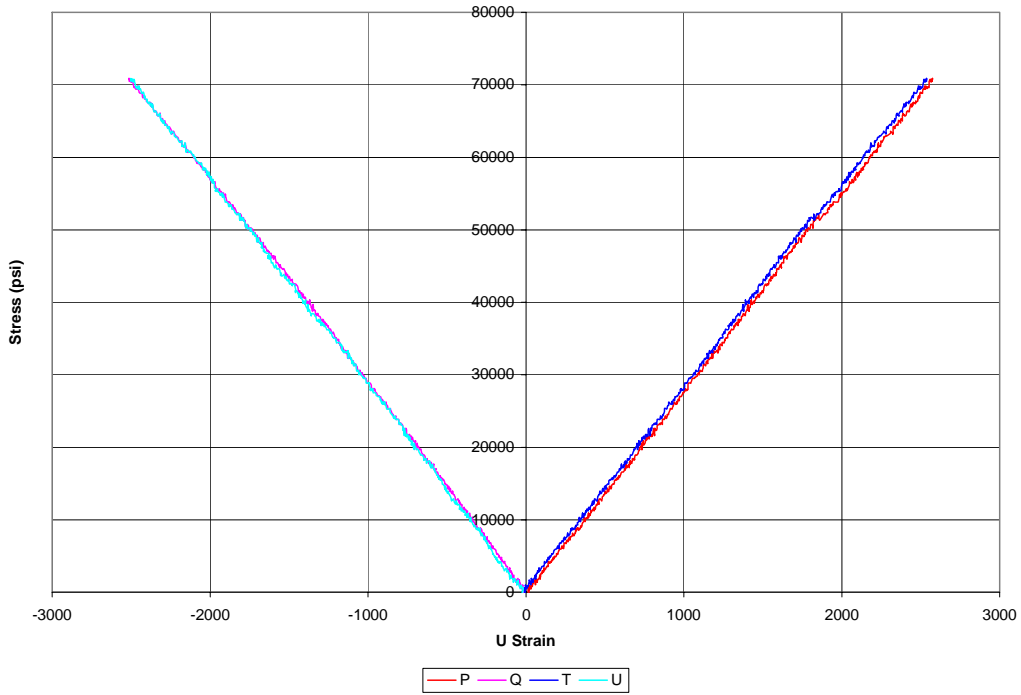
**Figure 134. Panel 425B average stress versus micro strain from non 0° oriented strain gages**
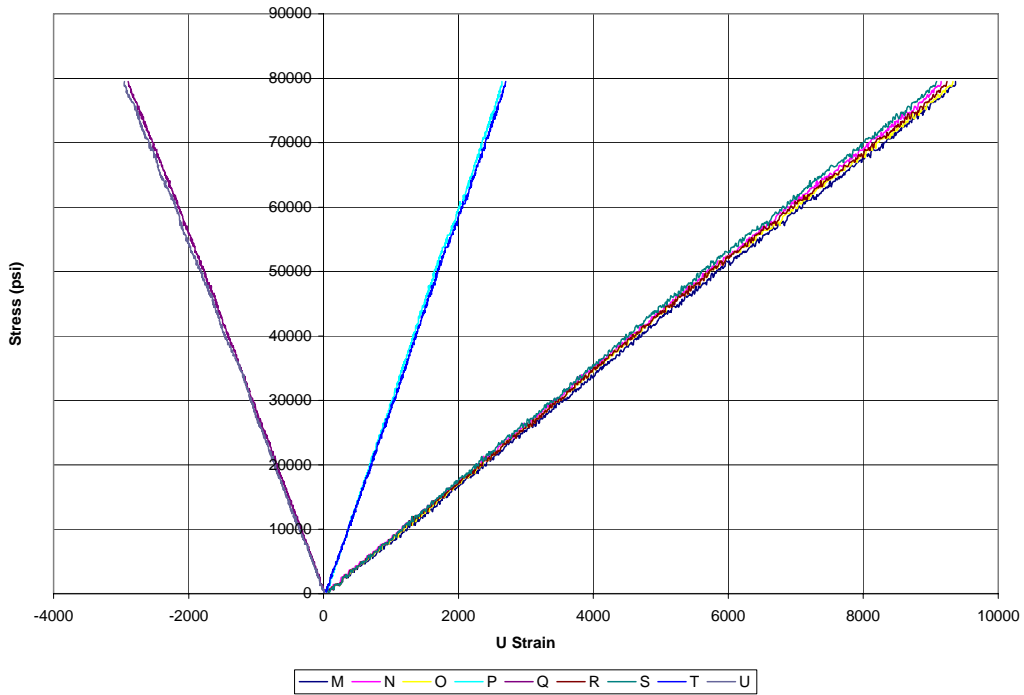


**Figure 135. Panel 422T average stress versus micro strain from all strain gages**

136
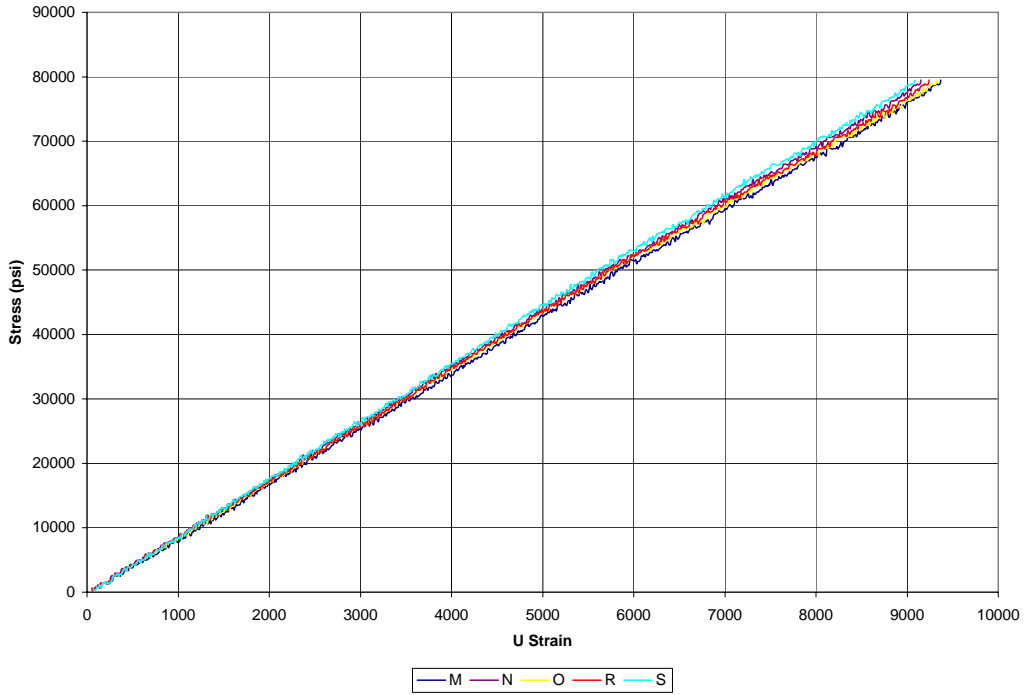
**Figure 136.  Panel 422T average stress versus micro strain from 0° oriented strain gages**
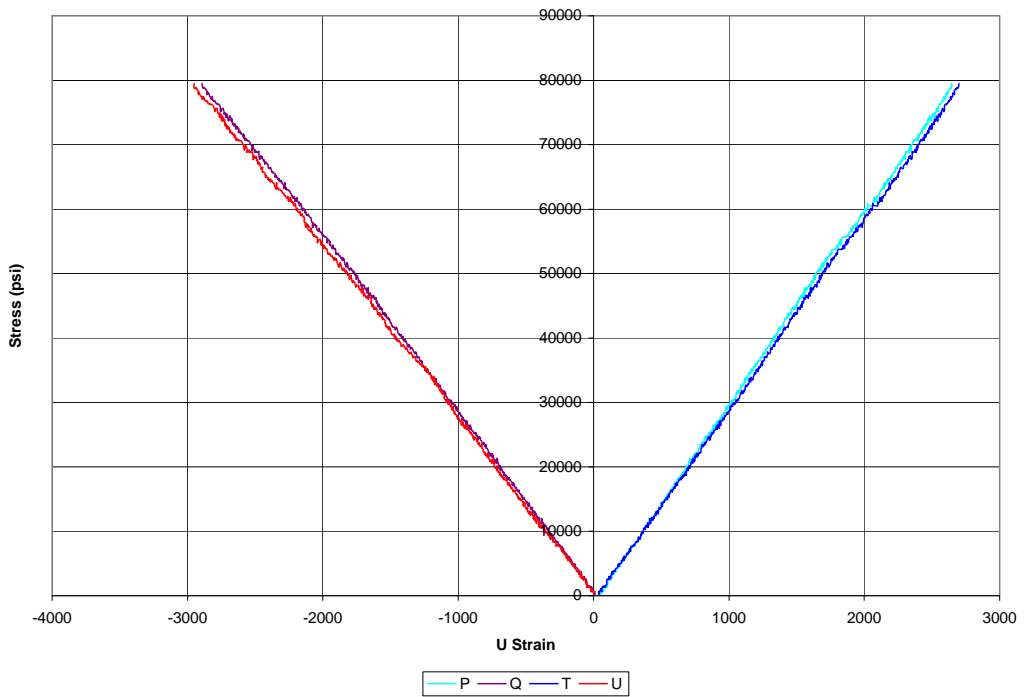


**Figure 137.  Panel 422T average stress versus micro strain from non 0° oriented strain gages**

137
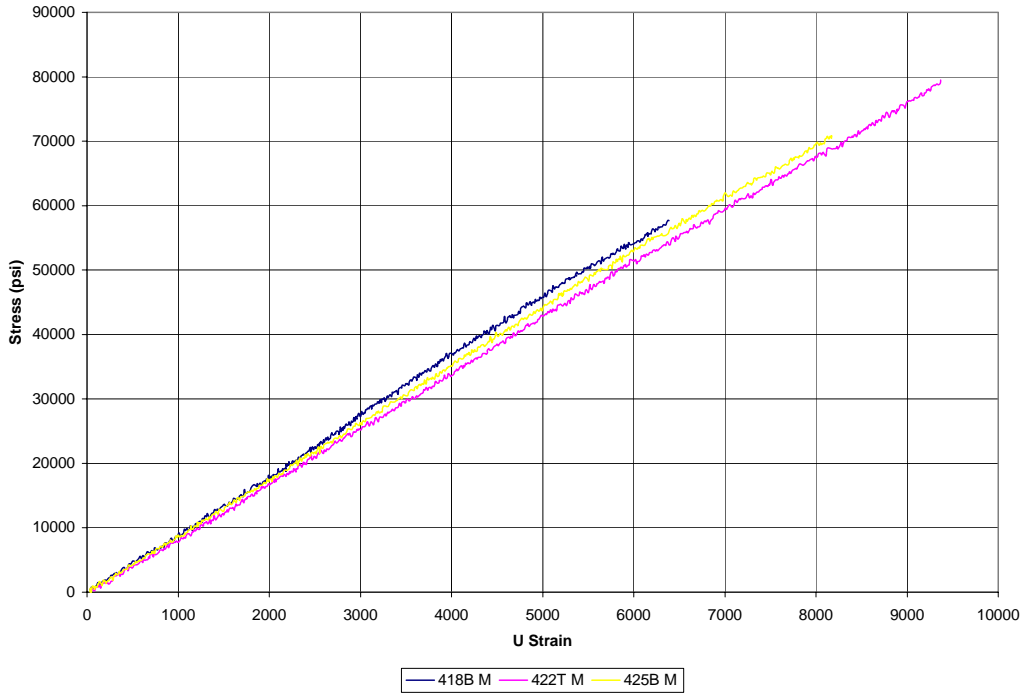
**Figure 138.  Comparison of all virgin panels stress versus micro strain on channel M**
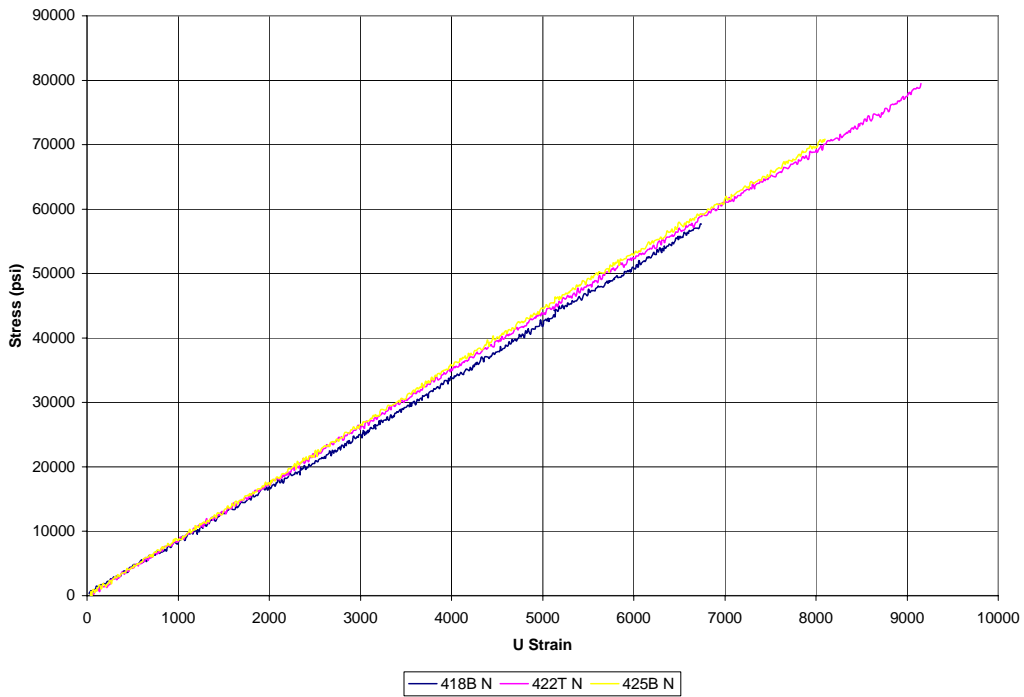


**Figure 139.  Comparison of all virgin panels stress versus micro strain on channel N**

138
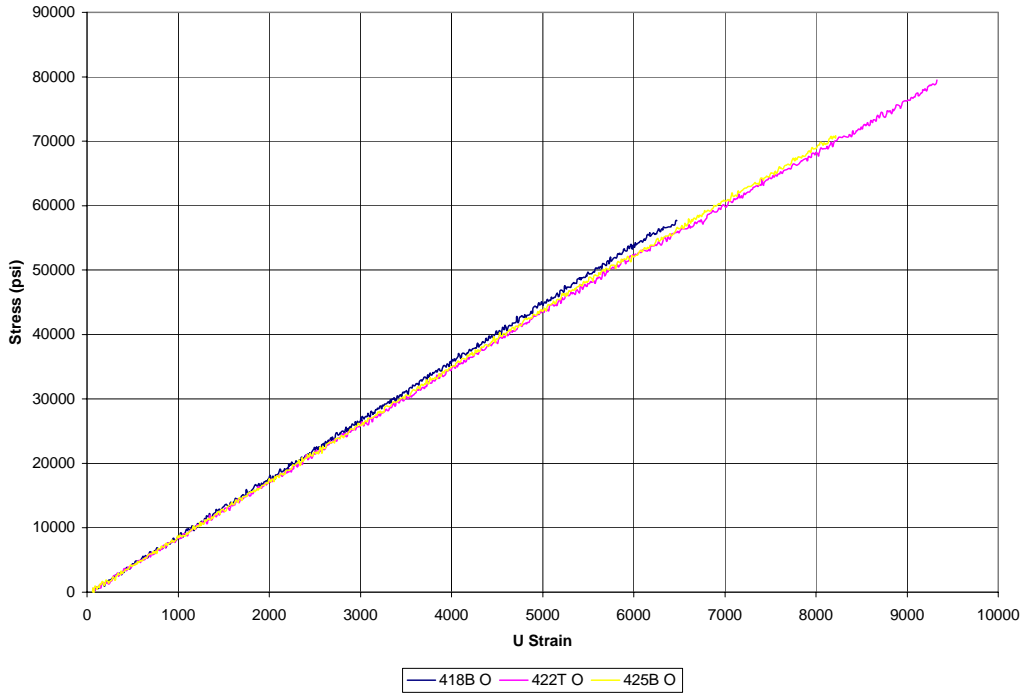
**Figure 140.  Comparison of all virgin panels stress versus micro strain on channel O**
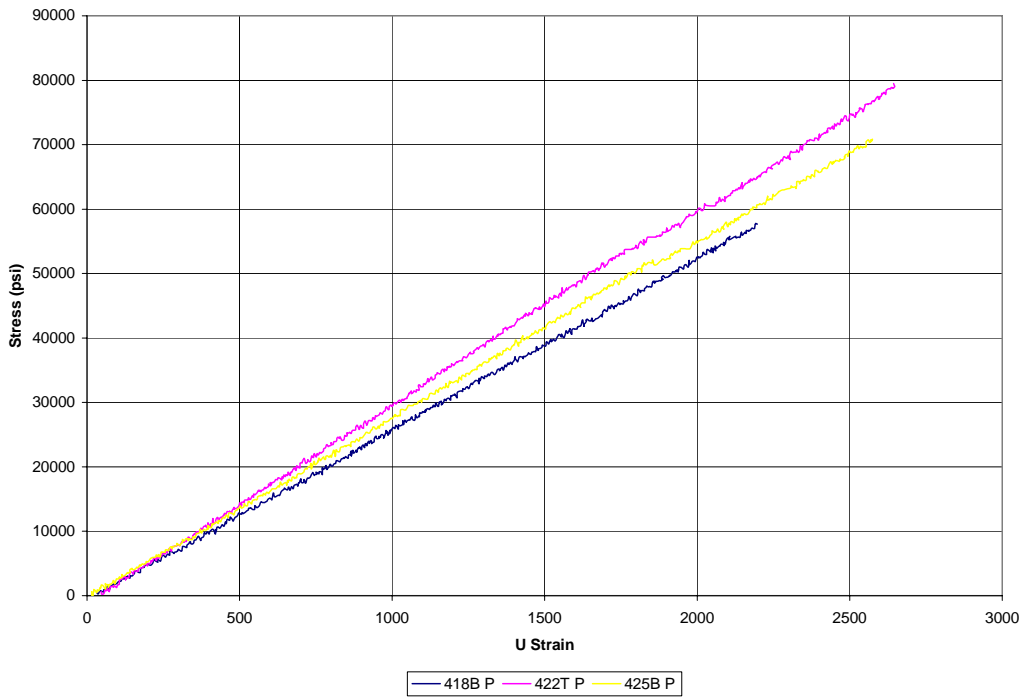


**Figure 141.  Comparison of all virgin panels stress versus micro strain on channel P**

139
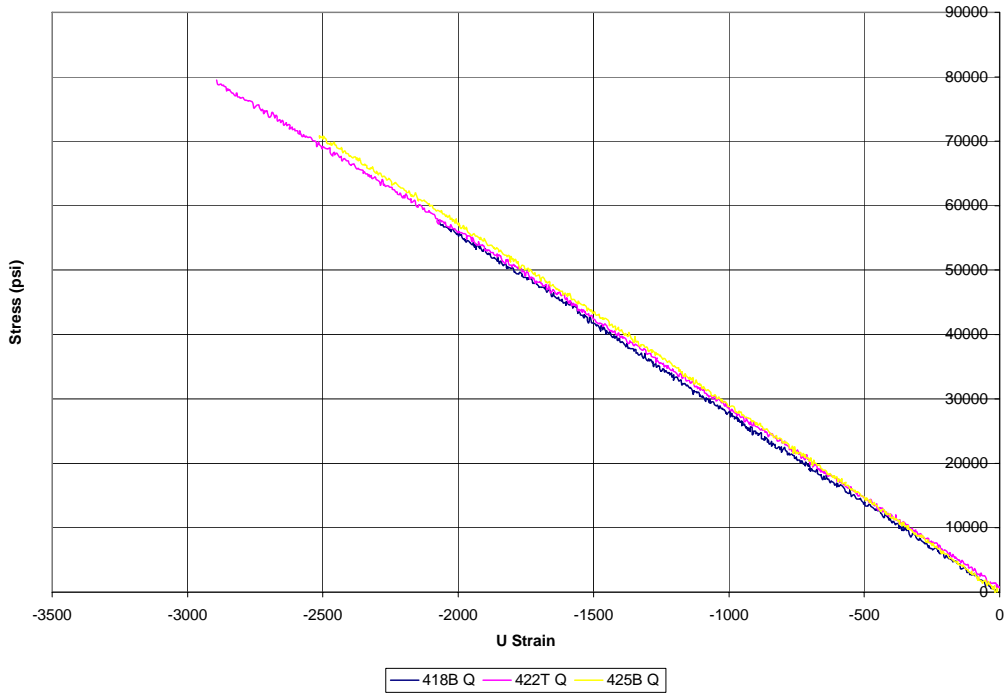
**Figure 142.  Comparison of all virgin panels stress versus micro strain on channel Q**
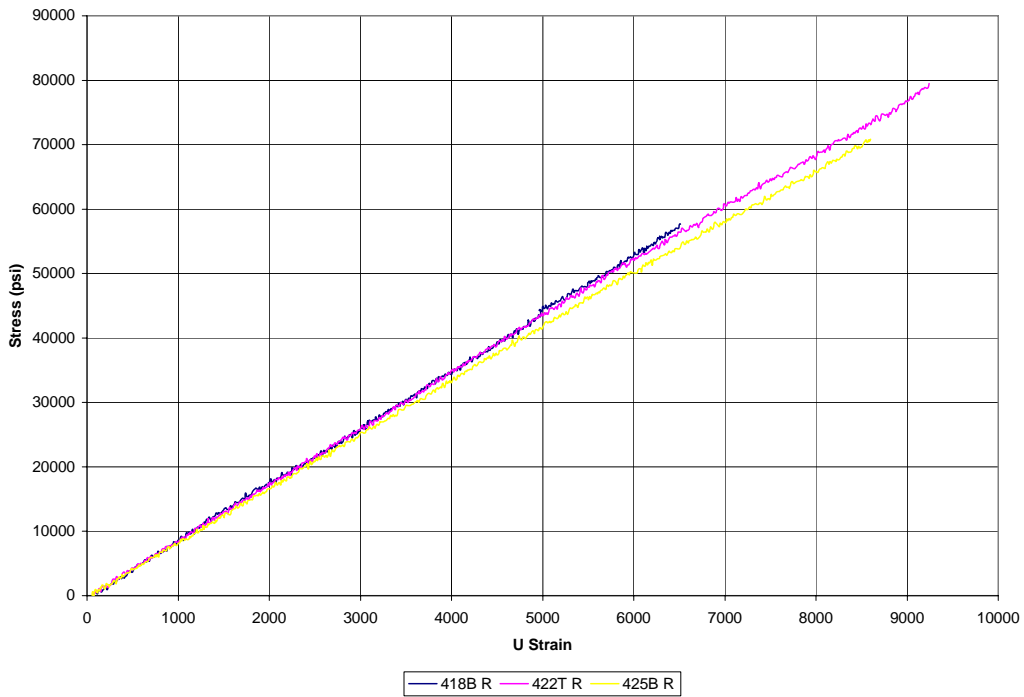


**Figure 143.  Comparison of all virgin panels stress versus micro strain on channel R**
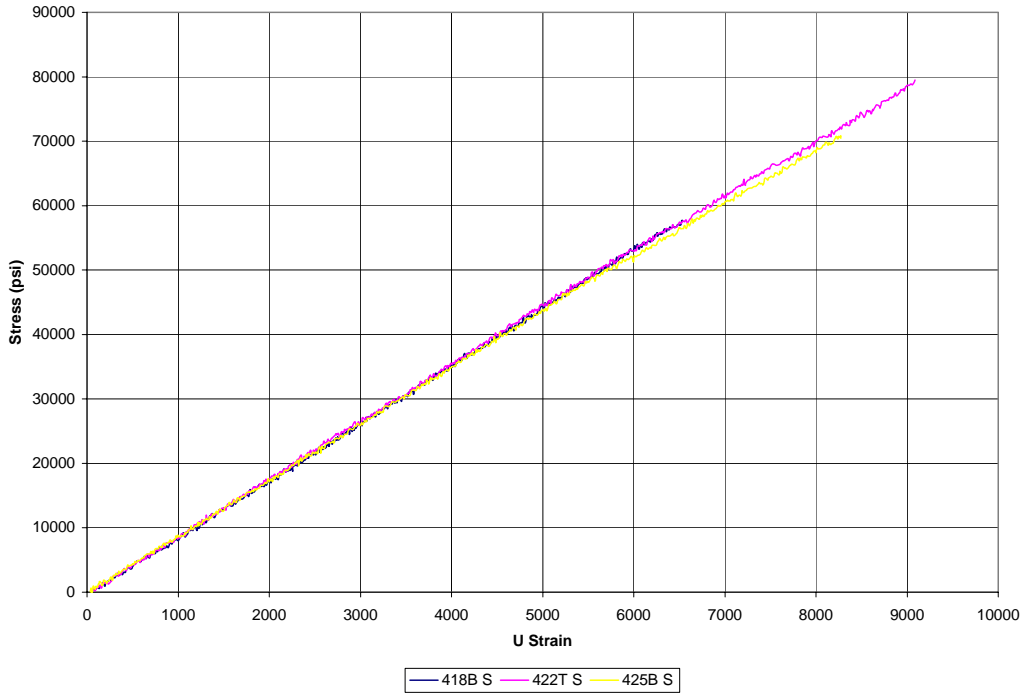
**Figure 144. Comparison of all virgin panels stress versus micro strain on channel S**
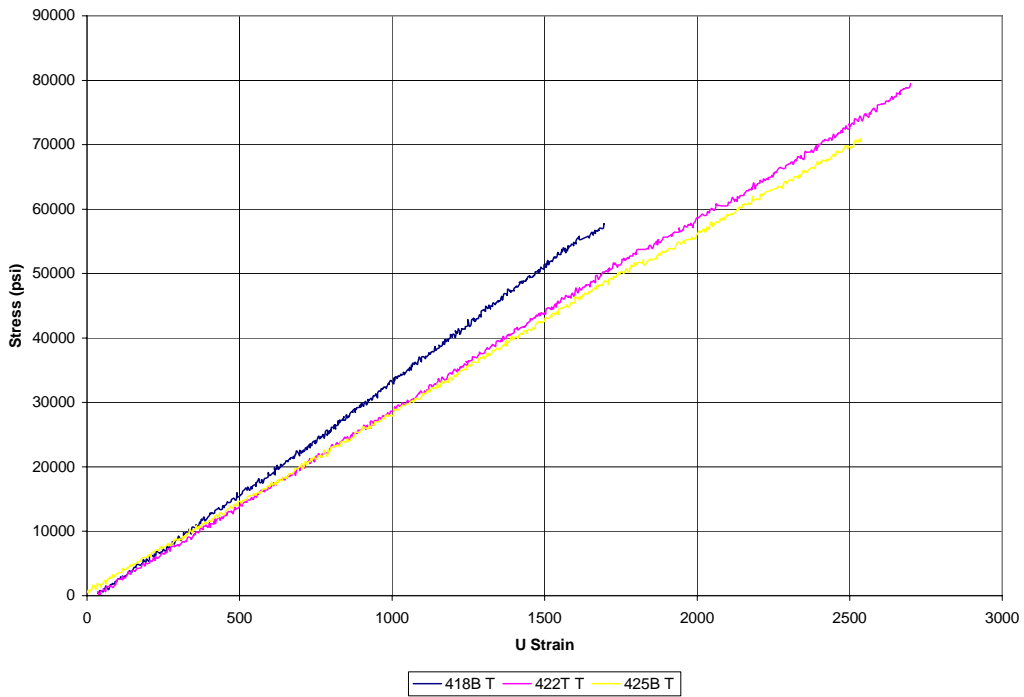


**Figure 145. Comparison of all virgin panels stress versus micro strain on channel T**

141
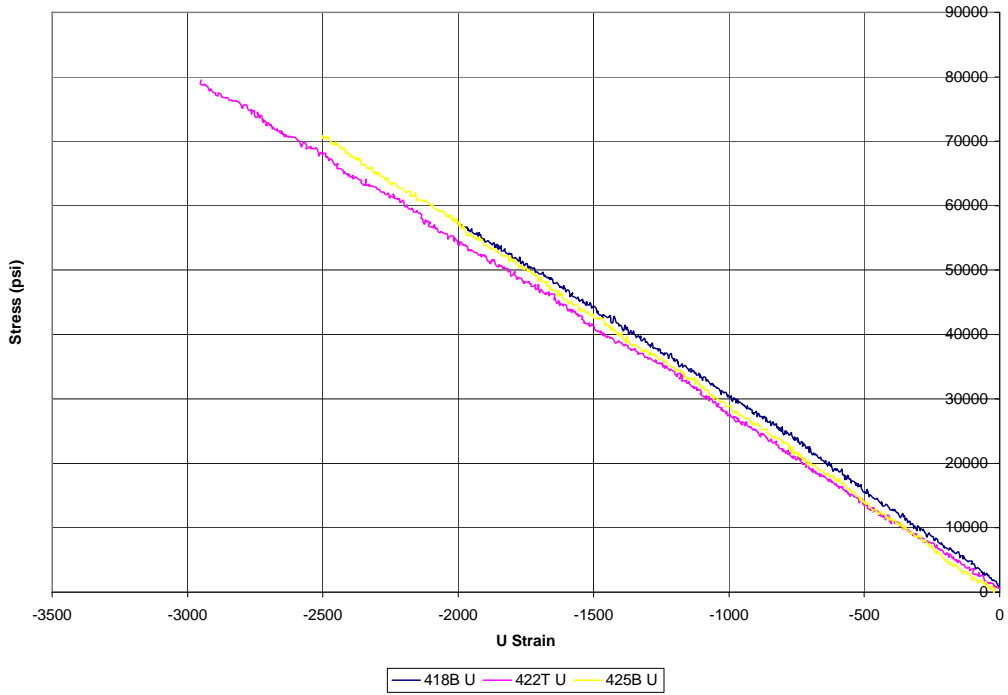
**Figure 146.  Comparison of all virgin panels stress versus micro strain on channel U**
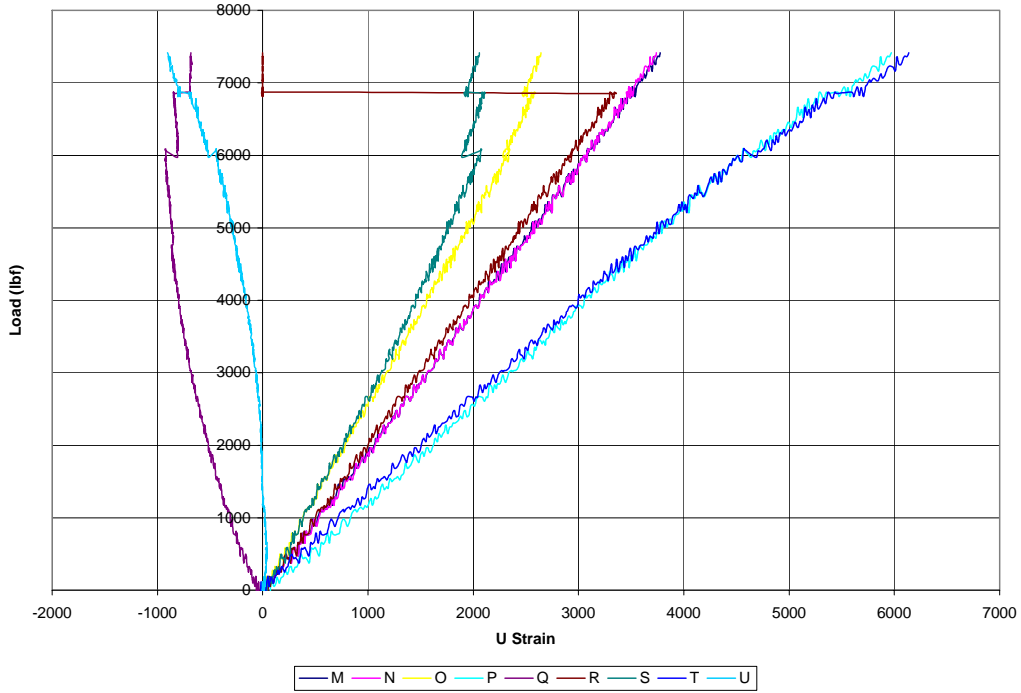
**Results from Scarfed Panels**
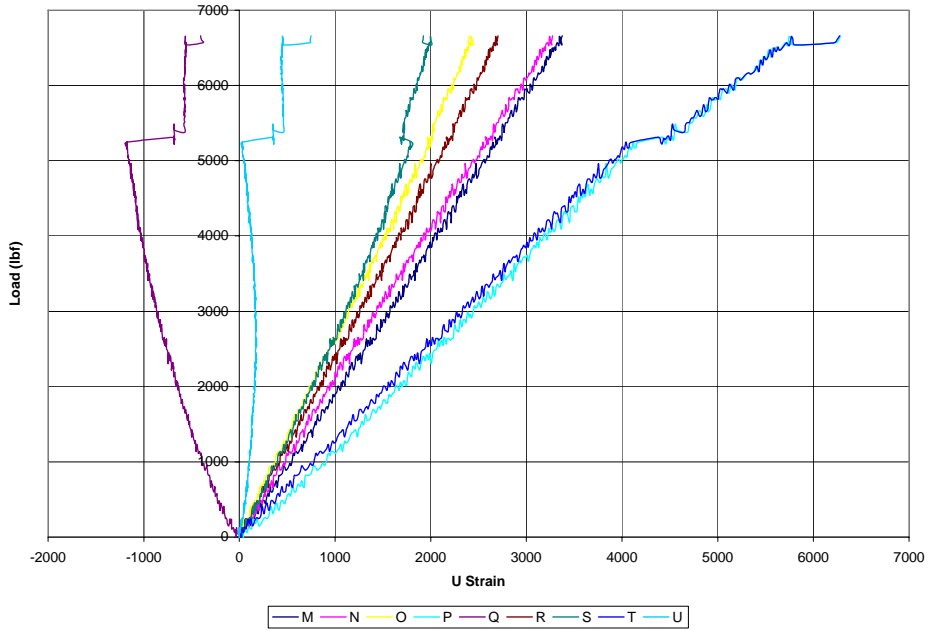


**Figure 147. Panel 419T load versus micro strain from all strain gages**
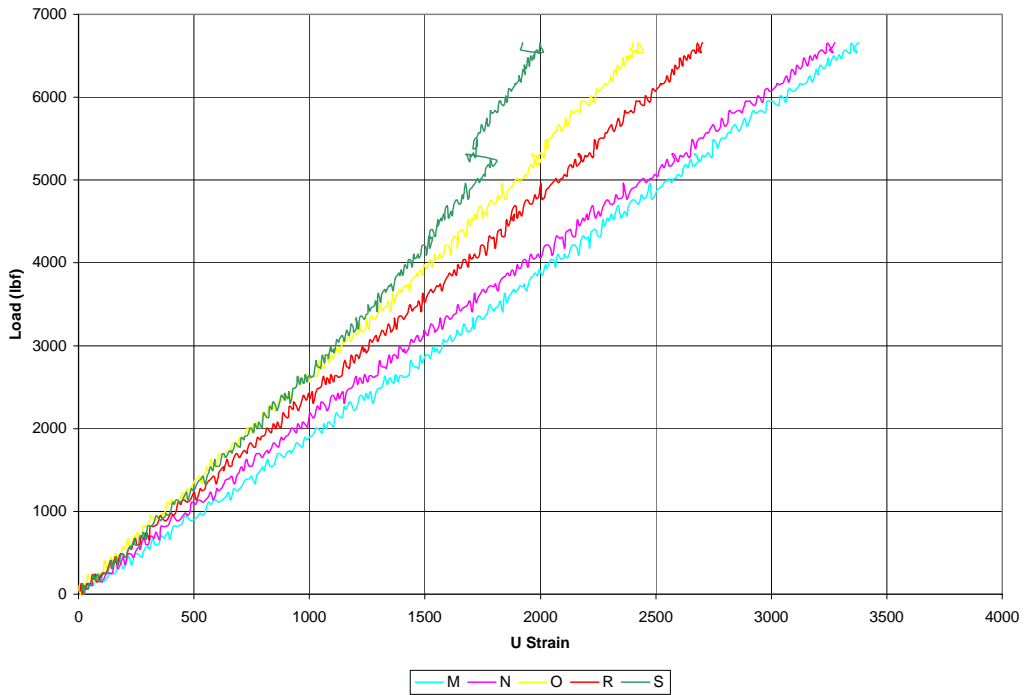


**Figure 148. Panel 419T load versus micro strain from select 0° oriented strain gages**
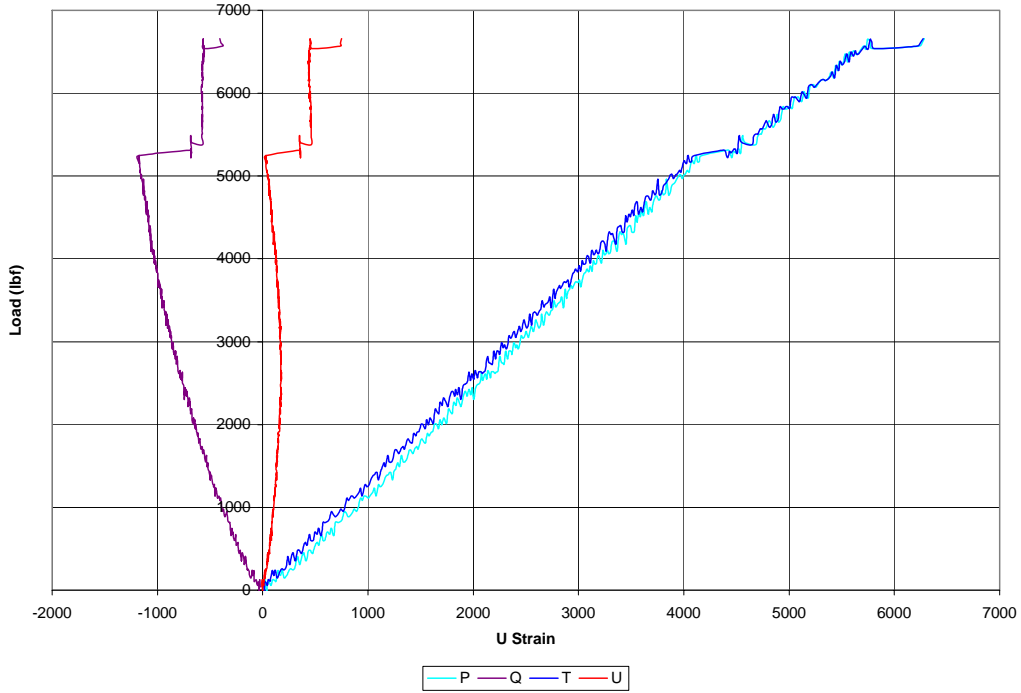
**Figure 149. Panel 419T load versus micro strain from strain gages located on side of scarf**
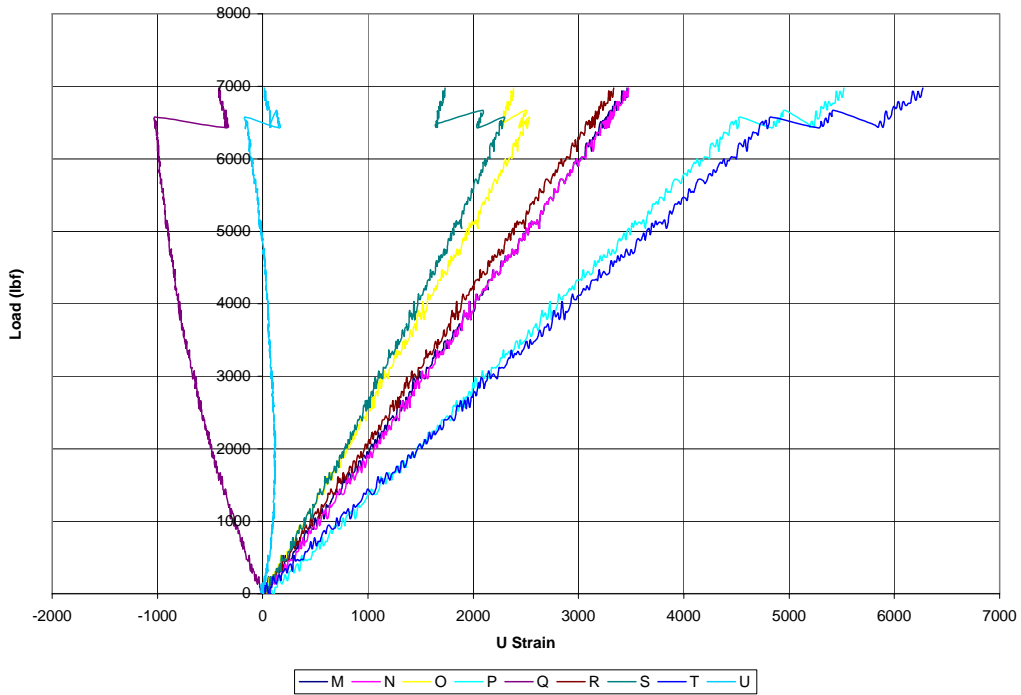


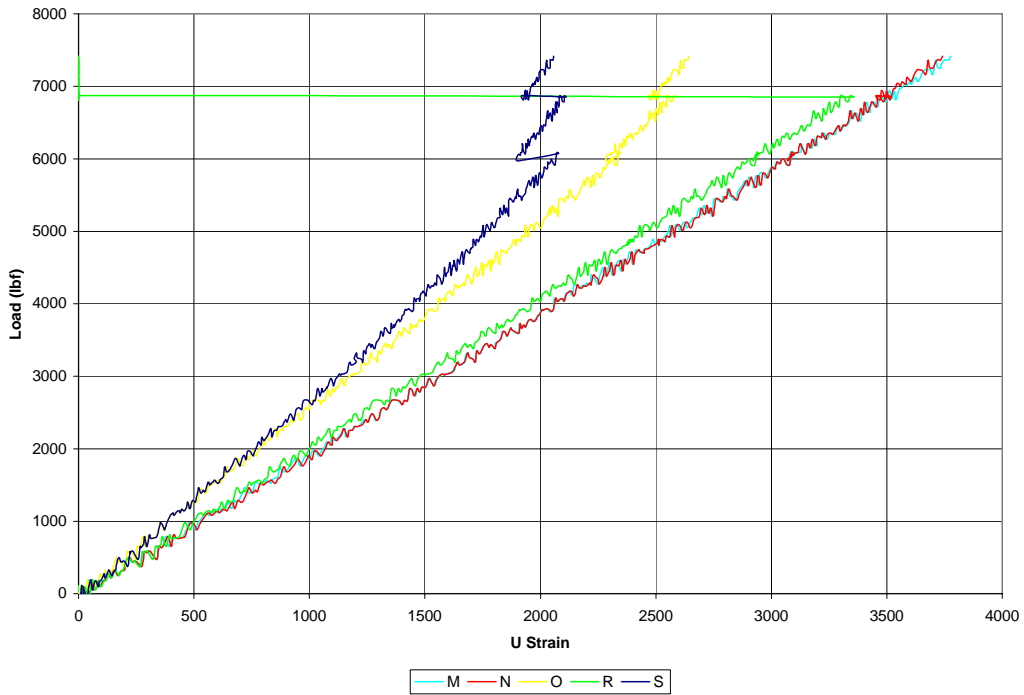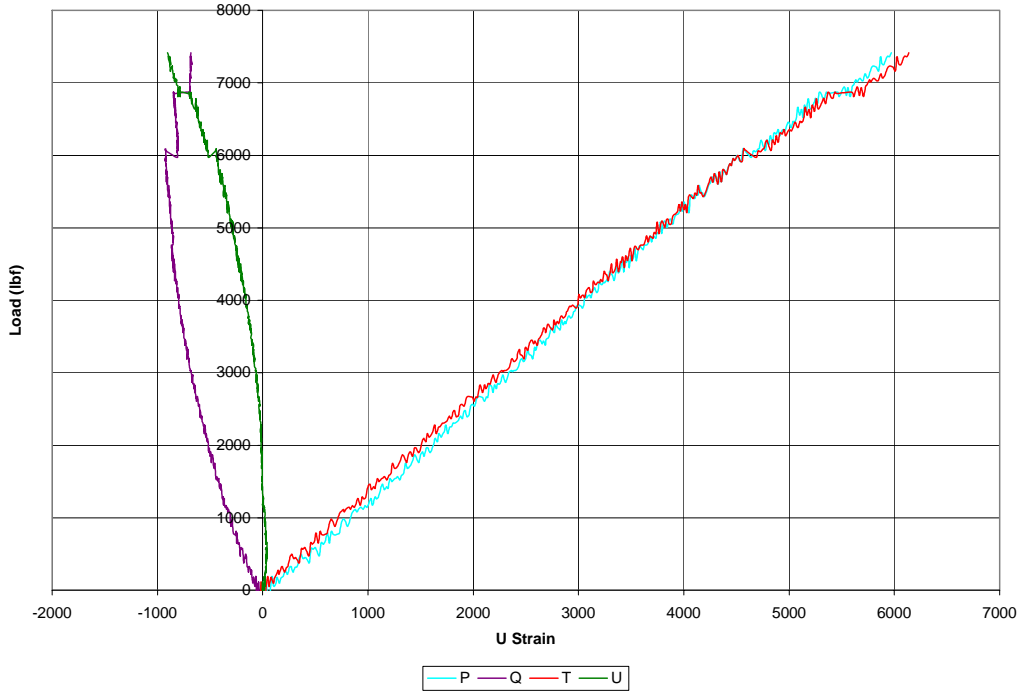**Figure 150. Panel 423T load versus micro strain from all strain gages**

144
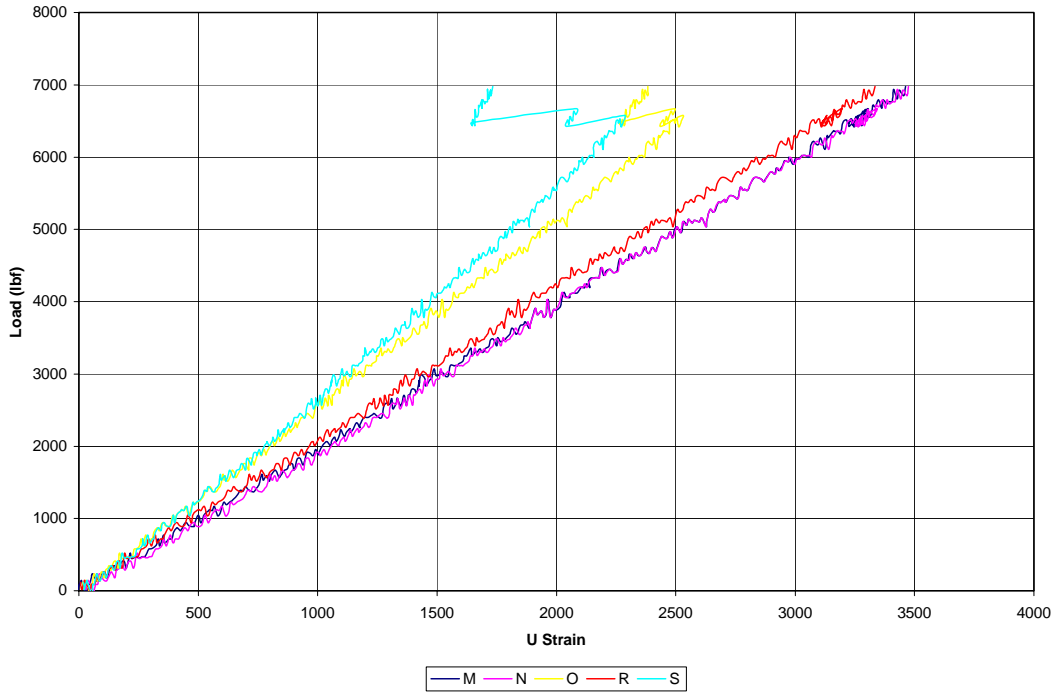
**Figure 151. Panel 423T load versus micro strain from select 0° oriented strain gages**
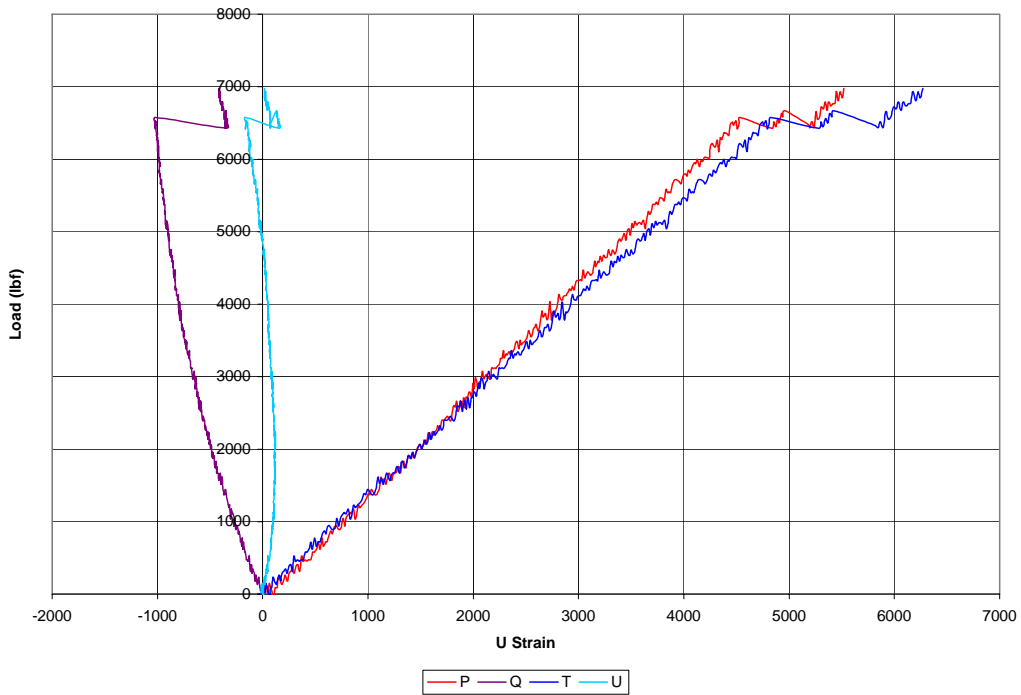


**Figure 152. Panel 423T load versus micro strain from strain gages located on side of scarf**
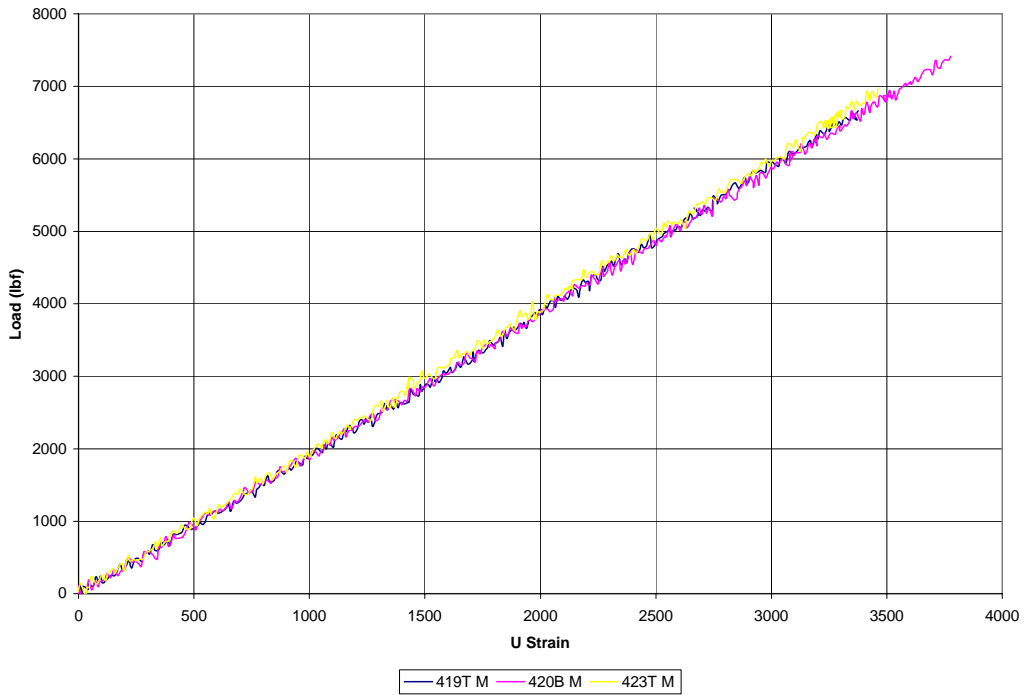
**Figure 153. Panel 420B load versus micro strain from all strain gages**



**Figure 154. Panel 420B load versus micro strain from select 0° oriented strain gages**

146

**Figure 155.  Panel 420B load versus micro strain from strain gages located on side of scarf**



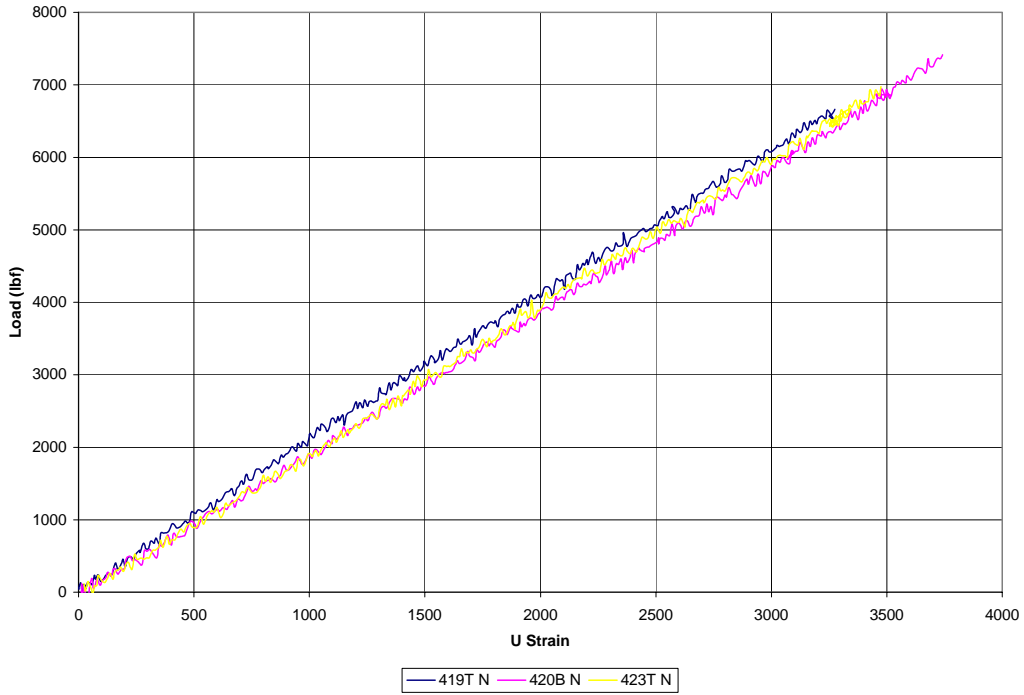**Figure 156.  Comparison of all scarfed panels stress versus micro strain on channel M**

**Figure 157. Comparison of all scarfed panels stress versus micro strain on channel N**
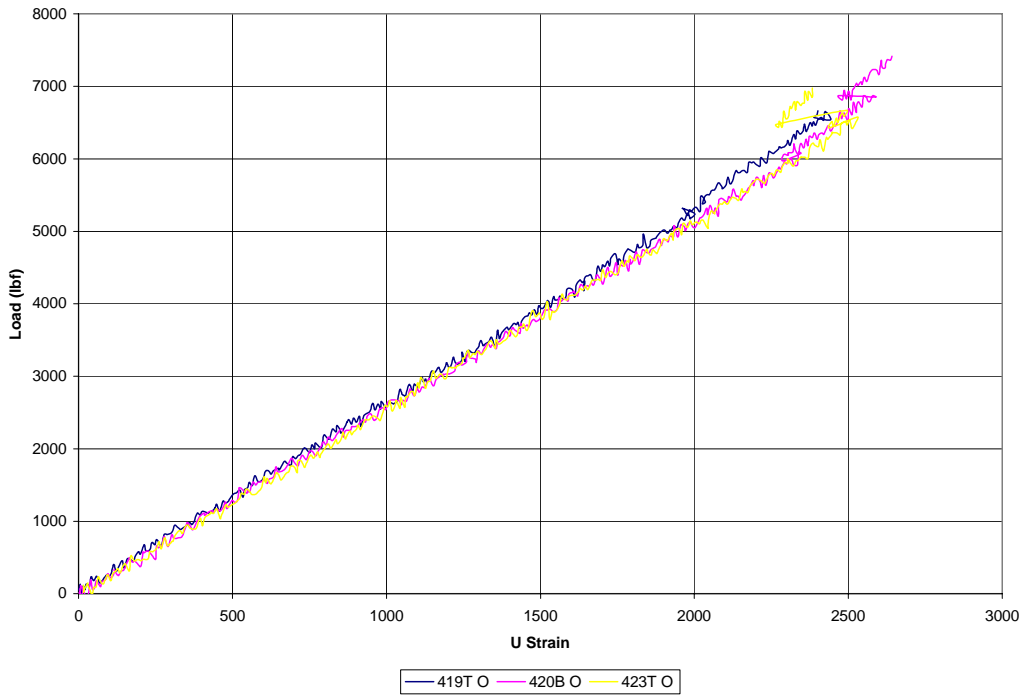


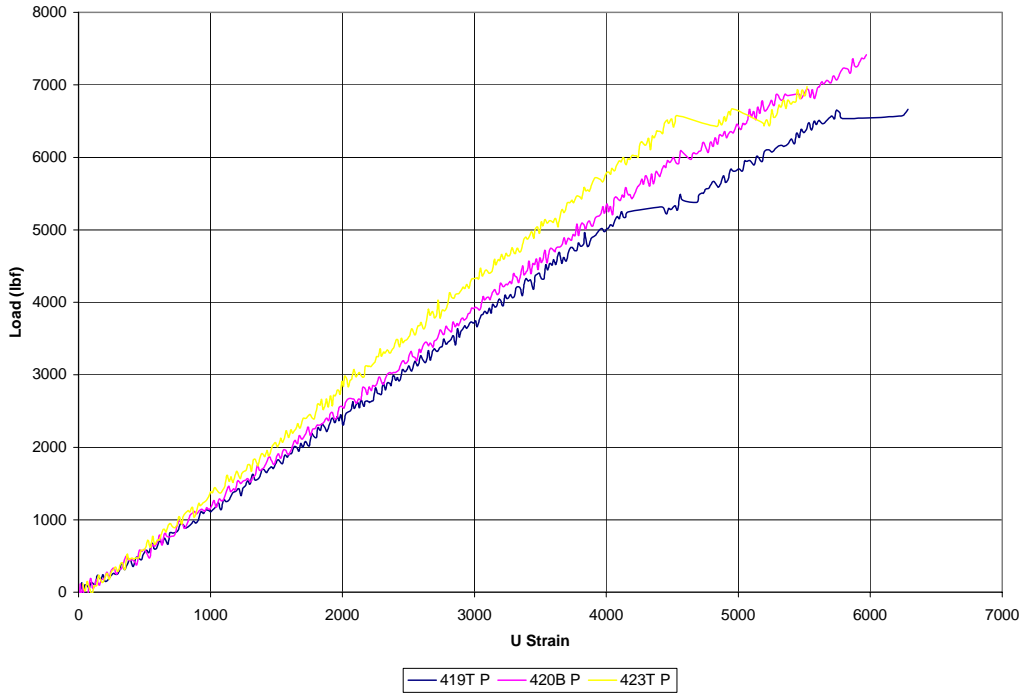**Figure 158. Comparison of all scarfed panels stress versus micro strain on channel O**

148

**Figure 159. Comparison of all scarfed panels stress versus micro strain on channel P**



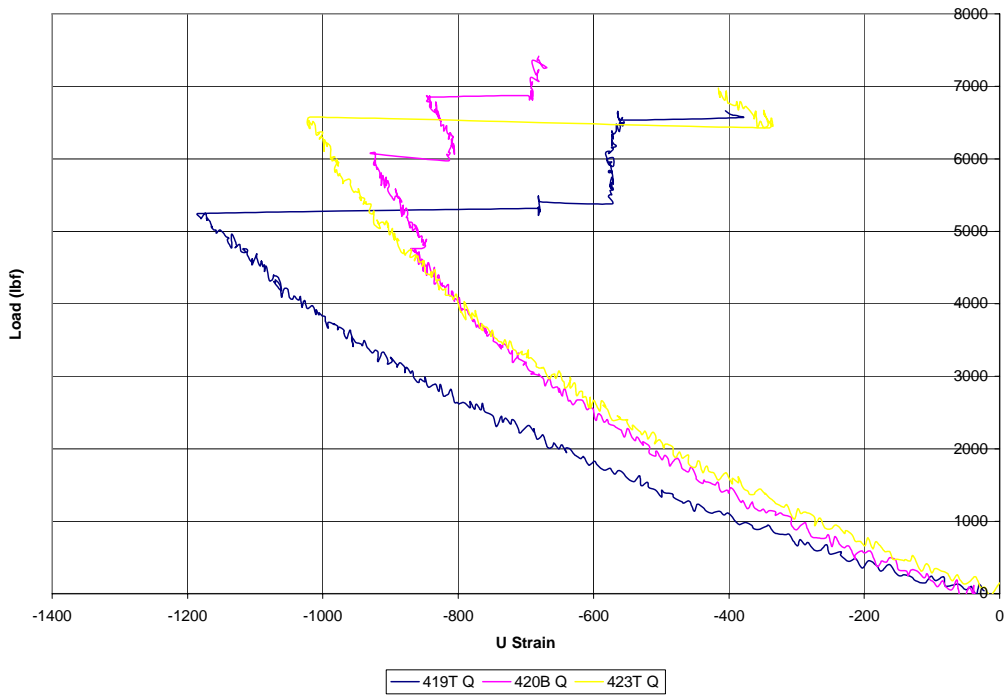**Figure 160. Comparison of all scarfed panels stress versus micro strain on channel Q**
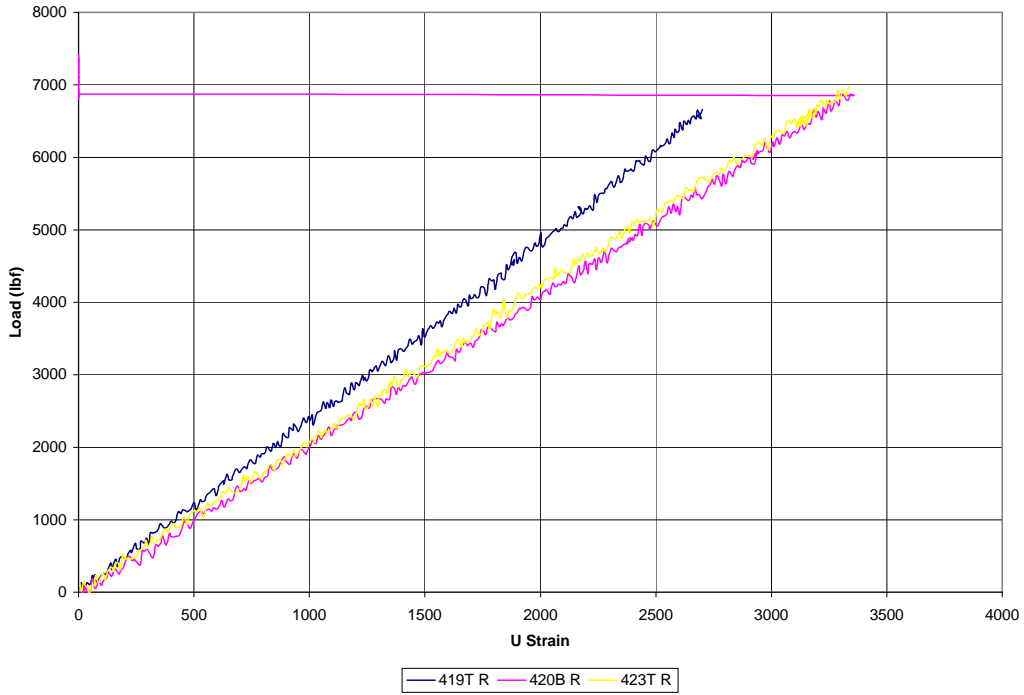
149

**Figure 161.  Comparison of all scarfed panels stress versus micro strain on channel R**
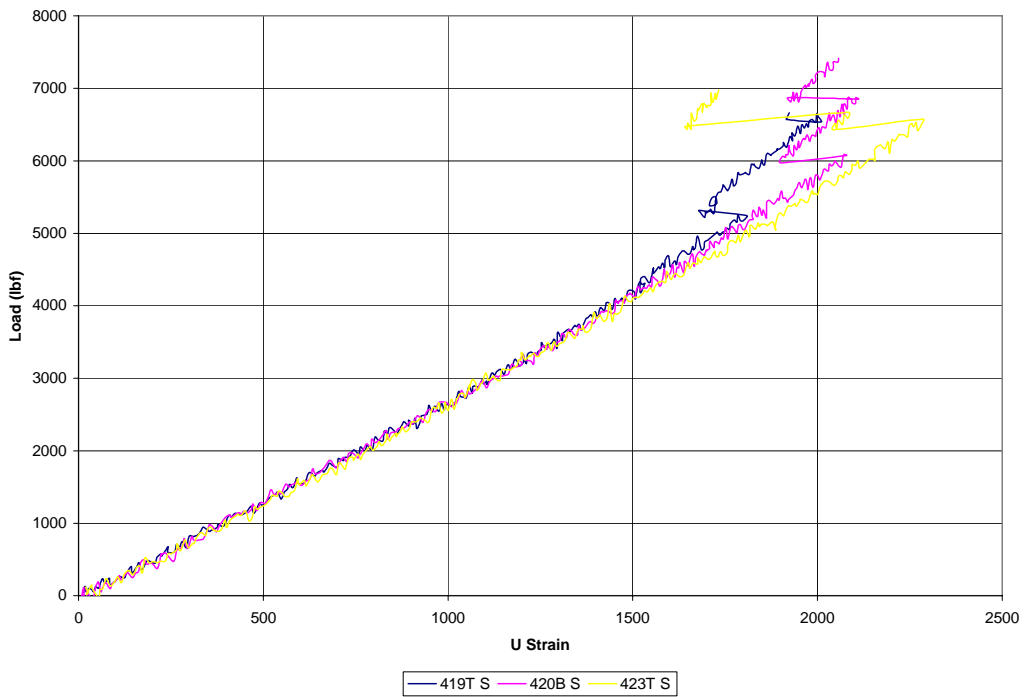


**Figure 162.  Comparison of all scarfed panels stress versus micro strain on channel S**
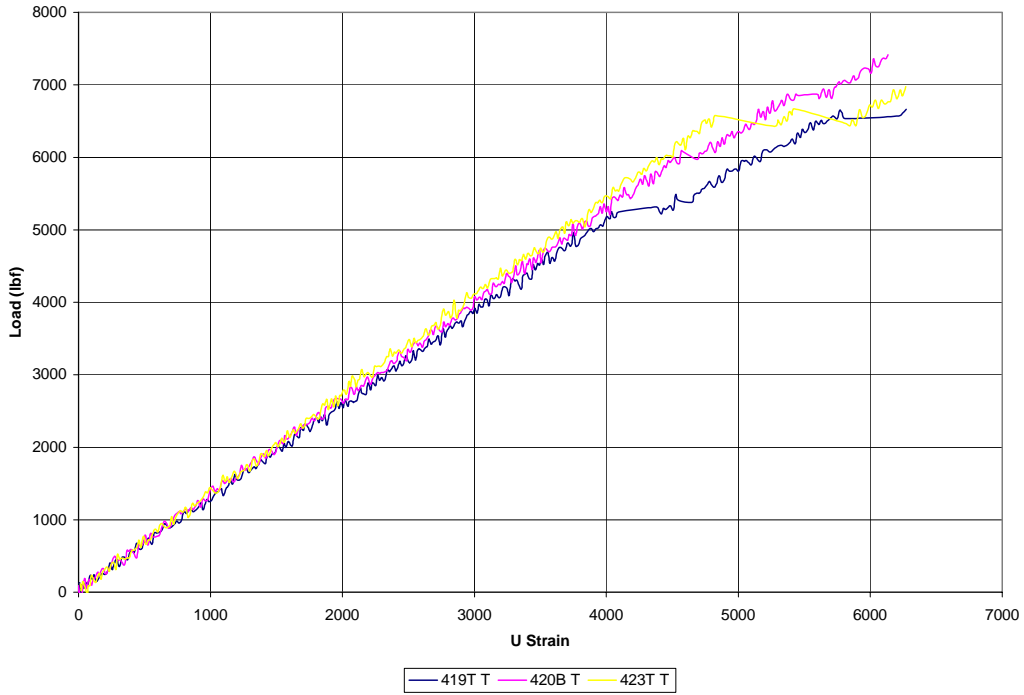
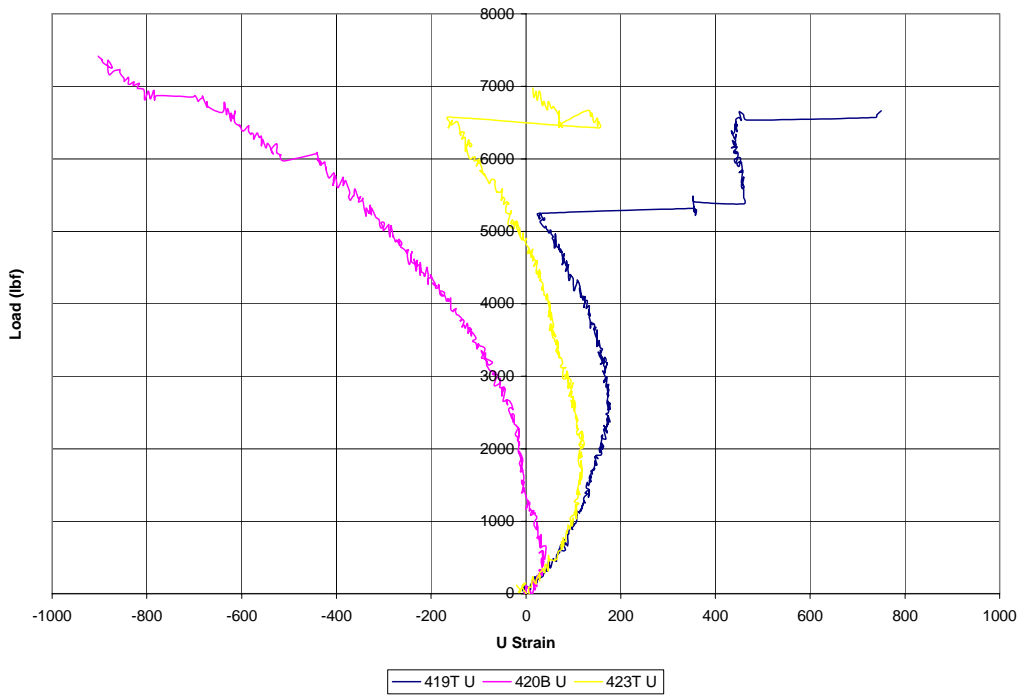**Figure 163. Comparison of all scarfed panels stress versus micro strain on channel T**



**Figure 164. Comparison of all scarfed panels stress versus micro strain on channel U**
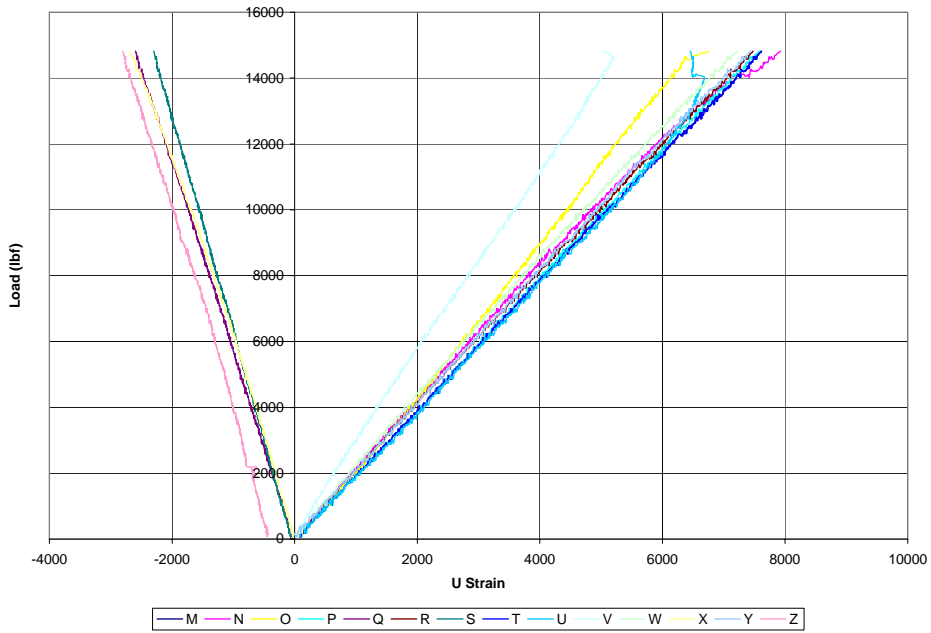
**Results from Repaired Panels**



**Figure 165. Panel 423B load versus micro strain from all strain gages**



**Figure 166. Panel 423B load versus micro strain from all strain gages in compression**

152

**Figure 167.  Panel 423B load versus micro strain from strain gages M, N, O, P, and R**



**Figure 168.  Panel 423B load versus micro strain from strain gages T, U, V, W, and Y**

**Figure 169.  Panel 418T load versus micro strain from all strain gages**
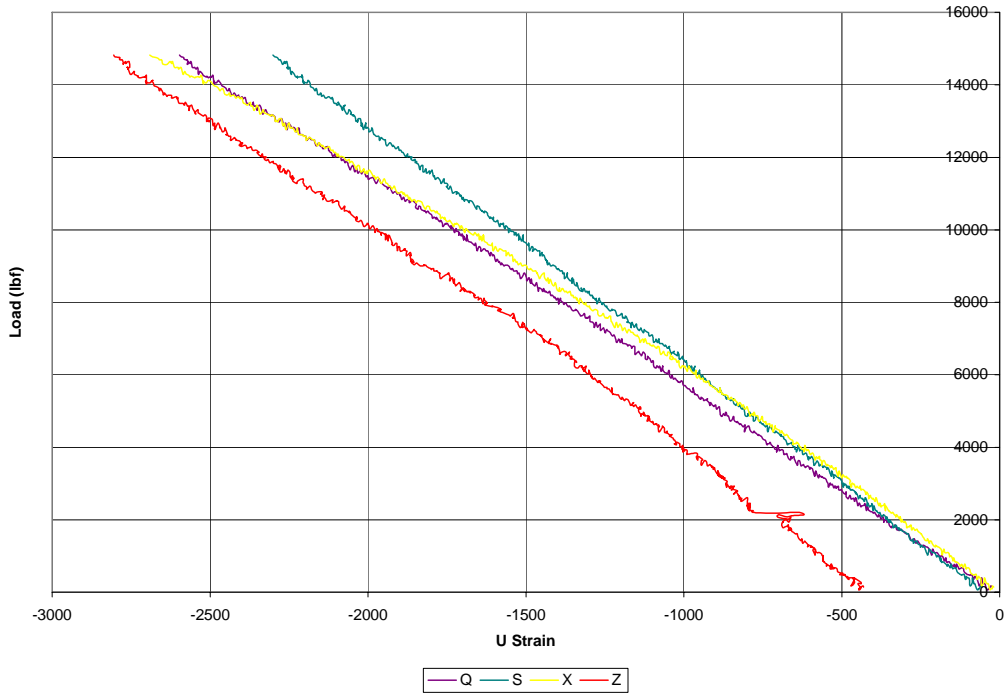


**Figure 170.  Panel 418T load versus micro strain from all strain gages in compression**

**Figure 171.  Panel 418T load versus micro strain from strain gages M, N, O, P, and R**



**Figure 172.  Panel 418T load versus micro strain from strain gages T, U, V, W, and Y**
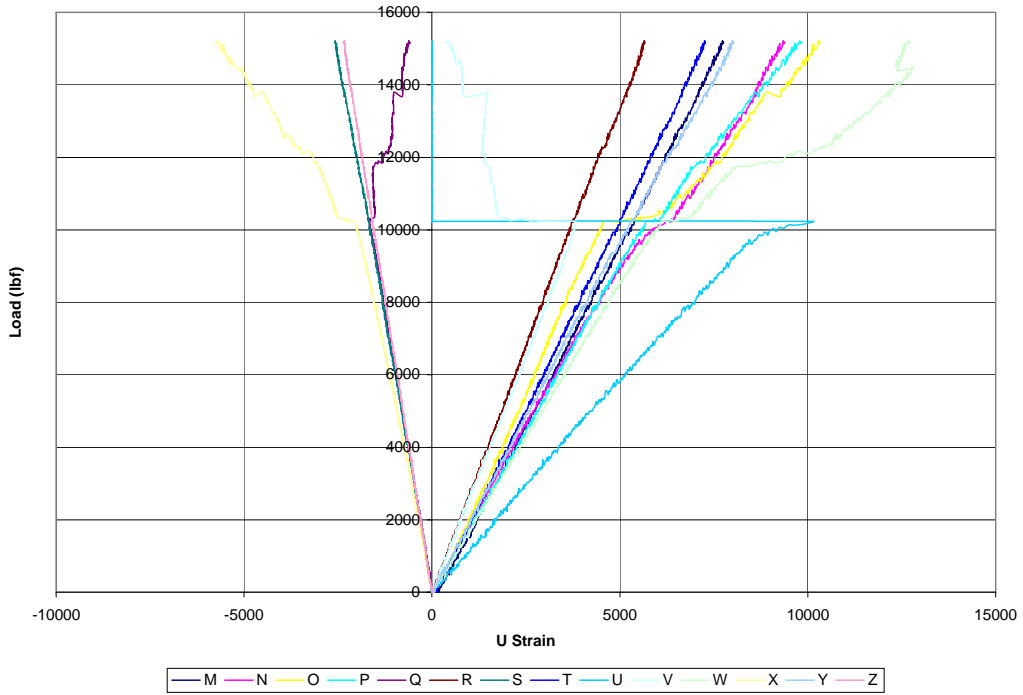
**Figure 173. Panel 419B load versus micro strain from all strain gages**
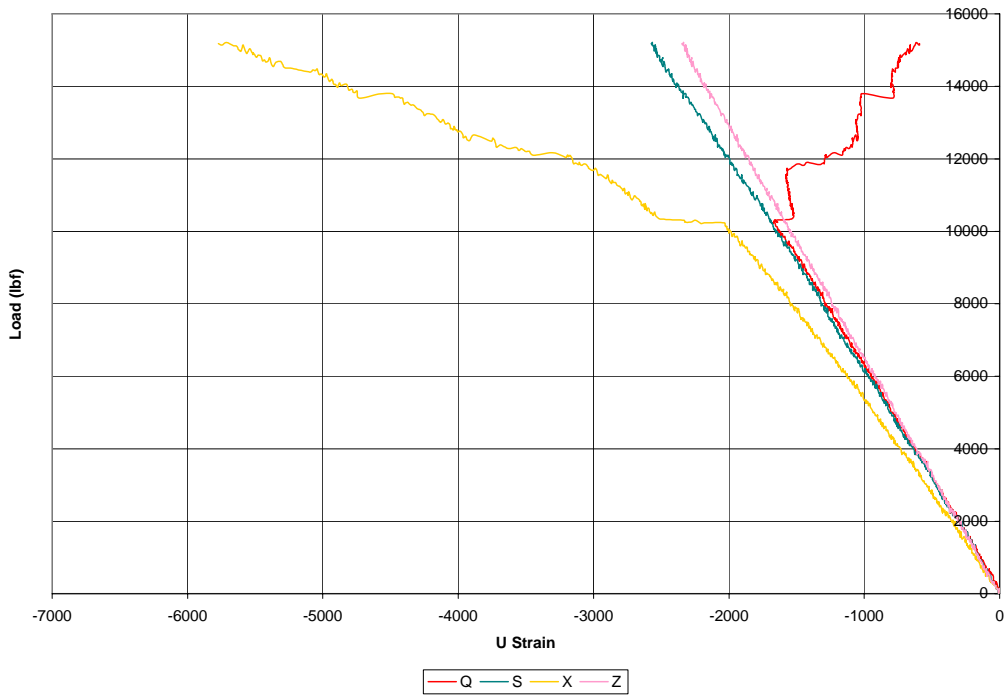


**Figure 174. Panel 419B load versus micro strain from all strain gages in compression**
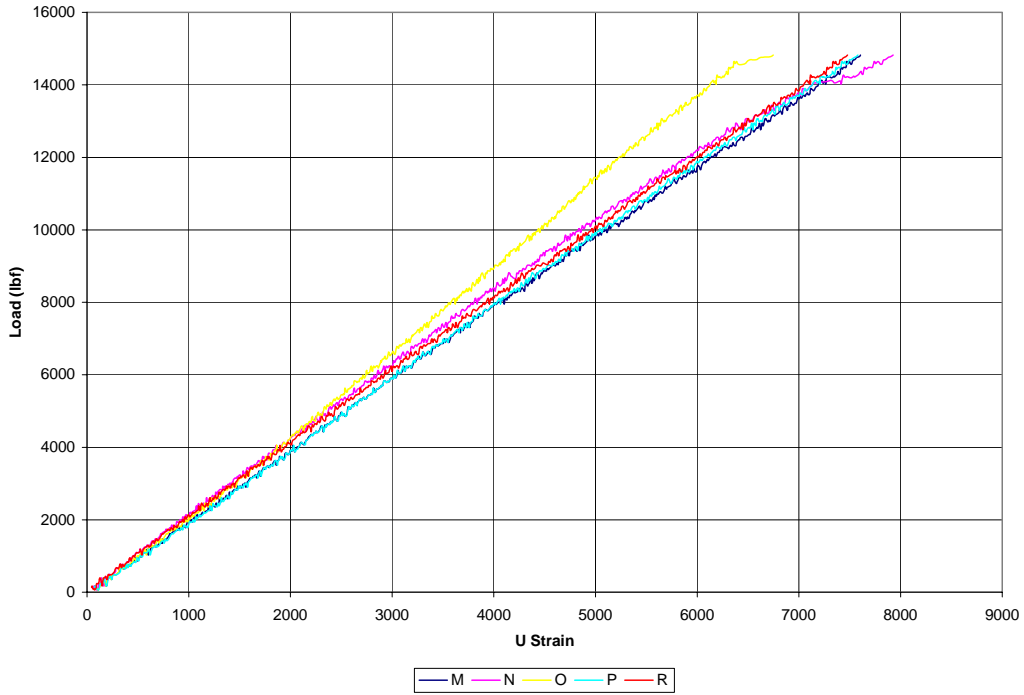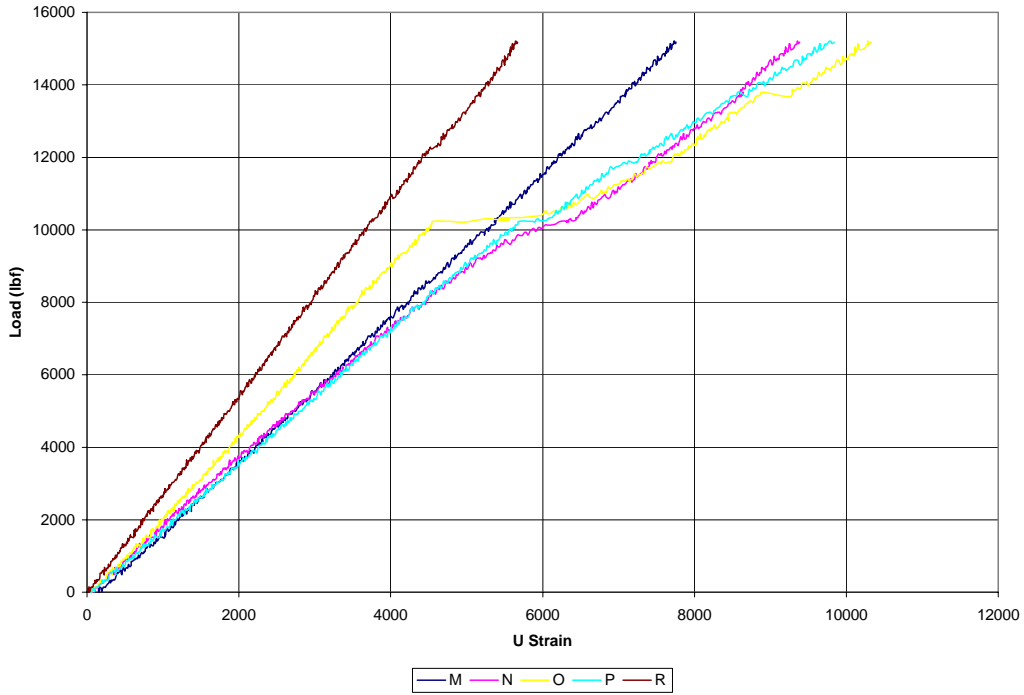
**Figure 175. Panel 419B load versus micro strain from strain gages M, N, O, P, and R**
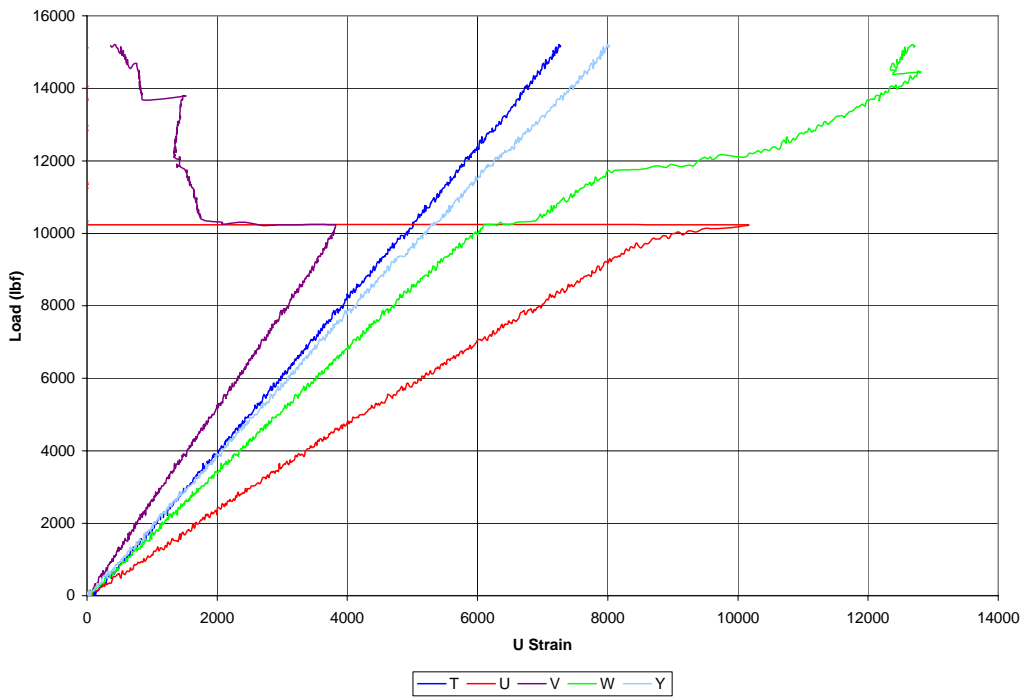


**Figure 176. Panel 419B load versus micro strain from strain gages T, U, V, W, and Y**
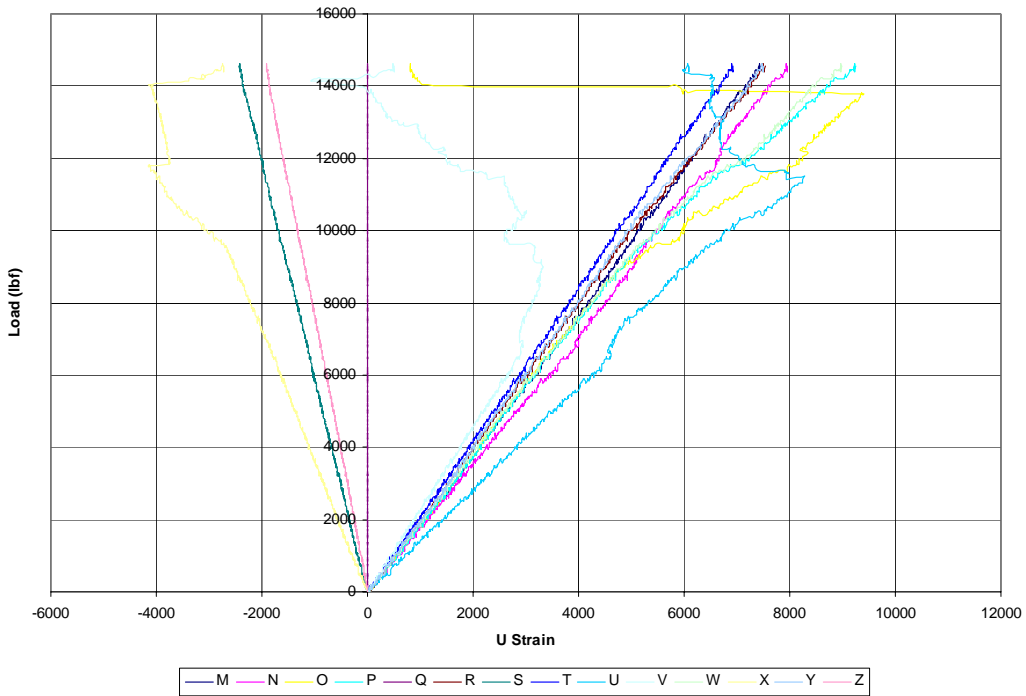
**Figure 177. Panel 422B load versus micro strain from all strain gages**
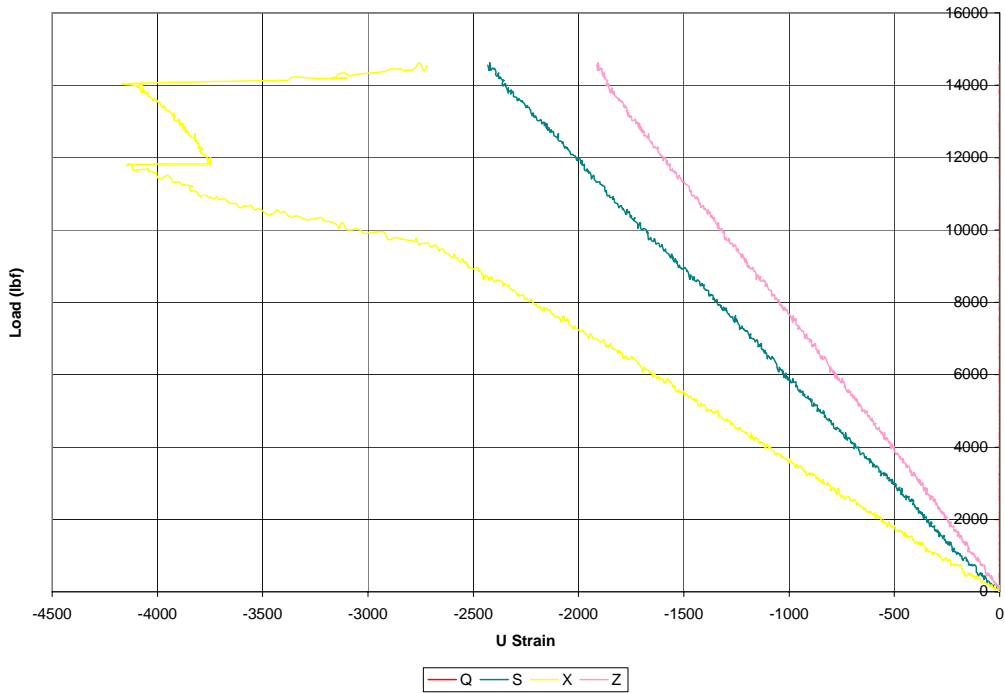


**Figure 178. Panel 422B load versus micro strain from all strain gages in compression**

158
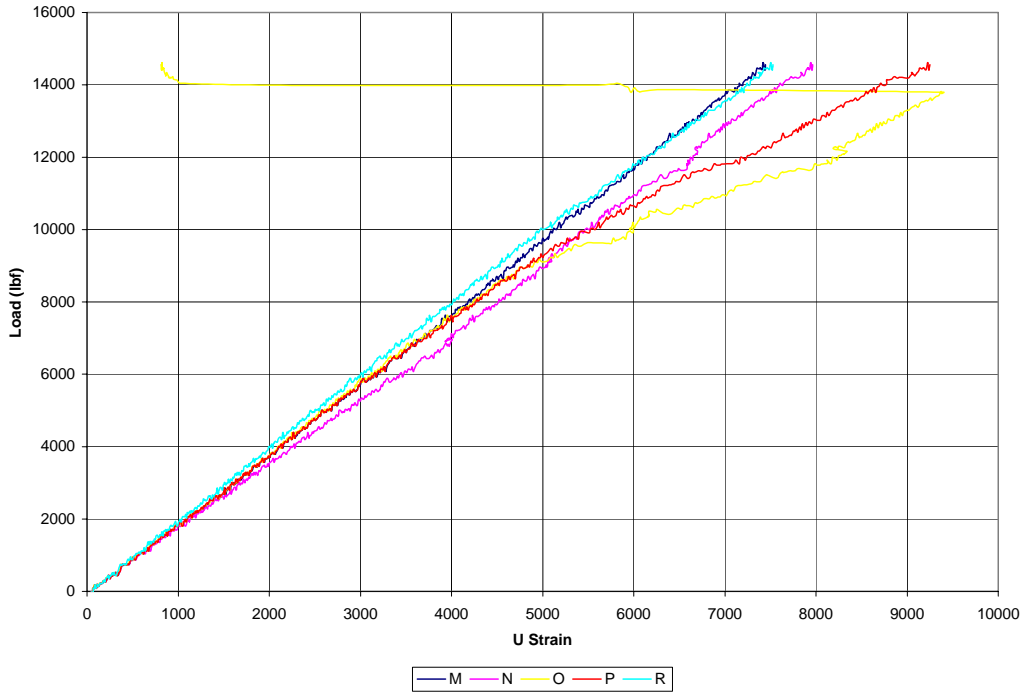
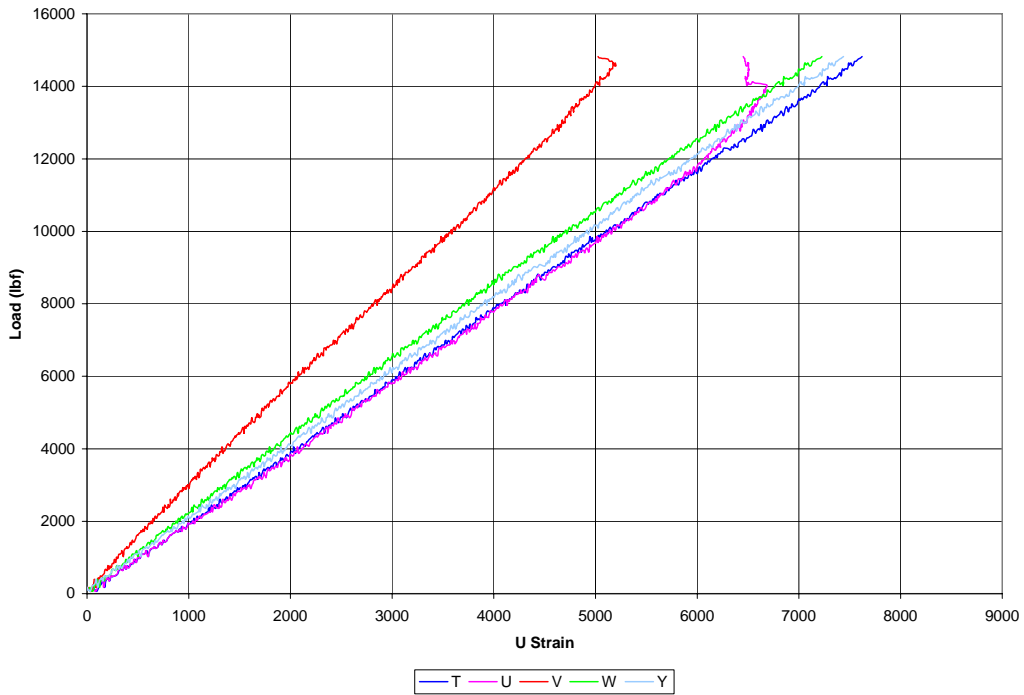**Figure 179. Panel 422B load versus micro strain from strain gages M, N, O, P, and R**



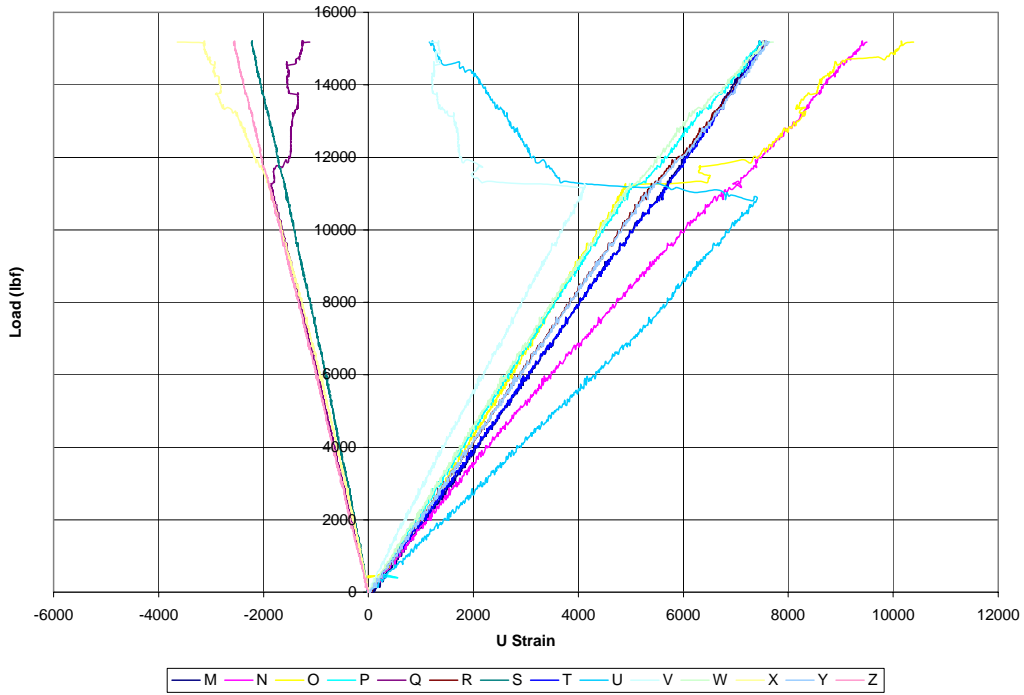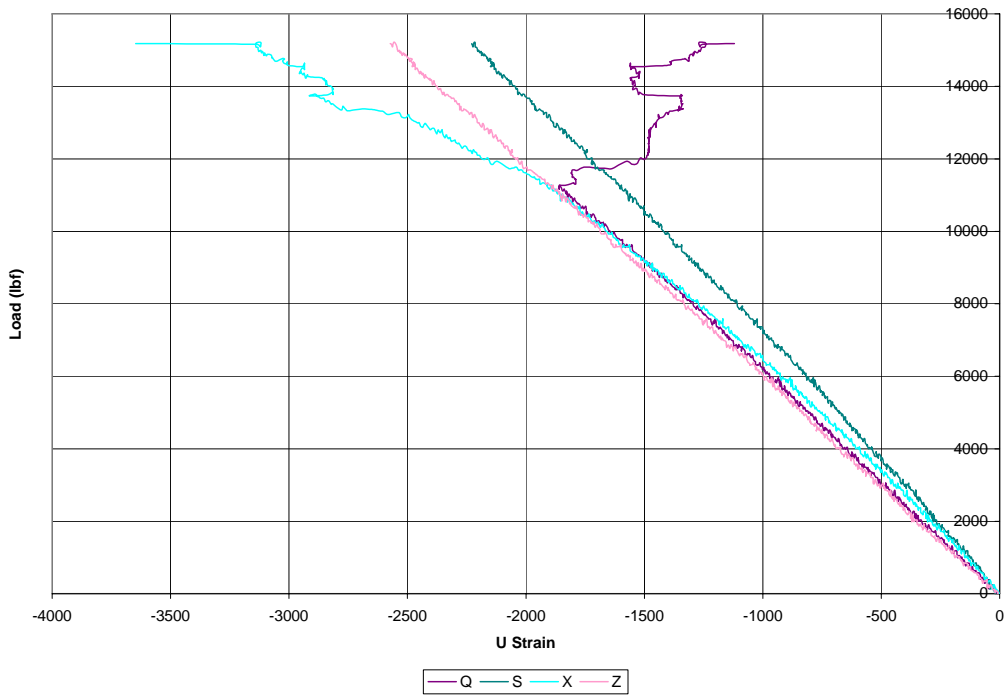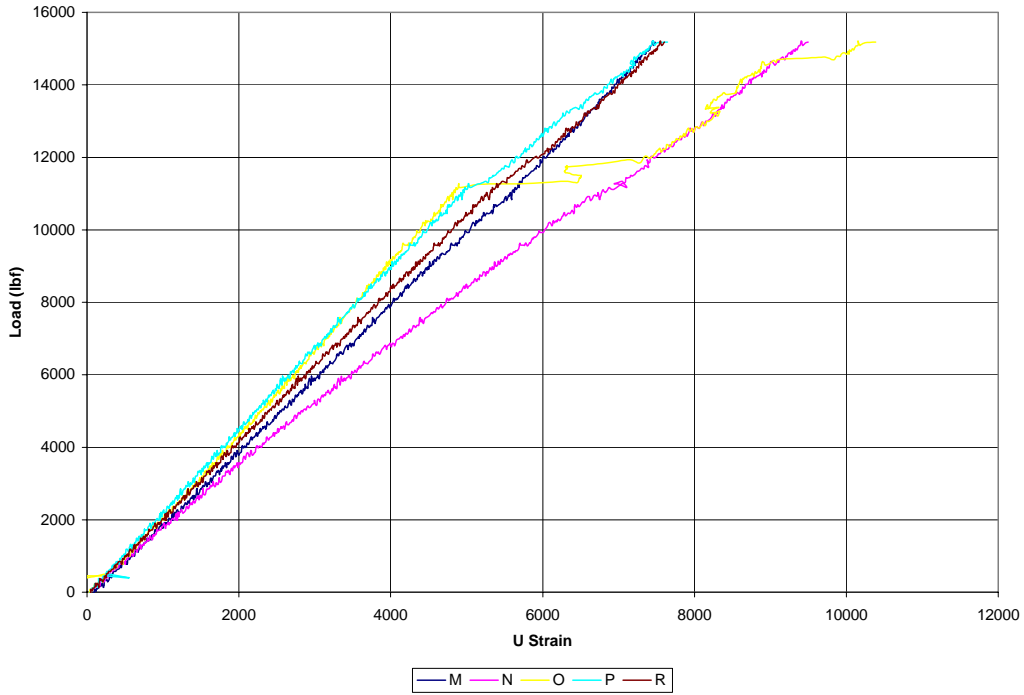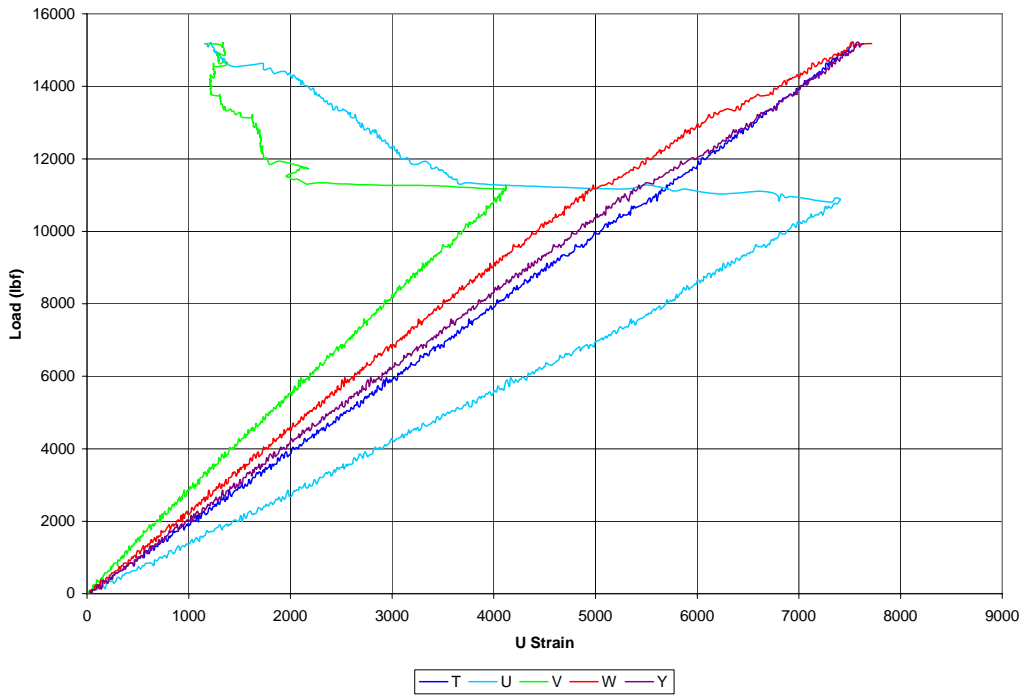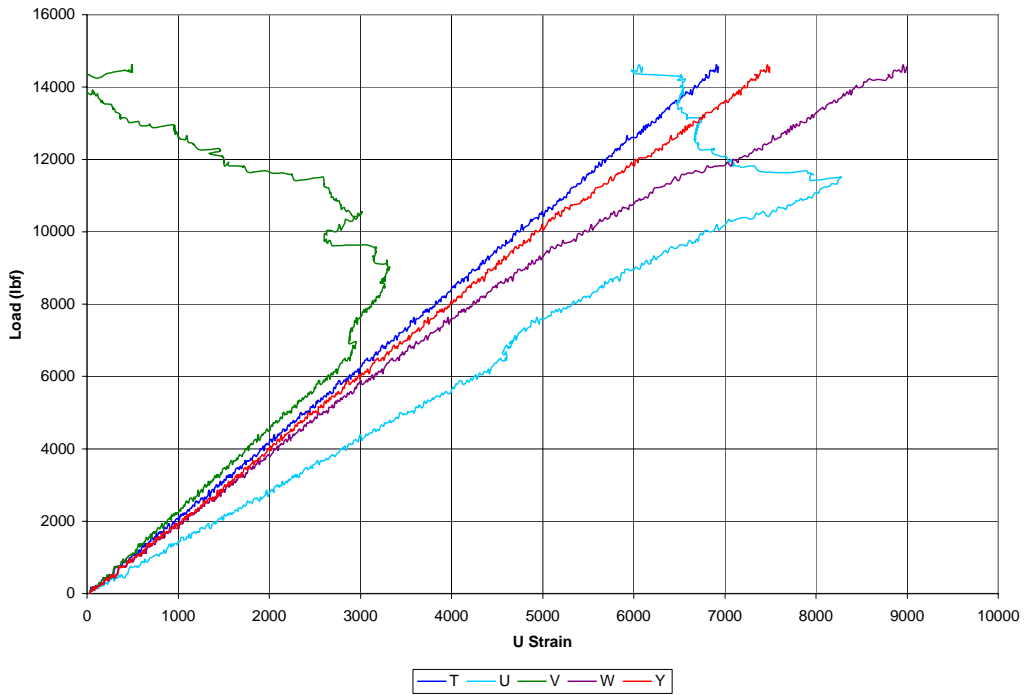**Figure 180. Panel 422B load versus micro strain from strain gages T, U, V, W, and Y**
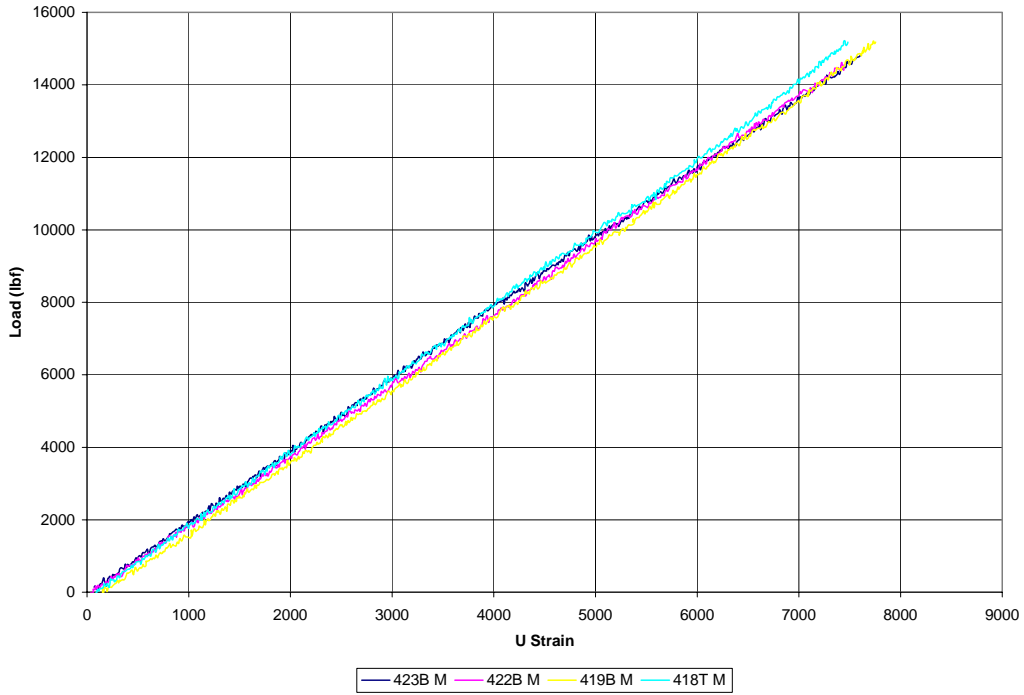
**Figure 181. Comparison of all repaired panels stress versus micro strain on channel M**
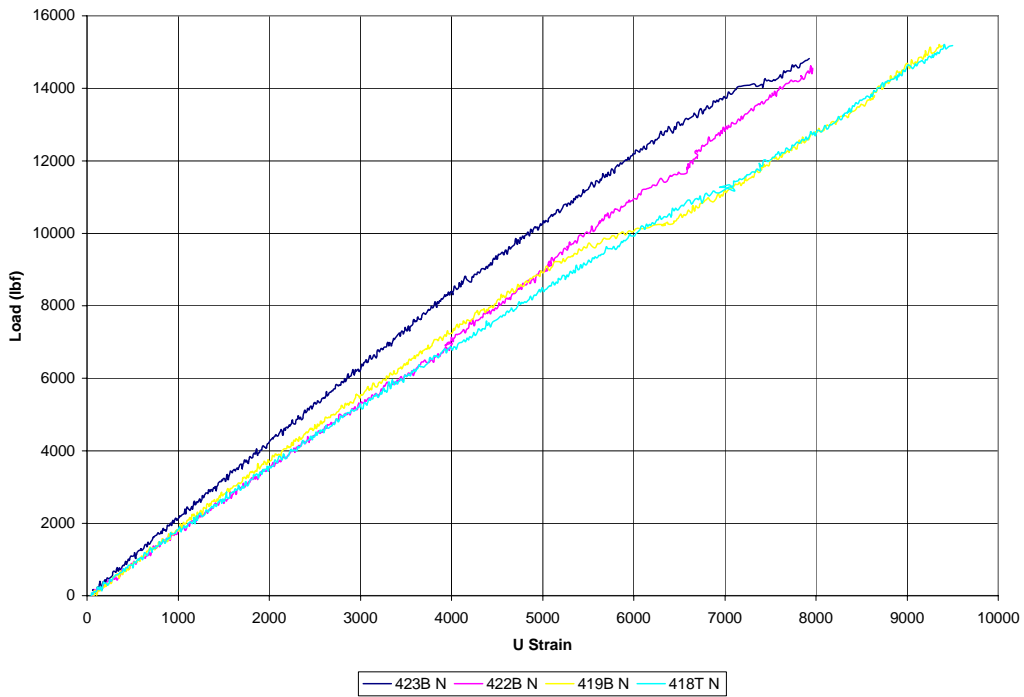


**Figure 182. Comparison of all repaired panels stress versus micro strain on channel N**

160
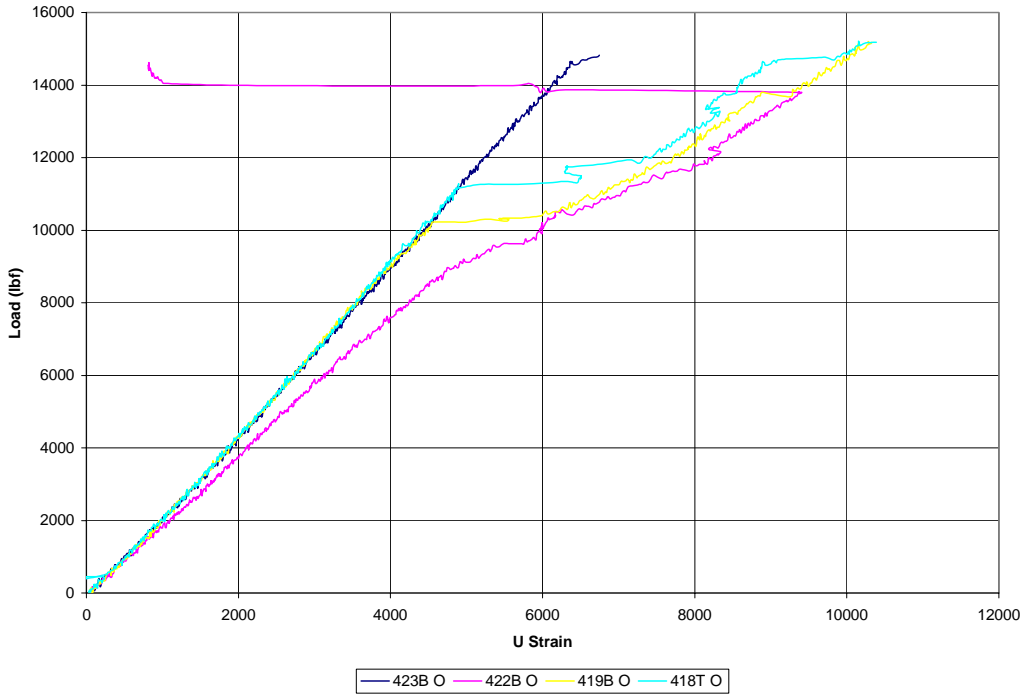
**Figure 183.  Comparison of all repaired panels stress versus micro strain on channel 0**
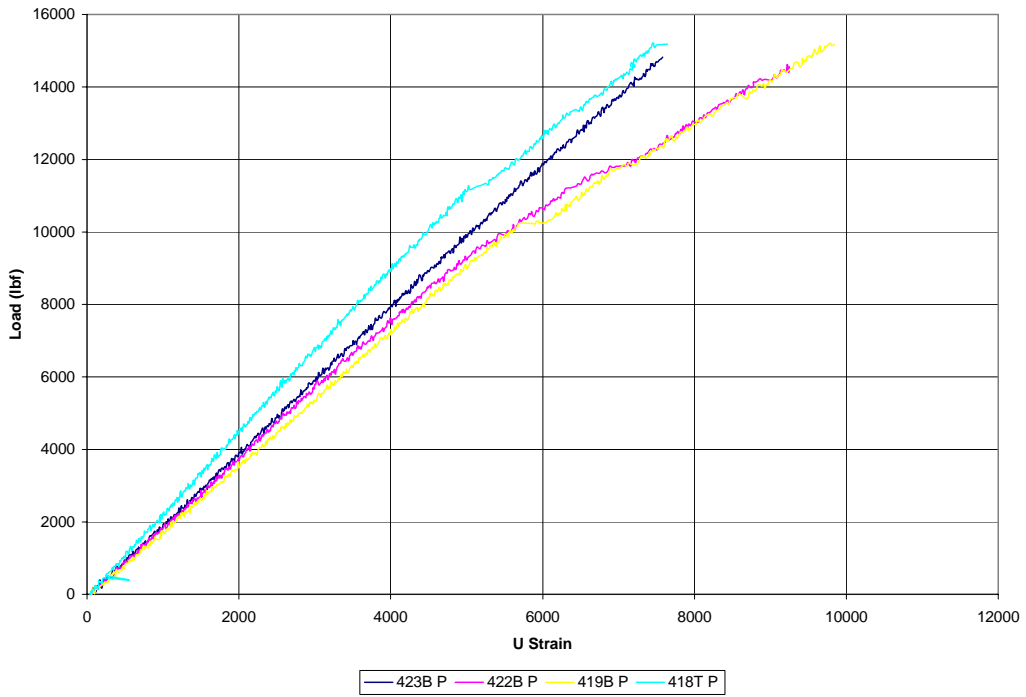


**Figure 184.  Comparison of all repaired panels stress versus micro strain on channel P**
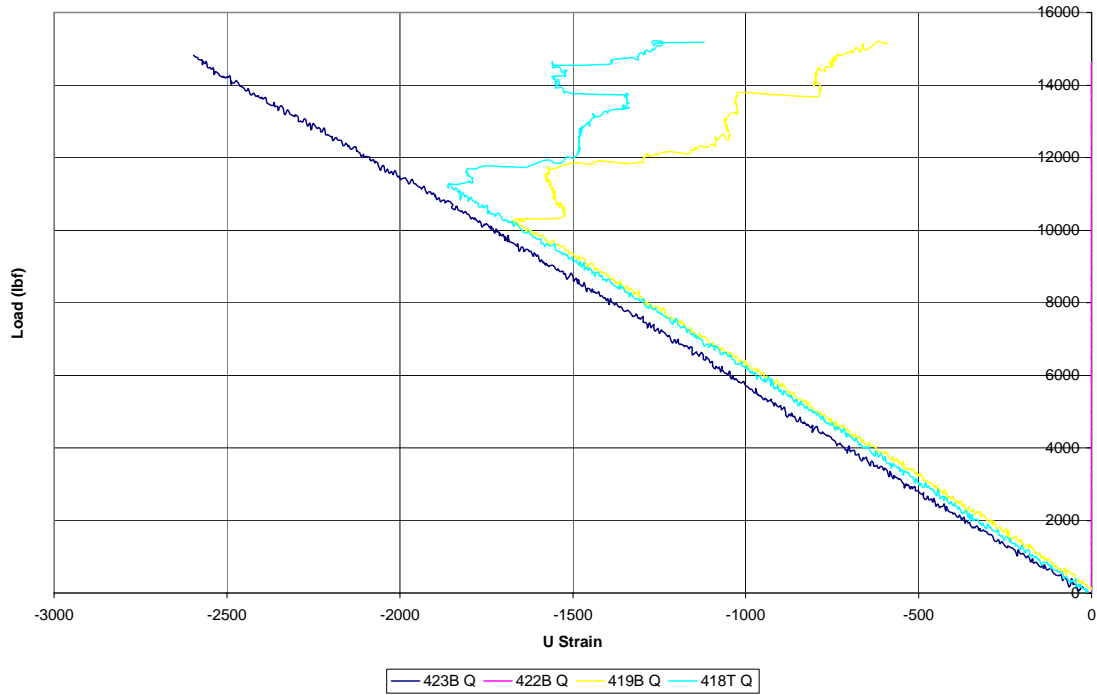
**Figure 185. Comparison of all repaired panels stress versus micro strain on channel Q**
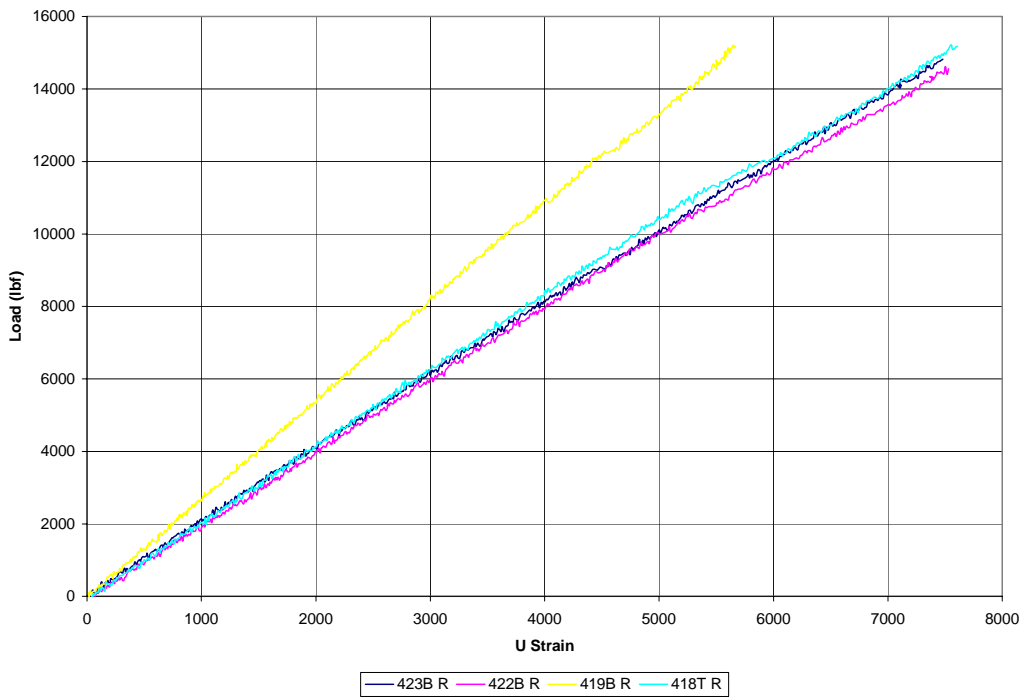


**Figure 186. Comparison of all repaired panels stress versus micro strain on channel R**
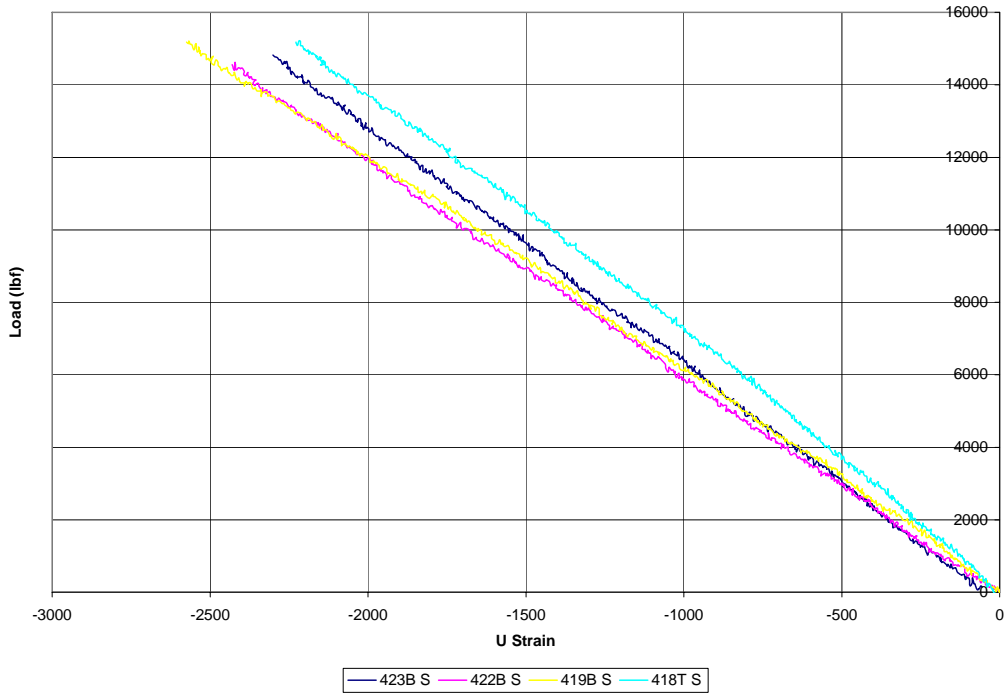
**Figure 187. Comparison of all repaired panels stress versus micro strain on channel S**
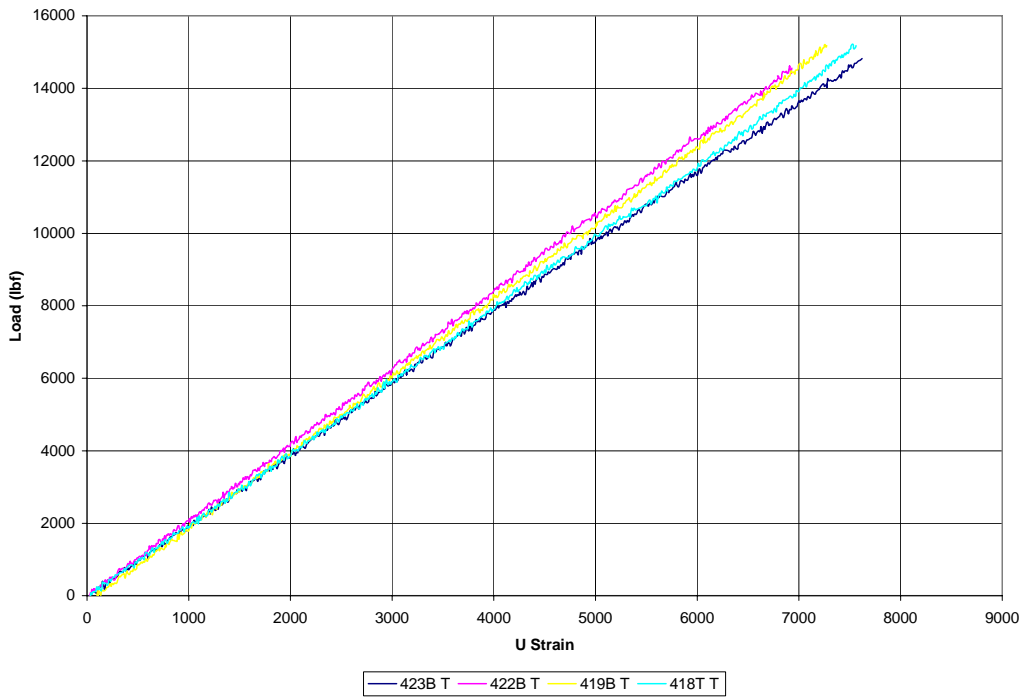


**Figure 188. Comparison of all repaired panels stress versus micro strain on channel T**

163
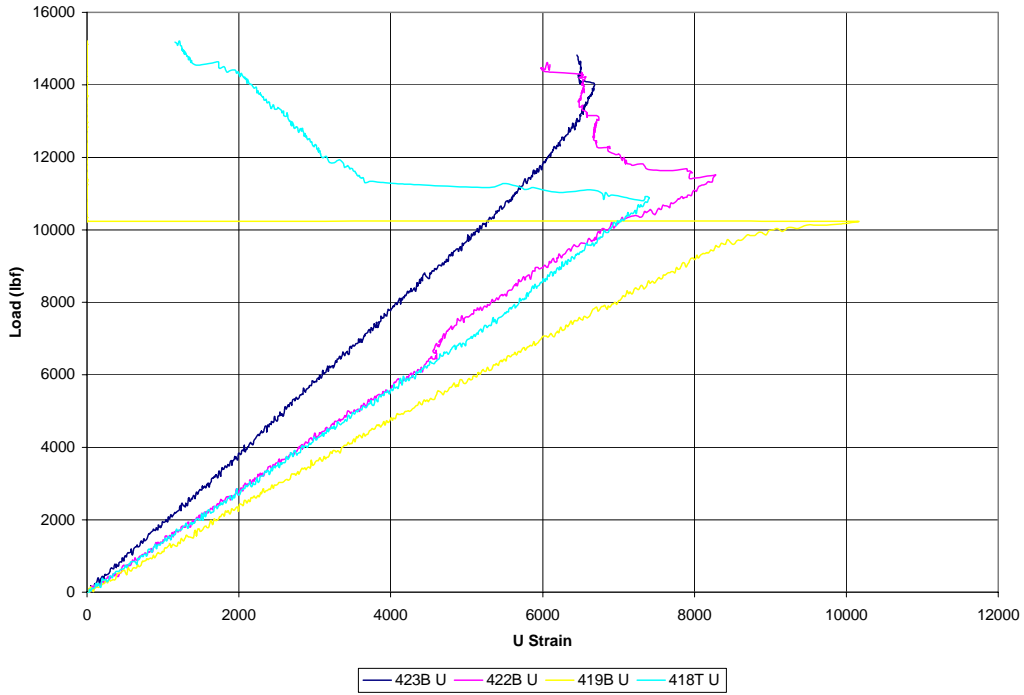
**Figure 189.  Comparison of all repaired panels stress versus micro strain on channel U**
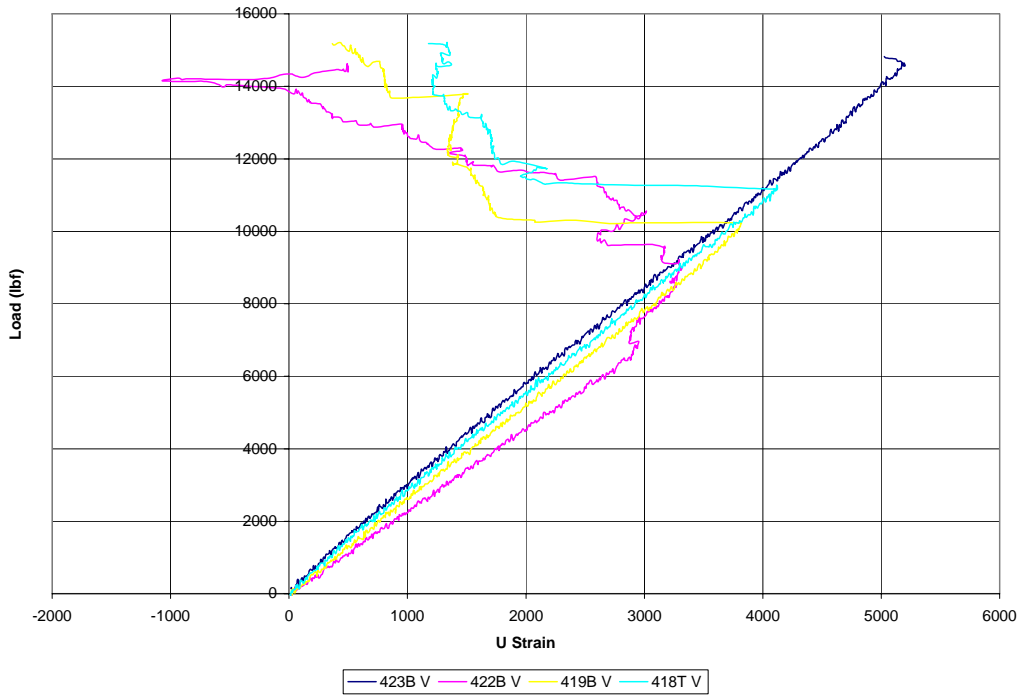


**Figure 190.  Comparison of all repaired panels stress versus micro strain on channel V**
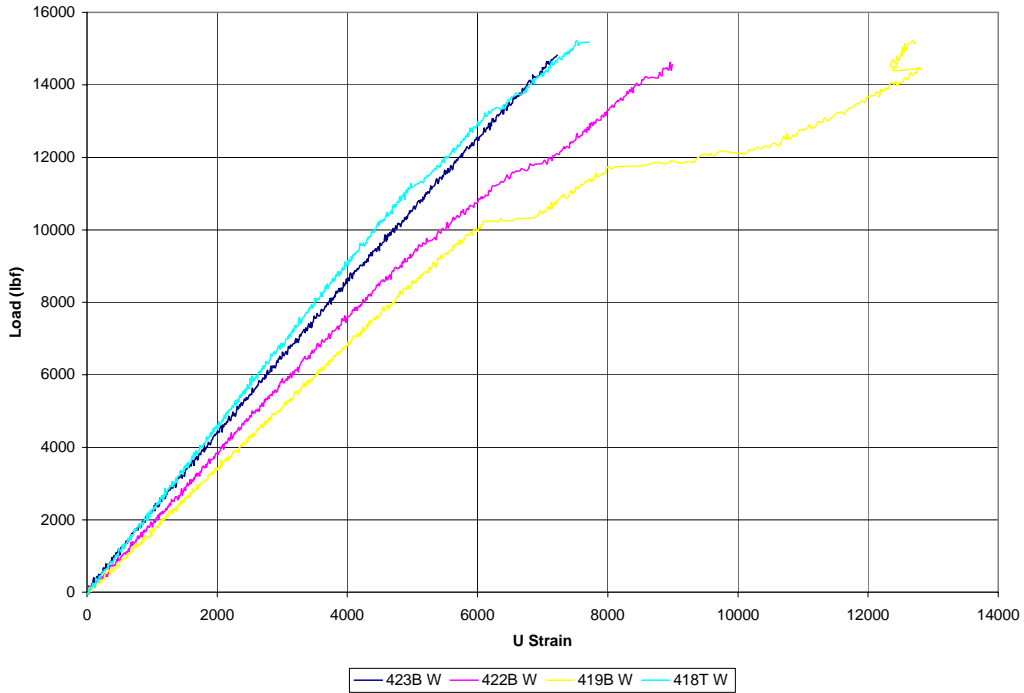
**Figure 191.  Comparison of all repaired panels stress versus micro strain on channel W**
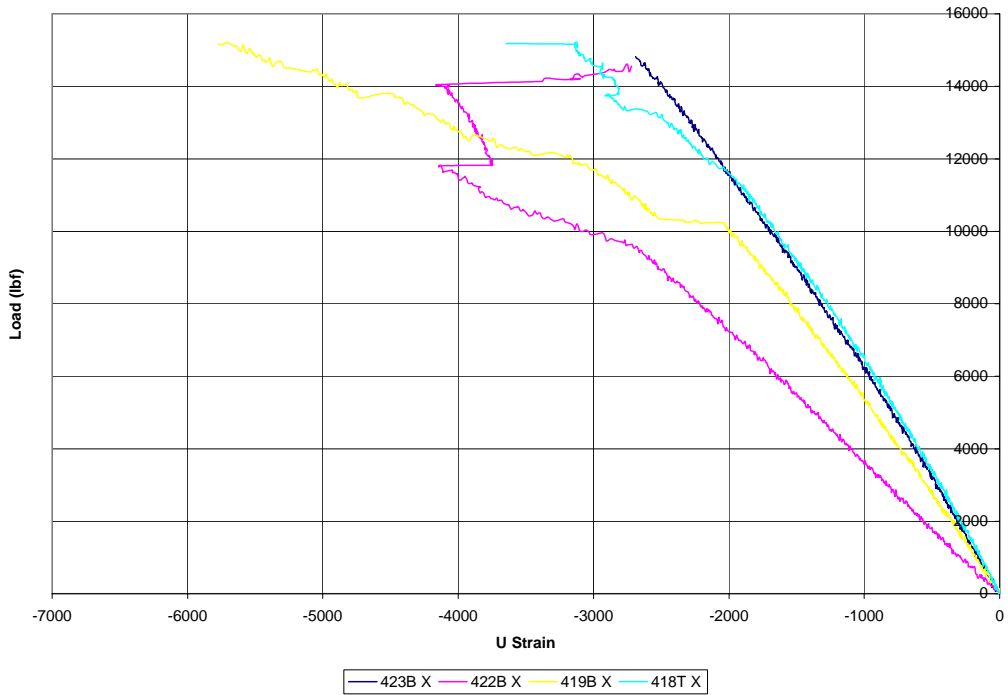


**Figure 192.  Comparison of all repaired panels stress versus micro strain on channel X**

165
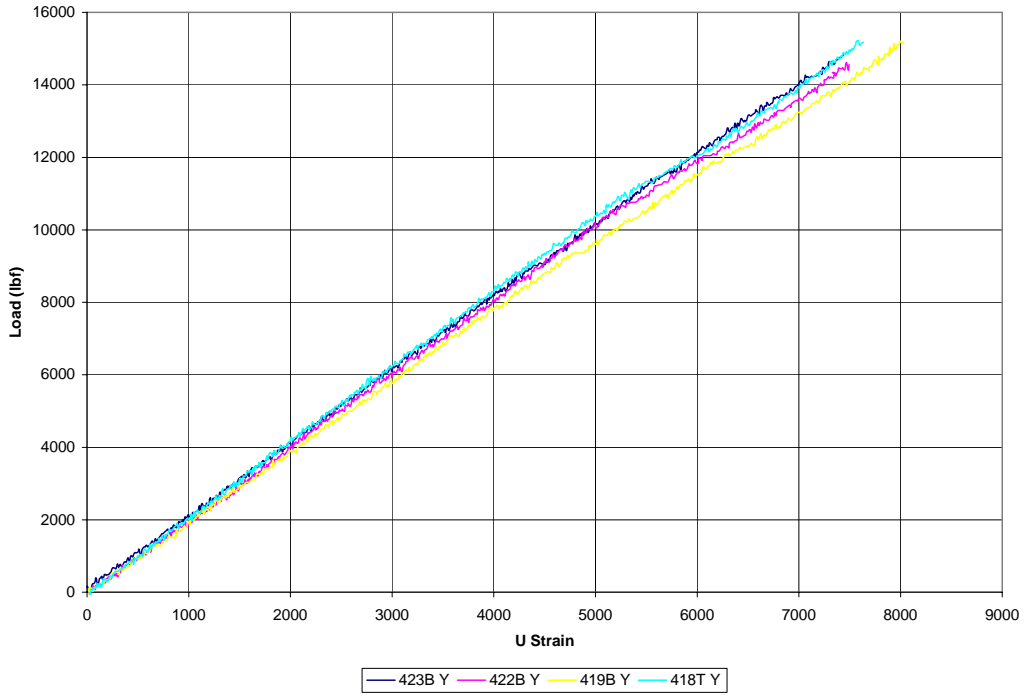
**Figure 193. Comparison of all repaired panels stress versus micro strain on channel Y**
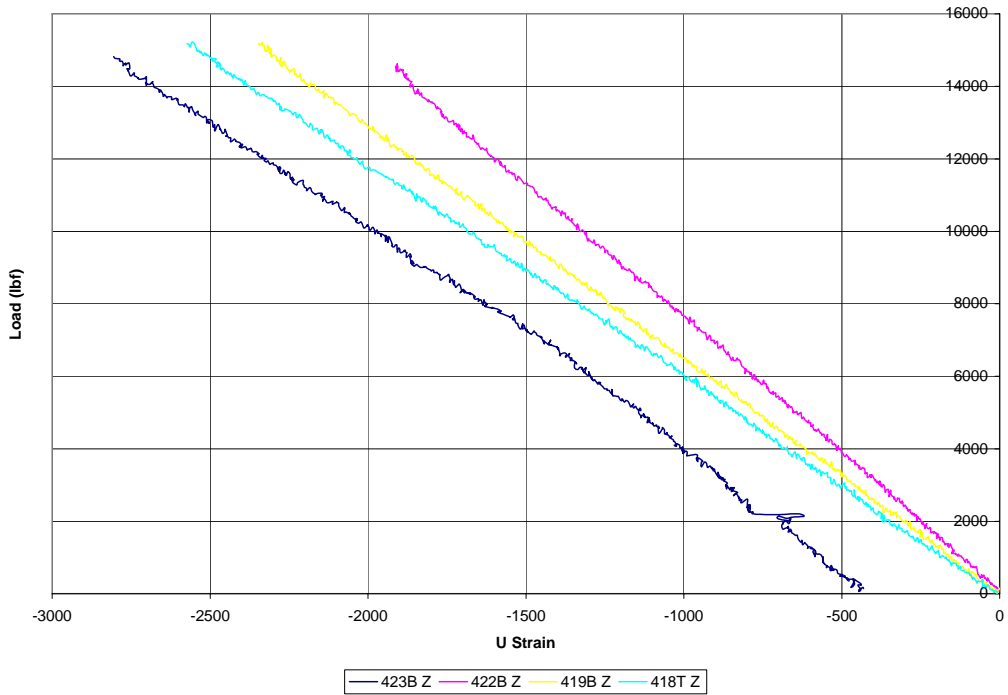


**Figure 194. Comparison of all repaired panels stress versus micro strain on channel Z**

166

**Comparison of Results from Virgin, Scarfed, and Repaired Panels**
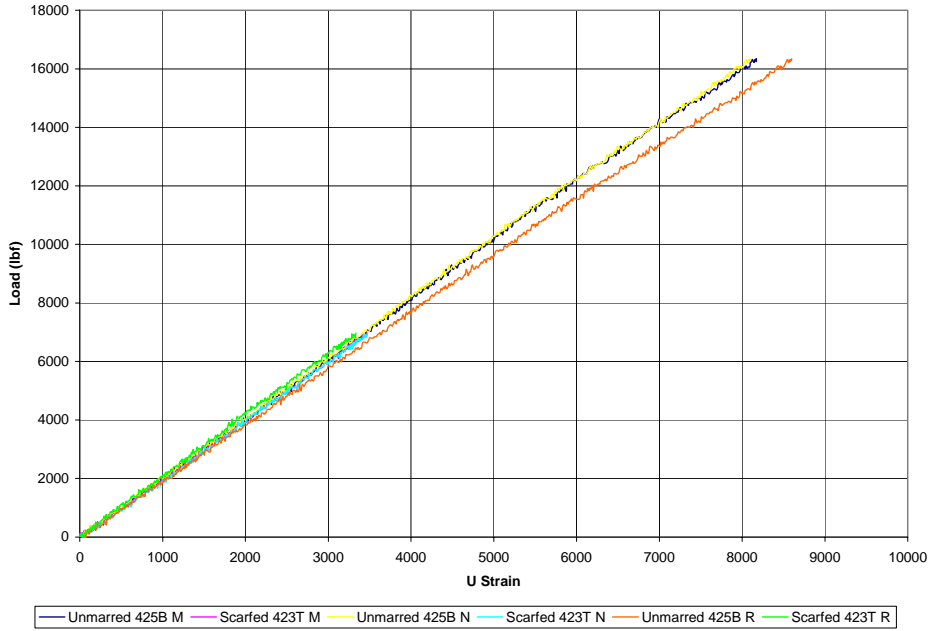


**Figure 195. Strain gages M, N, and R for typical virgin and typical scarfed panel**
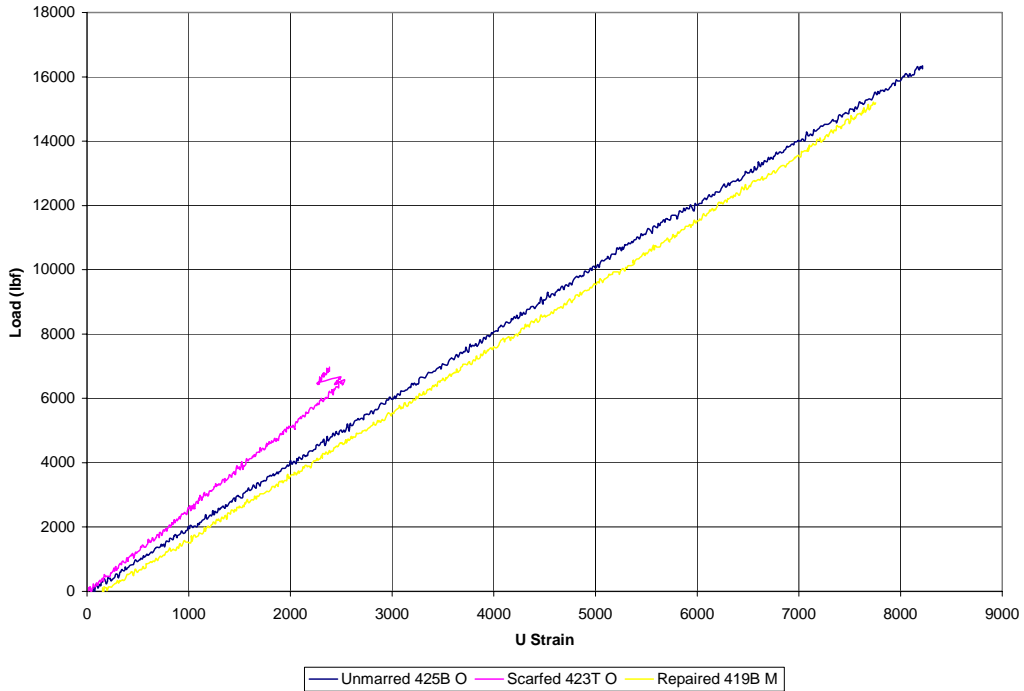


**Figure 196. Strain gage O for typical virgin and scarfed panel, and M for typical repaired panel**
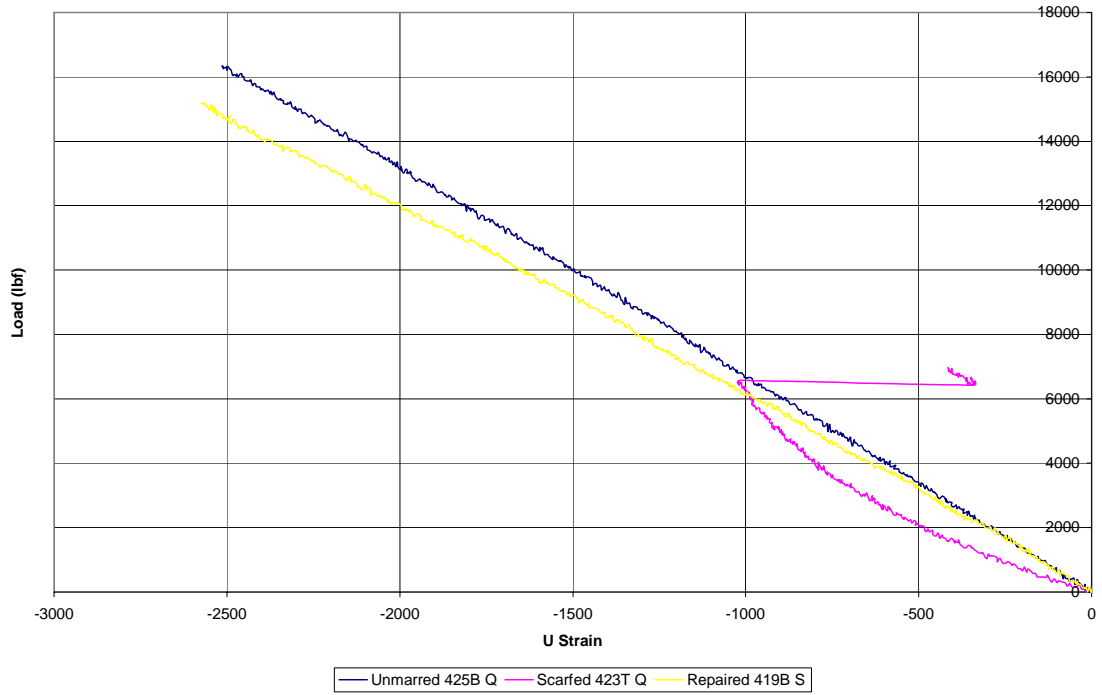
**Figure 197. Strain gage Q for typical virgin and scarfed panel, and S for typical repaired panel**
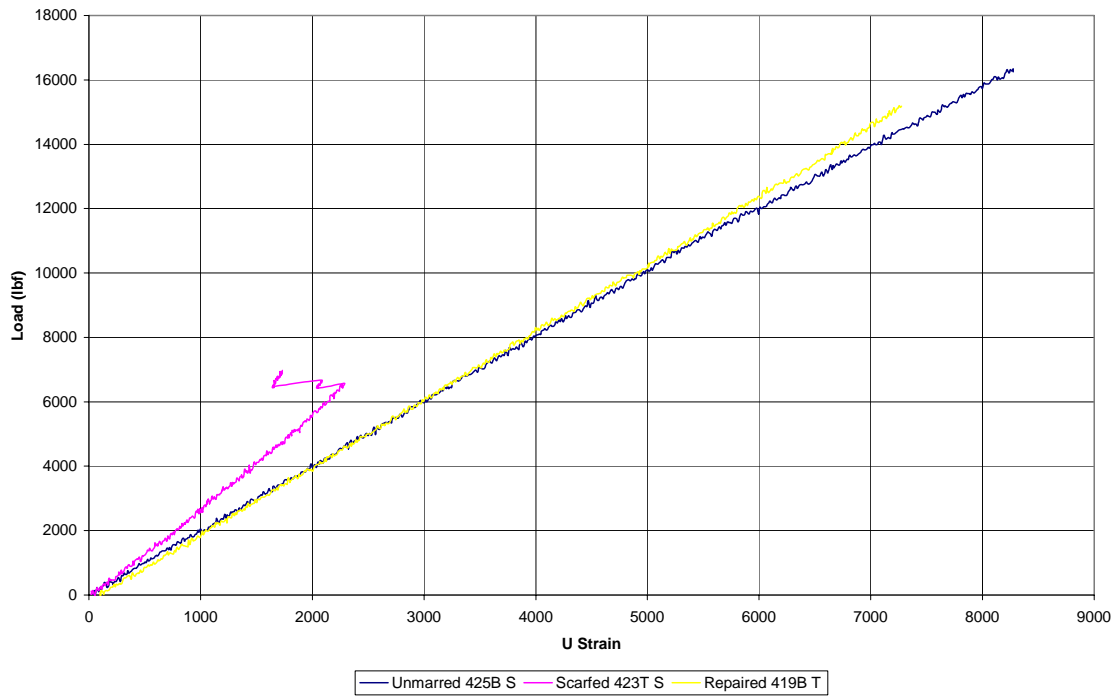


**Figure 198. Strain gage S for typical virgin and scarfed panel, and T for typical repaired panel**
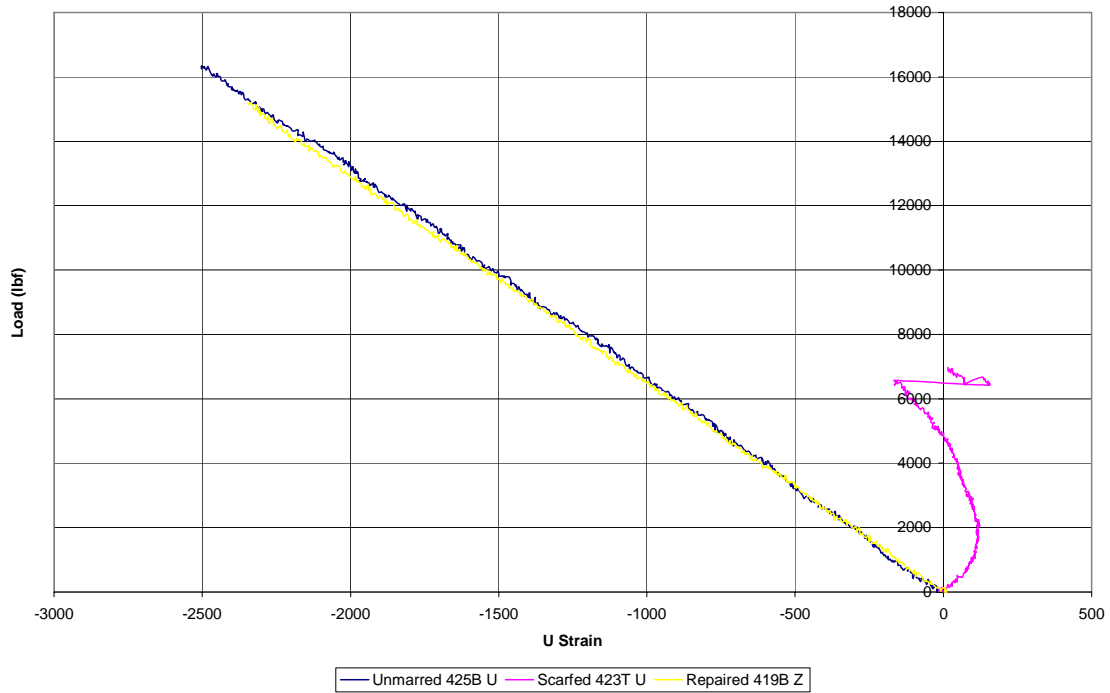
**Figure 199.  Strain gage U for typical virgin and scarfed panel, and Z for typical repaired panel**
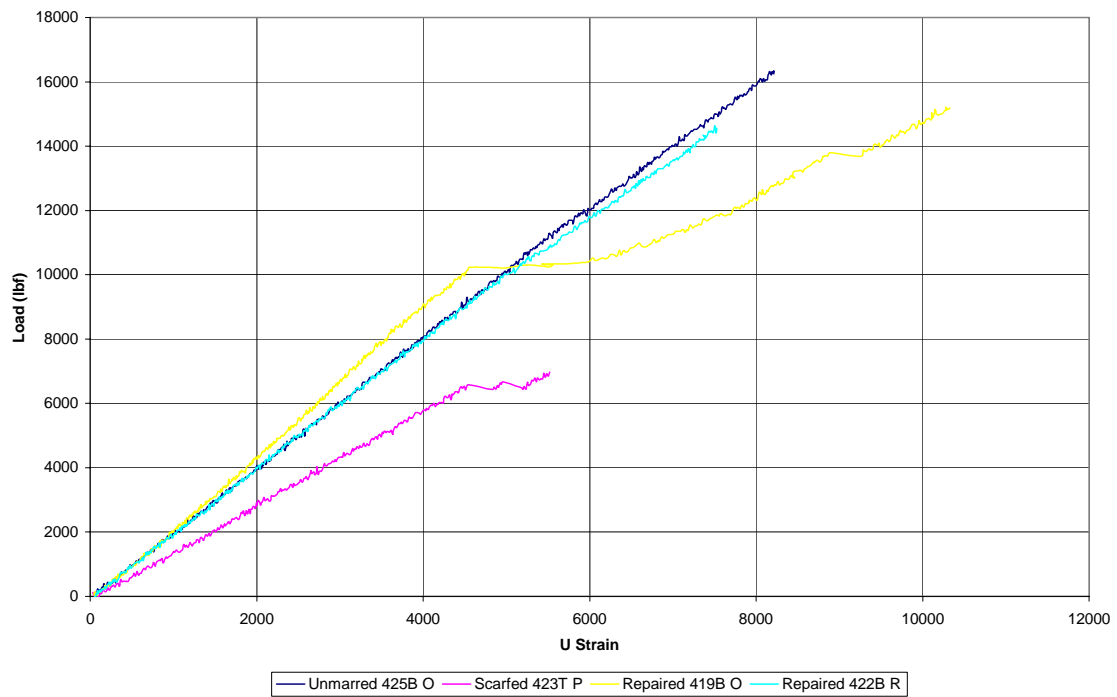


**Figure 200.  Select front strain gages on a typical virgin, scarfed, and repaired panel**

169
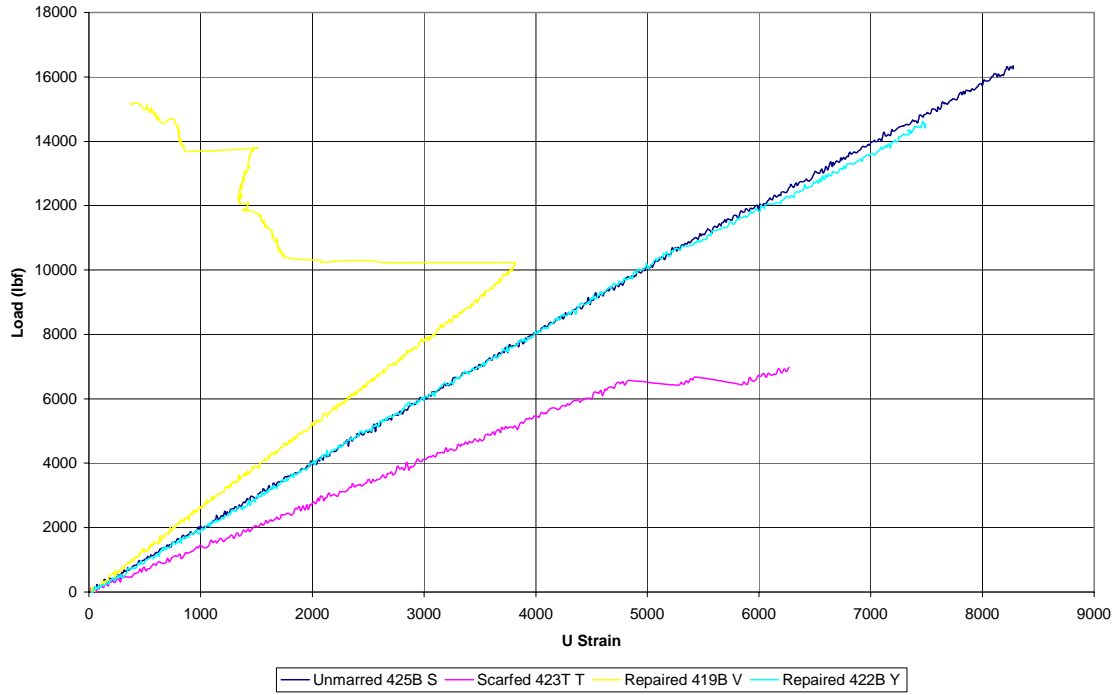
**Figure 201.  Select back strain gages on a typical virgin, scarfed, and repaired panel**

**Appendix D:  Data Processing and Image Analysis Guideline for Moiré**

**Interferometry**

**Introduction**

The following guide (Colleary, 2003) documents the Moiré data processing steps using the Transform program, a subprogram in Research Systems Noesys 2.0 that is not currently sold or supported by the parent company.  Modifications for minor formatting and error correction have been approved by Greg Schoeppner, the document owner. Most of the original formatting has been left to maintain readability.

The data collected by the camera has to be preprocessed, which includes unfolding the data thereby removing the $2\pi$ ambiguity in the dataset.  The data is then imported into the Transform program and converted from fringe pattern values to displacements values.  The displacement fields for the null state data and the affected state data are aligned and then subtracted from each other.  The resulting data is the displacements caused by the change from the null to the test state.  A zero mask is created by adding all the zero data locations together for both the x and z directional displacement data and then eliminating the smaller of the zero data locations caused by flaws in the diffraction grating and testing from the mask.  All of the zero data in the displacement fields is filled in by interpolating the values from the data.  The zero mask is then multiplied by the fields, thereby maintaining the larger zero value locations, such as at the top and bottom edges of the specimen.  The displacements can be smoothed at this point, but were not smoothed for this thesis.  The data was then scaled to the

specimen size, in SI units, and the origin is set. Strains are then calculated by taking the derivatives of the data. A final comparison of the data is done against the model as a verification that no mistakes were made and to determine how many times the strains should be smoothed.

**Assumptions**

1. Data collected has been unfolded (with any unfolding errors corrected) and unfolded files have the suffix ".unf".
2. Rotation of the specimen during the test is not a factor, and no "photo-stitching" is necessary.

**Beginning Notes**

1. See Step 8 before beginning, to decide what files to process.
2. See David Mollenhauer with any questions during processing.

**Step 1: Convert Unfolded Data into Displacement**

In your data directory, add a folder called "UNF Files". Copy all of the '.unf' files into this new folder.

Open the *Transform* program in Classic Mac mode.
    Click on the apple→System Prefs→Classic and check to see if running.
    Transform is under Mac HD→Apps→Work Apps→Transform PPC

Select Macros→b_UNF_to_DISP_Moiré
(For PC, select macros → b_UNF_to_DISP_Moiré_PC)

Select a '.unf' file

At the prompt "Set the filename" type   *_dsp where * is the unique identifier for that set of data (ie, Ua_dsp, Vc_dsp)

This generates a table and transform file of the name you supplied.

Generate an image (Command-G), choose Colortables→Rainbow Banded

For Mac, Hit Command-W twice to close the window, then the prompt to save the data will come up. Hit enter three times to save the data and clear all the messages.
For PC, save data and close all of the windows.

Go through the above procedure using the macro until all your .unf files have been converted.  Drag the original unf files into your "UNF Files" directory.  This acts as a backup point. Hold down the command key to select more than one file.

Make folder "Displacements".  Drag new dsp files into this directory.

Make folder "Fringe Data".  Drag all the rest of the files into this directory.

Duplicate the Displacement folder.  This is again a backup point.


**Step 2:  Image Synchronizing- Match Null and Test Fields**

Open the displacement files for a set of null and test fields.  (ie, Ua and Uaa)

Generate an image of the null field (command-G).

Image→Rectangle Size→Change zoom factors to 1:1

Select the test field (loaded data) and generate a contour plot by using Command-K.  For the PC, remove axes from the contour plot (go to the burgundy axes tool on the left side of the transform window and then use the on/off toggle at the upper left hand corner of the transform window).  Default settings for the contour plot should be acceptable.  Cut and paste the contour plot onto the null field image, and check the fit.  (To zoom in, adjust the zoom factor of the null field after you have overlaid the contour plot)  If fit is OK, move on to next dataset.

To correct the fit of the contour plot over the null image, use the commands "rotrows" and "rotcols" to move the contour plot:

Open the notebook for the null data by selecting the null set and using Numbers→ Notebook (or Command-N).  Add lines as needed.  A negative sign moves the plot left and up.

***Keep track of the shifts you make because you will need to delete some of the shifted columns and rows later.***

***The V field must be changed the same amount as the U field.***

Example: To shift the plot "Uaa" three columns down, type:
Uaa_dsp_shift=rotcols(Uaa_dsp,3)
Example: To shift the plot "Uaa" three columns up and one row right:
Uaa_dsp_shift=rotrows(rotcols(Uaa_dsp,1),-3)

Press Command-R to calculate from notebook, creating a dataset called "Uaa_dsp_shift". Regenerate the plot from this using Command-K, then cut and paste over the null field to check the fit. Adjust the notebook settings as needed. Once the fit is good, save the "Uaa_dsp_shift" file, not the other files. Repeat as needed for all of the displacement files.

After all of the null fields and test fields are synchronized, you will need to rename the "_shift" files. This *cannot* be done simply by renaming the file. Open up all of the files that have the name "_shift", and open the notebook of one of them. Enter the command "*newfile=oldfile*", ie "Uaa_dsp=Uaa_dsp_shift". This will overwrite the _dsp file with the synchronized data.

Next, to delete the shifted datapoints, open the data windows. Select the data from the next line or column over from the shifted data, copy, and paste into shifted data. Backup files.

If significant synchronization changes are performed, common data areas must be extracted from all of the files.


**Step 3:  Subtract Null Data from Test data**

Open a null and test data set for both the U and V fields.  This should be four files: a U null and test, and a V null and test.  Then, open a new dataset by clicking on File→New, and name the new dataset "Formula_Template".  Save the dataset, then open the notebook.

The following notebook entries perform the operations of rotating the specimen 90° CCW (to make specimen data appear spatially correct), subtracting the null from the test data, changes signs if necessary, and multiplies by a zero mask.

*Ideally, use the same zero field for both U and V fields as executed with the Zero_a command line below.  (Execute each of the lines below individually or highlight multiple lines to run using Ctrl-R)  The rowflip() and transpose() commands do not have to be used if the specimen configuration is correct.  See note below.*

Zero_a=rowflip(transpose(NEmask(Ua_dsp,0)*NEmask(Uaa_dsp,0)*NEmask(Va_dsp,0)
*NEmask(Vaa_dsp,0)))
    Ua245=rowflip(transpose(Uaa_dsp-Ua_dsp+0.0+.0000))*Zero_a
    Va245=rowflip(transpose(Vaa_dsp-Ua_dsp+0.0+.0000))*Zero_a
    Print(min(Ua245))
    Print(min(Va245))

*or*

Zero_a=
NEmask(Ua_dsp,0)*NEmask(Uaa_dsp,0)*NEmask(Va_dsp,0)*NEmask(Vaa_dsp,0)
 Ua245= (Uaa_dsp-Ua_dsp+0.0+.0000)*Zero_a
 Va245= (Vaa_dsp-Ua_dsp+0.0+.0000)*Zero_a
 Print(min(Ua245))
 Print(min(Va245))

***Record U and V minimums after running the calculations.***

Notes:
-The rowflip and transpose commands are necessary only to correct camera/specimen orientation.

The first line creates a NEmask in each of the sets, setting all points where no data occurs to zero. Ua245 and Va245 are the new datasets created by the subtraction of the null field from the test field. These files can be named as appropriate.

Run these calculations from the notebook once. In the notebook, a min value for Ua245 and Va245 will be printed. Cut and paste these values into the second and third lines over the 0.0 section. Do not use the negative sign from the minimum value. Change .0000 to .00001. Rerun these calculations to get the actual displacement data. Generate images of Ua245 and Va245, check the signs (This is accomplished during Moiré data collection. For details see David. Alternatively, the signs can be checked with an accurate analysis). If the displacements signs are incorrect, multiply the dataset by –1 using the notebook. Save the final displacement files.

Make a backup of these files in a separate directory.


**Step 4:  Create a Global Zero Mask, and Fill Data**


To make all "zero" data points equal to zero, use the mask functions. For example, if the zero points are equal to 6.03e-04, open the notebook and type:
 Junk=GTmask(U, 6.03e-04)
 U_245=Junk*U

Open the Formula_Template notebook and use the following:
 Zero_Mask=NEmask (U_245,0)  where U_245 is the filename

Generate an image of the mask, make sure rectangle sizes are all 1:1, and save it as a .tif file. Open this file in Adobe Photoshop and fill in black spots as needed.

Return to Transform. Open the file (ie, U_245)
 Numbers→Fill Missing Data, select Weighted Fill and Linear Interpolation.
This creates a file with extension "_md".

Open notebook of file.

       U245=U245_md*Zero_Mask

## Step 5: Smooth Data

Copy appropriate zero mask file to name "Zero_mask"

Open the files U245 and Zero_Mask.

Click on the U245 data set and go to Macros→Smoothing (Generates U245_s)

Enter number of desired smoothing passes. (typical value may be 25 or higher)

## Step 6: Determine Scale and Coordinate System

Open the zero mask.
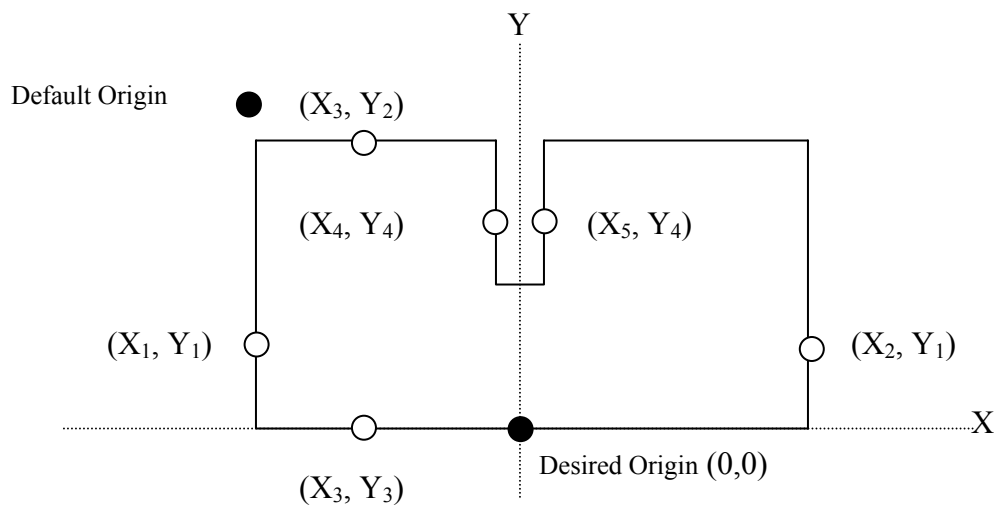


**Figure 202. Scaling and coordinate system schematic for Moiré data processing**

Pick a point on the specimen and its corresponding point on the image to use as your coordinate system origin.
Determine the coordinates of several points on the image and measure the corresponding points as closely as possible on the specimen to determine the mm-to-pixel ratio.

If only a single dimension can accurately be determined on the specimen, assume a 1:1 correspondence in the x and y directions, refer to Figure 202.

Open the notebook and generate a scale_mask

Scale_mask=Zero_mask*0+1

Change the entry corresponding to the new origin that was selected in the Scale_mask from a "1" to a "2" so that the new origin can be checked after running the scaling macro.

Calculate the new top left coordinate of the data set (which should be the coordinates based on the default origin.)

Go to the macros pull down menu and run d_scaling macro.  New file should have your desired origin at (0,0).  Check the new file to be sure that the "2" entry corresponds to the desired new origin.  If correct, change the "2" entry back to a "1".

Note: The required scale factor could be negative, due to the fact that the computer display has a "negative" coordinate system  (neg,neg) quadrant.

On the zero mask, go to Numbers→Generate Scales  (Creates Zero_Mask_s).  Close the original (Zero_Mask) and open the notebook.

Zero_mask=Scale_Mask*Zero_Mask_s
U=Scale_Mask*U245_s

Note: Generate Scales is performed to create a duplicate file with a different name because the notebook calculations can't create a file with the same name.

Backup files.


**Step 7:  Create Strains**

Open formula_template notebook.

Exx=ddx(U)*EQmask(smooth(NEmask(U,0),1),1)
Eyy=ddy(V)*EQmask(smooth(NEmask(V,0),1),1)
Gxy=(ddx(V)+ddy(U))*EQmask(smooth(NEmask(U,0),1),1)

Note: The 'NEmask(U,0)' and the 'NEmask(V,0)' can be replaced with the Zero_mask if the same zero field is use for both the U and V displacements.

The EQmask portion of the equations is done to eliminate edge differentiation errors.

**Step 8:  Compare Data**

A few choices present themselves:

1.  After processing of experimental data is complete, perform the same processing with the analytical model data, then compare

OR

2.  Process analytical data and experimental data side-by-side from the beginning.

Then compare strains with micrographs, etc to obtain the necessary data output.

## Appendix E:  BSAM Results for Tensile Load and Residual Strain Models

All of the full field strain views are shown on the same color scale (Figure 27), white is used to show strains larger than the set maximum bound and black is used to show all strains below the set lower bound with the colors of the rainbow (red, orange, yellow, green, blue, and indigo) distinguishing the strains in between the maximum and minimum bounds.  The upper and lower bounds for all full fields shown are 0.008 and -0,008 micro strain respectively.

## BSAM Results for Tensile Loaded Model



**Figure 203.  Full field $\varepsilon_{xx}$ strains extracted from BSAM at edge of model for tensile loaded specimen**
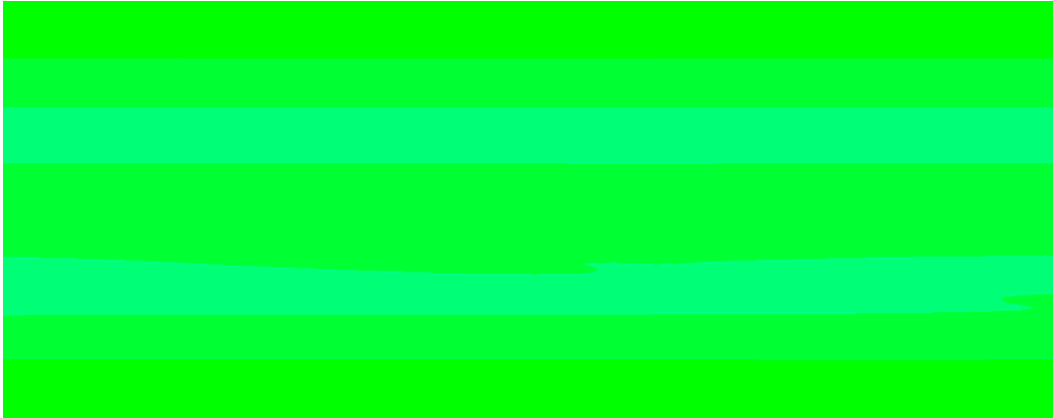
**Figure 204. Full field $\varepsilon_{xy}$ strains extracted from BSAM at edge of model for tensile loaded specimen**
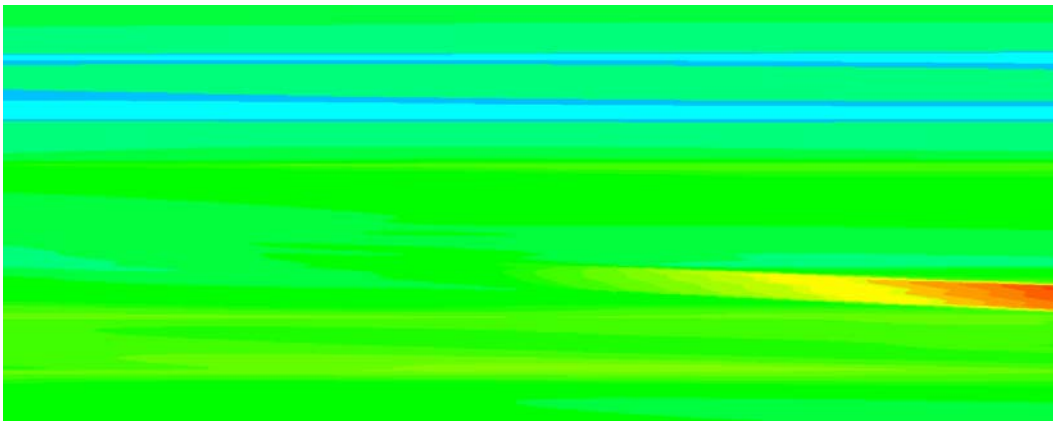


**Figure 205. Full field $\varepsilon_{xz}$ strains extracted from BSAM at edge of model for tensile loaded specimen**



**Figure 206. Full field $\varepsilon_{yy}$ strains extracted from BSAM at edge of model for tensile loaded specimen**
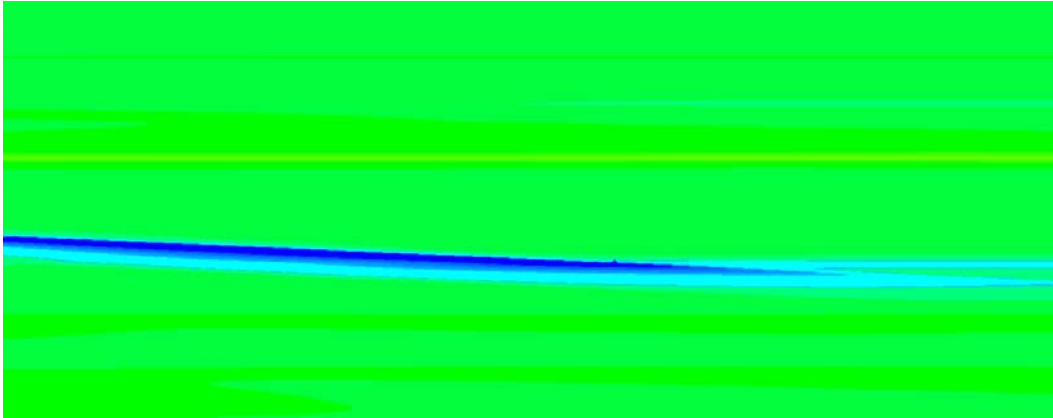
**Figure 207. Full field ε$_{yz}$ strains extracted from BSAM at edge of model for tensile loaded specimen**
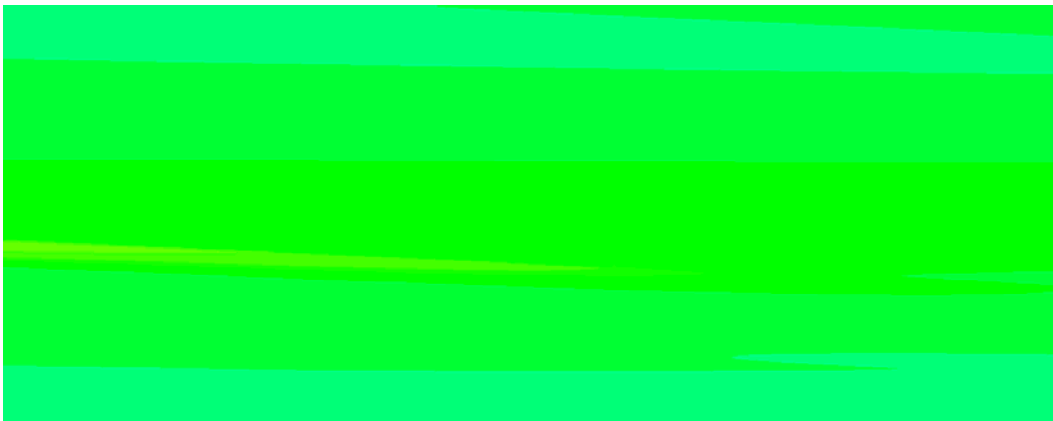


**Figure 208. Full field ε$_{zz}$ strains extracted from BSAM at edge of model for tensile loaded specimen**



**Figure 209. Full field ε$_{xx}$ strains extracted from BSAM at ¼" into model width for tensile loaded specimen**
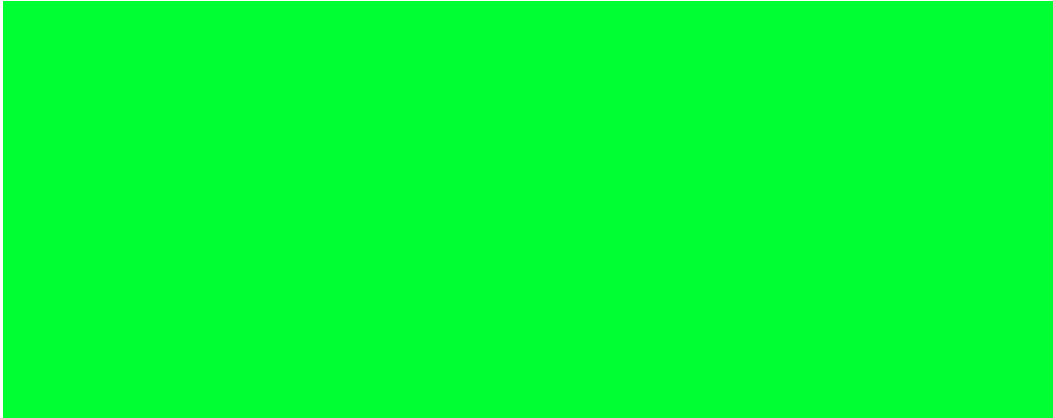
**Figure 210. Full field $\varepsilon_{xy}$ strains extracted from BSAM at ¼" into model width for tensile loaded specimen**



**Figure 211. Full field $\varepsilon_{xz}$ strains extracted from BSAM at ¼" into model width for tensile loaded specimen**



**Figure 212. Full field $\varepsilon_{yy}$ strains extracted from BSAM at ¼" into model width for tensile loaded specimen**
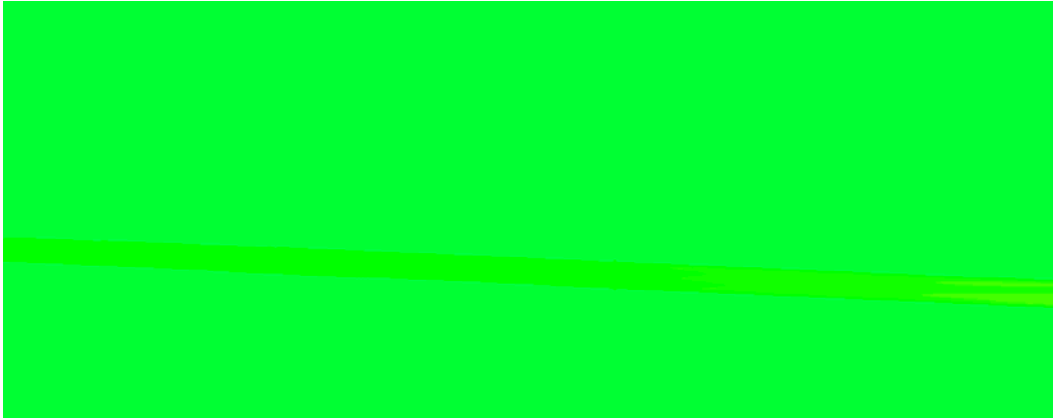
**Figure 213.  Full field $\varepsilon_{yz}$ strains extracted from BSAM at ¼” into model width for tensile loaded specimen**
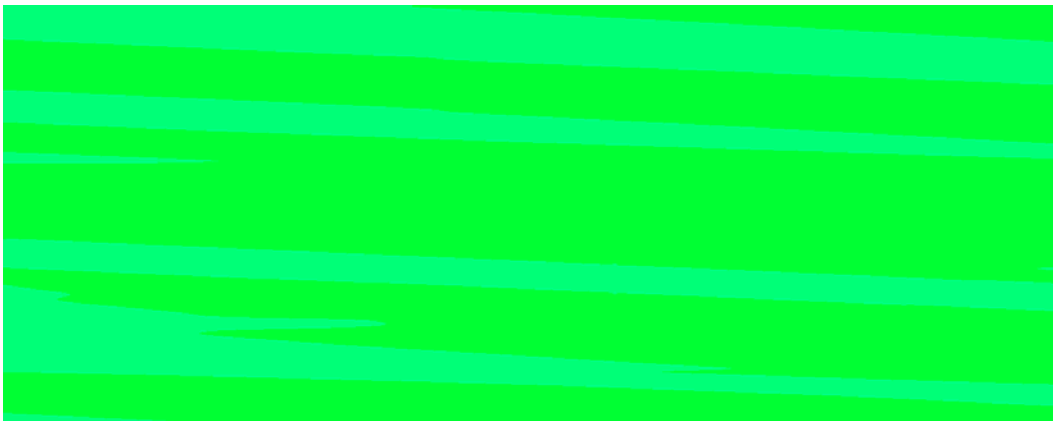


**Figure 214.  Full field $\varepsilon_{zz}$ strains extracted from BSAM at ¼” into model width for tensile loaded specimen**

**BSAM Results for Residual Strain Models**
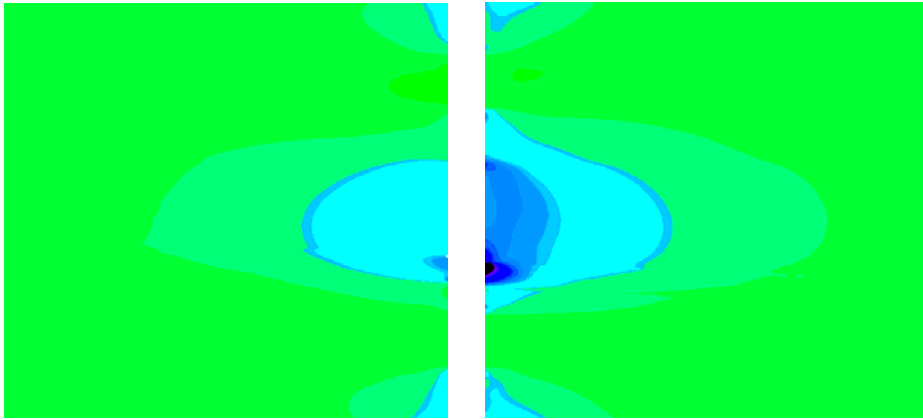


**Figure 215. Full field $\varepsilon_{xx}$ strains extracted from BSAM at edge of model for residual strain specimens**
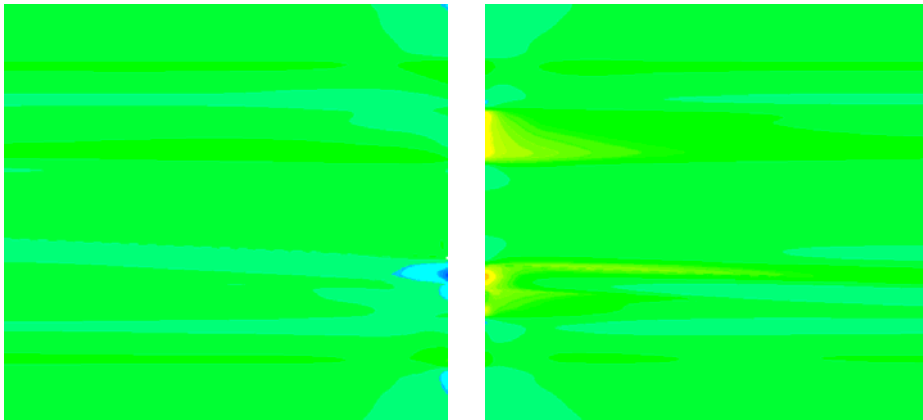


**Figure 216. Full field $\varepsilon_{xy}$ strains extracted from BSAM at edge of model for residual strain specimens**

184
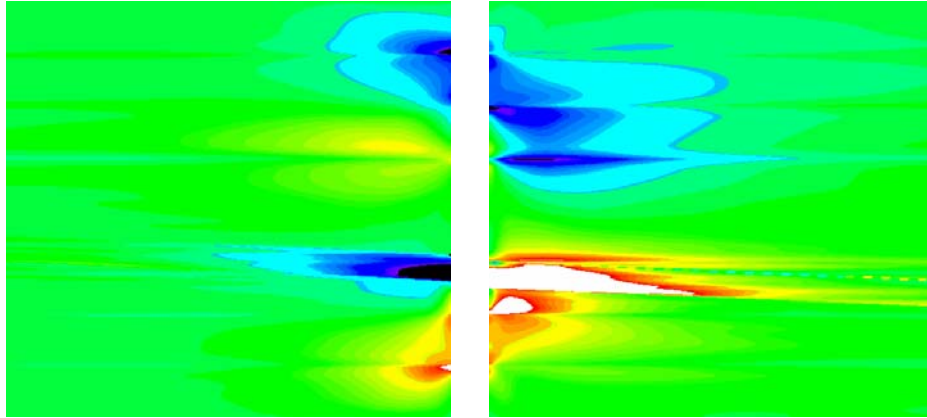
**Figure 217. Full field $\varepsilon_{xz}$ strains extracted from BSAM at edge of model for residual strain specimens**
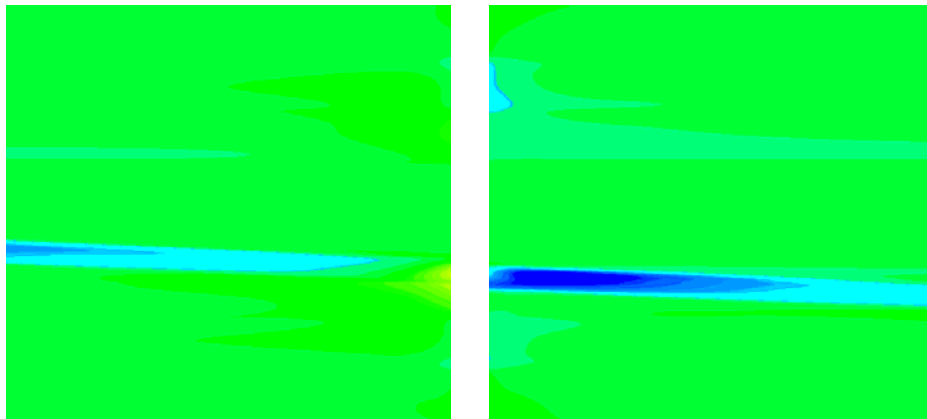


**Figure 218. Full field $\varepsilon_{yy}$ strains extracted from BSAM at edge of model for residual strain specimens**
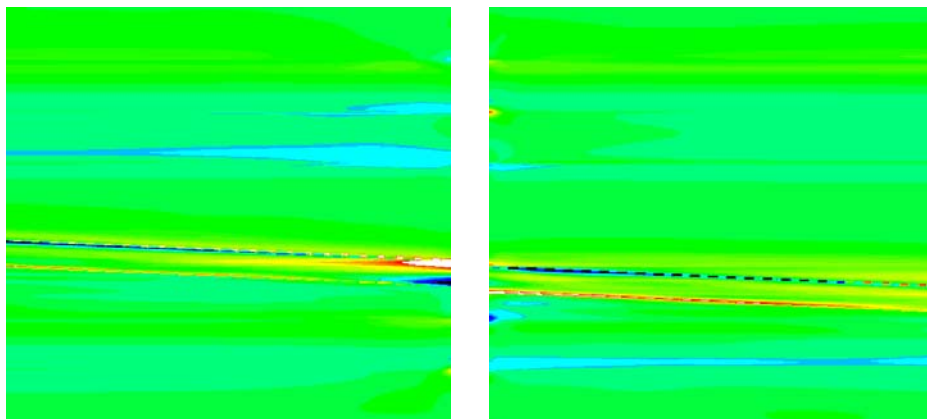


**Figure 219. Full field $\varepsilon_{yz}$ strains extracted from BSAM at edge of model for residual strain specimens**
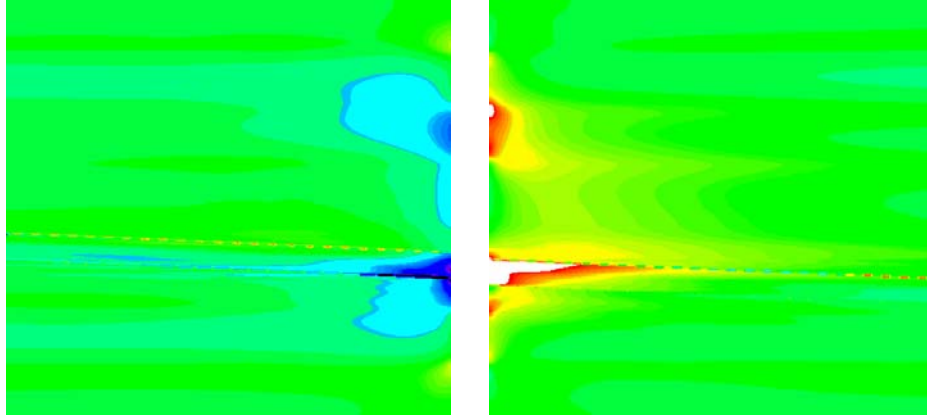
**Figure 220.  Full field $\varepsilon_{zz}$ strains extracted from BSAM at edge of model for residual strain specimens**
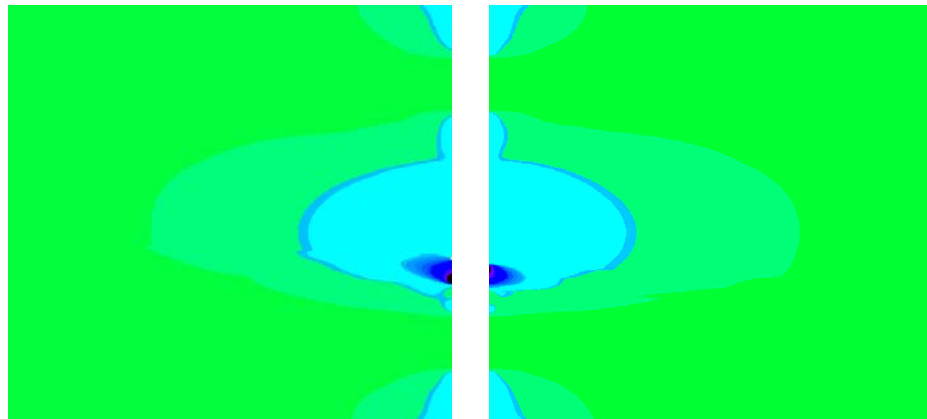


**Figure 221.  Full field $\varepsilon_{xx}$ strains extracted from BSAM at ¼" into width of model for residual strain specimens**
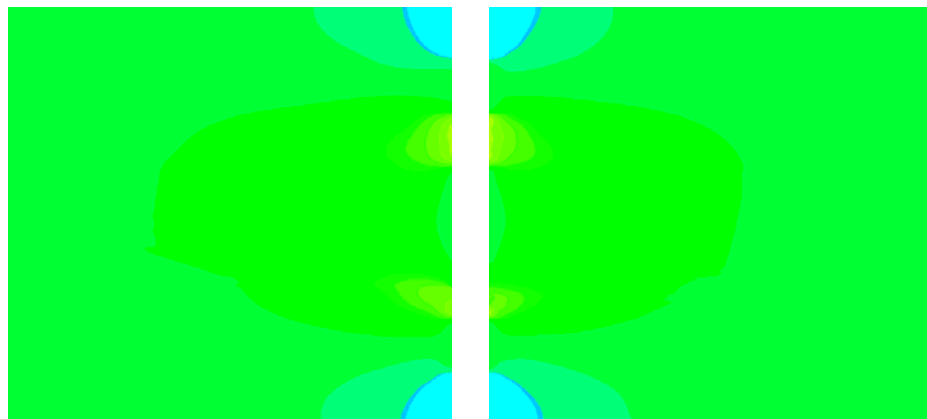


**Figure 222.  Full field $\varepsilon_{xy}$ strains extracted from BSAM at ¼" into width of model for residual strain specimens**

**Figure 223. Full field $\varepsilon_{xz}$ strains extracted from BSAM at ¼" into width of model for residual strain specimens**
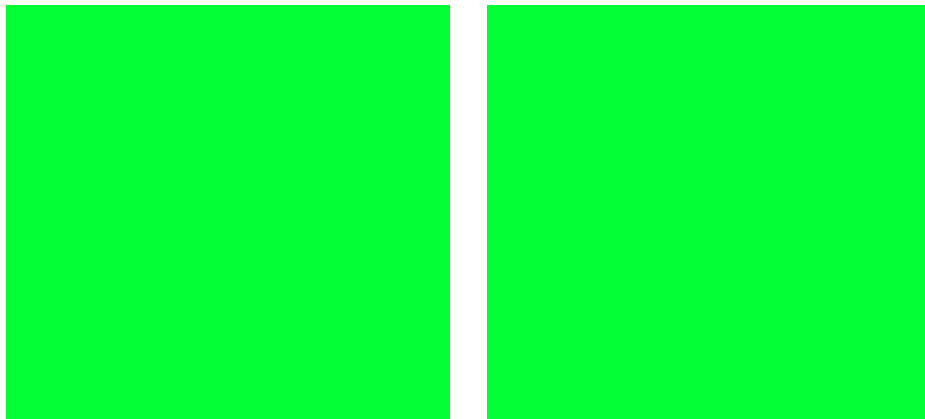


**Figure 224. Full field $\varepsilon_{yy}$ strains extracted from BSAM at ¼" into width of model for residual strain specimens**
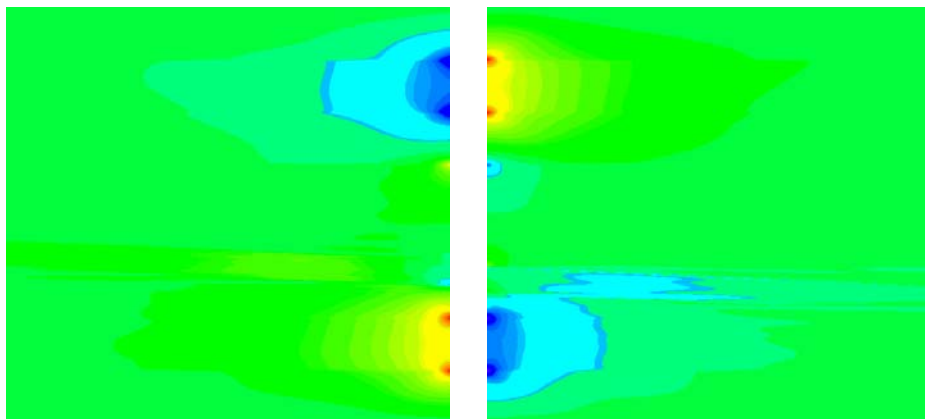


**Figure 225. Full field $\varepsilon_{yz}$ strains extracted from BSAM at ¼" into width of model for residual strain specimens**
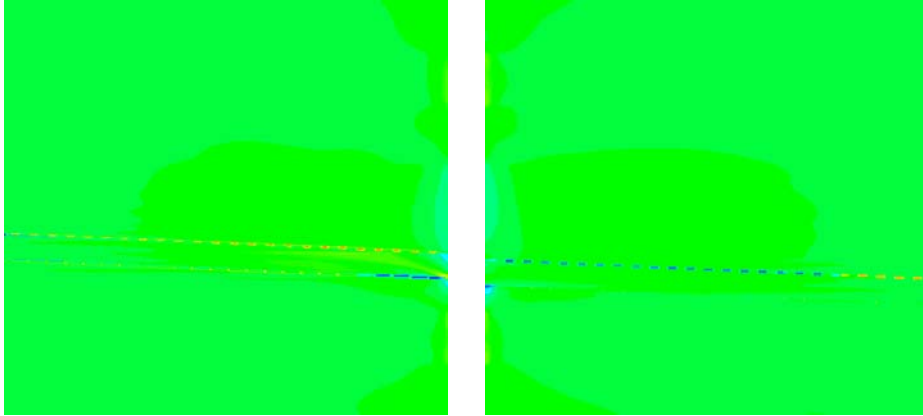
**Figure 226.  Full field ε_zz strains extracted from BSAM at ¼" into width of model for residual strain specimens**
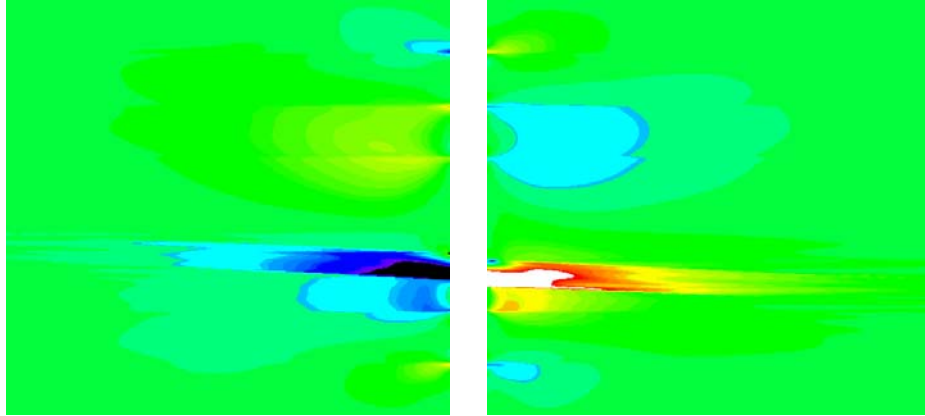
# Bibliography

Adkins, David Wilson. *Strength and Mechanics of Bonded Scarf Joints for Repairs of Composite Materials*. PhD Dissertation, CCM-82-14. Center for Composite Materials, College of Engineering, University of Delaware, Newark DE, December 1982 (AAG8309886).

Ahn, Sung-Hoon ad George S. Spinner. *Repair of Composite Laminates*. DOT/FAA/AR-00/46. U.S. Department of Transportation, Federal Aviation Administration, Office of Aviation Research, Washington DC, December 2000 (ADA388309).

Baker, Alan, Stuart Dutton, and Donald Kelly. *Composite Materials for Aircraft Structures*. Reston VA: American Institute of Aeronautics and Astronautics, Inc., 2004.

Bowman, Keith Bryan. "Development of an Experimental Technique to Evaluate the Residual Stresses on the Free-edges of Layered Material Systems", PhD Dissertation. University of Dayton, Dayton OH, 2001.

Charalambides, M.N., R. Hardouin, A.J. Kinloch, and F.L. Matthews. "Adhesively-bonded Repairs to Fibre-composite Materials I: Experimental" ", *Composites: Part A*, 29A:1371-1381 (1998).

Charalambides, M.N., R. Hardouin, A.J. Kinloch, and F.L. Matthews. "Adhesively-bonded Repairs to Fibre-composite Materials II: Finite Element Modelling" ", *Composites: Part A*, 29A:1383-1396 (1998).

Chotard, T.J., J. Pasquiet, and M.L. Benzeggagh. "Residual Performance of Scarf Patch-Repaired Pultruded Shapes Initially Impact Damaged", *Composite Structures*, 53:317-331 (2001).

Colleary, Amanda, Intern. "Data Processing and Image Analysis Guideline for Moiré Interferometry." Guide written for Greg Schoeppner by studying David Mollenhauer during data processing. Materials Directorate, Air Force Materials Laboratory, Wright-Patterson AFB OH, August 2003.

Hart-Smith, L.J. *Adhesive-Bonded Scarf and Stepped-Lap Joints*. Contract NAS1-11234. Hampton VA: Langley Research Center, January 1973 (NASA CR 112237).

Herakovich, Carl T. *Mechanics of Fibrous Composites.* New York: John Wiley & Sons, Inc., 1998.

Hinrichsen, R.L. and A.N. Palazotto. "Use of a Cubic Spline Function in Finite Elements", *Mathematical and Computer Modelling*, 10(1):37-47 (1988).

Hinrichsen, R.L. and A.N. Palazotto. "Nonlinear Finite Element Analysis of Thick
     Composite Plates Using Cubic Spline Functions", *American Institute of
     Aeronautics and Astronautics Journal*, 24:1836-1842 (November 1986).

Iarve, E.V.. Spline Variational Three Dimensional Stress Analysis of Laminated
     Composite Plates with Open Holes, *International Journal of Solids and
     Structures*, 33(14):2095-2118 (1996).

Iarve, E.V. and N.J. Pagano. "Singular Full-field Stresses in Composite Laminates with
     Open Holes", *International Journal of Solids and Structures,* 38(1):1-28 (2001).

Knox, E.M, S. Lafferty, M.J. Cowling, and S.A. Hashim. "Design Guidance and
     Structural Integrity of Bonded Connections in GRE Pipes", *Composites:  Part A:
     Applied Science and Manufacturing*, 32:231-241 (2001).

Lassahn, G., P. Taylor, V. Deason, and J. Lassahn, "Multiphase Fringe Analysis with
     Unknown Phase Shifts" *Optical Engineering*, 33(6):2039-2044 (1994).

Mollenhauer, David H. *Interlaminar Deformation at a Hole in Laminated Composites:  A
     Detailed Experimental Investigation Using Moiré Interferometry*.  PhD
     dissertation.  Virginia Polytechnic Institute and State University, Blacksburg VA,
     20 August 1997.

Mollenhauer, D.M. and M.W. Holl. "Characterization of Bundle-Level Residual Strains
     in Woven Composites Using Moiré Interferometry," 39th International SAMPE
     Symposium, 39: 2894-2904 (11-14 April 1994).

Mortensen, F. and O.T. Thomsen. "Analysis of Adhesive Bonded Joints:  A Unified
     Approach", *Composites Science and Technology*, 62:1011-1031 (2002).

Odi, Randolph A. and Clifford M. Friend. "An Improved 2D Model for Bonded
     Composite Joints", *International Journal of Adhesion and Adhesives*, 24:389-405
     (2004)

Post, Daniel, Bongtae Han, and Peter Ifju.  *High Sensitivity Moire: Experimental Anlaysis
     for Mechanics and Materials*.  New York: Springer-Verlag, 1994.

Schoeppner, G.A., D.M. Mollenhauer, and E.V. Iarve.  "Prediction and Measurement of
     Residual Strains for a Composite Bonded Joint", *Mechanics of Composite
     Materials*, 40:119-134 (February 2004)

Soutis, C. and F.Z. Hu. "A 3-D Failure Analysis of Scarf Patch Repaired CFRP Plates",
     *American Institute of Aeronautics and Astronautics, Inc.*, 1943:1971-1977 (1998).

*Unbrako$^\circledR$ Socket Screws*.  Product Catalog Federal Supply Code Manufacturers 56878. no location:SPS Technologies, 1988.

Wang, B.S, F.P. Chiang, and S.Y. Wu. "Whole-Field Residual Stress Measurement in Rail Using Moiré Interferometry and Twyman/Green Interferometry via Thermal Annealing," *Experimental Mechanics*, 39(1):71-76 (1999).

Zou, G.P., K. Shahin, and F. Taheri. "An Analytical Solution for the Analysis of Symmetric Composite Adhesively Bonded Joints", *Composite Structures*, 65:499-500 (2004).

**Vita**

Captain Benjamin M. Cook graduated from Auburn High School in Auburn, Washington.  After graduation he entered undergraduate studies at Brigham Young University, located in Provo, Utah where he graduated with a Bachelor of Science degree in Mechanical Engineering in April 1997.  He was commissioned through Detachment 855 AFROTC at Brigham Young University.

His first assignment in May of 1997 was at Robins Air Force Base in Warner Robins, GA as a civil engineer for the 78th Civil Engineering Group.  In May 2000 he was assigned to the Defense Contract Management Agency located in Sunnyvale, California.  In August 2003 his third assignment was at Wright-Patterson Air Force Base in Dayton, Ohio where he entered the Graduate School of Engineering and Management at the Air Force Institute of Technology.  Upon graduation in March 2005, he will be assigned to Hill Air Force Base working for the Advanced Composites Office, Air Force Research Labs.

| REPORT DOCUMENTATION PAGE | | | *Form Approved* <br> *OMB No. 074-0188* |
|---|---|---|---|
| The public reporting burden for this collection of information is estimated to average 1 hour per response, including the time for reviewing instructions, searching existing data sources, gathering and maintaining the data needed, and completing and reviewing the collection of information. Send comments regarding this burden estimate or any other aspect of the collection of information, including suggestions for reducing this burden to Department of Defense, Washington Headquarters Services, Directorate for Information Operations and Reports (0704-0188), 1215 Jefferson Davis Highway, Suite 1204, Arlington, VA 22202-4302. Respondents should be aware that notwithstanding any other provision of law, no person shall be subject to an penalty for failing to comply with a collection of information if it does not display a currently valid OMB control number. **PLEASE DO NOT RETURN YOUR FORM TO THE ABOVE ADDRESS.** | | | |

| 1. REPORT DATE *(DD-MM-YYYY)* <br> 21 MAR 2005 | 2. REPORT TYPE <br> **Master's Thesis** | | 3. DATES COVERED *(From – To)* <br> Aug 2003 – Mar 2005 |
|---|---|---|---|
| 4.    TITLE AND SUBTITLE <br><br> Experimentation and Analysis of Composite Scarf Joint | | | 5a. CONTRACT NUMBER |
| | | | 5b. GRANT NUMBER |
| | | | 5c. PROGRAM ELEMENT NUMBER |
| 6.    AUTHOR(S) <br><br> Cook, Benjamin M. ., Captain, USAF | | | 5d. PROJECT NUMBER |
| | | | 5e. TASK NUMBER |
| | | | 5f. WORK UNIT NUMBER |
| 7. PERFORMING ORGANIZATION NAMES(S) AND ADDRESS(S) <br> Air Force Institute of Technology <br> Graduate School of Engineering and Management (AFIT/EN) <br> 2950 Hobson Way <br> WPAFB OH 45433-7765 | | | 8. PERFORMING ORGANIZATION REPORT NUMBER <br><br> AFIT/GA/ENY/05-M03 |
| 9. SPONSORING/MONITORING AGENCY NAME(S) AND ADDRESS(ES) <br> AFRL/Material and Manufacturing Directorate <br> Attn: Dr. Greg Schoeppner <br> 2941 Hobson Way <br> WPAFB OH 45433-7750   DSN: 59072   PHONE: (937) 255-9072 | | | 10. SPONSOR/MONITOR'S ACRONYM(S) |
| | | | 11. SPONSOR/MONITOR'S REPORT NUMBER(S) |

| 12. DISTRIBUTION/AVAILABILITY STATEMENT <br>     APPROVED FOR PUBLIC RELEASE; DISTRIBUTION UNLIMITED |
|---|
| 13. SUPPLEMENTARY NOTES |

**14. ABSTRACT**

Composite bonded scarf repairs were examined by experimentally measuring and analytically predicting the residual curing strains and strains due to mechanical loading. To accomplish this a three prong approach was used: a full strain field through a repaired laminate's thickness was measured for both a loaded specimen and a specimen with the residual strain released, models were developed for comparison to both states, and data was collected for large tensile test specimens at various stages of being scarf repaired. A ~14:1 straight scarfed one-inch wide specimen was used to collect Moiré interferometry data to calculate a full strain field due to mechanical loading and strain release. A three-dimensional thermo mechanical linear elastic analysis using an Air Force Research Laboratory in-house stress analysis program B-Spline Analysis Method (BSAM) results were correlated to the Moiré interferometry test results. Three large tensile test specimens were tested as manufactured, three were tested with a scarfed hole in the center, and the remaining were tested with a scarf repair centered on a hole in the center. The strain gage results from the panels are presented. An additional feature of this work was to document each of the difficulties present in the given methods incorporated in this research.

**15. SUBJECT TERMS**
   Scarf Joint, Composite Repair, Full Field Strain, BSAM, B-Spline Analysis Method, Through Thickness Strain
   Scarf Repair, Moiré Interferometry, 3-D Strain, Residual Strain, Tensile Testing

| 16. SECURITY CLASSIFICATION OF: | | | 17. LIMITATION OF ABSTRACT | 18. NUMBER OF PAGES | 19a. NAME OF RESPONSIBLE PERSON <br> ANTHONY N PALAZOTTO |
|---|---|---|---|---|---|
| REPORT <br> **U** | ABSTRACT <br> **U** | c. THIS PAGE <br> **U** | **UU** | 215 | 19b. TELEPHONE NUMBER *(Include area code)* <br> (937) 255-3069, e-mail: <br> ANTHONY.PALAZOTTO@afit.edu |

**Standard Form 298 (Rev: 8-98)**
Prescribed by ANSI Std. Z39-18